



**HAL**  
open science

# Measurement of the $\eta c (1S)$ production cross-section via the decay $\eta c$ to proton-antiproton final state

Maksym Teklishyn

► **To cite this version:**

Maksym Teklishyn. Measurement of the  $\eta c (1S)$  production cross-section via the decay  $\eta c$  to proton-antiproton final state. High Energy Physics - Experiment [hep-ex]. Université Paris Sud - Paris XI, 2014. English. NNT: 2014PA112224 . tel-01151708

**HAL Id: tel-01151708**

**<https://theses.hal.science/tel-01151708>**

Submitted on 13 May 2015

**HAL** is a multi-disciplinary open access archive for the deposit and dissemination of scientific research documents, whether they are published or not. The documents may come from teaching and research institutions in France or abroad, or from public or private research centers.

L'archive ouverte pluridisciplinaire **HAL**, est destinée au dépôt et à la diffusion de documents scientifiques de niveau recherche, publiés ou non, émanant des établissements d'enseignement et de recherche français ou étrangers, des laboratoires publics ou privés.



# Université Paris-Sud

Ecole Doctorale Particules, Noyaux et Cosmos — ED 517

Laboratoire de l'Accélérateur Linéaire

Physique

THÈSE DE DOCTORAT

présentée par

**Maksym Teklishyn**

**Measurement of the  $\eta_c(1S)$  production cross-section  
via the decay  $\eta_c \rightarrow p\bar{p}$**

La mesure de la section efficace de la production  $\eta_c(1S)$  avec la  
désintégration  $\eta_c \rightarrow p\bar{p}$

Soutenue le 22 septembre 2014 devant le Jury composé de:

Sergey Barsuk	Directeur de thèse
Valeri Khoze	Examinateur
Giulia Manca	Rapporteur
Ginés Martínez	Rapporteur
Pavel Pakhlov	Examinateur
Achille Stocchi	Président
Hermine Woehri	Examinateur

# Contents

Contents	4
Introduction	5
<b>1 Heavy quarkonium</b>	<b>7</b>
1.1 Elementary particles and fundamental forces . . . . .	7
1.1.1 Introduction . . . . .	7
1.1.2 Elementary particles in the Standard Model . . . . .	8
1.1.3 Electroweak interaction . . . . .	9
1.1.4 Strong interaction . . . . .	13
1.2 Quark systems . . . . .	16
1.2.1 Introduction . . . . .	16
1.2.2 Mesons and baryons . . . . .	17
1.2.3 Exotic states . . . . .	21
1.3 Previous quarkonium studies . . . . .	22
1.4 Spectroscopy . . . . .	23
1.5 Quarkonium production and effective theories . . . . .	27
1.5.1 Prompt production . . . . .	27
1.5.2 Charmonium production from $b$ -hadron decays . . . . .	33
1.6 Decay modes . . . . .	35
<b>2 Quarkonium production</b>	<b>41</b>
2.1 Introduction . . . . .	41
2.2 $J/\psi$ production in $b$ -hadron decays . . . . .	42
2.2.1 Production at hadron machines . . . . .	42
2.2.2 Production at the B-factories . . . . .	43
2.3 $\eta_c$ production in $b$ -hadron decays . . . . .	44

2.4	Production of other charmonium states in $b$ -hadron decays . . . . .	45
2.5	Prompt $J/\psi$ production . . . . .	46
2.6	Prompt $\eta_c$ and $\eta_b$ production . . . . .	47
2.7	Studies of the $\eta_c$ properties . . . . .	47
<b>3</b>	<b>The LHCb experiment</b>	<b>51</b>
3.1	The Large Hadron Collider . . . . .	51
3.2	The LHCb detector . . . . .	52
3.2.1	Tracking system . . . . .	54
3.2.2	Particle identification . . . . .	57
3.2.3	Trigger . . . . .	64
3.2.4	LHCb physics program . . . . .	66
<b>4</b>	<b>Charmonim production measurements with <math>p\bar{p}</math></b>	<b>68</b>
4.1	Introduction . . . . .	68
4.2	Monte-Carlo simulation and data sets . . . . .	69
4.3	Trigger and stripping . . . . .	69
4.4	Selection criteria . . . . .	70
4.5	Analysis procedure . . . . .	72
4.5.1	Effect from cross-talk between the samples . . . . .	74
4.5.2	$J/\psi$ polarisation . . . . .	75
4.5.3	Fit of the invariant $p\bar{p}$ mass distribution . . . . .	76
4.5.4	Signal parametrisation . . . . .	77
4.5.5	Background parametrisation . . . . .	80
4.5.6	Possibility of alternative approach . . . . .	81
4.6	Inclusive $\eta_c$ and $J/\psi$ production in $b$ -hadron decays . . . . .	83
4.6.1	Analysis with the 2011 and 2012 data samples . . . . .	83
4.6.2	Analysis with the combined data sample . . . . .	85
4.7	Prompt charmonium production . . . . .	85
4.7.1	Fit with Gaussian constraints on the $J/\psi$ and $\eta_c$ masses . . . . .	86
4.7.2	Fit with the released $J/\psi$ and $\eta_c$ masses . . . . .	89
4.7.3	Possible background description with the event mixing technique . . . . .	91
4.8	Systematic uncertainties . . . . .	93
4.8.1	Inclusive $\eta_c$ and $J/\psi$ production in $b$ -hadron decays . . . . .	93
4.8.2	Prompt charmonium production . . . . .	97
4.9	Results on the $\eta_c$ state production . . . . .	102

---

4.9.1	Ratios of the inclusive yield from $b$ -hadron decays . . . . .	103
4.9.2	Prompt production ratios . . . . .	104
4.9.3	$J/\psi$ production cross-section in the required kinematic region . . . . .	105
4.9.4	$\eta_c$ production cross-section . . . . .	108
4.9.5	Dependence of the $J/\psi$ and $\eta_c$ production cross-section on transverse momentum . . . . .	109
4.9.6	Summary . . . . .	110
4.10	The $\eta_c$ and $J/\psi$ angular distributions . . . . .	112
4.11	Measurement of the $\eta_c$ mass and natural width . . . . .	116
4.12	Search for prompt production of the $\chi_{ci}$ and $h_c$ states . . . . .	120
<b>5</b>	<b>Summary</b>	<b>124</b>
<b>6</b>	<b>List of the main results</b>	<b>128</b>
	<b>Appendix</b>	<b>131</b>
.1	Selection criteria optimisation . . . . .	131
.2	$J/\psi$ cross-section in $p_T$ and rapidity bins . . . . .	134
	<b>List of Figures</b>	<b>144</b>
	<b>List of Tables</b>	<b>147</b>
	<b>Bibliography</b>	<b>156</b>

# Introduction

This thesis addresses a study of the  $\eta_c$  (1S) charmonium state using decays to proton-antiproton final state. The production cross-section of the  $\eta_c$  meson in parton interactions and in  $b$ -hadron decays are reported.

The Standard Model, which is the main theoretical framework of the elementary particles and their interactions, provides precise predictions in the electroweak sector, reaching up to  $\mathcal{O}(10^{-8})$  precision for quantum electrodynamics. A compatible level of precision is obtained also for high-energy (more than hundreds of MeV) strong interactions. However, for the medium energy range between tens and hundreds of MeV the coupling constant of the strong interaction  $\alpha_s$  is compatible with one, so perturbative calculations are not possible. The quark-quark interactions occur in hadrons at this energy scale. Quarkonium is a composite of a heavy quark and its own antiquark. It is the simplest system to probe such kind of physics. Two quarkonium systems, charmonium  $c\bar{c}$  and bottomonium  $b\bar{b}$  are used for QCD studies.

Since its discovery in 1974, the quarkonium system became an important tool for precision quantum chromodynamics tests. The natural widths of the states below the  $D\bar{D}$  threshold for charmonia and the  $B\bar{B}$  threshold for bottomonia are in the range of hundreds of keV to tens of MeV. Quarkonium states thus can be properly explored experimentally. Using non-relativistic potential models, that include a colour Coulomb term at short distances and a linear scalar confining term at large distances. The  $1S$ ,  $1P$  and  $2S$   $c\bar{c}$  levels and up to  $3S$  level for  $b\bar{b}$  systems can be built. Spin-orbit and spin-spin interactions manifest themselves in the splitting of states within these multiplets, and the observed states are consistent with the predictions of a one gluon exchange model.

Recent results at the  $e^+e^-$  experiments operating at a centre-of-mass energy corresponding to  $\Upsilon(4S)$  resonance (BaBar and Belle experiments), revived interest in studies of quarkonium properties. In addition, new precision results were reported by an experiment, dedicated to charm physics, performed on  $e^+e^-$  collider, BESIII, and experiments, operating at the Tevatron and LHC hadron machines.

In this thesis, the  $\eta_c$  charmonium state is studied. The  $\eta_c$  meson is a 1S charmonium state. It is the lightest  $c\bar{c}$  compound, which was discovered in 1980. At present, limited precision results are available, mainly because of the low production cross-section at the  $e^+e^-$  machines comparing to the  $J^{PC} = 1^{--}$  states. Using decays to  $p\bar{p}$  final states, the  $\eta_c$  cross-section from parton interactions and the inclusive yield from  $b$ -hadron decays is measured for the first time. Recent improvement in the world average precision due to the new BESIII results caused a tension with the previous results. The value of the relative inclusive  $\eta_c$  production to  $J/\psi$  is important for distinguishing between a variety of theoretical models.

The LHCb experiment is well designed for studies of quarkonia decays to hadronic final states. The precision tracking system provides a reconstruction of charmonium decay vertex, which is well distinguished from the vertex of  $pp$  interaction for charmonia coming from  $b$ -hadron decays. Powerful particle identification distinguishes between the charged (pseudo-)stable hadrons:  $\pi^\pm$ ,  $K^\pm$  and  $p(\bar{p})$ . The flexible trigger system effectively selects signatures corresponding to the signal decays of heavy flavour states. For the current analysis a trigger line dedicated to the charmonium decays to  $p\bar{p}$  final state is used.

Chapter 1 of the thesis focuses on theoretical aspects of quark-antiquark interactions. The concept of the Standard Model is briefly discussed in sec. 1.1, followed by an overview of the quark compounds given in sec. 1.2. The history of quarkonium studies, its spectroscopy, production and decays is also mentioned. Chapter 2 includes a digest of recent experimental results on quarkonium studies, focusing mainly on the  $J/\psi$  and  $\eta_c$  states. The results on the prompt quarkonium production in parton interactions and inclusive charmonium production from  $b$ -hadron decays are discussed. The LHCb detector design and performance are described in Chapter 3. One can find more details about the detector systems, which are important for our analysis: tracking system, ring image Cherenkov detectors, and the LHCb trigger system. In Chapter 4 studies of the  $\eta_c$  state with  $\eta_c \rightarrow p\bar{p}$  decay channel are described. We find the  $\eta_c$  prompt production cross-section and the inclusive yield of  $\eta_c$  meson in  $b$ -hadron decays. Momentum dependencies of the production cross-sections are obtained. Measurements of the  $\eta_c$  mass  $m_{\eta_c}$  and natural width  $\Gamma_{\eta_c}$  are also addressed. The results are summarised in Chapter 5.

# Chapter 1

## Heavy quarkonium

### 1.1 Elementary particles and fundamental forces

#### 1.1.1 Introduction

Elementary particles and their interactions are considered by a theoretical framework called the Standard Model (SM). It describes the electromagnetic, weak and strong fundamental interactions. The SM was basically developed in 1970-s. It was experimentally confirmed when the quarks were observed [1, 2]. Experimental observation of the elementary SM particles was completed by the discoveries of the top quark (1995) [3], direct interaction of the tau neutrino (2000) [4], and the Higgs boson production (2013) [5, 6].

The full Lagrangian of the SM is rather cumbersome and can be found in Ref [7]. A graphical representation of elementary particle interactions is shown on Fig. 1.1

Three major groups of true elementary particles are distinguished in the framework of the SM: fermions, in particular quarks and leptons, gauge bosons, which are interaction carriers and the Higgs boson, responsible for the masses of elementary particles. Fermions have spin equal to  $n/2$ ,  $n = 1, 2, 3 \dots$  and obey Fermi-Dirac statistics. Quarks, charged leptons and neutrinos belong to the SM fermions. Bosons have an integer spin and are described by Bose-Einstein statistics. The SM interaction carriers are the gauge bosons  $\gamma$ ,  $Z$ ,  $W^\pm$  (vectors) and the Higgs boson  $H$  (scalar).

All SM particles interact via three fundamental forces: the electromagnetic, weak and strong interactions [8], see a more detailed description in section 1.1.3 and section 1.1.4. The SM does not include a gravity description. It is supposed that elementary particles participate in gravitational interactions as well, though there is no sufficient quantum

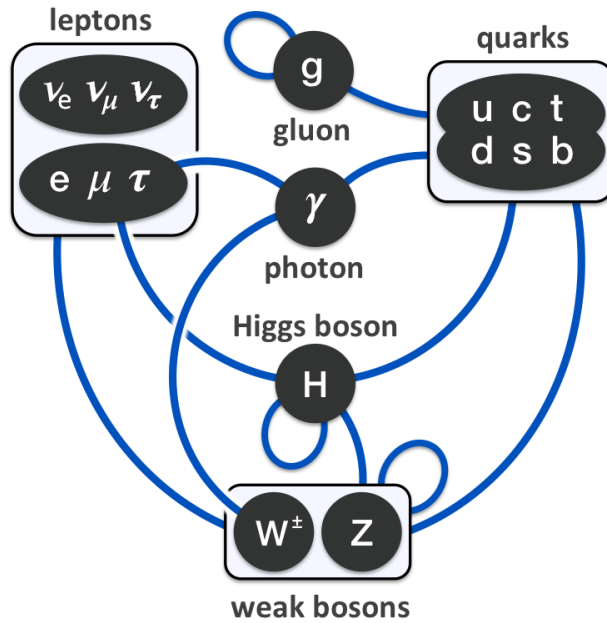


Figure 1.1: Elementary particle interactions in the Standard Model.

gravity theory. A set of mathematical and conceptual problems has to be solved, including a superposition principle which requires a linear vector field and quantisation of space-time itself [9]. An experimental observation of the graviton, the gravitational force carrier, is extremely hard due to small coupling [10].

In the SM interactions are determined by a gauge quantum field theory containing the internal symmetries of the unitary group product  $SU(3)_C \times SU(2)_L \times U(1)_Y$  [?]. The  $SU(3)_C$  symmetry corresponds to the strong interaction ( $C$  index marks colour charge, see section 1.1.4), and the product  $SU(2)_L \times U(1)_Y$  is responsible for the electroweak interaction (indices  $L$  and  $Y$  correspond to the left-handed interaction of weak currents and hypercharge, respectively, see section 1.1.2). A more detailed description of each fundamental force is given below.

### 1.1.2 Elementary particles in the Standard Model

Presently, the matter is considered to be constructed out of three kinds of elementary particles: leptons, quarks, and interaction carriers. Six leptons, classified according to their charge and flavour, form three known families. There are also six corresponding antileptons with inverted quantum numbers. Similarly, three families of quarks are classified according to charge, isospin and flavour quantum numbers [8]. The SM fermion

are shown in Table 1.1.

Quarks participate in strong interactions and carry the colour charge. Quarks can be represented by Dirac fields [9]. In addition to strong interactions, quarks participate in electroweak (EW) interactions as leptons, forming electroweak doublets. The electrical charge associated with quarks, in units of the electron charge  $e = 1.6 \times 10^{-19} C$ , [11], is  $+2/3$  for Up type ( $u, c, t$ ) quarks and  $-1/3$  for Down type ( $d, s, b$ ) quarks. Generalisation of the baryon charge assumes it to be equal to  $1/3$  for quarks and  $-1/3$  for antiquarks. Free quarks can not be observed due to the confinement effect of strong interaction. Only colourless hadrons, mesons ( $q\bar{q}$ ) and baryons ( $qqq$ ), are observed.

Neutrinos are weakly interacting chargeless particles. Left handed neutrinos form three doublets with electrons, muons and  $\tau$  leptons and are named after them. In the basic model, developed in 1960-s, neutrinos were assumed to be massless. It was supposed that right handed neutrinos did not exist. However, recent experiments have confirmed neutrino oscillations and therefore non-zero masses are required [?]. Until now no neutrino mass was directly measured, see Table 1.1 for the recent limits [11]. Different models of neutrino mass generations have been developed, *e. g.* the See-saw mechanism, which involves the Majorana type of neutrino field [?].

Neutral and charged weak currents couple to the  $Z$  and  $W^\pm$  vector bosons, respectively. They are the mediators of the weak interaction. Their masses are important parameters in the EW theory, and are linked via the Weinberg angle  $M_Z = M_W / \cos \theta_W$  [7]. The  $M_Z = 91.2 \text{ GeV}/c^2$  and  $M_{W^\pm} = 80.4 \text{ GeV}/c^2$  [11]. The photon ( $\gamma$ ) is massless vector gauge boson, the carrier of the electromagnetic interaction. The  $\gamma$ ,  $Z$  and  $W^\pm$  bosons are produced from the EW interaction fields  $\vec{A}$  and  $B$  in the spontaneous symmetry breaking [7].

The Higgs boson  $H$  is a true neutral scalar with  $M_H = 125.9 \pm 0.4 \text{ GeV}/c^2$  [11]. In the SM it is responsible for the generation of the SM particle masses under spontaneous symmetry breaking [7]. The experimental observation of the Higgs boson was recently reported by the CMS [5] and ATLAS [6] experiments.

### 1.1.3 Electroweak interaction

The Electroweak interaction was proposed as a unification of the two fundamental forces: electromagnetic and weak interactions. They form the EW interaction above the unification energy of the order of 100 GeV. It is described by the Glasgow-Weinberg-Salam (GWS) model of the EW interactions. The GWS is a non-Abelian gauge theory and incorporates also the Higgs mechanism [7]. The ability of the particle to participate

leptons mass	I generation		II generation		III generation	
	$e$	$\nu_e$	$\mu$	$\nu_\mu$	$\tau$	$\nu_\tau$
$Q$	$511.00 \text{ eV}/c^2$	$< 2 \text{ eV}/c^2$	$105.66 \text{ MeV}/c^2$	$< 0.19 \text{ MeV}/c^2$	$1776.82 \pm 0.16 \text{ MeV}/c^2$	$< 18.2 \text{ MeV}/c^2$
$T_3^{W \text{ left}}$	-1	0	-1	0	-1	0
$T_3^{W \text{ right}}$	-1/2	1/2	-1/2	1/2	-1/2	1/2
$Y_W \text{ right}$	0	-	0	-	0	-
$Y_W \text{ left}$	-1	-1	-1	-1	-1	-1
$Y_W \text{ right}$	-2	-	-2	-	-2	-
quarks mass	$u$	$d$	$c$	$s$	$t$	$b$
$Q$	$2.3_{-0.5}^{+0.7} \text{ MeV}/c^2$	$4.8_{-0.3}^{+0.5} \text{ MeV}/c^2$	$1.275 \pm 0.025 \text{ GeV}/c^2$	$95 \pm 5 \text{ MeV}/c^2$	$173.07 \pm 0.89 \text{ GeV}/c^2$	$4.18 \pm 0.03 \text{ GeV}/c^2$
$T_3^{W \text{ left}}$	+2/3	-1/3	+2/3	-1/3	+2/3	-1/3
$T_3^{W \text{ right}}$	+1/2	-1/2	+1/2	-1/2	+1/2	-1/2
$Y_W \text{ left}$	0	0	0	0	0	0
$Y_W \text{ right}$	+1/3	+1/3	+1/3	+1/3	+1/3	+1/3
$T_3$	+4/3	-2/3	+4/3	-2/3	+4/3	-2/3
$S$	0	0	0	-1	0	0
$C$	0	0	1	0	0	0

Table 1.1: A list of the SM fermions. The corresponding quantum numbers are given for the leptons and quarks: mass, electrical charge  $Q$ , weak isospin  $T_3^{W}$  and hypercharge  $Y_W$  for the left handed and right handed states. The  $e$  and  $\mu$  masses are known with  $\mathcal{O}(10^{-8})$  precision. Neutrino mass limits are given at 95% Confidence Limit for  $\nu_e$  and  $\nu_\tau$  and at 90% for  $\nu_\mu$ . For quarks only isospin projection  $T_3$ , strangeness  $S$  and charm  $C$  are defined [?, 11]. Different quantum numbers, associated with the rest of the quark Flavours, are not considered in this overview, but may be found in Ref. [?].

in electroweak interactions is defined by the hypercharge  $Y_W$  and the third projection of weak isospin  $T_3^W$ . Their values for fermions are given in Table 1.1. They are related with the electric charge  $Q$  in the Gell-Mann–Nishijima formula:

$$Q = T_3^W + \frac{1}{2}Y_W. \quad (1.1)$$

Assuming neutrinos to be massless (see sec 1.1.2), the GWS model in the lepton sector is the  $SU(2)_L \times U(1)_Y$  gauge theory, which includes a right-handed singlet  $R$  and a left-handed doublet  $L$  of the  $SU(2)$  group, represented as

$$L = \begin{pmatrix} \nu_\ell \\ \ell \end{pmatrix}_L, \quad R = \ell_R, \quad (1.2)$$

where  $\ell = e, \mu, \tau$ . The quark sector enters the Lagrangian of EW interactions with one doublet and two singlets:

$$Q = \begin{pmatrix} q^u \\ q^d \end{pmatrix}_L, \quad U = q_R^u, \quad D = q_R^d, \quad (1.3)$$

where  $q^u$  corresponds to the  $u, c, t$  quarks and  $q^d$  corresponds to the  $d, s, b$  quarks. The gauge invariant Lagrangian for leptons is constructed as

$$\mathcal{L}_F^{\text{lepton}} = \bar{L}i\gamma^\mu(\partial_\mu - ig\frac{\vec{\tau}}{2}\vec{A}_\mu)L + \frac{i}{2}g'B_\mu + \bar{R}i\gamma^\mu(\partial_\mu + ig'B^\mu)R, \quad (1.4)$$

where  $A_\mu^i (i = 1, 2, 3)$  and  $B_\mu$  are gauge boson fields associated with  $SU(2)_L$  and  $U(1)_Y$ , respectively,  $g$  and  $g'$  are the gauge coupling constants corresponding to  $SU(2)_L$  and  $U(1)_Y$ , respectively. The electroweak coupling constants are related with the electromagnetic coupling via the Weinberg angle  $\theta_W$  [8]:

$$g = \frac{\sqrt{4\pi\alpha_{\text{em}}}}{\sin\theta_W \cos\theta_W}, \quad g' = \frac{\sqrt{4\pi\alpha_{\text{em}}}}{\sin\theta_W}, \quad (1.5)$$

where  $\alpha_{\text{em}} = e^2/\hbar c$  is the fine structure constant.

The Lagrangian for the quark sector is built in a similar way:

$$\begin{aligned} \mathcal{L}_F^{\text{quark}} &= \bar{Q}i\gamma^\mu(\partial_\mu - ig\frac{\vec{\tau}}{2}\vec{A}_\mu Q + \frac{i}{6}g'B_\mu) \\ &+ \bar{U}_R \frac{2i}{3}\gamma^\mu(\partial_\mu + ig'B^\mu)U_R + \bar{D}_R \frac{i}{3}\gamma^\mu(\partial_\mu + ig'B^\mu)D_R. \end{aligned} \quad (1.6)$$

It differs from the corresponding Lagrangian for leptons since all right-handed quarks (left-handed antiquarks) participate in EW interactions. The kinetic term of the gauge fields which should be added to the Lagrangian is

$$\mathcal{L}_G = -\frac{1}{4}F_{\mu\nu}^i F^{i\mu\nu} - \frac{1}{4}B_{\mu\nu}B^{\mu\nu}, \quad (1.7)$$

where

$$F_{\mu\nu} = \partial_\mu A_\nu^i - \partial_\nu A_\mu^i + g_{em}\epsilon_{ijk}A_\mu^i A_\nu^k, \quad (1.8)$$

$$B_{\mu\nu} = \partial_\mu B_\nu - \partial_\nu B_\mu. \quad (1.9)$$

$F_{\mu\nu}^i (i = 1, 2, 3)$  and  $B_{\mu\nu}$  are field strength tensors of the gauge fields. In order to generate masses fermions and gauge bosons, the spontaneous breakdown of gauge invariance is needed. [7]

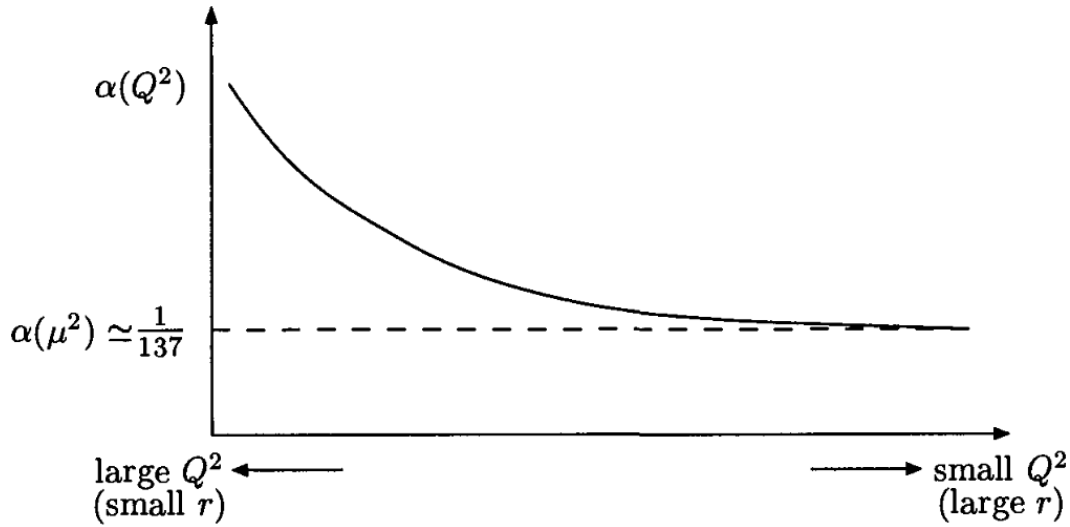


Figure 1.2: The dependency of the  $\alpha_{em}(Q^2)$  running coupling constant on the  $Q^2$ . [7]

The EM coupling strength increases when the interacting particles get closer together. This fact is interpreted as vacuum polarisation, when the vacuum functions screen the charge like the dielectric medium. Introducing higher order corrections to the virtual photon current, one can find that the dominant deposit comes from the chains of fermion loops. With the increase of the interacting particle momenta, the electric coupling constant gets larger, see Fig. 1.2. This effect is known as the running

coupling constant:

$$\alpha_{\text{em}}(Q^2) = \frac{\alpha_{\text{em}}(\mu^2)}{\left(1 - \frac{\alpha_{\text{em}}(\mu^2)}{3\pi}\right) \ln\left(\frac{Q^2}{\mu^2}\right)}, \quad Q^2 \gg \mu^2, \quad (1.10)$$

where  $\mu^2$  is a scale parameter,  $Q$  is the interaction energy. [8]

### 1.1.4 Strong interaction

The strong interaction (SI) is a fundamental force. The SI is responsible for bounding quarks and gluons inside hadrons, including protons and neutrons, that dominate a visible baryonic matter. [?]

The strong interaction is described by quantum chromodynamics (QCD). QCD is a non-Abelian gauge theory based on symmetry group  $SU(3)$ . The idea of strong interactions was first introduced by Yukawa in 1930s to explain the nuclear forces between nucleons. Nowadays it is known that all hadrons, including nucleons, are composite particles made of quarks. The quark model was developed and proved in 1960s–1970s [1, 2, 12]. According to it, baryons are composed of three quarks  $qqq$  and mesons of a quark-antiquark pair  $q\bar{q}$ . [7]

Quarks exist in three different colour states, denoted as red, green and blue. The colour charge of quarks and gluons in strong interactions is a quantum number similar to the hypercharge and weak isospin projection in electroweak interactions. The number of existing colours was confirmed by a large variety of experimental results.

Historically, the colour charge was first introduced to solve a problem in the relation of spin and statistics in the baryon spectroscopy. Introducing an antisymmetric colour space wave function, one can explain the  $3/2$  spin of the  $\Delta^{++}$  baryon, which consists of the three  $1/2$  spin  $u$  quarks. Another evidence of the three colours comes from the experimental results on the  $e^+e^-$  annihilation cross-section. At energies of hundreds MeV, above  $s\bar{s}$  pair and below  $c\bar{c}$  pair production threshold, the production ratio is

$$R = \frac{\sigma(e^+e^- \rightarrow \text{hadrons})}{\sigma(e^+e^- \rightarrow \mu^+\mu^-)}, \quad (1.11)$$

based on the quark model, predicts  $R = e_u^2 + e_d^2 + e_s^2 = 2/3$  without colour and  $R = 2$  with 3 colours. [7]

The quark definition in QCD requires the Dirac spinor and the three element colour

vector  $c$ , that gives the quark's colour:

$$c = \begin{pmatrix} 1 \\ 0 \\ 0 \end{pmatrix}, \begin{pmatrix} 0 \\ 1 \\ 0 \end{pmatrix}, \begin{pmatrix} 0 \\ 0 \\ 1 \end{pmatrix} \quad (1.12)$$

for the red, green and blue states, respectively. The quark colour changes at the quark-gluon vertex and the difference is carried out by the gluon. Each gluon carries one unit of colour and one unit of anticolour, so there are  $3 \otimes \bar{3} = 1 \oplus 8$  — colour-singlet colour-octet that gives nine types of gluons. In terms of the  $SU(3)_C$  symmetry, these nine combinations form a colour-octet:

$$\begin{aligned} |1\rangle &= (r\bar{b} + b\bar{r})/\sqrt{2} & |5\rangle &= -i(r\bar{g} - g\bar{r})/\sqrt{2} \\ |2\rangle &= -i(r\bar{b} - b\bar{r})/\sqrt{2} & |6\rangle &= -i(b\bar{g} + g\bar{b})/\sqrt{2} \\ |3\rangle &= (r\bar{r} - b\bar{b})/\sqrt{2} & |7\rangle &= -i(b\bar{g} - g\bar{b})/\sqrt{2} \\ |4\rangle &= (r\bar{g} + g\bar{r})/\sqrt{2} & |8\rangle &= -i(r\bar{r} + b\bar{b} - 2g\bar{g})/\sqrt{6} \end{aligned} \quad (1.13)$$

and a colour-singlet state:

$$|9\rangle = (r\bar{r} + b\bar{b} + g\bar{g})/\sqrt{6} \quad (1.14)$$

The phenomenon of confinement requires all hadrons to be colour-singlets. [8]

The QCD Lagrangian, that describes the interaction between quarks  $q$  and gluons  $A_\mu^i$  is written as [7]

$$\mathcal{L}_{QCD} = \bar{q}(i\partial_\mu + g_s \frac{\lambda^i}{2} A_\mu^i - m)q - \frac{1}{4} F_{\mu\nu}^i F^{i\mu\nu}, \quad (1.15)$$

where  $g_s$  is the strong coupling constant and  $\lambda^i$  are the Gell-Mann matrices. Summation over  $i = 1, 2 \dots 8$  is implied. The quark field is given both by the Dirac field and the colour field components.  $F_{\mu\nu}^i$  are the field strength tensor for the gluon fields  $A_\mu^i$ :

$$F_{\mu\nu}^i = \partial_\mu A_\nu^i - \partial_\nu A_\mu^i + g_s \varepsilon_{ijk} A_\mu^j A_\nu^k \quad (1.16)$$

where  $\varepsilon_{ijk}$  is the fully asymmetric tensor.

The gluons enter self-interaction because of the non-Abelian nature of QCD. It leads to drastically different behaviour of the running coupling constant  $\alpha_s(|q|^2) = g_s^2/4\pi$  comparing to the  $\alpha_{em}$  behaviour in Quantum Electrodynamics (QED). Two diagrams shown on Fig 1.3 illustrate one-loop corrections to  $\alpha_s$ . Apart from the colour factor, the contribution from the quark-loop diagram Fig. 1.3 (left) is similar to the corrections in

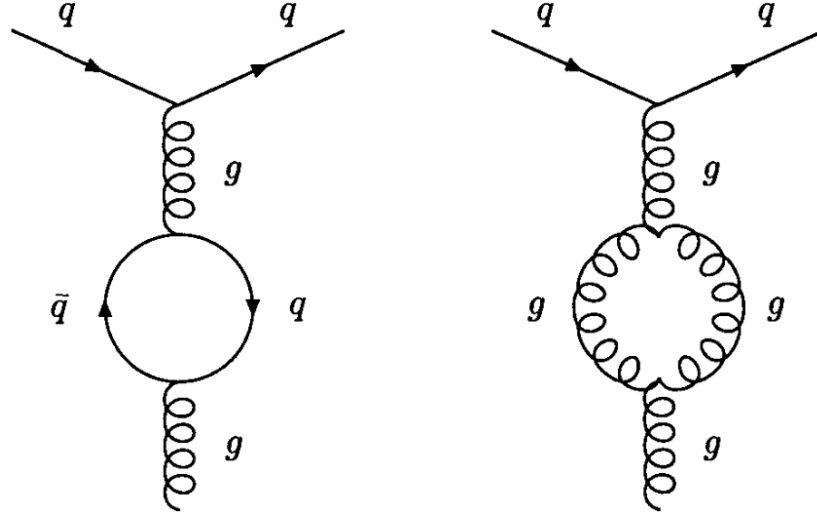


Figure 1.3: The quark loop (left) and the gluon loop (right) corrections to the running coupling constant  $\alpha_s$ . [7]

QED. The gluon-loop diagram on Fig. 1.3 (right) give rise to another numerical factor,  $-\frac{11}{4\pi}\alpha_s(\mu)$  with a sign that is opposite to quark-loop contribution. The QCD running coupling constant is then:

$$\alpha_s(Q^2) = \frac{\alpha_s(\mu^2)}{1 + \frac{(33 - 2n_f)\alpha_s(\mu^2)}{12\pi} \ln\left(\frac{Q^2}{\mu^2}\right)}. \quad (1.17)$$

The  $\mu$  is the renormalisation scale and  $n_f$  is the number of flavours, taking part in the scattering process. The denominator of Equation 1.17 becomes zero for  $Q^2$  value equal to  $\Lambda_{\text{QCD}}$ , so that

$$Q^2 = \Lambda_{\text{QCD}}^2 = \mu^2 e^{-\frac{12\pi}{(33 - 2n_f)\alpha_s(\mu^2)}} \quad (1.18)$$

Thus we can rewrite  $\alpha_s(Q^2)$  as

$$\alpha_s(Q^2) = \frac{12\pi}{(33 - 2n_f) \ln\left(\frac{Q^2}{\Lambda_{\text{QCD}}^2}\right)} \quad (1.19)$$

The value of  $\Lambda_{\text{QCD}}$  can not be determined theoretically in QCD, but it was extracted from experimental data:  $\Lambda_{\text{QCD}} \simeq 200 \text{ MeV}$  for  $Q^2 \simeq 100 \text{ GeV}^2$ . The behaviour of the

$\alpha_s(Q^2)$  is shown on Fig. 1.4

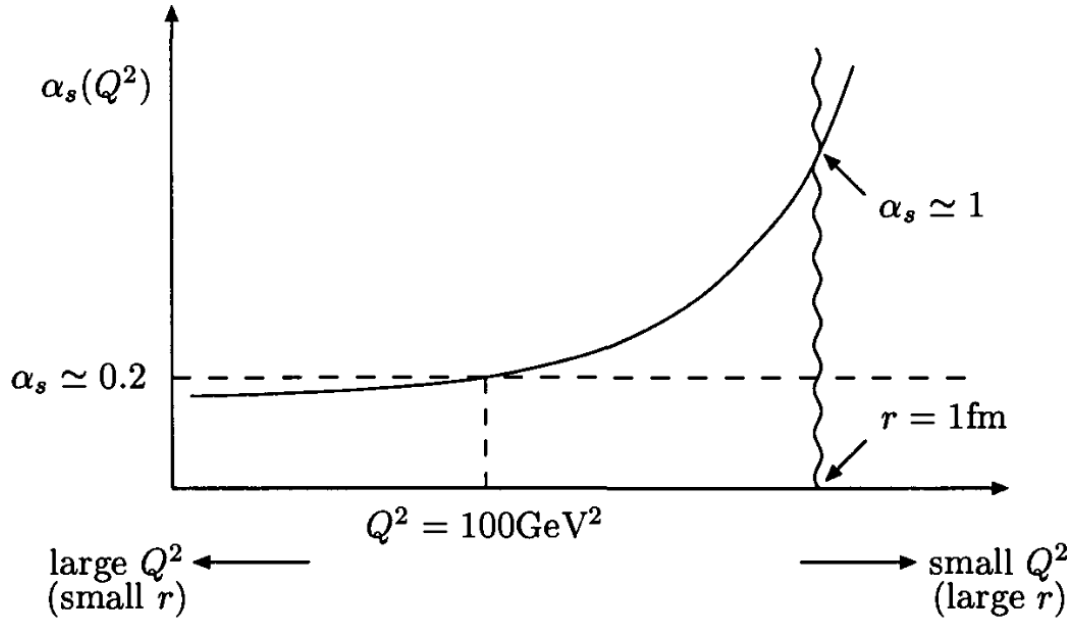


Figure 1.4: The  $Q^2$  dependence of the  $\alpha_s(Q^2)$  coupling constant. [7]

For large  $Q^2$  values,  $Q^2 \gg \Lambda_{\text{QCD}}^2$ , effective couplings between quarks and gluons become small. It allows to use perturbative approximation for strong interactions at large transferred energies, corresponding to small distances. Quarks and gluons behave as free particles in this energy region, which is known as asymptotic freedom. On the contrary, at small energy scales,  $Q^2 \lesssim \Lambda_{\text{QCD}}^2$ , corresponding to large distances, the coupling constant becomes large and the quark and gluons are confined in hadrons [7]. Effective theories are applied to describe hadron interactions at low energies [13].

## 1.2 Quark systems

### 1.2.1 Introduction

The first valuable theory of strong interactions was suggested by Yukawa in 1934 [14]. He suggested an assumption that protons and neutrons interact via the exchange of a mediator, following the same principle as electromagnetism. The mass of the interaction carrier was estimated to be nearly 300 electron masses. Because its mass was expected to be nearly between the masses of an electron ( $511 \text{ keV}/c^2$ ) and nucleons ( $\simeq 1 \text{ GeV}/c^2$ ) it was named a meson. In 1947 the presence in cosmic rays of two middle-weight particles,

the muon and pion, were observed. The latter one was attributed to be the Yukawa meson. [8]

A variety of particles, including resonances decaying via strong interactions, were discovered in the period of 1950–1970.

The observation of the neutral kaon in cosmic rays had preceded the first resonance observation. The first discovered particles, containing quark of the second generations were neutral kaons. They were observed in the  $K^0 \rightarrow \pi^+\pi^-$  decay mode [8]. In 1949 the charged kaon decay  $K^+ \rightarrow \pi^+\pi^+\pi^-$  was observed in a bubble chamber [8]. Next year a new heavy neutral particle,  $\Lambda$ , decaying to a proton and pion, was found. These new particles were called “strange” because of significant discrepancy in the lifetime and production cross-section.

The first resonance in particle physics was  $\Delta^{++}$ , discovered by Fermi. It was found as a sharp peak in the pion-nucleon cross-section to the process  $\pi^+ + p \rightarrow \Delta^{++} \rightarrow \pi^+ + p$ . [8] A typical property of the resonances is a short lifetime of the order of  $\tau \simeq 10^{-23}$ . Usually, it is not measured directly but is determined from the particle natural width  $\Gamma = \hbar/\tau$ . The  $\Gamma$  can be obtained from the fit to the cross-section distribution with the Breit-Wigner function:

$$p(M) = \frac{1}{2\pi} \frac{\Gamma}{(M - M_0)^2 + \Gamma^2/4}, \quad (1.20)$$

where  $M_0$  is the resonance mass [11].

In the mid 1960s several hundreds of strongly interacting particles and resonance were known. Naturally, they had to be classified with an introduction of new quantum numbers and corresponding conservation laws.

## 1.2.2 Mesons and baryons

All known strongly interacting particles (hadrons) are considered to be made of quarks. The hadrons with integer spin are called mesons, and the hadrons with semi-integer spin are called baryons. Ordinary mesons and baryons are made of  $q\bar{q}$  and  $qqq$  quark combinations respectively. The antiparticles are obtained by flipping the quarks and antiquarks. The baryon number is a quantum number associated with baryons. Each baryon (antibaryon) has  $B = 1$  ( $B = -1$ ). For mesons and the rest of the elementary particles  $B = 0$ . Baryon number conservation can be interpreted as quark number conservation. [9]

Historically, the first effort to classify existing hadrons was made by Murray Gell-Mann in 1961. He arranged baryons and mesons into geometrical patterns according

to their charge and strangeness. The eight lightest baryons form an octet, see Fig. 1.5. The diagonal top-left to bottom-right lines links particles with the same electric charge, horizontal lines links particles with the same strangeness.

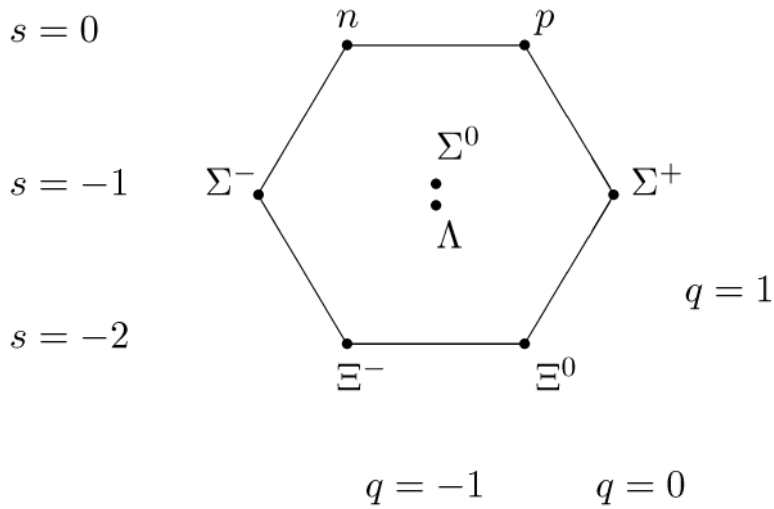


Figure 1.5: Octet and singlet of the lightest baryons with spin 1/2.

The eight lightest pseudo-scalar mesons fill a similar pattern, forming the meson octet (see Fig. 1.6) and a one meson singlet.

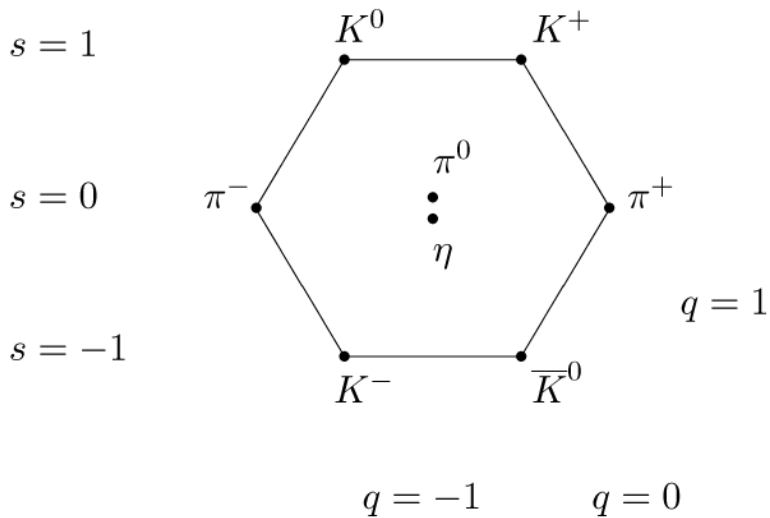


Figure 1.6: Octet and singlet of the lightest pseudo-scalar mesons.

The 3/2 spin baryons form the baryon decuplet and are presented on Fig. 1.7 as a

triangular pattern.

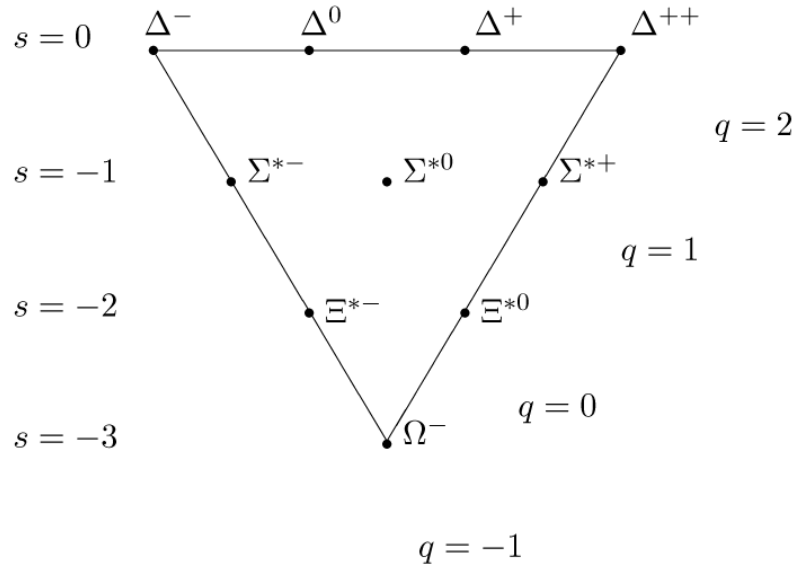


Figure 1.7: Ten baryons with the spin  $3/2$  form the baryon decuplet.

After the discovery of  $\Omega^-$  baryon in 1963, the success of Gell-Mann model became evident [15]. Gell-Mann predicted the existence of the particle with  $S = -3$  and  $Q = -1$ , which was missing in the initial decuplet. He was able to estimate its mass and lifetime before its first experimental observation. [8]

The quark model allows a representation of existing multiplets with the  $SU(3)$  flavour symmetry. With the three quark flavours  $u, d, s$ , quark-antiquark combinations form triplet-antitriplet

$$3 \otimes \bar{3} = 8 \oplus 1$$

of meson states with a given spin value. Here  $3$  ( $\bar{3}$ ) is a multiplicity of possible flavour state for quark (antiquark). Similarly for baryons, with a combination of three quarks in three flavours, there are

$$3 \otimes 3 \otimes 3 = 10 \oplus 8 \oplus 8 \oplus 1$$

states. The 27 combinations split to a decuplet, two octets and one singlet.

The  $SU(3)$  flavour is an exact symmetry only for equal quark masses. Hadron mass differences tell us that this symmetry is approximate. Furthermore, one can include a heavy  $c$  quark in this model to form the  $SU(4)$  flavour model. Since the  $c$  quark is significantly heavier than  $u, d$  and  $s$  quarks (see Table 1.1), the  $SU(4)$  flavour symmetry

is even less precise than the SU(3) flavour . The 1/2 spin baryon multiplet is shown on Fig. 1.8 and the psedo-scalar meson multiplet is shown on Fig. 1.9. [9]

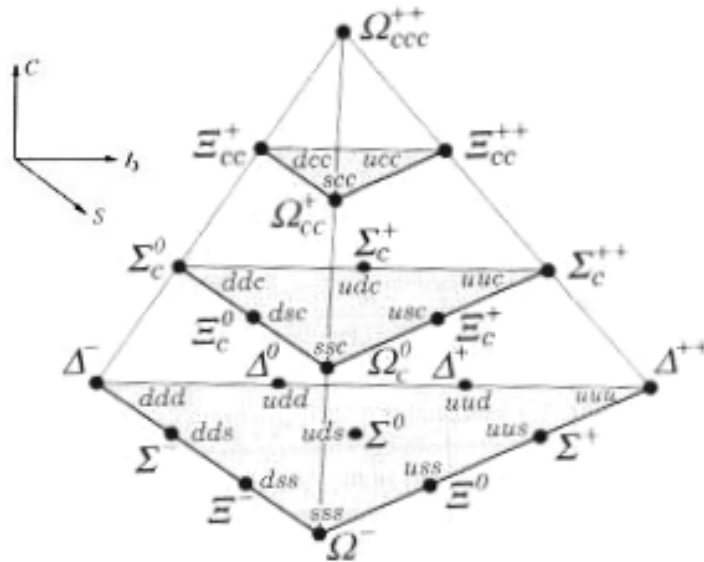


Figure 1.8: Multiplets of the 1/2 spin baryon in SU(4) flavour model.

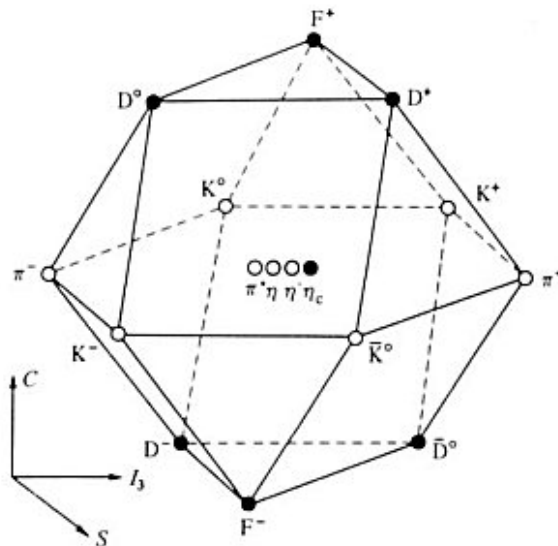


Figure 1.9: Multiplets of the psedo-scalar mesons in SU(4) flavour model.

In the framework of SU(4) flavour model, the electric charge is linked with the isospin projection  $I_3$ , baryon number  $B$ , strangeness  $S$  and charm  $C$  by a different form

(see eq. 1.1) of the Gell-Mann-Nishijima formula: [8]

$$Q = I_3 + \frac{1}{2}(B + S + C). \quad (1.21)$$

The majority of the known hadrons can be classified as conventional mesons or baryons. The quark model gives powerful predictions in spectroscopy, including hadron masses, spin, parity and other quantum numbers.

### 1.2.3 Exotic states

The hadrons with quark composite, different from the conventional  $q\bar{q}$  or  $qqq$  states, are called exotic. They can be divided in the following main groups:

- Exotic baryons: pentaquarks
- Exotic mesons: tetraquarks, meson molecule, hybrid mesons and glueballs (also called gluonia).

An example of an exotic baryon, pentaquark, is the  $qqqq\bar{q}$  state, which is not forbidden by QCD. Some experiments reported the evidence of a pentaquark in the 2000s [16], but their results were not confirmed later and were shown to be due to statistical fluctuations [17, 18, 19].

The combination of the pair of quarks with a pair of antiquarks in the 3 representation provides a light nonet of four-quark scalar states. If one lets the  $s$  quark to determine the mass splitting, the mass spectrum will form isosinglet ( $ud\bar{u}\bar{d}$ ), a medium heavy isodoublet (*e. g.*  $ud\bar{s}\bar{d}$ ) and a heavy isotriplet (*e. g.*  $ds\bar{u}\bar{s}$ ) and an isosinglet (*e. g.*  $us\bar{u}\bar{s}$ ). Then one can interpret the lightest state with the  $f_0(500)$ , and the heaviest states as  $a_0(980)$ , and  $f_0(980)$ . Then the meson with strangeness  $\kappa(800)$  would enter in-between. [11]

In 2003 the  $X(3872)$  narrow charmonium like state was observed by Belle experiment [20]. It can be interpreted as a tetraquark or meson molecule candidate. Then the  $Z(4430)$  resonance with a mass of  $4430 \text{ MeV}/c^2$  was discovered by Belle, then seen by BaBar [21] and was confirmed by the LHCb experiment with a  $13.9 \sigma$  significance [22, 23]. It is a charged particle and its quark content is consisted with  $ccdu$  state, making it a tetraquark candidate.

States consisting of  $q\bar{q}$  pairs bound with the excited gluons  $g$  are also predicted. Their masses are predicted to be around the  $1.9 \text{ GeV}/c^2$  region, according to gluon flux

tube models [11]. Lattice QCD also predicts the lightest hybrid with the  $J^{PC} = 1^{-+}$  quantum numbers with about  $1.8 \text{ GeV}/c^2$  mass. [11]

The existence of bound states of gluons is a consequence of gluon self-interaction. The first model of the glueball spectroscopy, based on the quark-gluon field theory with hadrons as colour-singlets, has been developed in 1985. Much effort was devoted during the last 40 years to the theoretical analysis as well as the experimental searches of this new type of hadron. [24]

### 1.3 Previous quarkonium studies

Quarkonium is a bound state of a quark and its own antiquark. Conventionally, we call charmonium only the compounds of heavy quarks where the interaction energy is smaller than the quark masses (see Table 1.1 for quark masses). The  $b\bar{b}$  and  $c\bar{c}$  states are named bottonium and charmonium respectively. [11] The  $t$  quark does not participate in the creation of any bound states. The  $t$  quark with a mass about  $m_t \lesssim 125 \text{ GeV}/c^2$  could form narrow toponium states. The width of the single top quark decay  $\Gamma_t \simeq 175 \text{ MeV} (m_t/m_W)^3$ . The top quark decays faster than the  $(t\bar{t})$  bound state creation happens. [25]

Unlike the hydrogen atom, where only electromagnetic interaction occurs, quarks are bound by the strong force. However, the QCD is similar in structure to electrodynamics except for some non-linear terms which probably do not contribute much at short distances, see about asymptotic freedom in section 1.1.4. The short-distance behaviour is dominated by one-gluon exchange. Since the gluon and the photon are both massless vector particles, the interactions in the given approximation are identical, apart from the coupling constant  $g_s$  and the colour factor.

At short range we expect a Coulomb potential interaction  $V \sim 1/r$ . At large distances one should take into account the quark confinement, therefore the potential must increase without a limit. The precise functional form of  $V(r)$  at large  $r$  is rather speculative and can be parametrised like the harmonic oscillator potential  $V \sim r^2$  or logarithmic dependence  $V \sim \ln(r)$ . With the simplest case of linear dependence, we obtain

$$V(r) = -\frac{4}{3} \frac{\alpha_s}{r} + br, \quad (1.22)$$

where  $4/3$  is related to the colour factor,  $\alpha_s$  is the strong coupling constant and the constant  $b$  can be obtained experimentally [8]. The non-relativistic quarkonium potential including spin-spin interaction are given in section 1.4.

The light quark mesons are intrinsically relativistic since their bounding energies (about hundreds of MeV) are not small compared to quark masses (see Table 1.1)[8]. Strictly speaking, the light unflavoured mesons are made by the superposition of light quark-antiquark pairs: the  $(u\bar{u} - d\bar{d})/\sqrt{2}$  state for  $\pi^0$ ,  $\rho^0$ , and the  $(u\bar{u} + d\bar{d} - 2s\bar{s})/\sqrt{6}$  state for  $\eta$ ,  $\omega$ , the  $(u\bar{u} + d\bar{d} + s\bar{s})/\sqrt{3}$  state for  $\eta'$ ,  $s\bar{s}$  for  $\phi$  [11].

The first quarkonium system was discovered in 1974, when two experimental groups at Brookhaven and SLAC announced almost simultaneously the discovery of a narrow resonance, later called  $J/\psi$  [26, 27]. This discovery was followed by the  $\psi(2S)$  (also called  $\psi'$ ) state observation by the SLAC group [28].

## 1.4 Spectroscopy

It is assumed that QCD itself can describe the spectroscopy of heavy quarkonium, however there are important difficulties to do so in practice. There are two main approaches: the phenomenological and the theoretical one.

The phenomenological approach operates with models that are believed to be the features of QCD relevant to heavy quarkonium. Their aim is to produce concrete results which can be confirmed or falsified by experiment. These results than may guide further experimental searches. The theoretical approach describes quarkonium with QCD calculations and approximations. [29]

Heavy quarkonia are bound states composed of two heavy quarks, each having mass  $m$  much larger than the QCD confinement scale  $\Lambda_{\text{QCD}}$ .

The typical velocity  $v$  of the heavy quark decreases as the mass  $M$  increases. If  $m$  is large enough,  $v$  is proportional to the running coupling constant  $\alpha_s(m)$ , and it therefore decreases asymptotically like  $1/\log(m)$ . Thus, if  $m$  is sufficiently large, the heavy quark and antiquark are nonrelativistic, with typical velocities  $v \ll 1$ . We assume in this paper that the mass  $m$  is heavy enough that the momentum scales  $m$ ,  $mv$  and  $mv^2$  are well-separated:  $(mv^2)^2 \ll (mv)^2 \ll m^2$  [30].

Because the system is non-relativistic, quarkonium can be described in terms of the heavy quark bound state velocity,  $v \ll 1$ , ( $v^2 \sim 0.3$  for  $c\bar{c}$  and  $v^2 \sim 0.1$  for  $b\bar{b}$ ) and by the energy scales: the mass  $m$ , the relative momentum  $p \sim mv$  and the binding energy  $E \sim mv^2$ . Since  $m \gg \Lambda_{\text{QCD}}$  and  $\alpha_s \ll 1$  all processes that occur at the scale  $m$  can be treated perturbatively. The strong interaction coupling constant may also be small in case if  $mv \gg \Lambda_{\text{QCD}}$  and  $mv^2 \gg \Lambda_{\text{QCD}}$ . It works only for the lowest quarkonium states, see Fig. 1.10. Direct measurements of charmonium radius are not accessible, and thus

distinguishing between the perturbative or the non-perturbative soft regime of some of the lowest bottomonia and charmonia states is challenging.

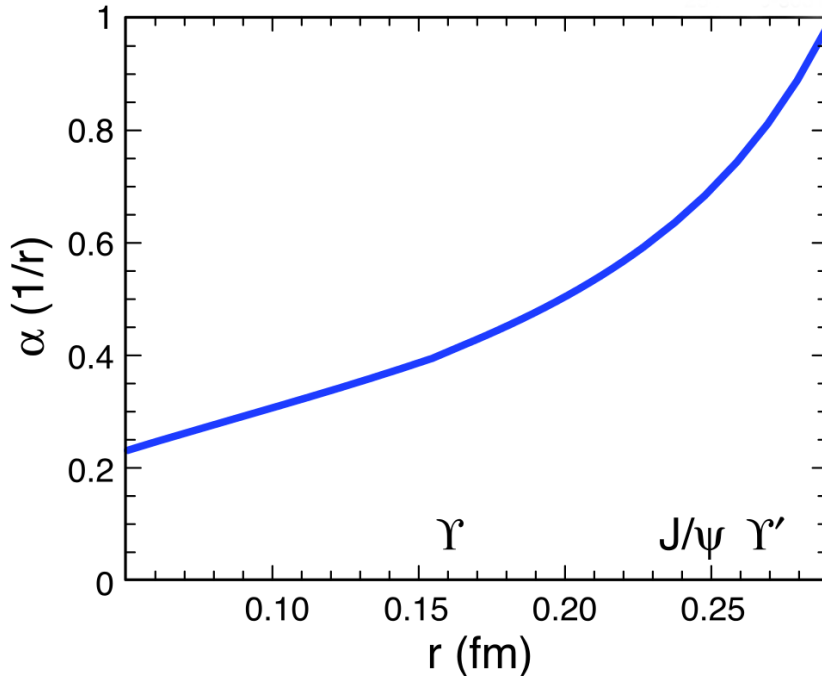


Figure 1.10: The  $\alpha_s$ , at one loop, as a function of quarkonium radius  $r$ , with labels indication approximate values of  $mv$  for  $\Upsilon(1S)$ ,  $J/\psi$ , and  $\Upsilon(2S)$ . [31]

The hierarchy of these scales separates quarkonia from the heavy-light mesons (*e.g.*  $B^+$ ,  $B^0$ ,  $D$  mesons) which can be described using just two scales:  $m$  and  $\Lambda_{\text{QCD}}$ . This makes the theoretical description of quarkonium physics more complicated. In particular, quarkonium production and decay happens at the scale  $m$ , quarkonium binding occurs at the scale  $mv$ , while very low-energy gluons and light quarks (also called ultrasoft degrees of freedom) are relatively long-lived and therefore are sensitive to the scale  $mv^2$ . [31]

Quarkonium has many separated energy states which makes it well-suited for the confinement region of QCD, its interplay with perturbative QCD, and of the behaviour of the perturbation series in QCD. States with different radii have varying sensitivities to the Coulomb and confining interactions, see Fig. 1.11

### Theoretical approach

Heavy quark effective theory (HQET) [32] and nonrelativistic quantum chromodynamics (NRQCD) are two effective theories that describe the interactions of almost on-shell

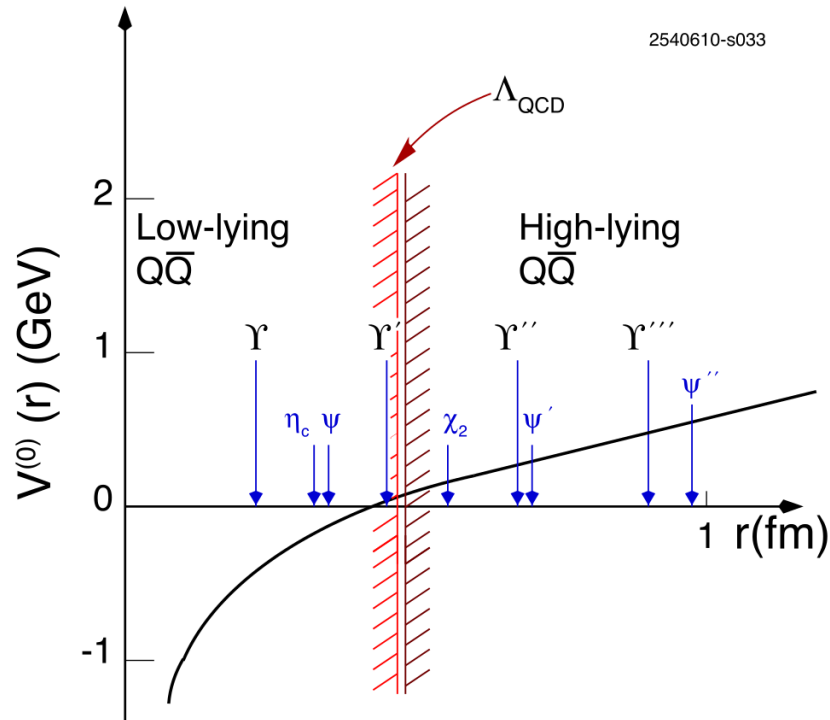


Figure 1.11: The  $q\bar{q}$  potential as a function of quarkonium radius  $r$ . [31]

heavy quarks. NRQCD is based in the fact that the masses of the charm and bottom quarks are much larger than  $\Lambda_{\text{QCD}}$  in order to build an effective field theory (EFT) which is equivalent to QCD at any desired order in  $1/m$  and  $\alpha_s(m)$ . In the frame of the NRQCD two approaches may be followed for spectrum computations: direct lattice calculations or further integration of the scale of the momentum transfer to arrive at an EFT in which only the ultrasoft degrees of freedom remain dynamical, pNRQCD. [31]

The use of non-relativistic EFT allows to handle only scales that correspond to the physics of the non-relativistic bound states without having to spend a lot of computer power on the large scale associated with the heavy quark mass which is irrelevant to the bound state dynamics. This makes the calculations simpler so that more hadron correlators can be calculated for better precision.

### Phenomenological approach

From the various dynamical scales that play a role in the heavy quarkonium systems, namely  $m$ ,  $mv$ ,  $mv^2$  and  $\Lambda_{\text{QCD}}$ , only the hard scale  $m$  has been factorized in NRQCD and becomes explicit in its Lagrangian. Only the fact that  $m \gg mv$ ,  $mv^2$ ,  $\Lambda_{\text{QCD}}$  is

exploited but no use is made of the scale separation,  $mv \gg mv^2$ . Much of simplification is achieved by building another EFT, where degrees of freedom of order  $\sim mv$  are integrated out as well, i.e., an EFT where only the ultrasoft degrees of freedom with energies  $\sim mv^2$  remain dynamical [29]. The effective Lagrangian of NRQCD is organised as an expansion in  $1/m$  and  $\alpha_s(m)$ :

$$\mathcal{L}_{\text{NRQCD}} = \sum_n \frac{c_n(\alpha_s(m), \mu)}{m^n} \times O_n(\mu, mv, mv^2, \dots), \quad (1.23)$$

where  $O_n$  are the operators of NRQCD that are dynamical at the low-energy scales  $mv$  and  $mv^2$ ,  $\mu$  is the NRQCD factorisation scale, and  $c_n$  are the Wilson coefficients of the EFT that encode the contributions from the scale  $m$  and are non analytic in  $m$  [31].

The pNRQCD is based on the assumption that the scale associated to the size of the system  $k \sim mv$  is much larger than the binding energy  $E \sim mv^2$ . Therefore one can integrate out the scale of the momentum transfer  $k$  in a way such that pNRQCD is equivalent to NRQCD at any desired order in  $E/k$ ,  $k/m$  and  $\alpha_s(\mu)$ . There are two dynamical situations. If  $k \gg \Lambda_{\text{QCD}}$ , then the matching from NRQCD to pNRQCD may be performed in perturbation theory, expanding in terms of  $\alpha_s$ . In the case when  $k \approx \Lambda_{\text{QCD}}$ , the matching has to be non-perturbative, i.e., no expansion in  $\alpha_s$  is allowed. Recalling that  $k \sim r^{-1} \sim mv$ , these two situations correspond to systems with inverse typical radius smaller or bigger than  $\Lambda_{\text{QCD}}$ , or systems respectively dominated by short range or long range (with respect to the confinement radius) physics. [29]

### Non-relativistic potential model of charmonium

A non-relativistic potential model is the simplest model of the charmonium system. Its wave-functions are determined by the Schrödinger equation with the conventional charmonium potential. The potential is a standard colour Coulomb plus linear scalar form with a Gaussian-smeared contact hyperfine interaction in the zero-order potential. The central potential is thus

$$V_0^{c\bar{c}}(r) = -\frac{4}{3} \frac{\alpha_s}{r} + br + \frac{32\pi\alpha_s}{9m_c^2} \tilde{\delta}_\sigma(r) \vec{S}_c \cdot \vec{S}_{\bar{c}}, \quad (1.24)$$

where  $\tilde{\delta}_\sigma(r) = (\sigma/\pi)^3 e^{-\sigma r}$ . The four parameters  $(\alpha_s, b, m_c, \sigma)$  are determined fit of the measured spectrum.

The spin-spin interaction is predicted by one gluon exchange forces. The contact form, proportional to  $\delta(\vec{x})$  is an artefact of an  $\mathcal{O}(v_q^2/c^2)$  expansion of T-matrix, so

replacing it by an interaction with a range  $1/\sigma$  comparable to  $1/m_c$  is a valid modification. On the LO level, the one gluon exchange spin-orbit and tensor and a longer-ranged inverted spin-orbit term, which arises from the assumed Lorentz scalar confinement, are

$$V_{\text{spin}} = \frac{1}{m_c^2} \left[ \left( \frac{2\alpha_s}{r^3} - \frac{b}{2r} \right) \vec{L} \cdot \vec{S} + \frac{4\alpha_s}{r^3} \mathbb{T} \right] \quad (1.25)$$

The diagonal elements of the spin-orbit operator are  $\langle \vec{L} \cdot \vec{S} \rangle = \frac{1}{2}[J(J+1) - L(L+1) - S(S+1)]$ , other elements equal to zero. The tensor operator  $\mathbb{T}$  has non-zero diagonal elements only for  $L > 0$  spin triplet states:

$$\langle {}^3L_J | \mathbb{T} | {}^3L_J \rangle = \begin{cases} -\frac{L}{6(2L+3)}, & J = L+1 \\ +\frac{1}{6} & J = L \\ -\frac{(L+1)}{6(2L-1)} & J = L-1 \end{cases} \quad (1.26)$$

The parameters that follow from fitting these masses are  $(\alpha_s, b, m_c, \sigma) = (0.5461, 0.1425 \text{ GeV}^2, 1.4794 \text{ GeV}/c^2, 1.0946 \text{ GeV})$ . Given these values, we can predict the masses and matrix elements of the currently unknown  $c\bar{c}$  states. The resulting prediction, shown on Fig. 1.12, is compatible with all known charmonium masses. [33]

## 1.5 Quarkonium production and effective theories

### 1.5.1 Prompt production

The heavy-quark mass  $m$  is much larger than  $\Lambda_{\text{QCD}}$ , and, in the case of production, the transverse momentum  $p_T$  can be much larger than  $\Lambda_{\text{QCD}}$  as well. This implies that the associated values of the QCD running coupling constant are less than one ( $\alpha_s(m_c) \approx 0.25$  and  $\alpha_s(m_b) \approx 0.18$ ). Therefore, it should be possible to calculate the rates for heavy quarkonium decay and production accurately in perturbation theory. However, there are clearly low-momentum, non-perturbative effects which are corresponding to the dynamics of the quarkonium bound state. It makes impossible the direct application of the perturbative approach. A calculation algorithm, called **factorisation**, allows to separate short-distance/high-momentum, perturbative effects from long-distance/low-momentum, non-perturbative effects. [29]

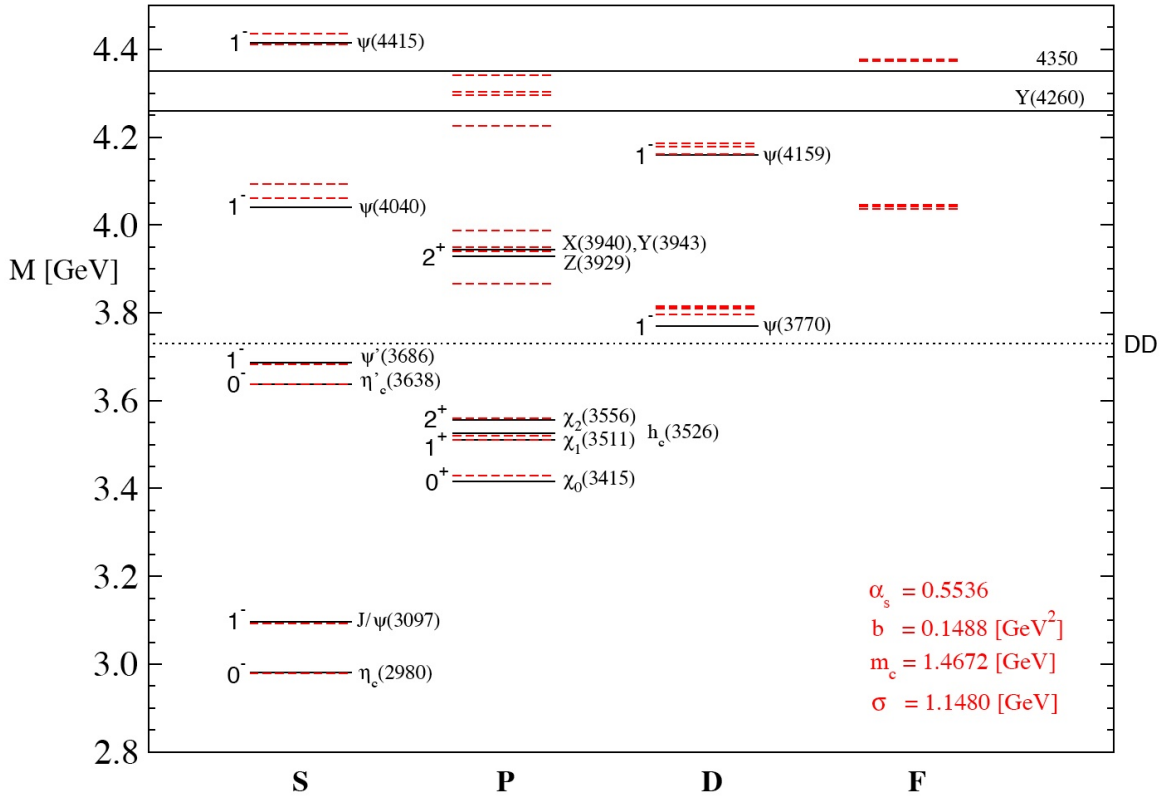


Figure 1.12: The current experimental status of charmonium spectroscopy, compared to the predictions of a non-relativistic potential model. Experimental levels are solid lines, and theoretical levels are dashed. The open-charm threshold at 3.73 GeV is also shown. Taken from Ref [33] with the Ref [34] updates.

One of the common ways to perform such separation is to use effective Non-relativistic QCD (NRQCD). NRQCD reproduces QCD at order of  $mv$  momentum accuracy and smaller, where  $v$  is the typical heavy-quark velocity in the bound state in the centre-of-mass frame defined in section 1.4). NRQCD factorisation is a consequence of QCD in the limit  $\Lambda_{\text{QCD}}/m \rightarrow 0$  [29].

Since the heavy quark pair production occurs at momentum scales of order  $m$  or larger, it manifests itself in NRQCD through contact interactions. Therefore the resulting prompt production cross-section of the quarkonium at the transverse momentum range  $p_T \gtrsim m$  is given by the sum of products of the NRQCD matrix elements and short-distance coefficients:

$$\sigma(m) = \sum_n \sigma_n(\Lambda) \langle \mathcal{O}_n^m(\Lambda) \rangle, \quad (1.27)$$

where  $\Lambda$  is the ultraviolet cut off of the effective theory, the  $\sigma_n$  are short-distance coefficients, and the  $\langle \mathcal{O}_n^m \rangle$  are vacuum expectation values of four-fermion operators in NRQCD. [29]

The short-distance coefficients  $\sigma_n$  strongly depends on the process. They corresponds to the probability to create a  $q\bar{q}$  pair in parton interactions. They are convolved with parton distributions of the initial state hadrons in case of  $pp$ ,  $p\bar{p}$  or  $pe$  initial interactions.

The vacuum matrix element is the probability for a  $q\bar{q}$  pair to form a quarkonium plus anything else. These matrix elements are somewhat analogous to the parton fragmentation functions. They contain all of the non-perturbative physics associated with the evolution of the  $q\bar{q}$  quarkonium state. [29]

The colour-singlet and the colour-octet operators that appear in Eq 1.27 correspond to the transformation of the created  $q\bar{q}$  pair to a colour-singlet or a colour-octet state respectively. The importance of the terms in Eq 1.27 is determined by magnitudes of the matrix elements and also by the magnitudes of the coefficients  $\sigma_n$ . The size of the coefficient depends on its order in  $\alpha_s$ , colour factors and kinematic factors such as  $m^2/p_T^2$ .

NRQCD counting rules allow to perform the sum over operators from Eq 1.27 as an expansion in powers of  $v$ . At the given power of  $v$  only a finite number of matrix elements contribute. Moreover, some simplifications between matrix elements can be applied, such as the heavy quark spin symmetry and the vacuum saturation approximation. This reduces the amount of independent elements. Some examples of relations between colour-singlet matrix elements that follow from heavy quark spin symmetry are

$$\langle \mathcal{O}_1^{J/\psi}({}^3S_1) \rangle = 3 \langle \mathcal{O}_1^{\eta_c}({}^1S_0) \rangle, \quad (1.28)$$

$$\langle \mathcal{O}_1^{\chi_{cJ}}({}^3P_J) \rangle = \frac{(2J+1)}{3} \langle \mathcal{O}_1^{h_c}({}^1P_1) \rangle, \quad (1.29)$$

These relations are valid up to the  $v^2$  order. The coefficients before matrix elements in Eqs 1.28 and 1.29 are ratios of the numbers of spin states. Similar relations between

colour-octet matrix elements can be written:

$$\langle \mathcal{O}_8^{J/\psi}({}^3S_1) \rangle = 3 \langle \mathcal{O}_8^{\eta_c}({}^1S_0) \rangle, \quad (1.30)$$

$$\langle \mathcal{O}_8^{J/\psi}({}^1S_0) \rangle = \langle \mathcal{O}_8^{\eta_c}({}^3S_1) \rangle, \quad (1.31)$$

$$\langle \mathcal{O}_8^{J/\psi}({}^3P_J) \rangle = \frac{(2J+1)}{3} \langle \mathcal{O}_8^{\eta_c}({}^1P_1) \rangle, \quad (1.32)$$

$$\langle \mathcal{O}_8^{\chi_{cJ}}({}^3S_1) \rangle = \frac{(2J+1)}{3} \langle \mathcal{O}_8^{h_c}({}^1S_0) \rangle, \quad (1.33)$$

These relations hold up to corrections of order  $v^2$ .

The colour-octet terms in Eq 1.27 are expected to dominate in some cases, such as  $J/\psi$  production at large  $p_T$  in hadron colliders. Still, there are also situations in which colour-singlet terms are expected to make the dominant contribution such as  $J/\psi$  production in continuum  $e^+e^-$  annihilation at the  $B$ -factories. [29]

The proof of the factorisation formula in Eq 1.27 relies both on NRQCD and on the all-orders perturbative machinery for proving hard-scattering factorisation. At a large transverse momentum  $p_T \gtrsim m$ , corrections to hard-scattering factorisation are expected to be of order  $(mv)^2/p_T^2$  (not  $m^2/p_T^2$ ) in the unpolarised case and of order  $mv/p_T$  (not  $m/p_T$ ) in the polarised case. At the transverse momentum range  $p_T \leq mv$  the soft gluons in the quarkonium binding process leads to significant difficulties in the factorisation technique application. It is not clear if there is a factorisation formula for  $d\sigma/dp_T^2$  at small  $pt$  or for  $d\sigma/dp_T^2$  integrated over  $p_T$ . [29]

There are many uncertainties in practical calculations of the quarkonium decay and production rates. The series of  $\alpha_s$  and  $v$  factors in Eq. 1.27 in many cases converge slowly, that leads to the large uncertainties — 100% or larger. The matrix elements are also poorly determined, either from phenomenology or lattice calculations, and their linear combinations vary from process to process, which makes difficult tests of universality. There are also large uncertainties in the  $b$  and  $c$  quarks masses,  $\sim 8\%$  for  $m_c$  and  $\sim 2.4\%$  for  $m_b$  [11], which makes a significant deposit in the quarkonium rates calculations since they depend on the squares of quark masses.

A lot of large uncertainties in the theoretical predictions, as well as some uncertainties in the experimental measurements, can be cancelled in the cross-section ratios. [29]

The polarisation variables make another set of observables in which many of the uncertainties cancel out. They are defined as ratios of cross-sections for the production of different spin states of the same quarkonium. The polarisation of the  $J/\psi$  with  $J^{PC} =$

$1^{--}$  can be measured from the angular distribution of its decay products.

The choice of the reference axis depends on the process. In the helicity frame [35] the polarisation axis is defined by the direction of quarkonium momentum in the laboratory frame. In the Collins-Soper frame [36] the polarisation axis is the direction of the relative velocity of the colliding beams in the charmonium rest frame.

The differential cross-section, apart from a normalisation factor, can be written as [37]

$$\frac{d^2N}{d\cos\theta d\phi} \propto 1 + \lambda_\theta \cos^2\theta + \lambda_{\theta\phi} \sin^2\theta \cos\phi + \lambda_\phi \sin^2\theta \cos^2\phi, \quad (1.34)$$

where  $\theta$  is the polar angle between the direction of the positively charged decay particle and polarisation axis, and  $\phi$  is the angle between decay and production planes. Parameters  $\lambda_\theta$ ,  $\lambda_{\theta\phi}$  and  $\lambda_\phi$  are defined in range  $(-1, 1)$ . The  $\lambda_\theta = 1$ ,  $\lambda_{\theta\phi} = \lambda_\phi = 0$  configuration corresponds to a totally transverse polarisation, and the  $\lambda_\theta = -1$ ,  $\lambda_{\theta\phi} = \lambda_\phi = 0$  configuration is valid for a totally longitudinal polarisation. If all polarisation parameters are equal to zero then no polarisation is observed. The  $\lambda_\theta$ ,  $\lambda_{\theta\phi}$  and  $\lambda_\phi$  depend on the polarisation axis choice. However, their combination

$$\lambda_{inv} = \frac{\lambda_\theta + 3\lambda_\phi}{1 - \lambda_\phi} \quad (1.35)$$

does not depend on the polarisation axis choice [38, 39].

There are different theoretical models for inclusive quarkonium production. The most important of them are the colour-singlet model (CSM), the colour-evaporation model (CEM), the NRQCD factorisation approach, and the fragmentation approach. [31]

### Colour-singlet model

The CSM was suggested soon after the  $J/\psi$  meson discovery. According to this model, it is assumed that the  $q\bar{q}$  pair transforms directly into the colour-singlet quarkonium state and thus have the same spin and angular-momentum quantum numbers. In CSM the production rate of the quarkonium state depends on the absolute values of the colour-singlet  $q\bar{q}$  wave function and its derivatives. They can be obtained with the comparison of the theoretical expressions for quarkonium decay rates with experimental measurements. Apart from these quantities CSM has no free parameters [31]. The CSM is useful in predicting quarkonium production rates at the relatively low energy scale [40]. However, in 1995 the experiments at the Tevatron showed that it underestimates

the prompt charmonium production cross-section in  $p\bar{p}$  collisions by more than an order of magnitude [29]. However, given the very large corrections at NLO and NNLO, the perturbative expansion in  $\alpha_s$  can be not convergent. Moreover, in the production and decay of P-wave and other  $J \geq 1$  quarkonium states, the CSM leads to uncanceled infra-red divergences [31]. Thus, the CSM is theoretically inconsistent for quarkonium states with non-zero orbital angular momentum. The NRQCD factorisation approach involves the colour-singlet model and generalises it [31].

### Colour-evaporation model

The CEM involves the assumption that every  $q\bar{q}$  pair transforms into a quarkonium if it has an invariant mass that is less than the threshold for producing a pair of open flavour heavy mesons. Thus the cross-section for a quarkonium state  $H$  is some fraction  $F_H$  of the cross-section for producing  $q\bar{q}$  pairs. It has an upper limit on the  $q\bar{q}$  pair mass but no constraints on the spin or colour of the final state. The  $q\bar{q}$  pair loses its colour in interaction with the collision-induced gluon field, which is called ‘‘colour evaporation’’. The sum of the fractions  $F_H$  over all quarkonium states  $H$  can be less than 1, since the additional energy, needed for heavy meson pair production from  $q\bar{q}$ , can be obtained from the non-perturbative colour field. The fractions  $F_H$  are assumed to be universal so they are applicable in different kinematic regions. [29, 31]

At the leading order in  $\alpha_s$ , the production cross-section for the quarkonium state  $H$  in collisions of the light hadrons  $h_A$  and  $h_B$  is:

$$\sigma_{\text{CEM}}[h_A R \rightarrow H + X] = F_H \sum_{i,j} \int_{4m^2}^{4m_M^2} d\hat{s} \int dx_1 dx_2 f_i^{h_B}(x_2, \mu) \hat{\sigma}_{ij}(\hat{s}) \delta(\hat{s} - x_1 x_2 s), \quad (1.36)$$

where  $ij = q\bar{q}$  or  $gg$ ,  $\hat{s}$  is the square of the partonic centre-of-mass energy, and  $\hat{\sigma}_{ij}$  is the  $ij \rightarrow q\bar{q}$  subprocess cross-section.

### Fragmentation approach

In the fragmentation-function approach to factorisation for inclusive quarkonium production [41, 42], the production cross-section is expressed in terms of a convolution of parton production cross-sections and light-cone fragmentation functions. This procedure provides a convenient way to consider the contributions to the cross-section in terms of decomposition in powers of  $m_q/p$ . In addition, it might also represents the first

step of the NRQCD factorisation [41, 42]. The light-cone fragmentation functions could be expanded in terms of NRQCD matrix elements.

A contribution to the cross-section at the leading power in  $m_q/p_T$  is given by the production of a single parton (e.g. a gluon) at a distance scale of the order of  $1/p_T$ , which subsequently fragments into a heavy quarkonium. The contribution to the cross-section at the first subleading order power in  $m_q/p_T$  is given by the  $q\bar{q}$  pair production in a vector- or an axial-vector state, at a distance scale of order  $1/p_T$ , which then fragments into a heavy quarkonium.

The fragmentation-function approach for the specific case of a single inclusive heavy-quarkonium production at transverse momentum  $p_T \gg m_q$  is given by

$$\begin{aligned}
d\sigma_{A+B \rightarrow H+X}(p_T) = & \\
& \sum_i d\hat{\sigma}_{A+B \rightarrow i+X}(p_T/z, \mu) \otimes D_{i \rightarrow H}(z, m_q, \mu) + \\
& \sum_{[q\bar{q}(\kappa)]} d\hat{\sigma}_{A+B \rightarrow [q\bar{q}(\kappa)]+X}(P_{[q\bar{q}(\kappa)]} = p_T/z, \mu) \\
& \otimes D_{[q\bar{q}(\kappa)] \rightarrow H}(z, m_q, \mu) + \mathcal{O}(m_q^4/p_T^4),
\end{aligned} \tag{1.37}$$

where the first term corresponds to the contribution of a leading order in  $m_q/p$ , and the second term reflects the contribution of the subleading order in  $m_q/p$ . The  $A$  and  $B$  are the initial particles in the hard-scattering process and  $\otimes$  represents a convolution in the momentum fraction  $z$ . The cross-section of the inclusive production of a particle  $i$ ,  $d\hat{\sigma}_{A+B \rightarrow i+X}$ , contains all the information about the incoming state and includes convolutions with parton distributions in the cases in which  $A$  or  $B$  is a hadron [29, 31].

### 1.5.2 Charmonium production from $b$ -hadron decays

B-meson decays are a common phenomena for studying charmonium production because B-mesons decay into charmonia with branching fractions greater than a percent. At a B factory operating near the peak of the  $\Upsilon(4S)$  resonance, about 25% of the events consist of a  $B^+B^-$  pair or a  $B^0\bar{B}^0$ . [29]

The Feynman diagram of B-meson decay into a charmonium state is shown on Fig. 1.13.

The inclusive branching fractions of B-mesons into charmonium states can be measured most accurately for the mixture of  $B^+$ ,  $B^0$ , and their antiparticles that are pro-

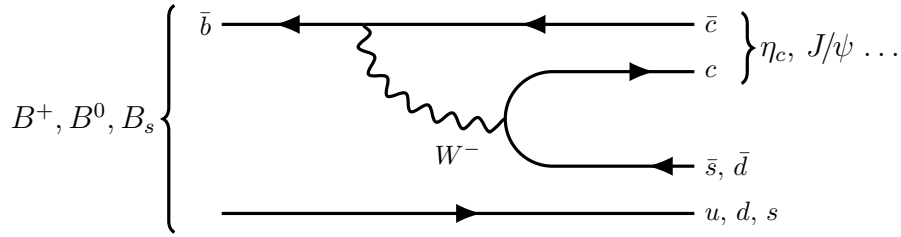


Figure 1.13: The diagram of the charmonium production from a B-meson decay.

duced in the decay of the  $\Upsilon(4S)$  resonance, see Table 1.2.

production energy	$J/\psi$	$\psi(2S)$	$\chi_{c1}$	$\chi_{c2}$
$\Upsilon(4S)$ energy, light B mesons	$11.5 \pm 0.6$	$3.5 \pm 0.5$	$3.6 \pm 0.5$	$0.7 \pm 0.4$
$Z^0$ energy, all B hadron species	$11.6 \pm 1.0$	$4.8 \pm 2.4$	$11.5 \pm 4.0$	

Table 1.2: Inclusive branching fractions  $\times 10^{-3}$  for mixtures of  $b$ -hadrons to decay into charmonium states. [29]

The observed inclusive branching fractions of B-mesons into  $J/\psi$  and  $\psi(2S)$  are larger than the predictions of the colour-singlet model by about a factor of three. So the NRQCD factorisation approach to the production of  $J/\psi$  and  $\psi(2S)$  in B decays has been applied. The colour-octet  $^3S_1$  term in the production rate is suppressed by a factor of  $v^4$  that comes from the NRQCD matrix element. However, the production rate also involves Wilson coefficients that arise from evolving the effective weak Hamiltonian from the scale  $M_W$  to the scale  $m_b$ . The Wilson coefficient for the colour-octet  $^3S_1$  term is significantly larger than that for the colour-singlet term, although the smallness of the colour-singlet term may be due to an accidental cancellation that occurs in the leading-order treatment of the the coefficient evolution. Moreover, the colour-singlet contribution is decreased by a relativistic correction of order  $v^2$ . The inclusion of a colour-octet  $^3S_1$  term allows one to explain the factor of three discrepancy between the data and the colour-singlet model prediction. [29]

The observed branching fraction for decays of B directly into  $J/\psi$ , which excludes the feed down from decays via  $\psi(2S)$  or  $\chi_c$ , is much larger than the prediction of the colour-evaporation model. The CEM prediction for the branching fraction of the direct  $b \rightarrow J/\psi X$  transition is in the range of 0.24–0.66, where the uncertainty comes from the error in the CEM parameters.

The effect of colour-octet terms on the  $J/\psi$  polarisation in  $b$ -decays was studied. In B-meson decays, the most convenient choice of the polarisation axis is the direction of the boost vector from the  $J/\psi$  rest frame to the rest frame of the B-meson. The CEM

predicts no polarisation. The predictions of NRQCD factorisation and of the colour-singlet model depend on the effective mass of the  $b$  quark. For  $m_b = 4.7 \pm 0.3 \text{ GeV}/c^2$ , the prediction of NRQCD factorisation is  $\alpha_s = -0.33 \pm 0.08$  and the prediction of the colour-singlet model is  $\alpha_s = -0.40 \pm 0.07$ . The uncertainties that arise from the  $m_b$  value have been added in quadrature with other uncertainties. [29]

## 1.6 Decay modes

Quarkonium dominantly decays via the electromagnetic or strong interaction decay channels [40]. The quark-antiquark annihilation is the main mechanism of quarkonium decay into light particles. Since this process occurs with the energy transfer of the order of charmonium mass  $m$ , that is perturbative, heavy quarks annihilate into the minimal number of gluons, allowed by quantum number selection rules. Intermediate gluons create light quark-antiquark pairs that forms the final state hadrons:  $Q\bar{Q} \rightarrow ng^* \rightarrow q\bar{q}$ , where  $q = u, d, s$ . The value of  $n$  depends on the quarkonium state  $Q\bar{Q}$ , see Table 1.3.

	$^{2S+1}L_J$	$I^G(J^{PC})$	gluons	photons
$\eta_c, \eta_b$	$^1S_0$	$0^+(0^{-+})$	$2g$	$2\gamma$
$J/\psi, \Upsilon(1S)$	$^3S_1$	$0^-(1^{--})$	$(3g)_d$	$\gamma$
$h_c, h_b$	$^1P_1$	$0^-(1^{+-})$	$(3g)_d$	$3\gamma$
$\chi_{c0}, \chi_{b0}$	$^3P_0$	$0^+(0^{++})$	$2g$	$2\gamma$
$\chi_{c1}, \chi_{b1}$ [43]	$^3P_1$	$0^+(1^{++})$	$3g$	$3\gamma$
$\chi_{c2}, \chi_{b2}$	$^3P_2$	$0^+(2^{++})$	$2g$	$2\gamma$

Table 1.3: Quantum numbers of quarkonium states and a minimal number of virtual gluons and photons produced in annihilation. The subscript  $d$  refers to a gluonic colour-singlet state that is totally symmetric under permutations of gluons. [29] [43]

The  $J/\psi$  decay into light hadrons proceed via three real gluons. The decay width to the light hadrons is expressed as

$$\Gamma(J/\psi \rightarrow l.h.) = \frac{10}{81} \frac{\pi^2 - 9}{\pi e_c^2} \frac{\alpha_s^3}{\alpha_{\text{em}}^2} \Gamma(J/\psi \rightarrow e^+e^-) = 205 \text{ keV} \pi e_c^2 \alpha_{\text{em}}^2 \left( \frac{\alpha_s}{0.3} \right)^3, \quad (1.38)$$

Although this value is somewhat larger than the experimental one it explains the small partial width of the hadronic decays of the quarkonia. Corrections like relativistic,  $\alpha_s$  or colour-octet ones, may lead to a better agreement with experiment. A systematic way to include these corrections is provided by nonrelativistic effective field theories of QCD. [33]

The colour-singlet model assumption is that only heavy-quarkonium states with quark-antiquark in a colour-singlet configuration can exist, only colour-singlet four-fermion operators contribute and the matrix elements reduce to heavy-quarkonium wave functions (or derivatives of them) calculated at the origin.

Quark diagrams describing quarkonium decays into the proton-antiproton final state are shown on Fig. 1.14 for  $J^P = 1^-$  states and on Fig. 1.15 for other states.

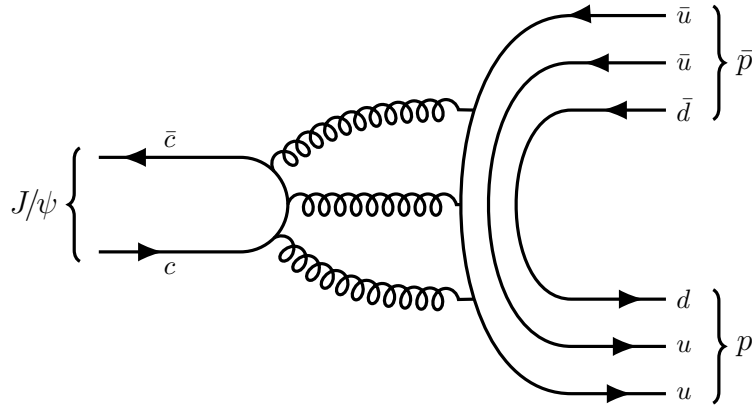


Figure 1.14: Quark diagram of charmonium decay to the  $p\bar{p}$  pair via emission of three gluons. This process is valid for  $J^P = 1^-$  states:  $J/\psi$ ,  $h_c$ ,  $\psi(2S)$ .

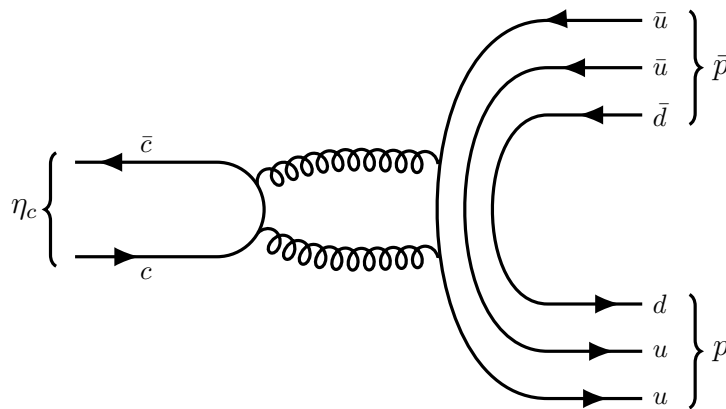


Figure 1.15: Quark diagram of charmonium decay to the  $p\bar{p}$  pair via emission of two gluons. This process is allowed for the most of charmonia, except  $J^P = 1^-$  states:  $\eta_c$ ,  $\chi_{c0}$ ,  $\chi_{c1}$ ,  $\chi_{c2}$ .

For  $^1S_0$  states hadronic decays into light hadrons involve contributions from three-gluon  $ggg$  and  $q\bar{q}g$  final states up to  $\mathcal{O}(\alpha_s^3)$ :

$$\Gamma(n^1S_0 \rightarrow l.h.) = \Gamma(n^1S_0 \rightarrow gg) + \Gamma(n^1S_0 \rightarrow ggg) + \sum_q \Gamma(n^1S_0 \rightarrow q\bar{q}g), \quad (1.39)$$

in other words:

$$\Gamma(n^1S_0 \rightarrow l.h.) = \Gamma(n^1S_0 \rightarrow gg) \left[ 1 + \frac{\alpha_s(\mu)}{\pi} \left( \beta_0 \ln \frac{\mu}{m_q} + C[{}^1S_0] \right) \right], \quad (1.40)$$

where  $C[{}^1S_0]$  is a known correction,  $C[{}^1S_0] = 4.85$  for  $\eta_c$  and  $C[{}^1S_0] = 4.42$  for  $\eta_b$ . [40]

The total decay width of the  ${}^3S_1$  is composed by the electromagnetic decays  ${}^3S_1 \rightarrow \ell\bar{\ell}$ ,  $q\bar{q}$ , radiative decays and gluonic decays  $ggg$  and  $gg\gamma$ . The leptonic width at the first order corrections is expressed as

$$\Gamma(n^3S_1 \rightarrow \ell\bar{\ell}) = 4e^2\alpha_{\text{em}}^2 \frac{|R_{nS}(0)|^2}{M_n^2} \left( 1 - \frac{16}{3} \frac{\alpha_s}{\pi} \right) \left( 1 + \frac{2m_\ell^2}{M_n^2} \right) \quad (1.41)$$

Electromagnetic transition between quarkonium states occurs via the emission of a photon and offers the distinctive experimental signature of a monochromatic photon, a useful production mechanism to observe and study the lower-lying state, and a unique window on the dynamics of such systems. Below we first review the status and open questions regarding the relevant theoretical framework and tools, and then describe important measurements of charmonium and bottomonium electromagnetic transitions. Some notable radiative transitions are shown on Fig. 1.16 for charmonium states and on Fig. 1.17 for bottomonium states. [31]

Electromagnetic transitions may be classified in terms of electric and magnetic transitions between eigenstates of the leading-order pNRQCD Hamiltonian. The states are classified in terms of the radial quantum number,  $n$ , the orbital angular momentum,  $l$ , the total spin,  $s$ , and the total angular momentum,  $J$ . In the non-relativistic limit, the spin dependence of the quarkonium wave function decouples from the spatial dependence. The spatial part of the wave function,  $\psi(\vec{x})$ , can be expressed in terms of a radial wave function,  $u_{nl}(r)$ , and the spherical harmonics,  $Y_{lm}$ , as  $\psi(\vec{x}) = Y_{lm}(\theta, \phi)u_{nl}(r)/r$ .

Magnetic transitions flip the quark spin. Transitions that do not change the orbital angular momentum are called magnetic dipole, or M1, transitions. Electric transitions do not change the quark spin. Transitions that change the orbital angular momentum by one unit are called electric dipole, or E1, transitions. The E1 transitions are more copiously observed than allowed M1 transitions, because the rates of the electric transitions are enhanced by  $1/v^2$  with respect to the magnetic ones. Clearly, the multipole expansion is always allowed for transitions between states with the same principal quantum numbers ( $E_\gamma \sim mv^4$  or  $mv^3 \ll mv$ ) or with contiguous principal quantum numbers ( $E_\gamma \sim mv^2 \ll mv$ ). For transitions that involve widely separated states, the hierarchy

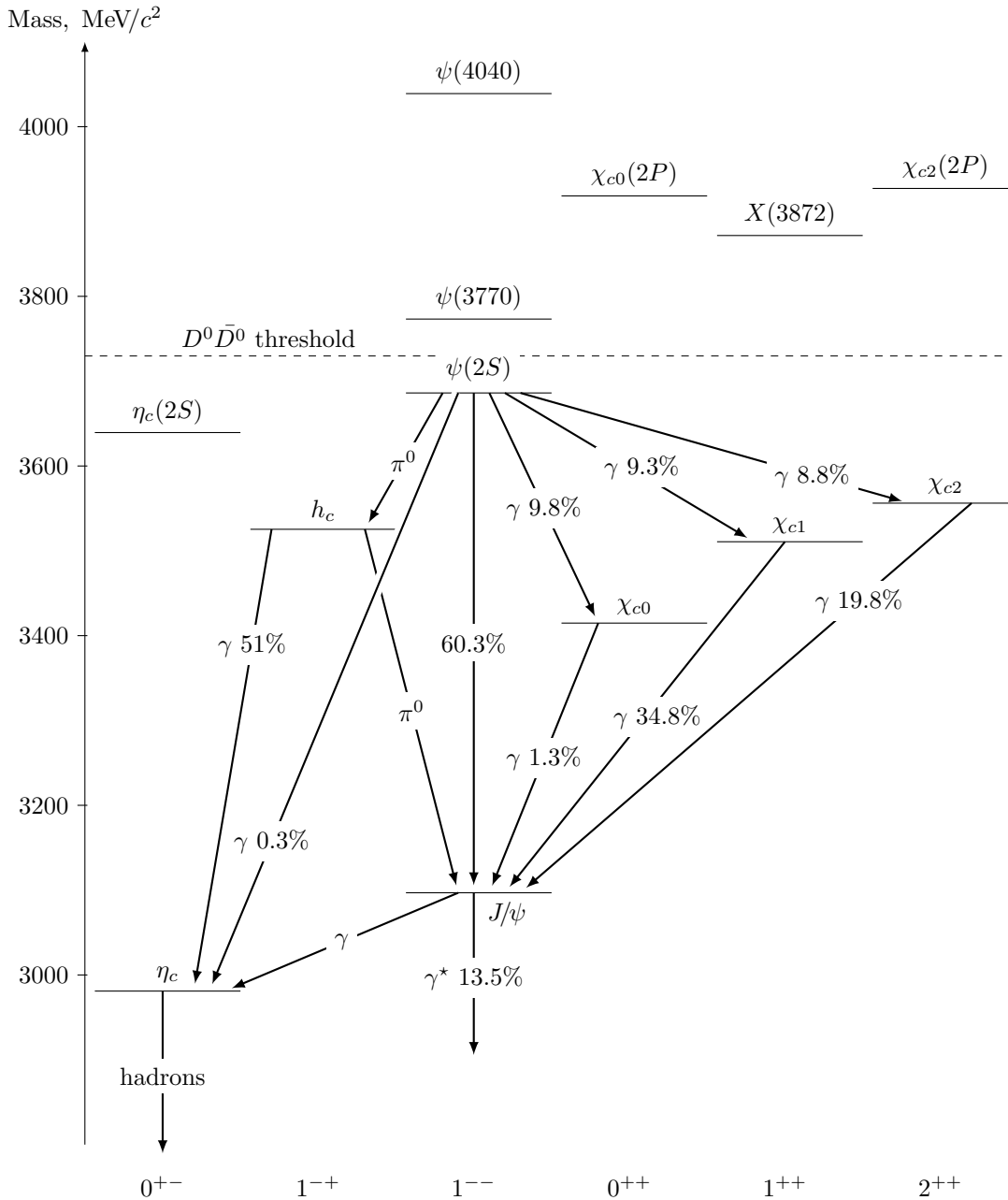


Figure 1.16: Scheme of the experimentally observed charmonium states and their notable decay channels with the branching ratios (if known). States above the  $D^0\bar{D}^0$  threshold decays preferably to the charmed meson-antimeson pair. [11]

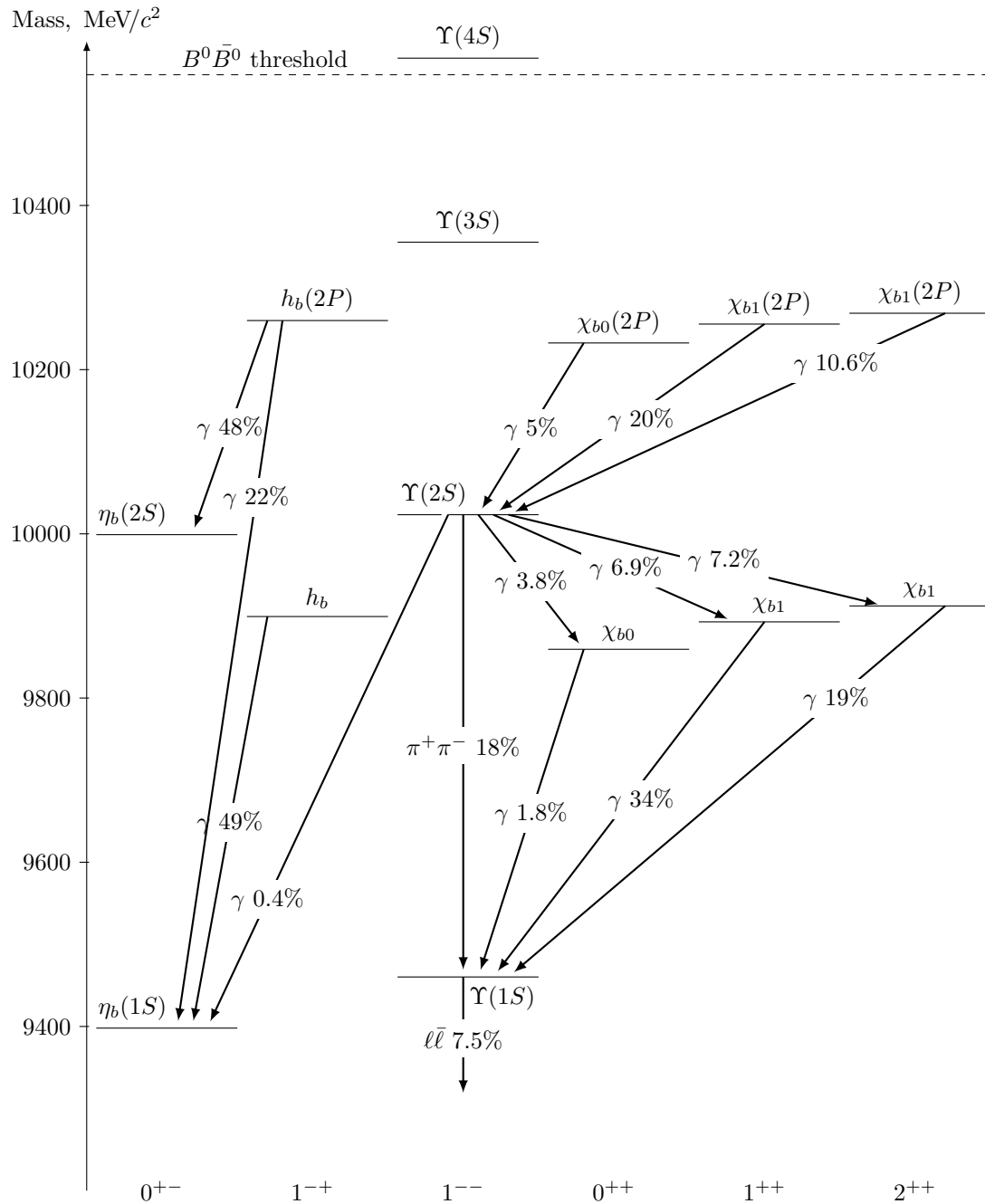


Figure 1.17: Scheme of the experimentally observed bottomonium states and their notable decay channels with the branching ratios (if known). States above the  $B^0\bar{B}^0$  threshold decays preferably to the beauty meson-antimeson pair. [11]

$E_\gamma \ll mv$  may not be realised [31]

# Chapter 2

## Quarkonium production

### 2.1 Introduction

There are two main sources of charmonium production. Prompt production occurs in the primary parton interaction. Secondary charmonium comes from the electroweak decays of  $b$ -hadrons, see section 1.5.2. Experimentally these two sources are distinguished by secondary vertex separation.

All known charmonium states with masses below the  $D\bar{D}$  threshold are listed in Table 2.1.

	mass, MeV/ $c^2$	$\Gamma$	$\mathcal{B}_{c\bar{c}\rightarrow p\bar{p}}, \times 10^{-3}$
$\eta_c(1S)$	$2983.7 \pm 0.7$	$32.0 \pm 0.9$ MeV	$1.51 \pm 0.16$
$J/\psi(1S)$	$3096.916 \pm 0.011$	$92.9 \pm 2.8$ keV	$2.120 \pm 0.029$
$\chi_{c0}(1S)$	$3414.75 \pm 0.31$	$10.3 \pm 0.6$ MeV	$0.213 \pm 0.012$
$\chi_{c1}(1P)$	$3510.66 \pm 0.07$	$0.86 \pm 0.05$ MeV	$0.073 \pm 0.004$
$h_c(1P)$	$3525.38 \pm 0.11$	$0.7 \pm 0.4$ MeV	$3.2 \pm 0.5$
$\chi_{c2}(1P)$	$3556.20 \pm 0.09$	$1.97 \pm 0.11$ MeV	$0.071 \pm 0.004$
$\eta_c(2S)$	$3639.4 \pm 1.3$	$11.3^{+3.2}_{-2.9}$ MeV	$< 0.29$
$\psi(2S)$	$3686.109^{+0.012}_{-0.014}$	$303 \pm 9$ keV	$0.275 \pm 0.012$

Table 2.1: Known charmonium states below the  $D\bar{D}$  pair mass threshold. Branching fractions of charmonium states decaying to a proton-antiproton pair are from [44] for  $h_c$ , and from Ref. [11] for all the other listed states

## 2.2 $J/\psi$ production in $b$ -hadron decays

The  $J/\psi$  meson was first observed as a narrow resonance in direct  $e^+e^-$  interactions in 1974 by the B. Richter and S. Ting teams independently [27, 26]. It is found to be a bound  $c\bar{c}$  state with the quantum numbers angular momentum and CP parity equal to  $1^{--}$ . The mass and the natural width  $\Gamma_{J/\psi}$  are listed in Table 2.1.

Because of its quantum numbers, the  $J/\psi$  can decay through a virtual photon to a lepton-antilepton pair with a relatively high branching ratio  $\mathcal{B}_{J/\psi \rightarrow e^+e^-} = 5.94 \pm 0.06\%$ ,  $\mathcal{B}_{J/\psi \rightarrow \mu^+\mu^-} = 5.93 \pm 0.06\%$  [11]. Therefore the relatively clean dimuon channel  $J/\psi \rightarrow \mu^+\mu^-$  is used in the most  $J/\psi$  studies.

All charmonium states and the  $J/\psi$  meson in particular can be produced in two main ways (see section 1.5). The world average of branching fraction of a mixture of  $b$ -hadrons into  $J/\psi$  is [11]:

$$\mathcal{B}_{b \rightarrow J/\psi X} = 1.16 \pm 0.10\%.$$

This value includes results from the DELPH, L3 and ALEPH experiments performed on the LEP collider at CERN [45, 46, 47]. All of them studied the  $J/\psi$  production with  $e^+e^-$  collisions at a centre-of-mass energy equal to the  $Z$  boson mass  $\sqrt{s} = M_Z = 91.2 \text{ GeV}/c^2$ . The decay channel  $e^+e^- \rightarrow Z \rightarrow b\bar{b}$ ,  $b \rightarrow J/\psi X$  was used, where  $J/\psi \rightarrow e^+e^-$  or  $J/\psi \rightarrow \mu^+\mu^-$ .

### 2.2.1 Production at hadron machines

Studying of the charmonium production at hadron machines is different from similar analyses at electron machines. The dense hadron medium causes a large amount of background.

A lot of measurements of the inclusive charmonium production in  $b$ -hadron decays were performed by the LHCb collaboration. It studied the  $J/\psi$  production in the  $pp$  collisions at 2.76 TeV, 7 TeV and 8 TeV centre-of-mass energies [48, 49, 50]. The  $J/\psi \rightarrow \mu^+\mu^-$  decay channel was used in all analyses. The results are summarised in Table 2.2.

$\sqrt{s}$ , TeV	data set	$\sigma_{J/\psi}$	$\sigma_{b\bar{b}} \times \mathcal{B}_{b \rightarrow J/\psi X}$	phase space volume
2.76 [48]	71 $\text{nb}^{-1}$	$5.6 \pm 0.1 \pm 0.4 \text{ } \mu\text{b}$	$400 \pm 35 \pm 49 \text{ nb}$	$p_T < 12 \text{ GeV}/c$
7 [49]	5.2 $\text{pb}^{-1}$	$10.52 \pm 0.04 \pm 1.40^{+1.64}_{-2.20} \text{ } \mu\text{b}$	$1.14 \pm 0.01 \pm 0.16 \text{ } \mu\text{b}$	$p_T < 14 \text{ GeV}/c$
8 [50]	18 $\text{pb}^{-1}$	$10.94 \pm 0.02 \pm 0.79 \text{ } \mu\text{b}$	$1.28 \pm 0.01 \pm 0.11 \text{ } \mu\text{b}$	$p_T < 14 \text{ GeV}/c$

Table 2.2: The LHCb results on the  $J/\psi$  production into  $2.0 < y < 4.5$

The absolute value of the  $\mathcal{B}_{b \rightarrow J/\psi X}$  can not be extracted since LHCb measurements do not yield a value of the total  $b\bar{b}$  cross-section [51].

The CMS experiment performed studies of the  $J/\psi$  production from  $b$ -hadron decays at  $\sqrt{s} = 7$  TeV centre-of-mass energy. Basing on the  $314 \text{ pb}^{-1}$  data set, in the transverse momentum range  $6.5 < p_{\text{T}}(J/\psi) < 30 \text{ GeV}/c$  it gives the value  $\sigma_{J/\psi} \times \mathcal{B}_{J/\psi \rightarrow \mu^+\mu^-} = 26.0 \pm 1.4 \pm 1.6 \pm 2.9 \text{ nb}$ , with the errors correspond to statistical, systematic and luminosity uncertainties [52].

The ATLAS collaboration measured the inclusive  $J/\psi$  yield from  $b$ -hadron decays. The  $2.3 \text{ pb}^{-1}$  data sample of  $\sqrt{s} = 7$  TeV centre-of-mass  $pp$  collisions was used. The  $J/\psi$  cross section from  $b$ -hadron decays in  $|y| < 2.4$ ,  $p_{\text{T}} > 7 \text{ GeV}/c$  phase space volume is found to be

$$\mathcal{B}_{J/\psi \rightarrow \mu^+\mu^-} \times \sigma(\sqrt{s} = 7 \text{ TeV}) = 23.0 \pm 0.6 \pm 2.8 \pm 0.2 \pm 0.8 \text{ nb},$$

and in  $1.5 < |y| < 2$ ,  $p_{\text{T}} > 1 \text{ GeV}/c$  phase space volume

$$\mathcal{B}_{J/\psi \rightarrow \mu^+\mu^-} \times \sigma(\sqrt{s} = 7 \text{ TeV}) = 61 \pm 24 \pm 19 \pm 1 \pm 2 \text{ nb},$$

with errors associated to the statistical, systematic, spin and luminosity uncertainties [53].

## 2.2.2 Production at the B-factories

The electromagnetic colliders, designed to produce a large number of  $B$  mesons are usually named B-factories. The Belle experiment [54] at the KEKB collider and the BaBar experiment [55] at the PEP-II collider at SLAC are examples of the B-factories. They operate with  $e^+e^-$  collisions at the centre-of-mass energy tuned to the mass of the  $\Upsilon(4S)$ ,  $\sqrt{s} = 9.46 \text{ GeV}/c$ . Therefore the  $B_s^0$  mesons with mass  $M_{B_s^0} = 5366.77 \pm 0.24 \text{ MeV}/c^2$  [11] and  $b$ -baryons with the lightest known mass  $M_{\Lambda_b^0} = 5619.4 \pm 0.6 \text{ MeV}/c^2$  [11] are not accessible: the centre-of-mass energy is not sufficient for their pair production.

The average fraction of  $B^\pm/B^0$  mesons admixture decaying to the  $J/\psi$  mesons is [11]:

$$\mathcal{B}_{b \rightarrow J/\psi X} = 1.094 \pm 0.032\%.$$

There are two recent results that contribute significantly to the number above.

Using  $9.1 \text{ fb}^{-1}$  of  $\Upsilon(4S)$  centre-of-mass energy data, the CLEO collaboration studied the inclusive branching fraction and the  $J/\psi$  momentum distribution in  $b$ -decay

production. The  $J/\psi$  meson was reconstructed with the  $J/\psi \rightarrow \mu^+\mu^-$  and  $J/\psi \rightarrow e^+e^-$  decay channels. The inclusive branching fraction from B-meson decays was found to be  $\mathcal{B}_{b \rightarrow J/\psi X} = 1.121 \pm 0.013 \pm 0.040 \pm 0.013\%$  for the total  $J/\psi$  creation including the feed-down from the higher states, and  $\mathcal{B}_{b \rightarrow J/\psi X}^{\text{direct}} = 0.813 \pm 0.017 \pm 0.036 \pm 0.010\%$  for the direct  $J/\psi$  production from B-meson decays. The given error values correspond to statistical, systematic, and the uncertainty in the  $\mathcal{B}_{J/\psi \rightarrow \mu^+\mu^-}$  and  $\mathcal{B}_{J/\psi \rightarrow e^+e^-}$  branching fractions [56].

Performing similar studies with the  $20.3 \text{ fb}^{-1}$  of data, using the same decay channels of the  $J/\psi$ , the BaBar experiment measured the inclusive branching fraction of the  $J/\psi$  from B-meson decays. It was found to be  $\mathcal{B}_{b \rightarrow J/\psi X} = 1.057 \pm 0.012 \pm 0.040\%$  for the total  $J/\psi$  creation, and  $\mathcal{B}_{b \rightarrow J/\psi X}^{\text{direct}} = 0.740 \pm 0.023 \pm 0.043\%$  for the direct  $J/\psi$  production [57], statistical and systematic errors are shown.

## 2.3 $\eta_c$ production in $b$ -hadron decays

The  $\eta_c$  is the lightest S-wave spin-singlet charmonium state. It has been observed at the SLAC experiment in 1980 [58] and stays poorly studied since that time. No studies have been performed on the  $\eta_c$  production from  $b$ -hadron decays at hadron machines. The  $\eta_c \rightarrow \ell\ell$  decay channel is not accessible since the  $\eta_c$  quantum numbers do not allow decay via a single virtual photon. The decay through two virtual photons is suppressed because of the two-loop diagram.

The current limit on the  $\eta_c$  production in the decays of  $B^\pm/B^0$  mesons admixture, obtained by the experiments on B-factories, is [59]:

$$\mathcal{B}_{b \rightarrow \eta_c X} < 0.9\%,$$

at 90% confidence level. The analysis was performed by the CLEO collaboration. The chosen decay channel was  $B \rightarrow \eta_c(\rightarrow \phi\phi)X$ , with each  $\phi$  decaying to a  $K^+K^-$  pair. It is a relatively clean channel though the branching ratio is small:  $\mathcal{B}_{\eta_c \rightarrow \phi\phi} \times (\mathcal{B}_{\phi \rightarrow K^+K^-})^2 = (0.42 \pm 0.05) \times 10^{-3}$  [11]. The  $\eta_c$  mass window was defined as a wide range from 2960 to 3010 MeV/ $c^2$  because of the non-precise knowledge of the  $\eta_c$  mass and natural width values.

## 2.4 Production of other charmonium states in $b$ -hadron decays

The current average values for the branching fractions of a mixture of  $b$ -hadrons into  $J/\psi$  are given in Table 2.3. The most precisely studied particles are the  $J/\psi$  and  $\psi(2S)$  mesons, while the branching fraction of  $B^\pm/B^0/B_s^0/b$ -baryon admixture into  $\chi_{c1}$  and the  $\chi_{c2}$  inclusive yield at the B-factories are known only with an error of three standard deviations.

$c\bar{c}$ state	$B^\pm/B^0$	$B^\pm/B^0/B_s^0/b$ -baryon
$\eta_c$	$< 9 \times 10^{-3}$	
$J/\psi$	$1.094 \pm 0.032\%$	$1.16 \pm 0.10\%$
$\chi_{c1}$	$(3.86 \pm 0.27) \times 10^{-3}$	$1.4 \pm 0.4\%$
$\chi_{c2}$	$(1.3 \pm 0.4) \times 10^{-3}$	
$\psi(2S)$	$(3.07 \pm 0.21) \times 10^{-3}$	$(2.83 \pm 0.29) \times 10^{-3}$

Table 2.3: The inclusive yield of charmonium from  $b$ -hadron decays [11].

The  $\chi_{c1}$  production studies were performed independently by the BaBar, CLEO (see section 2.2 for details of the analyses) and Belle collaborations [57, 56, 60]. Two data sets with a total integrated luminosity of  $32.4 \text{ fb}^{-1}$  were used by the Belle collaboration. Performing an analysis with the  $B \rightarrow \chi_{c1}X$  decay channel they found a branching fraction of a mixture of  $B^\pm/B^0$  into  $\chi_{c1}$  to be  $\mathcal{B}_{b \rightarrow \chi_{c1}X}^{B^\pm/B^0} = (3.63 \pm 0.22 \pm 0.34) \times 10^{-3}$  [60]. The BaBar collaboration reported  $\mathcal{B}_{b \rightarrow \chi_{c1}X}^{B^\pm/B^0} = (3.67 \pm 0.35 \pm 0.44) \times 10^{-3}$  [57] and the CLEO result is  $\mathcal{B}_{b \rightarrow \chi_{c1}X}^{B^\pm/B^0} = (4.35 \pm 0.29 \pm 0.40) \times 10^{-3}$  [56]. The inclusive  $\chi_{c1}$  yield from the  $B^\pm/B^0/B_s^0/b$ -baryon admixture was studied by the DELPHI and L3 collaborations [45, 46] (see section 2.2 for details of the analyses). The resulting branching fractions are  $\mathcal{B}_{b \rightarrow \chi_{c1}X}^{B^\pm/B^0/B_s^0/b\text{-baryon}} = 0.014 \pm 0.006^{+0.004}_{-0.002}$  [45] and  $\mathcal{B}_{b \rightarrow \chi_{c1}X}^{B^\pm/B^0/B_s^0/b\text{-baryon}} = 0.024 \pm 0.009 \pm 0.002$  [46] respectively.

The  $\chi_{c2}$  branching fraction from the  $B^\pm/B^0$  admixture was studied simultaneously with the  $\chi_{c1}$  in Refs. [60, 57]. The resulting branching fractions  $\mathcal{B}_{b \rightarrow \chi_{c1}X}^{B^\pm/B^0}$  were measured with about three-sigma errors, their average value is shown in Table 2.3. The same analyses studied the  $\psi(2S)$  inclusive yield from the  $B^\pm/B^0$  admixture.

The studies of the  $\psi(2S)$  inclusive yield from the  $B^\pm/B^0$  admixture were performed by the BaBar and CLEO collaborations in 2002-2003 years [57, 56] (see section 2.2 for details of the analyses). Both analyses used the  $\psi(2S) \rightarrow e^+e^-$  and  $\psi(2S) \rightarrow \mu^+\mu^-$  decay modes, and the  $\psi(2S) \rightarrow \pi^+\pi^-J/\psi$  additionally in Ref. [57].

The  $\psi(2S)$  inclusive yield from the  $B^\pm/B^0/B_s^0/b$ -baryon admixture was measured by the LHCb and CMS collaborations [61, 62]. Both analyses studied the  $pp$  collision at  $\sqrt{s} = 7$  TeV data with an integrated luminosity  $36 \text{ pb}^{-1}$  and  $37 \text{ pb}^{-1}$  respectively. The resulting branching ratios from the LHCb is found to be  $\mathcal{B}_{b \rightarrow \psi(2S)X}^{B^\pm/B^0/B_s^0/b\text{-baryon}} = (2.73 \pm 0.06 \pm 0.16 \pm 0.24) \times 10^{-3}$  [61] with the errors corresponding to the statistical, systematic and branching fractions uncertainty. The CMS collaboration reported  $\mathcal{B}_{b \rightarrow \psi(2S)X}^{B^\pm/B^0/B_s^0/b\text{-baryon}} = (3.08 \pm 0.12 \pm 0.13 \pm 0.42) \times 10^{-3}$  [62] with the errors corresponding to the statistical and systematic (first), theoretical (second) and branching fractions (third) uncertainties.

## 2.5 Prompt $J/\psi$ production

All studies of the prompt  $J/\psi$  production are performed at the LHCb experiment with the  $J/\psi \rightarrow \mu^+\mu^-$  decay mode. The summary of the  $\sigma_{J/\psi}(\sqrt{s})$  is given in the Table 2.2.

The CMS experiment performed studies of the prompt  $J/\psi$  production at  $\sqrt{s} = 7$  TeV with the  $37 \text{ pb}^{-1}$  of  $pp$  collision data. The  $J/\psi \rightarrow \mu^+\mu^-$  decay channel was used. The total  $J/\psi$  cross section times the  $J/\psi \rightarrow \mu^+\mu^-$  branching ratio was found to be  $\sigma_{J/\psi}(\sqrt{s} = 7 \text{ TeV}) \times \mathcal{B}_{J/\psi \rightarrow \mu^+\mu^-} = 54.5 \pm 0.3 \pm 2.3 \pm 2.2$ , where the single muon cuts are extrapolated down to zero  $p_T$ , within the phase space window of the measurement. More details on the phase space volume is given in Ref. [62].

The ALICE collaboration measured the prompt production  $J/\psi$  cross section at  $\sqrt{s} = 2.76$  TeV. Using  $1.1 \text{ nb}^{-1}$  of  $J/\psi \rightarrow e^+e^-$  and  $19.9 \text{ nb}^{-1}$  of  $J/\psi \rightarrow \mu^+\mu^-$  event data, the  $J/\psi$  cross section in the central region  $|y| < 0.9$  was found to be

$$\sigma_{J/\psi}(\sqrt{s} = 2.76 \text{ TeV}) = 7.75 \pm 1.78 \pm 1.39_{-1.63}^{+1.16} \mu\text{b},$$

and in the forward region  $2.5 < y < 4.0$

$$\sigma_{J/\psi}(\sqrt{s} = 2.76 \text{ TeV}) = 3.34 \pm 0.13 \pm 0.27_{-1.07}^{+0.53} \mu\text{b},$$

with the errors associated to the statistical, systematic and polarisation uncertainties [63]. The result for the forward region is compatible with the LHCb result for the same energy in Table 2.2, though LHCb rapidity range is wider.

The ATLAS collaboration found the prompt production  $J/\psi$  cross section in  $|y| <$

2.4,  $p_T > 7$  GeV phase space volume to be

$$\mathcal{B}_{J/\psi \rightarrow \mu^+\mu^-} \times \sigma(\sqrt{s} = 7 \text{ TeV}) = 59 \pm 1 \pm 8_{-6}^{+9} \pm 2 \text{ nb},$$

and in  $1.5 < |y| < 2$ ,  $p_T > 1$  GeV/ $c$  phase space volume

$$\mathcal{B}_{J/\psi \rightarrow \mu^+\mu^-} \times \sigma(\sqrt{s} = 7 \text{ TeV}) = 450 \pm 70_{-110}^{+90} \pm 20_{-110}^{+740} \pm 20 \text{ nb},$$

with errors associated to the statistical, systematic, spin and luminosity uncertainties [53]. For the detailed description of the analysis see section 2.2.

The  $J/\psi$  prompt production cross section at  $\sqrt{s} = 0.2$  TeV was measured at the STAR detector [64] for the transverse momentum region  $p_T < 14$  GeV/ $c$  [65].

## 2.6 Prompt $\eta_c$ and $\eta_b$ production

The  $\eta_c$  meson was never studied at the hadron machines. Its prompt production from the  $e^+e^-$  annihilation was performed at the BaBar, Belle and CLEO experiments [66, 67, 68, 69], see section 2.7 for details.

The  $\eta_b$  meson is the ground  $b\bar{b}$  state with the quantum numbers  $0^{-+}$  [11]. It was observed for the first time by the ALEPH collaboration in 2002 [70] and then studies by the B-factories [71, 72, 73]. The current limit on the  $\eta_b$  production at the hadron machine is set by the CDF collaboration, based on the  $1.1 \text{ fb}^{-1}$  of  $p\bar{p}$  collision data. With the  $\eta_b \rightarrow J/\psi J/\psi$ ,  $J/\psi \rightarrow \mu^+\mu^-$  decay mode, in the phase space volume  $|y| < 0.6$ ,  $p_T > 3$  GeV/ $c$ , the production cross section upper limit at 90% confidence level was found to be [74]

$$\sigma_{\eta_b}(\sqrt{s} = 1.96 \text{ TeV}) < 2.6 \text{ pb} \quad (2.1)$$

## 2.7 Studies of the $\eta_c$ properties

For a long time, there was a significant discrepancy in the  $\eta_c$  width measurements at the  $b$ -factories and from charmonium transitions [11]. The possible reasons of such a divergence may be the low statistic or inadequate description of the interference of the  $\eta_c$  with non-resonant components. The latest results on studies of the  $\eta_c$  properties are summarised in Table 2.4.

The distortion in the  $\psi(2S) \rightarrow \eta_c \gamma$  decay was observed by the CLEO collaboration. It was found that the reason is the photon-energy dependence of the magnetic

dipole transition rate [80]. Based on this observation, the BESIII collaboration in 2012 performed an analysis with the  $\psi(2S) \rightarrow \eta_c \gamma$  decay channel, where the  $\eta_c$  is reconstructed with six different final states:  $K_S K^+ \pi^-$ ,  $K^+ K^- \pi^0$ ,  $\pi^+ \pi^- \eta$ ,  $K_S K^+ \pi^- \pi^+ \pi^-$ ,  $K^+ K^- \pi^+ \pi^- \pi^0$ , and  $3(\pi^+ \pi^-)$ . The simultaneous fit with the all six decay channels was performed. The Breit-Wigner probability density function was modified by the  $E_\gamma^7$  factor to take into account the energy dependence of the radiative transition [75]. Another BESIII analysis deals with the  $h_c \rightarrow \gamma \eta_c$  decay channel, involving simultaneous fit of the 16 different  $\eta_c$  decay modes. The  $\eta_c$  invariant mass spectrum in E1 transition is not as distorted as in the M1 case [76]. The obtained mass and natural width values are shown in Table 2.4.

The B-factories also studied the  $\eta_c$  properties. With a data sample of 535 million  $B\bar{B}$ -meson pairs, Belle measured the  $\eta_c$  invariant mass  $B^\pm \rightarrow K^\pm \eta_c (\rightarrow K_S K^\pm \pi^\mp)$  channel. In advantage to the  $\gamma\gamma^*$  transition, this process has fixed quantum numbers of the initial state. A 2D-fit for the  $M(K_S K \pi)$  to  $\cos\theta$  distributions was performed to separate P- and D-waves from the S-wave in the non-resonant background. The resulting mass and natural width values fill Table 2.4.

Using  $519.2 \text{ fb}^{-1}$  of  $e^+e^-$  collision data, BaBar measured the  $\eta_c$  mass and natural width with the  $\eta_c \rightarrow K^+ K^- \pi^+ \pi^- \pi^0$  decay channel [66]. The obtained  $M_{\eta_c}$  and  $\Gamma_{\eta_c}$  values are in agreement with BESIII [75, 76] and Belle [77, 68] results, see Table 2.4 for details of the analyses.

Despite the many studies, the average values of the  $\eta_c$  mass and natural width according to Ref. [11] are not stable. Figs. 2.1 and 2.2 show their changes in the last years. Both mass and natural width have been changed by more than  $2\sigma$  from 2012 to 2013 year.

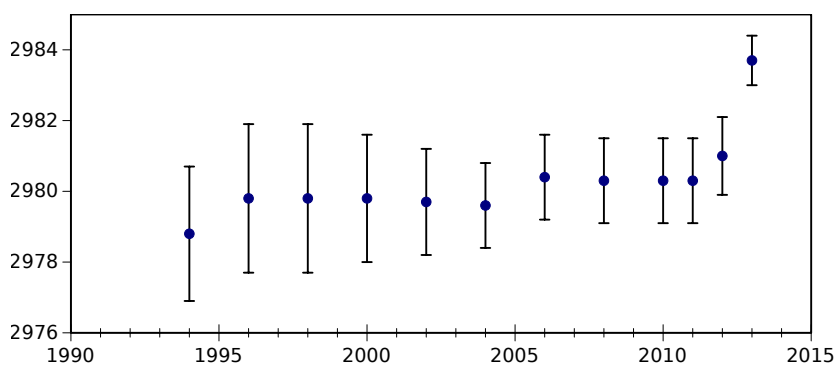


Figure 2.1: “Evolution” of the  $\eta_c$  mass world average according to the Particle Data Group. [11, 81, 82, 83, 84, 85, 86, 87, 88, 89]

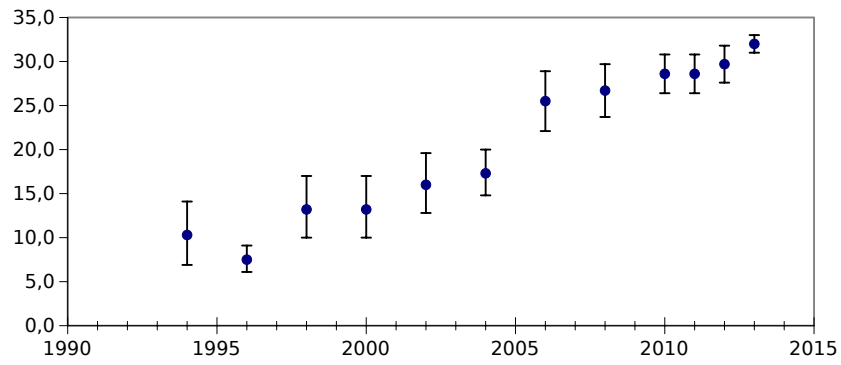


Figure 2.2: “Evolution” of the  $\eta_c$  natural width world average according to the Particle Data Group. [11, 81, 82, 83, 84, 85, 86, 87, 88, 89]

Any additional results on the  $\eta_c$  properties, especially from hadron machines, would be helpful for the cross-check.

experiment	year	decay channel	mass, MeV/ $c^2$	$\Gamma$ , MeV
BESIII [75]	2012	$\psi(2S) \rightarrow \gamma\eta_c$	$2984.3 \pm 0.6 \pm 0.6$	$32.0 \pm 1.2 \pm 1.0$
BESIII [76]	2012	$\psi(2S) \rightarrow \pi^0 h_c, h_c \rightarrow \gamma\eta_c$	$2984.49 \pm 1.16 \pm 0.52$	$36.4 \pm 3.2 \pm 1.7$
BaBar [66]	2011	$\gamma\gamma^* \rightarrow \eta_c(\rightarrow K^+ K^- \pi^+ \pi^- \pi^0)$	$2984.5 \pm 0.8 \pm 3.1$	$36.2 \pm 2.8 \pm 3.0$
Belle [77]	2011	$B^\pm \rightarrow K^\pm \eta_c(\rightarrow K_S^0 K^\pm \pi^\mp)$	$2985.4 \pm 1.5_{-2.0}^{+0.5}$	$35.1 \pm 3.1_{-1.6}^{+1.0}$
BaBar [67]	2010	$e^+e^- \rightarrow e^+e^- \eta_c(\rightarrow K_S^0 K^\pm \pi^\mp)$	$2982.2 \pm 0.4 \pm 1.6$	$31.7 \pm 1.2 \pm 0.8$
BaBar [78]	2008	$B \rightarrow K^{(*)} \eta_c(\rightarrow \bar{K} \pi)$	$2985.8 \pm 1.5 \pm 3.1$	$36.3_{-3.6}^{+3.7} \pm 4.4$
Belle [68]	2008	$\gamma\gamma^* \rightarrow \eta_c(\rightarrow 4K, 2K2\pi, 4\pi)$	$2986.1 \pm 1.0 \pm 2.5$	$28.1 \pm 3.2 \pm 2.2$
Belle [79]	2007	$e^+e^- \rightarrow J/\psi(\rightarrow \mu^+ \mu^-) \eta_c$	$2970 \pm 5 \pm 6$	
CLEO [69]	2004	$\gamma\gamma^* \rightarrow \eta_c(\rightarrow K^\pm \pi^\mp)$	$2981.8 \pm 1.3 \pm 1.5$	$24.8 \pm 3.4 \pm 3.5$

Table 2.4: Measurement of the  $\eta_c$  properties. Refs. [75] and [76] perform simultaneous fit of the 6 and 16  $\eta_c$  decay channels respectively. Ref. [79] uses recoil mass of the  $\eta_c$ .

# Chapter 3

## The LHCb experiment

### 3.1 The Large Hadron Collider

LHCb is a particle physics experiment operated on the Large Hadron Collider (LHC). The LHC is the world largest particle accelerator. It is located in CERN (European Organization for Nuclear Research) at the border of France and Switzerland. The LHC is a 27 kilometre long ring of super conductive magnets and a number of accelerating structures. Two high-energy proton (or lead) beams are colliding at a 7 TeV and 8 TeV (2.76 TeV) centre-of-mass energy.

The first stage of acceleration after injection begins at the LINAC2 linear accelerator. There protons reach the energy of 50 MeV. Then they are passed to the Proton Synchrotron Booster and to the Proton Synchrotron. Protons are accelerated to 26 GeV at this stage. The last accelerator before the LHC, the Super Proton Synchrotron (SPS) raises proton energy up to 450 GeV [90].

There are four big experiments installed on the LHC ring (see Fig. 3.1). The first two, ATLAS and CMS, are designed for the direct searches for new physics beyond the Standard Model (SM) and the Higgs boson discovery. The ALICE experiment is dedicated to the quark-gluon plasma studies with heavy ion collisions.

The LHCb experiment is designed for flavour physics searches, in particular for the studies of the CP violation mechanism. It has collected about  $3.2 \text{ fb}^{-1}$  of integrated luminosity till the end of 2012, see Fig. 3.2.

The LHC operated at a  $pp$  centre-of-mass energy  $\sqrt{s} = 7 \text{ TeV}$  in 2010 and 2011 years, and at 8 TeV in 2012. It is planned to have the first  $\sqrt{s} = 14 \text{ TeV}$   $pp$  collisions in 2015 after the LHC shut down. Lead-lead and lead-proton collisions were also performed at 2.76 TeV per nucleon centre-of-mass energy. It is the second large hadron machine

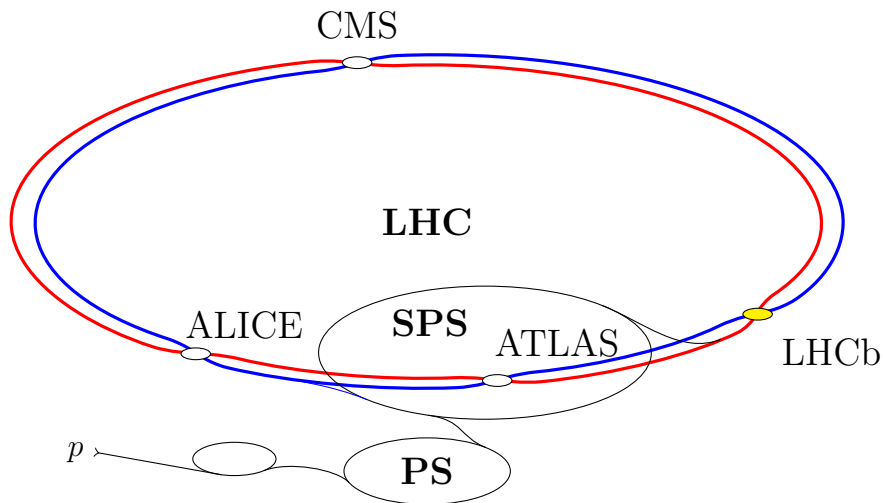


Figure 3.1: The LHC acceleration cascade and positions of four main experiments.

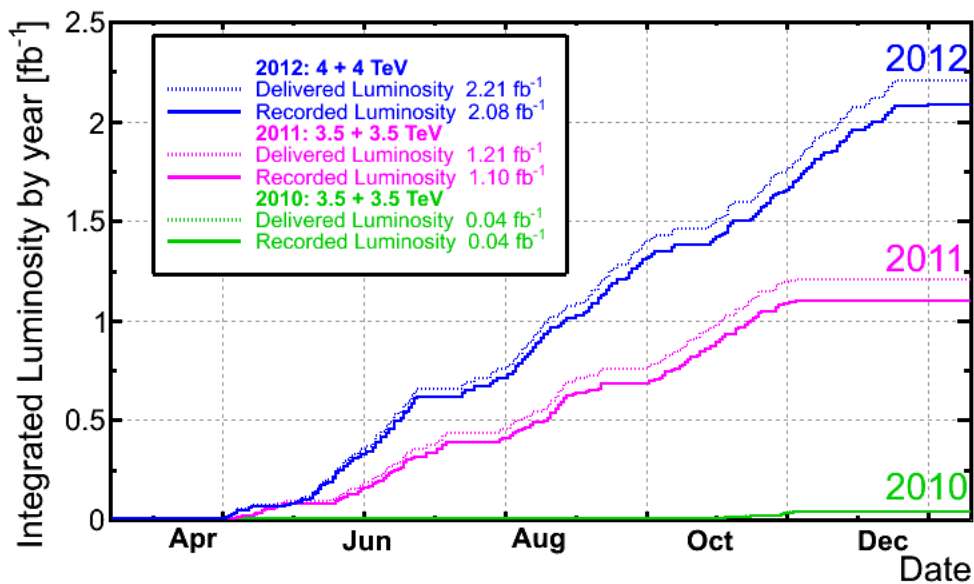


Figure 3.2: The LHCb integrated luminosity in 2010-2012 years and the luminosity, delivered by the LHC.

after the Tevatron

## 3.2 The LHCb detector

The LHCb detector is a forward single arm spectrometer with angular coverage up to 300 mrad in the bending plane and 250 mrad in the non-bending plane. Such a

geometry was chosen because of the fact that  $b$ - and  $\bar{b}$ -hadrons at high energies are produced in a correlated way mostly in the forward and backward directions, see Fig. 3.3. The side view ( $y/z$  plane cross-section,  $z$  axis goes along the beam direction) of the LHCb installation is shown on Fig. 3.4.

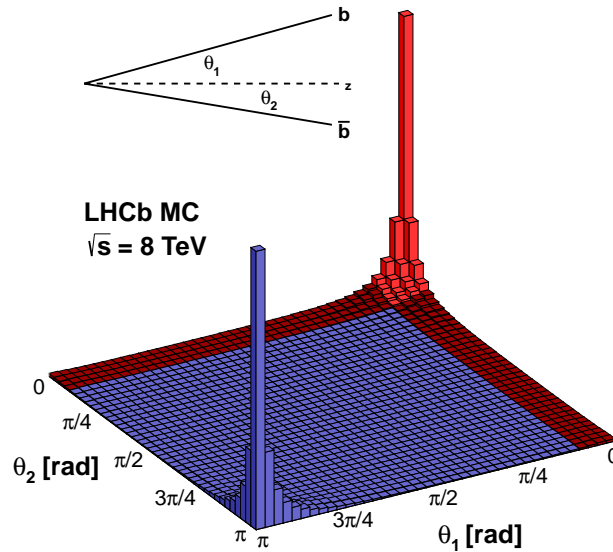


Figure 3.3: The  $b\bar{b}$  production angle plot  $\sqrt{s} = 8$  TeV, Monte-Carlo simulation.

It is located at Point 8 in place of the former DELPHI experiment (see Fig. 3.1 for the LHCb position on the LHC ring).

The detection system consists of several sub-detectors. They perform precise reconstruction of the primary and secondary vertices (VELO) and tracks (VELO and Tracker). The  $\gamma$  and  $\pi^0$  energies are measured by the Electromagnetic Calorimeter (ECAL) and momentum is measured by the Tracker System. Particle identification is performed by ECAL for  $\gamma$ ,  $\pi^0$ ,  $e^\pm$ , Muon chambers for muons and the Ring imaging Cherenkov detectors (RICH) for all charged pseudo-stable particles. With known particle momentum and type (mass) one can find its energy. Scintillator Pad Detector (SPD) and Preshower are located in front of the calorimeters and are used for the  $\gamma/\pi^0$  and  $\gamma/e^\pm$  discrimination. The Hadron Calorimeter (HCAL) is used only for triggering. [91, 92]

In the following sections we describe briefly all subsystems of the LHCb installation, focusing on the tracking, Cherenkov particle identification and trigger systems that play

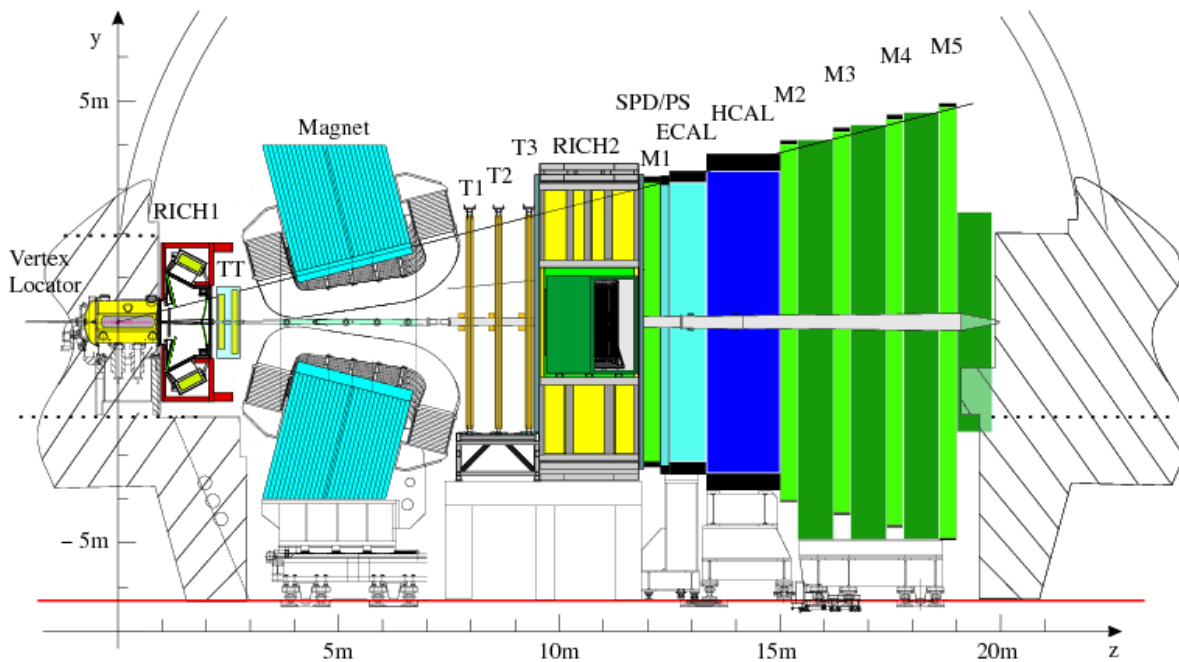


Figure 3.4: The side view of the LHCb detector.

a major role in the current analysis.

### 3.2.1 Tracking system

The tracking system at the LHCb experiment consists of the vertex locator (VELO) and four tracking stations: the Tracker Turicensis (TT) before the dipole magnet and T1-T3 after of the magnet.

#### VELO

The vertex locator (VELO) consists of silicon modules, placed along the beampipe close to the interaction point. The VELO silicon plates before installation into LHCb are shown on Fig. 3.6. It performs precise measurements of the interaction vertices coordinates, thus it allows to separate primary interaction vertices from secondary ones. The VELO detector contains about 180000 readout channels [91]. It plays a big role in  $b$ - and  $c$ -physics: e. g. with the help of vertex detector one can distinguish between  $J/\psi$  created in a primary interaction and in the decay of  $b$ -hadrons. The VELO detector plays a big role in the HLT2 (High Level Trigger 2) functionality and helps to enrich off-line data samples with  $b$ -hadron decay events [93]

The VELO aperture is smaller than one required by the LHC initial injection condi-

tions. It is a unique tracking detector that approaches about 8 mm to the beam. Since the beam is focused, the VELO plates are moved towards the interaction spot. To minimise material between the VELO and the interaction point, it is separated from the machine vacuum in the beampipe by a thin aluminium RF-foil. The VELO radiation length is about 17.5% of a radiation length, the main deposit comes from the RF-foil [91].

To perform sufficient longitudinal and angular resolution, R-sensors and  $\phi$ -sensors have been implemented, see Fig 3.5. They are made of n-on-n silicon plates

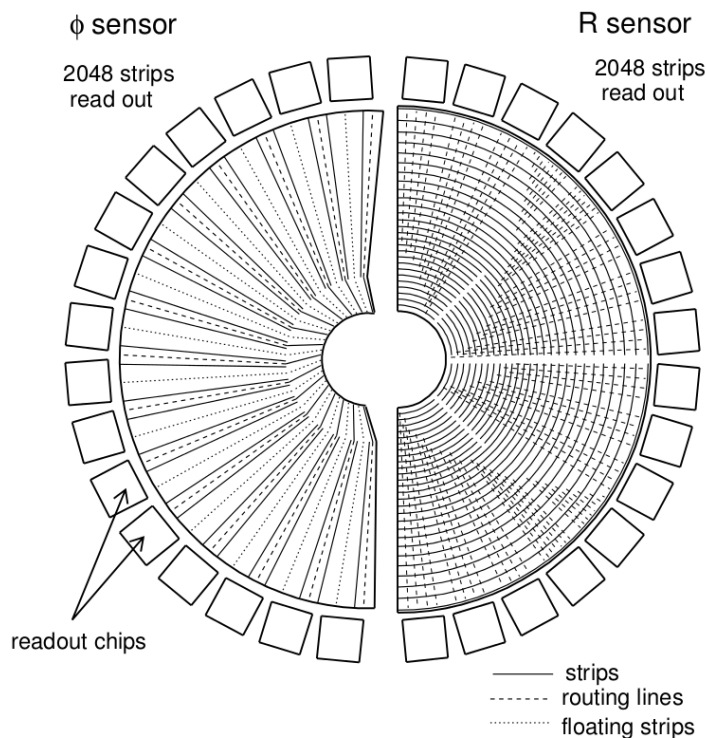


Figure 3.5: Scheme of the R and the  $\phi$ -sensors. [93]

For proper trigger operating, the signal to noise ratio of the VELO system stays greater than 14 [93]. The spatial resolution is about  $4 \mu\text{m}$ , it is required that the resolution should not degrade with the total dose increasing. A track in the LHCb acceptance must cross at least three VELO plates. For alignment reasons two parts of the detector are designed to be overlapped, see Fig. 3.7.

The vertex locator resolution can be parametrised as

$$\sigma_{\text{IP}} = 17 \mu\text{m} + \frac{32 \mu\text{m}}{p_{\text{T}}}, \quad (3.1)$$

where  $p_{\text{T}}$  is in  $\text{GeV}/c$  units. The resolution typically ranges between 20 and  $40 \mu\text{m}$  for

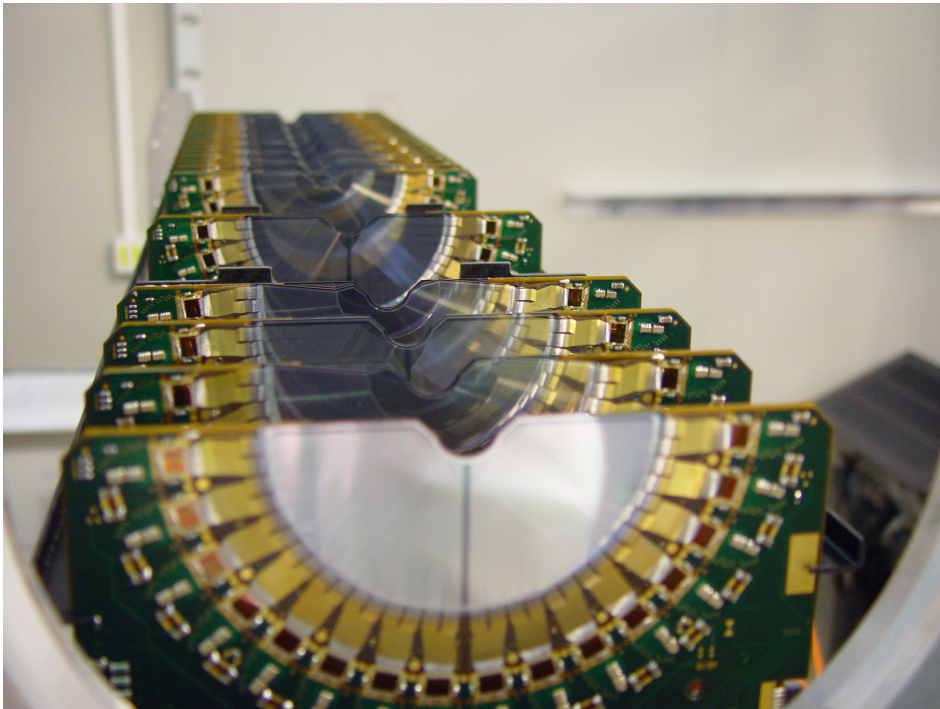


Figure 3.6: VELO detector plates before installation.

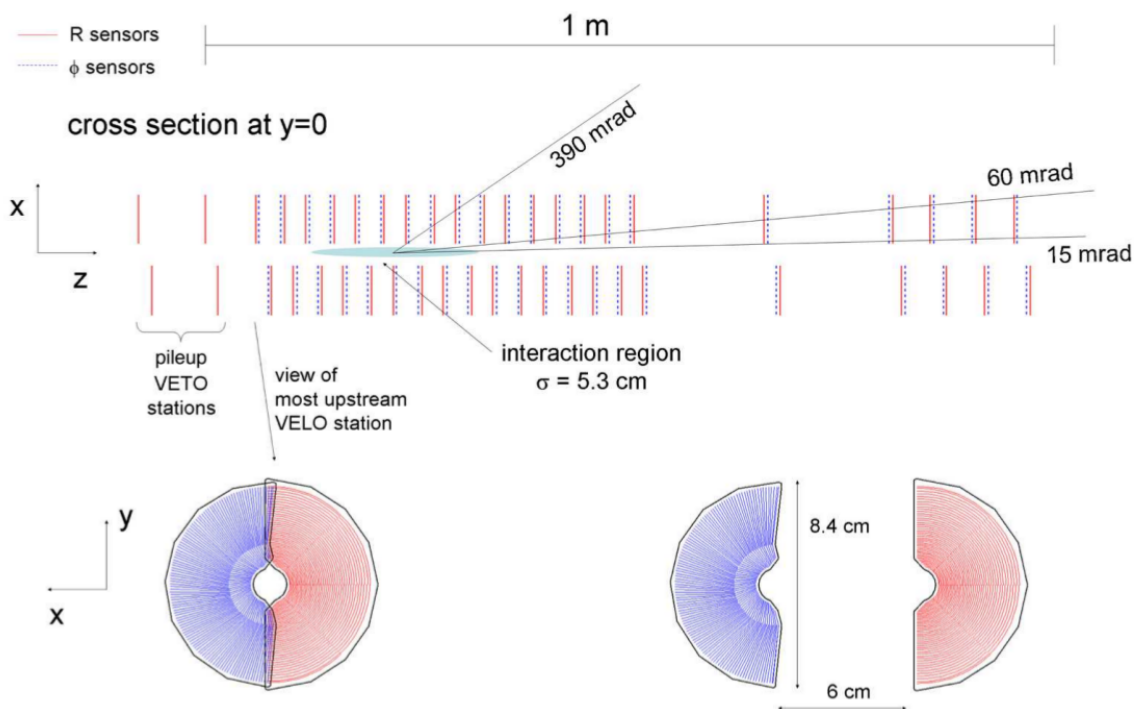


Figure 3.7: Cross-sections of the VELO silicon layers in the  $x/z$  plane (top). Closed (bottom left) and opened (bottom right) VELO stations.

$B$  decay tracks [94]. The VELO spatial resolution depending on the inverse transverse momentum  $1/p_T$  is shown on Fig. 3.8 (right).

### Tracker and dipole magnet

Both the Tracker Turicensis (TT) and the Inner Tracker (IT) use silicon microstrip sensors with a strip pitch about  $200\ \mu\text{m}$ . The TT has an active area of about  $8.4\ \text{m}^2$  with 143360 readout strips and the IT has an active area of  $4.0\ \text{m}^2$  with 129024 readout strips. The tracker system was designed for the reconstruction of the charged particle tracks and measuring their momenta juggling on the path curvature in magnetic field.

All four TT detection layers are composed in one large tight, electrically and thermally insulated detector volume. Since the temperature below  $5^\circ\ \text{C}$  is maintained in the detector volume, it is continuously flushed with nitrogen in order to avoid condensation on the surfaces.

The T1-T3 stations consist of silicon microstrips in the inner region (Inner Tracker, IT). Straw-tubes are employed in the outer region (Outer Tracker, OT). The OT is an array of individual, gas-tight straw-tube modules. Each module contains two layers of drift-tubes with  $4.9\ \text{mm}$  inner diameters. A mixture of Argon (70%) and  $\text{CO}_2$  (30%) is used for the fast drift time  $> 50\ \text{ns}$ , and high spatial resolution ( $200\ \mu\text{m}$ ). [91]

The magnet at LHCb is a warm magnet designed with saddle-shaped coils in a window-frame yoke. It covers the LHCb angular acceptance. The integrated magnetic field reaches  $4\ \text{Tm}$ .

The momentum from a long track (traversing the full tracking set-up from the VELO to the T stations) fit in average has resolution of  $0.35\%$  (the  $0.1$  tail fraction with  $\sigma = 1.0\%$ ). The resolution dependence of the momentum value is shown on Fig. 3.8 (left).

Precise vertex reconstruction allows LHCb to perform accurate lifetime measurements. The latest results on the  $B$  mesons lifetime measurements was performed with a total error  $< 1\%$  [95]. The lifetime distribution of the  $B_s$  candidates is shown on Fig. 3.9.

### 3.2.2 Particle identification

Precise particle identification is crucial for the LHCb experiment. The Electromagnetic calorimeter (ECAL) is responsible for the  $\gamma$ , electron identification and  $\pi^0$  identification vis  $\pi \rightarrow \gamma\gamma$  decay channel ( $\mathcal{B}_{\pi \rightarrow \gamma\gamma} = 98.8\%$  [11]). Hadron calorimeter (HCAL) is

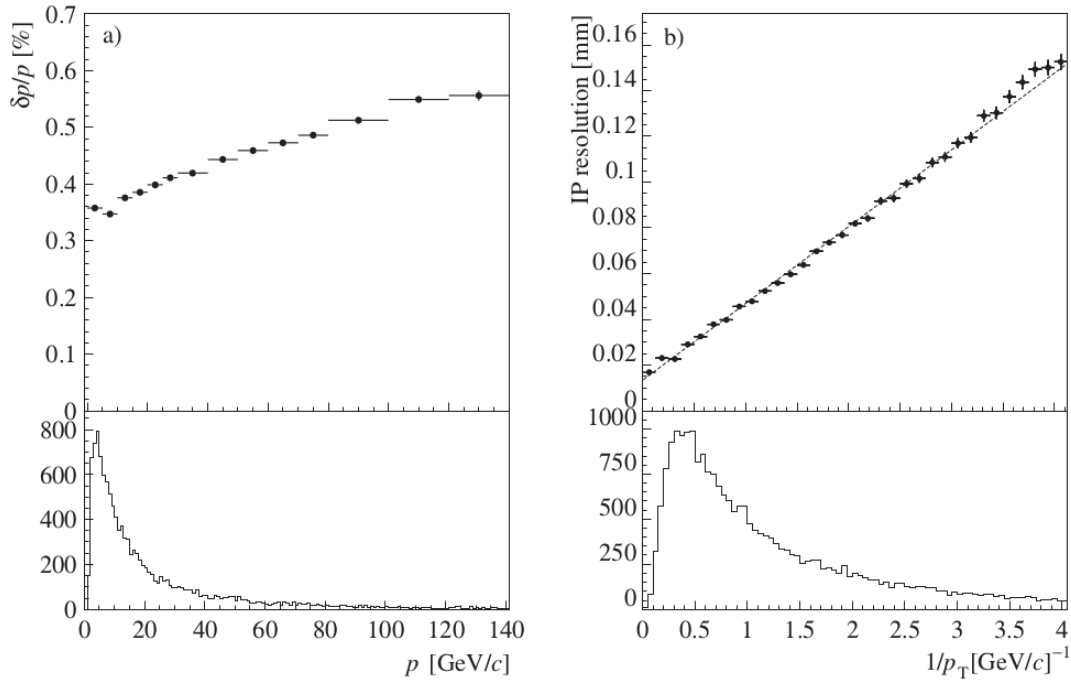


Figure 3.8: Resolution on the reconstructed track parameters at the production vertex of the track: momentum resolution as a function of track momentum (left), impact parameter resolution as a function of  $1/p_T$  (right). For comparison, the momentum and transverse-momentum spectra of B-decay particles are shown in the lower part of the plots. [92]

designed for trigger needs. It marks the presence of neutral hadrons. Muon stations, placed behind the rest of the detection modules are designed to detect muons which are the unique case of highly penetrative charged particles. The Ring imaging Cherenkov detectors provides separation of different types of quasi-stable hadrons.

## RICH

Unlike the ATLAS and CMS experiments, the LHCb detector includes powerful instruments for particle identification. There are two RICH detectors in LHCb, covering intervals of low (RICH1) and high (RICH2) momenta, see Fig 3.11 (right). RICH1 detector is set between the VELO and the Trigger Tracker. It contains aerogel and fluorobutane ( $C_4F_{10}$ ) gas radiators, providing particle identification in momenta range (1..60) GeV/c. The second detector, RICH2, is placed between the last tracking station and the first muon station. It contains a  $CF_4$  gas radiator, providing particle identification in the (15..100) GeV/c range for particles within the reduced polar angle acceptance of  $\pm 120$  mrad in horizontal and  $\pm 100$  mrad in vertical projections [91]. Their goal is par-

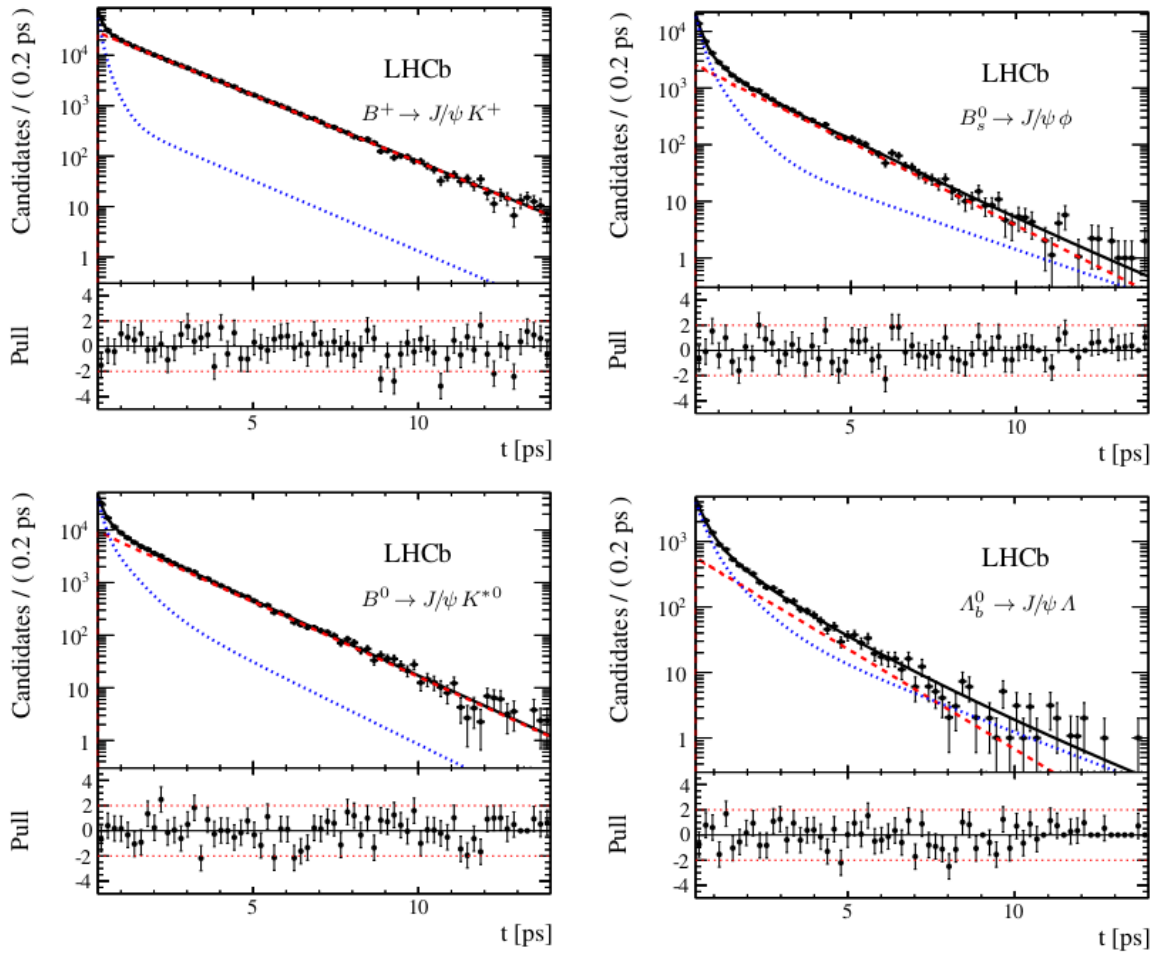


Figure 3.9: Distributions of the decay time of  $B^+ \rightarrow J/\psi K^+$  (top left),  $B^0 \rightarrow J/\psi K^{*0}$  (bottom left),  $B_s \rightarrow J/\psi \phi$  (top right),  $\Lambda_b^0 \rightarrow J/\psi \Lambda$  (bottom right) and associated residual uncertainties. The data are shown by the black points; the total fit function by the black solid line; the signal contribution by the red dashed line and the background contribution by the blue dotted line. [95]

tile identification which is a fundamental requirement for the LHCb. Mostly they are designed for hadron discrimination. Basically, the RICH detectors allow to distinguish between pseudo-stable hadrons:  $p(\bar{p})$ ,  $K^\pm$ ,  $\pi^\pm$ .

Both RICH detectors are aligned to the LHCb coordinate axes. RICH1 is placed between 990 mm and 2165 mm along  $z$  axis. The material budget of the detector is minimised to radiation length  $8\% X_0$ . The lower value of the acceptance  $25$  mrad interval is limited by the beryllium beam pipe. The Hybrid Photo-Detectors of the RICH need to be shielded from the LHCb dipole magnet with iron shield boxes [96]. A schematic view of the RICH1 detector is shown on Fig 3.10(a). Charged hadrons come to the detector

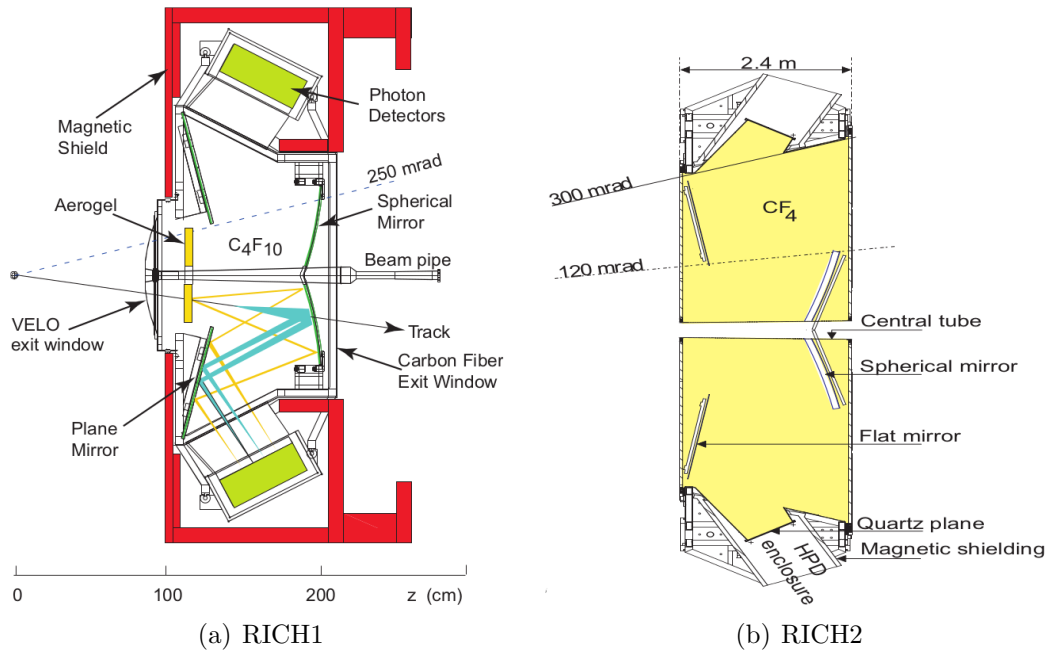


Figure 3.10: Side scheme of the RICH1 (left) and RICH2 (right) detectors.

volume from the VELO exit window at the left. They pass aerogel plates, producing cones of Cherenkov light. The light rings projections are reflected by spherical mirrors to flat mirrors. Then light goes to the sensitive surface of photomultipliers.

RICH2 detector is placed between the last tracking station and the first muon station M1 ( $9450 \text{ mm} \leq z \leq 11900 \text{ mm}$ ). As for RICH1, the HPDs of the RICH2 are hidden in large iron shielding boxes. Due to the necessary void space of 45 mm around the beampipe, the RICH2 has a smaller angular coverage, 15 mrad. The photon detectors and the supporting structures are placed outside the acceptance and the HPDs are located left and right of the beampipe [97]. The RICH2 geometry is similar to the RICH1 turned around  $z$ -axis except there is no aerogel plates. A schematic view of the RICH2 detector is shown on Fig 3.10(b).

Cherenkov rings generally overlap with many others. A track is defined as isolated when its Cherenkov ring does not overlap with another ring from the same radiator. The rings from isolated tracks provide a performance test, since their Cherenkov angle can be predicted. In Fig. 3.11 one can find the Cherenkov angle as a function of particle momentum. It is clearly seen, that events are separated into areas with respect to their mass. Despite the fact that the RICH detectors are designed mainly for the hadron identification, a distinct muon area can also be observed.

One can study the separation power between a pair of chosen particle types, using the

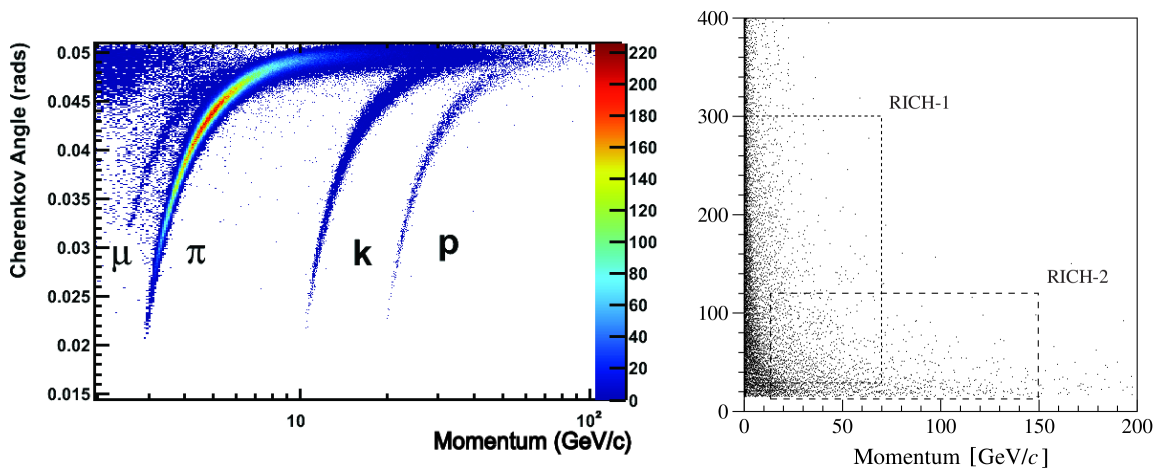


Figure 3.11: Reconstructed Cherenkov angle as a function of track momentum in the  $C_4F_{10}$  radiator (left) [98]. Polar angle  $\theta$  versus momentum, for all tracks in simulated  $B_d^0 \rightarrow \pi^+\pi^-$  events. The regions of interest for RICH 1 and RICH 2 are indicated by the dashed lines (right) [99].

log-likelihood values obtained from the control channels. Fig. 3.14 shows discrimination of protons and pions when imposing the PID requirements  $\log \mathcal{L}(p-\pi) > 0$  and  $\log \mathcal{L}(p-\pi) > 5$ , and the discrimination achievable between protons and kaons when imposing the requirements  $\log \mathcal{L}(p-K) > 0$  and  $\log \mathcal{L}(p-K) > 5$ . Particle identification plays an important role in the current. For  $p\bar{p}$  candidates spectra with different PID selection criteria see sec. 4.4.

Low background signals can be reached using PID information from the RICH detectors. On Fig 3.12 one can see how information from RICH detectors allows to distinguish different decay modes of  $B$ -mesons.

The high purity samples of the control modes can be reached through kinematic requirements, but the residual background must still be accounted for. To distinguish background from signal, the  $sPlot$  technique [100] is used, where the invariant mass of the resonance is used as the discriminating variable. The mass distribution of the  $\Lambda \rightarrow p\pi^-$  decay in Fig 3.13 is given as an example.

## Calorimeters

The calorimeter system of LHCb consists of the Preshower detector for  $e^\pm/\gamma$  discrimination, Scintillating Pad Detector (SPD), Electromagnetic and Hadron calorimeters.

The LHCb includes a sampling electromagnetic calorimeter, which consists of layers of plastic as a sensitive volume and lead plates as an absorber. Light is transported from

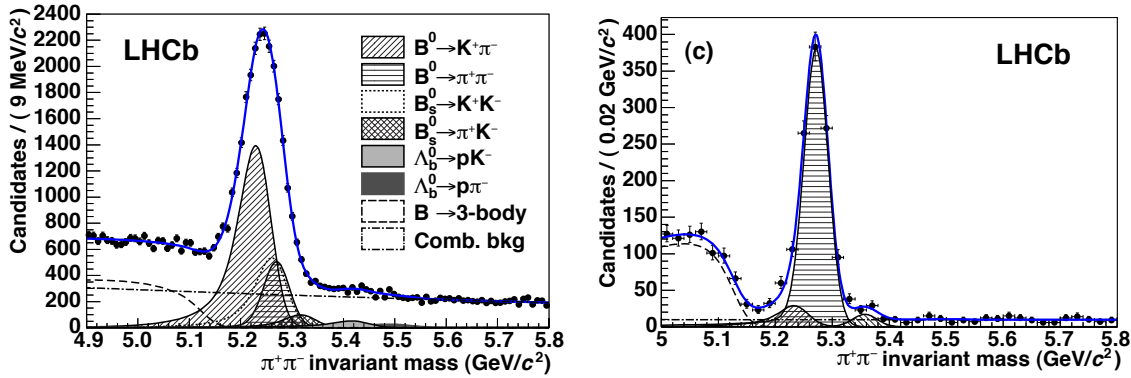


Figure 3.12: Invariant  $\pi^+\pi^-$  mass before (left) and after (right) PID selection applied. The result of an unbinned maximum likelihood fit is overlaid. The main contributions to the fit model are also shown. [101]

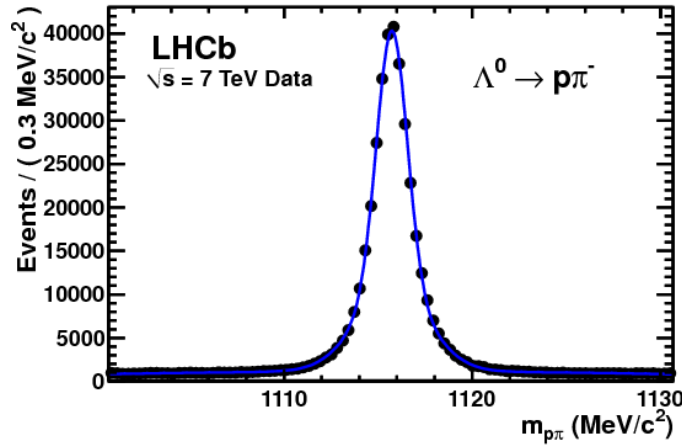


Figure 3.13: Invariant mass distributions of the  $\Lambda \rightarrow p\pi^-$  both background and signal, is superimposed in blue [98].

the scintillation layers by wave-length shifting plastic fibers. In general, the main goals of the ECAL are electron and  $\gamma$  identification and energy measurement. The energy resolution of the ECAL is estimated to be [102]

$$\sigma_E/E = 10\%/\sqrt{E} \oplus 0.9\%, \quad (3.2)$$

energy  $E$  in GeV. Due to the high granularity, it also performs the  $\gamma/\pi^0$  discrimination.

The HCAL consists of an iron absorber and plastic scintillator tiles. Because of insufficient energy resolution, it is mostly used at the trigger level. The HCAL provides about 70% of L0 trigger output. The energy resolution of the HCAL can be estimated

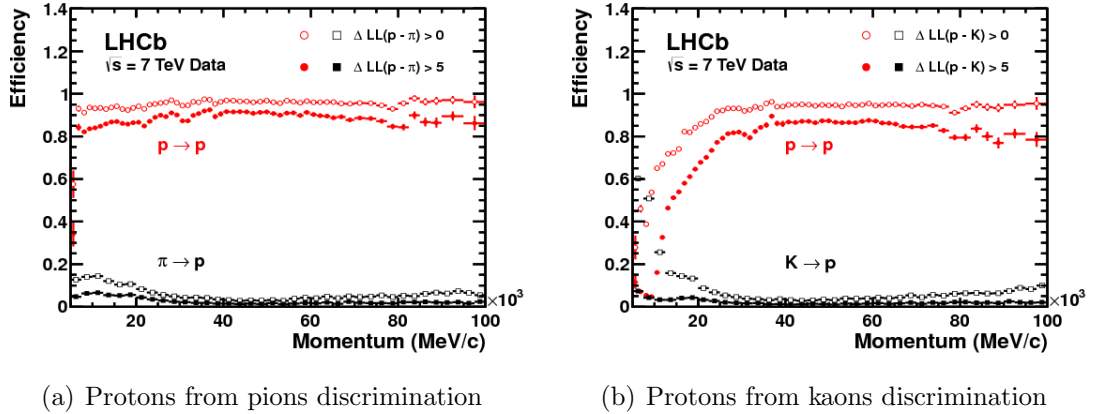


Figure 3.14: Proton identification efficiency and pion misidentification rate (left) and kaon misidentification (right) measured on data as a function of track momentum. Two different  $\log \mathcal{L}(p - \pi)$  (left) and  $\log \mathcal{L}(p - K)$  requirements have been imposed on the samples, resulting in the open and filled marker distributions, respectively.

as [102]

$$\sigma_E/E = 69\%/\sqrt{E} \oplus 9\%, \quad (3.3)$$

energy  $E$  in GeV.

The ECAL and HCAL are performed in a similar way. Both detectors have a rectangular shape with  $300 \times 250$  mrad angular coverage. The ECAL consists of 6016 cells in the inner, middle and outer regions, and the HCAL consists of 1488 cells in the inner and outer regions. The light collected in each cell is delivered to the photomultiplier.

### Muon system

Muon triggering is one of the fundamental requirements in the LHCb experiment. Muons occur in many  $B$ -meson decay modes, several quarkonium states also decay to the pair of muons.

The muon system consists of five rectangular muon stations separated by a thick layers of iron absorber. The minimal muon momentum, sufficient to cross all five stations, is about 6 GeV/c [91]. Stations M2 to M5 are placed after the calorimeters, while the M1 station is installed before the ECAL. Stations M1–M3 have a high spatial resolution along the  $x$  coordinate axis. Thus they are used to define the track direction and to calculate the momentum of the candidate muon with a resolution of 20%. Stations M4 and M5 have a lower spatial resolution, they are used mainly for the identification of the penetrating particles. The muon system solves two tasks: triggering muon events

and measurements of muon momenta. Multi-wire proportional chambers (MWPC) are used for all regions except the inner region of station M1 where the particle flux exceeds radiation damage limit.

For the sufficient spatial resolution and rate capability that vary over the detector system, several technical solutions are employed for the MWPC in regions. The chambers are divided into pads: anode wire pads or cathode pads in the MWPCs and anode pads in the GEM chambers. Each physical pad is read out by one front-end electronics channel [91].

### 3.2.3 Trigger

The LHCb experiment operates at an average luminosity of about  $2 \times 10^{32} \text{cm}^{-2} \text{s}^{-1}$ , which leads to a crossing frequency of about 10 MHz. To reduce it to storable event rates, LHCb employs a two-level trigger system, including a hardware (L0) trigger and a software (HLT) trigger implemented in a processor farm. The LHCb trigger system design is shown in Fig. 3.15. The L0 reduces the rate to about 1 MHz, and the L0 triggered events are passed to the first stage of the software trigger (HLT1), which partially reconstructs events, confirming (or not) the L0 decision. A second level of the software trigger (HLT2) processes fully reconstructed events, which are then stored. [103]

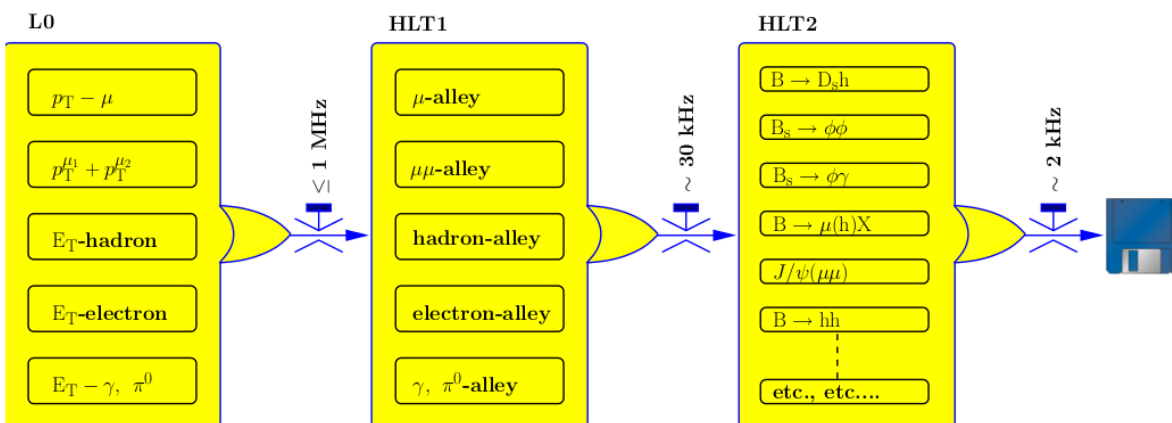


Figure 3.15: The LHCb trigger scheme.

At the nominal LHCb luminosity, the expected frequency of the  $b\bar{b}$  pair production is about 100 kHz. However, only about 15% of these events have at least one  $B$ -meson with all its decay products in the detector acceptance. In general, the trigger system is

optimised to obtain a high efficiency for the events, selected in the offline analysis and reject the background as strongly as possible. [91].

The L0 trigger is divided in three subsystems: the pileup, calorimeter and muon trigger. It reconstructs the highest  $E_T$  electron, photon and hadron clusters in calorimeters or the two highest  $p_T$  muons in the muon chambers. A pile-up system in the VELO estimates the number of primary vertices per each event. The total energy deposit in the calorimeters is integrated, and the number of tracks is estimated, using the number of hits in the SPD [91]. This information helps to reject potentially useless events, so they do not occupy the HLT system. The L0 Pile-Up system helps to calculate the luminosity [104].

The L0 Calorimeter system sums-up the transverse energy deposit in clusters of  $2 \times 2$  calorimeter cells, which is defined as

$$E_T = \sum_{i=1}^4 E_i \sin \theta_i, \quad (3.4)$$

where  $E_i$  is the energy deposited in cell  $i$  and  $\cos \theta_i$  is the angle between the  $z$ -axis and a neutral particle trajectory. Three types of event can be built, combining information from different parts of the calorimeters. A hadron candidate decision (**L0Hadron**) is based on the highest  $E_T$  in the HCAL cluster. It is used widely in the analyses, which employ hadron final states, see 3.16 for its efficiency for different flavour physics channels. A photon candidate (**L0Photon**) is defined by the highest  $E_T$  deposit in the ECAL cluster with at least one preshower (PS) cell hit and no hit in the corresponding scintillating plate detector (SPD) cells. An electron candidate has the same requirements as the photon candidate except it needs addition at least one SPD cell hit before the PS cells.

There are four L0 muon processors, corresponding to each quadrant of the muon detection system. Each of them tries to identify the two muons with the largest and second largest transverse momentum. They search for hits that makes a straight line through all the muon stations, starting at the interaction point. In the  $x/z$  plane only muons with  $p_T > 0.5 \text{ GeV}/c$  can be reconstructed.

The HLT is a program written in C++ language. It runs on the Event Filter Farm (EFF), which contains up to 2000 computing nodes. Due to the 1 MHz input rate and limited calculation power, the HLT system operates only with a part the information of the event [103]. The first trigger level, HLT1, processes the full L0 output and reduces the event rate to 43 kHz using partial event reconstruction. After this, the second trigger

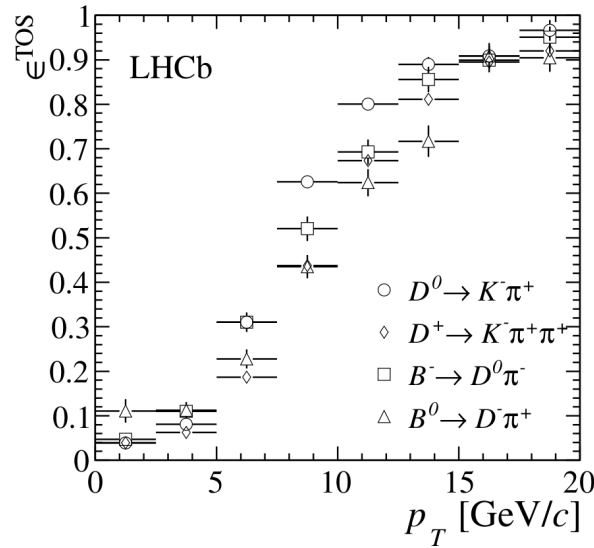


Figure 3.16: The efficiency  $\varepsilon^{\text{TOS}}$  of L0Hadron is shown for  $B^0 \rightarrow D^- \pi^+$ ,  $B^- \rightarrow D^0 \pi^-$ ,  $D^0 \rightarrow K^- \pi^+$  and  $D^+ \rightarrow K^- \pi^+ \pi^+$  as a function of  $p_T$  of the signal  $B$  and  $D$  mesons. [104]

level performs a more detailed event reconstruction [104].

The set of reconstruction algorithms and selections make "trigger lines". They return an accept or reject decision. Combinations of the trigger lines and L0 parameters form a trigger with the associated Trigger Configuration Key (TCK).

LHCb is going to perform detector detector upgrade in 2018. There will be a fully software based trigger that will be operated at higher luminosities. [104]

### 3.2.4 LHCb physics program

The LHCb experiment is a dedicated heavy flavour physics precision experiment whose main aim is to probe physics beyond the Standard Model, by studying the very rare decays of beauty and charm-flavoured hadrons and by measuring CP-violating observables precisely. In the past years, the B-factories have confirmed that the mechanism proposed by Kobayashi and Maskawa is the major source of CP violation observed so far. The SM description has been confirmed at a level of 10-20% accuracy in the  $b \rightarrow d$  transitions, while new physics effects can still be large in  $b \rightarrow s$  transitions. For example, by modifying the  $B_s$  mixing phase  $\phi_s$ , measured from  $B_s^0 \rightarrow J/\psi \phi$  decays, or in channels dominated by other loop diagrams, such as the very rare decay  $B_s^0 \rightarrow \mu^+ \mu^-$ . [105]

The LHCb physics program is inserted in the broader physics program of the other

experiments at the LHC accelerator, which is designed and built to achieve the highest energy collisions available at accelerators ( $\sqrt{s} = 7$  TeV in 2010 and 2011 and  $\sqrt{s} = 8$  TeV in 2012). In such an environment, high precision measurements can reveal new physics phenomena as differences with Standard Model predictions. Flavour physics can then provide hints of new phenomenology before the direct discoveries of new particles as performed by the two LHC general purpose detectors ATLAS and CMS. LHCb will extend the  $b$ -physics results from the B factories by studying decays of heavier  $b$  hadrons, such as  $B_s$  or  $B_c$ . LHCb explores a wide range of measured decays, reaching channels that are strongly suppressed in the SM and to improve the precision of the measurements to achieve the necessary sensitivity to new physics effects in loops. [105]

The LHCb experiment mainly focuses on studying CP violation and rare decays in the  $b$  sector. As in the case of the Tevatron, all flavours of  $b$ -hadrons are produced at the LHCb experiment ( $B_d, B_u, B_s, B_c, \Lambda_b, \dots$ ). Because of its unique parameters (angular coverage, hadron final states identification, trigger), the LHCb detector is optimal for precision studies of rear heavy flavour physics. [106]

# Chapter 4

## Measurement of charmonium production via decays to $p\bar{p}$ final state

### 4.1 Introduction

In the present analysis, the charmonium states are reconstructed using the  $p\bar{p}$  final state. This is done for the first time for the promptly produced charmonium states in a hadronic machine environment, while the analysis of charmonium production from  $b$ -hadron decays has been recently performed. Also, results from  $e^+e^-$  machines are available, see Chapter 2 for more details.

Using the  $p\bar{p}$  final state, we measure the prompt  $\eta_c$  production cross section in the  $pp$  collisions at  $\sqrt{s} = 7\text{ TeV}$  and  $\sqrt{s} = 8\text{ TeV}$  centre of mass energy, as well as the  $\eta_c$  inclusive yield from  $b$ -hadron decays. At the LHC energies, all the weakly decaying  $b$ -hadron species,  $B^+$ ,  $B^0$ ,  $B_s$ ,  $B_c$  mesons and  $b$ -baryons, contribute to the  $b$ -hadron sample.

The  $\eta_c$  production measurements are performed using the topologically and kinematically similar  $J/\psi \rightarrow p\bar{p}$  normalisation channel, which allows systematic uncertainties to partially cancel in the ratio. Indeed, the  $\eta_c \rightarrow p\bar{p}$  and  $J/\psi \rightarrow p\bar{p}$  decay topologies are similar and the masses of  $\eta_c$  and  $J/\psi$  states are close:  $2(M_{J/\psi} - M_{\eta_c})/(M_{J/\psi} + M_{\eta_c}) \simeq 4\%$ . The cancellation relies on approximately equal reconstruction, trigger and selection efficiencies.

The sample of charmonium produced in  $b$ -hadron decays, where charmonium states decay into proton-antiproton, was used to find the mass difference  $\Delta M_{J/\psi, \eta_c} = M_{J/\psi} -$

$M_{\eta_c}$ , and the  $\eta_c$  natural width  $\Gamma_{\eta_c}$ . The marginal agreement between the latest results on the  $\eta_c$  mass and natural width measurements motivates the determination of  $\Delta M_{J/\psi, \eta_c} = M_{J/\psi} - M_{\eta_c}$  and  $\Gamma_{\eta_c}$  using a different technique or final state in the present analysis.

In addition, the  $\chi_c$  subfamily and  $h_c$  state production studies are performed. We set limits on the relative production cross-sections for promptly produced charmonium states and for inclusive  $b$ -hadron decay production.

## 4.2 Monte-Carlo simulation and data sets

The present analysis uses the  $pp$  collision data recorded by the LHCb experiment at  $\sqrt{s} = 7$  TeV in 2011 and at  $\sqrt{s} = 8$  TeV in 2012. The analysis is based on an integrated luminosity  $\int \mathcal{L} dt \approx 0.7 \text{ fb}^{-1}$  accumulated in 2011 and an integrated luminosity of  $\int \mathcal{L} dt \approx 2.0 \text{ fb}^{-1}$  accumulated in 2012. All subsystems of the LHCb installation were stable and fully operational while data corresponding to the present analysis were recorded.

The Monte-Carlo simulated events (MC) for this analysis were obtained using the PYTHIA event generator and GEANT4 package. The following MC samples have been used to study the  $\eta_c$  and  $J/\psi$  mass resolution, as well as the contribution from the  $J/\psi \rightarrow p\bar{p}\pi^0$  channel: 1.2M events with  $J/\psi \rightarrow p\bar{p}$  (0.6M events magnet “up”, 0.6M events magnet “down”), 0.8M events with  $\eta_c \rightarrow p\bar{p}$  (0.3M events magnet “up”, 0.5M events magnet “down”), For the  $J/\psi \rightarrow p\bar{p}\pi^0$  process simulation a simple phase-space model has been used, 0.1M events were generated (all events magnet “down”).

## 4.3 Trigger and stripping

The basic level L0HadronDecision\_TOS trigger is applied for both prompt charmonium production analysis and the analysis of inclusive charmonium production from  $b$ -hadron decays.

The dedicated trigger lines HLT1,2DiProtonDecision\_TOS are used for the analysis of prompt charmonium production and charmonium production from  $b$ -hadron decays for both 2011 and 2012 data. The HLT1DiProtonDecision\_TOS trigger line selects two oppositely-charged tracks, pointing to the same vertex, with proton and charmonium transverse momentum cuts applied:  $p_T(p\bar{p}) > 6.5 \text{ GeV}/c$ ,  $p_T(p)$ ,  $p_T(\bar{p}) > 1.95 \text{ GeV}/c$ . In order to reduce the event rate, the information from Ring-Imaging Cherenkov (RICH)

detectors is used at the trigger level to separate protons from pions and kaons. To reduce the trigger rate, strong cuts on particle identification and event multiplicity are applied already on the trigger level, see Table 4.1. The dedicated  $p\bar{p}$  trigger lines were not operational at the beginning of the 2011 data taking, so that the integrated luminosity used for the analysis is reduced from  $1 \text{ fb}^{-1}$  to  $0.7 \text{ fb}^{-1}$  for the 2011 data sample.

The `HLT1Global_TOS`, potentially usable for the charmonium production from  $b$ -hadron decays analysis in order to increase statistics for the  $\eta_c$  and  $J/\psi$  signals, introduces a more complicated background shape close to the  $\eta_c$  peak, and to avoid ambiguous results, was not used.

Data were processed with the reconstruction algorithm `Reco14`, and then stripped with the stripping line `StrippingCcbbar2PpbarLineDecision` version 20r1. Trigger and stripping selection criteria are summarised in Table 4.1.

	variable	trigger	stripping
protons	$p_T$ , GeV/ $c$	$> 1.95$	$> 1.95$
	track $\chi^2/\text{NDF}$	—	$< 4$
	$\Delta \log \mathcal{L}^{p-\pi}$	$> 15$	$> 20$
	$\Delta \log \mathcal{L}^{p-K}$	$> 10$	$> 15$
charmonium	$p_T$ , GeV/ $c$	$> 6.5$	$> 6$
	vertex $\chi^2$	—	$< 9$
multiplicity	SPD multiplicity	$< 600$	$< 300$

Table 4.1: Selection criteria for prompt charmonium candidates and charmonium candidates from  $b$ -hadron decays

## 4.4 Selection criteria

Selection criteria are optimised using the  $J/\psi \rightarrow p\bar{p}$  sample by maximising the significance of the signal,  $S = N_{sig}/\sqrt{N_{bgr} + N_{sig}}$ , where  $N_{sig}$  and  $N_{bgr}$  are the numbers of signal and background events respectively. The number of background events is obtained by fitting data samples with the background fit function (see section 4.5 for the fit model description). The signal yield is taken from the Monte-Carlo sample with the corresponded normalisation (see section 4.2) and with all cuts applied. The selection criteria optimisation plots are shown on Figs. 2 (candidates from  $b$ -hadron decays) and 1 (prompt candidates) in Appendix .1.

The  $\eta_c$  and  $J/\psi$  candidates are reconstructed from oppositely charged tracks identified as protons by the LHCb detector. Both proton track candidates are required to

have a good quality of track reconstruction,  $\chi^2/\text{ndf} < 4$ . In order to suppress combinatorial background, the proton tracks are required to have transverse momenta larger than  $2 \text{ GeV}/c$  and momenta larger than  $10 \text{ GeV}/c$ .

Proton-pion and proton-kaon misidentification is suppressed using the information from the RICH detectors. The proton identification cuts  $\Delta \log \mathcal{L}^{p-K} > 15$  and  $\Delta \log \mathcal{L}^{p-\pi} > 20$  have been used. Because of quite similar kinematics between  $\eta_c$  and  $J/\psi$  decays, the proton identification related efficiency mainly cancels in the ratio. Larger values of the identification cuts,  $\Delta \log \mathcal{L}^{p-K} > 20$  and  $\Delta \log \mathcal{L}^{p-\pi} > 25$ , have been applied as a cross-check. The yield ratio  $N_{\eta_c}^P/N_{J/\psi}^P$  for prompt production was obtained to be  $1.15 \pm 0.35$  using the 2011 data sample, and  $1.22 \pm 0.20$  using the 2012 data sample. The yield ratio  $N_{\eta_c}^S/N_{J/\psi}^S$  for charmonium production from  $b$ -hadron decays, was obtained to be  $0.35 \pm 0.09$  using the 2011 data sample, and  $0.28 \pm 0.05$  using the 2012 data sample. The observed difference is small compared to the statistical error. In addition by tightening the PID cuts, statistical significance degrades, and comparison is only qualitative.

High transverse momentum of the charmonium candidates,  $p_T > 6.5 \text{ GeV}/c$ , is already required at the trigger level.

The chosen set of selection criteria for prompt production analysis and for the analysis of inclusive charmonium production from  $b$ -hadron decays, was aimed at keeping for the two analyses as close as possible, so that fit parameters can be translated from the analysis of inclusive charmonium production from  $b$ -hadron decays, to the prompt charmonium production analysis.

In order to distinguish between promptly produced charmonium candidates and charmonium candidates from the  $b$ -hadron decays, the impact parameter of the proton tracks and the pseudo-proper lifetime  $\tau_z$  are used. The impact parameter of the proton tracks is chosen to be  $\chi^2/\text{ndf} > 16$  in order to select charmonium candidates from  $b$ -hadron decays. The  $\tau_z$  value is defined as

$$\tau_z = \frac{(z_d - z_p)M_{p\bar{p}}}{p_z}, \quad (4.1)$$

where  $z_p$  and  $z_d$  are the  $z$ -coordinates of primary and secondary vertices respectively,  $M_{p\bar{p}}$  is a reconstructed charmonium mass and  $p_z$  is the longitudinal component of its momentum. The  $\tau_z < 80 \text{ fs}$  and  $\tau_z > 80 \text{ fs}$  selection criteria are used to select prompt charmonium candidates and charmonium candidates from  $b$ -hadron decays respectively. The  $\tau_z$  spectra for different sources of charmonium candidates are given on Figs. 4.1

and ?? for prompt and secondary charmonia candidates, respectively.

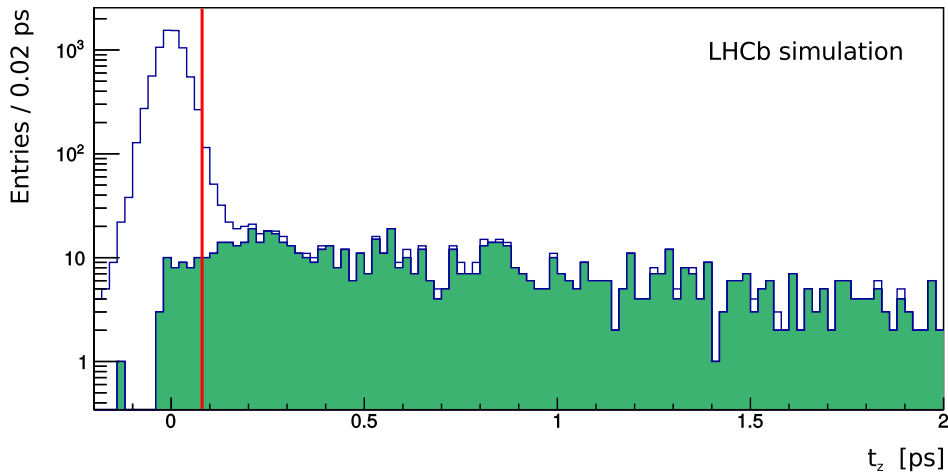


Figure 4.1: Distribution of the pseudo-decay time  $t_z$  for simulated  $J/\psi \rightarrow p\bar{p}$  signal selected by the prompt production analysis. All selection criteria but the  $t_z$  requirement are applied. The  $t_z$  threshold is shown with the red vertical line. Empty and filled histograms correspond to prompt charmonia and charmonia from  $b$ -hadron decays, respectively.

A stability of the  $\eta_c$  to  $J/\psi$  production ratios against the  $\tau_z$  cut value variation was checked by applying an alternative value of 120 ps of the cut. Then the yield ratio  $N_{\eta_c}^P/N_{J/\psi}^P$  for prompt production was obtained to be  $1.21 \pm 0.22$  using the 2011 data sample, and  $1.08 \pm 0.21$  using the 2012 data sample. The yield ratio  $N_{\eta_c}^S/N_{J/\psi}^S$  for charmonium production from  $b$ -hadron decays, was obtained to be  $0.30 \pm 0.06$  using the 2011 data sample, and  $0.31 \pm 0.04$  using the 2012 data sample. The difference of these values with respect to the values, corresponding to the 80 ps cut, is small compared to the statistical error.

Offline optimisation of the selection criteria finally suggests essentially to keep all events available after the trigger. Table 4.2 summarises selection criteria for both the prompt production analysis (set of cuts I) and the analysis of charmonium production from  $b$ -hadron decays (set of cuts II).

## 4.5 Analysis procedure

The main purpose of the analysis is the measurement of the cross section for prompt  $\eta_c$  production relative to that of  $J/\psi$ . For a given charmonium state  $A$ , the number of

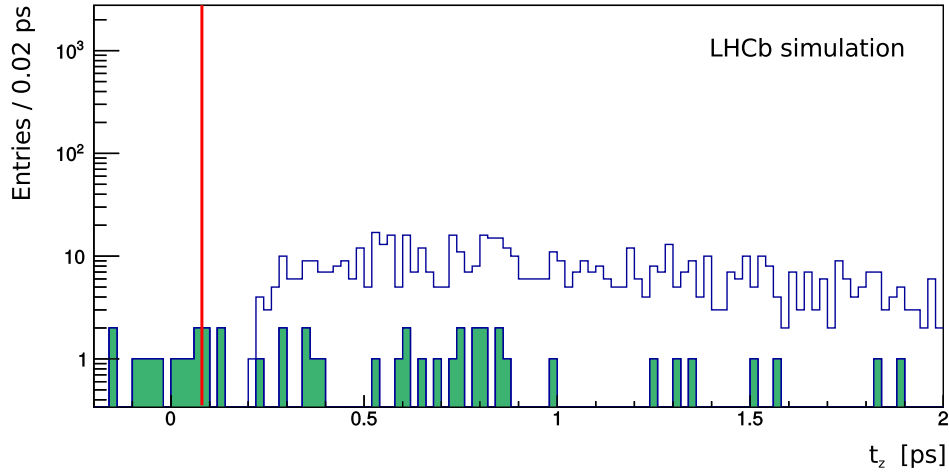


Figure 4.2: Distribution of the pseudo-decay time  $t_z$  for simulated  $J/\psi \rightarrow p\bar{p}$  signal selected by the analysis of charmonia production in  $b$ -hadron decays. All selection criteria but the  $t_z$  requirement are applied. The  $t_z$  threshold is shown with the red vertical line. Empty and filled histograms correspond to charmonia from  $b$ -hadron decays and prompt charmonia, respectively.

promptly produced  $A$  decaying to a  $p\bar{p}$  pair is given by

$$N^P = \int \mathcal{L} dt \times \sigma(A) \times \mathcal{B}_{A \rightarrow p\bar{p}}, \quad (4.2)$$

where  $\int \mathcal{L} dt$  is an integrated luminosity,  $\sigma(A)$  is a prompt production cross section and  $\mathcal{B}_{A \rightarrow p\bar{p}}$  is the branching fraction for the  $A \rightarrow p\bar{p}$  decay channel. For charmonia produced in  $b$ -hadron decays, we can write

$$N^S = \int \mathcal{L} dt \times \sigma(b) \times \mathcal{B}_{b \rightarrow AX} \times \mathcal{B}_{A \rightarrow p\bar{p}}, \quad (4.3)$$

where  $\sigma(b)$  is the  $b$ -quark production cross-section, and  $\mathcal{B}_{b \rightarrow AX}$  is an inclusive branching fraction of  $\eta_c$  production in  $b$ -hadron decays. The ratio of the  $\eta_c$  to  $J/\psi$  production can be written as:

$$\frac{N_{\eta_c}^P}{N_{J/\psi}^P} = \frac{\sigma(\eta_c) \times \mathcal{B}_{\eta_c \rightarrow p\bar{p}}}{\sigma(J/\psi) \times \mathcal{B}_{J/\psi \rightarrow p\bar{p}}} \quad (4.4)$$

for prompt production and

$$\frac{N_{\eta_c}^S}{N_{J/\psi}^S} = \frac{\mathcal{B}_{b \rightarrow \eta_c X} \times \mathcal{B}_{\eta_c \rightarrow p\bar{p}}}{\mathcal{B}_{b \rightarrow J/\psi X} \times \mathcal{B}_{J/\psi \rightarrow p\bar{p}}} \quad (4.5)$$

	variable	set of cuts I: prompt production analysis	set of cuts II: analysis of production in $b$ -hadron decays
protons	$p_T$ , GeV/ $c$ $p$ , GeV/ $c$ track $\chi^2$ /NDF $\Delta \log \mathcal{L}^{p-\pi}$ $\Delta \log \mathcal{L}^{p-K}$	$> 2.0$ $> 10.0$ $< 4$ $> 20$ $> 15$	$> 2.0$ — $< 4$ $> 20$ $> 15$
charmonium	$p_T$ , GeV/ $c$ vertex $\chi^2$ rapidity $y$	$> 6.5$ $< 9$ $2 < y < 4.5$	$> 6.5$ $< 9$ $2 < y < 4.5$
multiplicity	SPD multiplicity	$< 300$	$< 300$
separation of prompt production versus inclusive production in $b$ -hadron decays	proton track IP lifetime $\tau_z$ , fs	— $< 80$	$> 16$ $> 80$

Table 4.2: Selection criteria for prompt charmonium candidates and charmonium candidates from  $b$ -hadron decays

for charmonia from  $b$ -hadron decays.

#### 4.5.1 Effect from cross-talk between the samples

The cross-talk between the two samples, selecting prompt charmonium candidates and charmonium candidates from  $b$ -hadron decays respectively, is caused by the non-perfect separation using the proper time cut, and is estimated using MC. Production yields, i.e. the numbers of produced particles, which decay into the  $p\bar{p}$  final state, and the observed yields for prompt component and candidates for charmonium production from  $b$ -hadron decays are thus linked:

$$\begin{cases} n^P = \epsilon^{P \rightarrow P} N^P + \epsilon^{S \rightarrow P} N^S \\ n^S = \epsilon^{S \rightarrow S} N^S + \epsilon^{P \rightarrow S} N^P, \end{cases} \quad (4.6)$$

where  $n^P$  and  $n^S$  are yields of  $A$  observed in the prompt charmonium sample and the sample of charmonium produced in  $b$ -hadron decays,  $\epsilon_{P \rightarrow P}$  is an efficiency for promptly produced charmonium as selected using the set of cuts I for prompt production analysis,  $\epsilon_{P \rightarrow S}$  is an efficiency for promptly produced charmonium as selected using the set of cuts II for production from  $b$ -hadron decays analysis, and the efficiencies  $\epsilon_{S \rightarrow S}$  and  $\epsilon_{S \rightarrow P}$  for charmonium produced in  $b$ -hadron decays are defined in similar way. The values of the efficiencies  $\epsilon^{P, S \rightarrow P, S}$ , obtained from MC, are shown in Table 4.3.

	efficiency $\times 10^{-3}$	$J/\psi \rightarrow p\bar{p}$ ,	$J/\psi \rightarrow p\bar{p}\pi^0$ in the (2850..3250) MeV/ $c^2$ range
prompt charmonium production analysis	$\epsilon^{P \rightarrow P}$ $\epsilon^{S \rightarrow P}$	$6.03 \pm 0.06$ $0.45 \pm 0.06$	$0.76 \pm 0.04$
analysis of charmonium production in $b$ -hadron decays	$\epsilon^{S \rightarrow S}$ $\epsilon^{P \rightarrow S}$	$7.70 \pm 0.23$ $0.04 \pm 0.01$	$0.45 \pm 0.06$

Table 4.3: Efficiencies and cross-talk for prompt charmonium production and for charmonium production from  $b$ -hadron decays, as obtained from MC. The errors reflect the available MC statistics

Solving equations (4.6), the number of promptly produced charmonium:

$$N^P = \frac{\epsilon^{S \rightarrow S} n^P - \epsilon^{S \rightarrow P} n^S}{\epsilon^{P \rightarrow P} \epsilon^{S \rightarrow S} - \epsilon^{P \rightarrow S} \epsilon^{S \rightarrow P}} \quad (4.7)$$

and the number of charmonium produced in  $b$ -hadron decays:

$$N^S = \frac{\epsilon^{P \rightarrow P} n^S - \epsilon^{P \rightarrow S} n^P}{\epsilon^{P \rightarrow P} \epsilon^{S \rightarrow S} - \epsilon^{P \rightarrow S} \epsilon^{S \rightarrow P}} \quad (4.8)$$

Assuming efficiencies for  $\eta_c$  and  $J/\psi$  to be close (according to MC simulation the efficiencies differ by less than 0.5%),  $\epsilon_{\eta_c} \simeq \epsilon_{J/\psi}$ , the  $\eta_c$  to  $J/\psi$  event yield ratio can be written:

$$\frac{N_{\eta_c}^P}{N_{J/\psi}^P} = \frac{n_{\eta_c}^P \epsilon^{S \rightarrow S} - n_{\eta_c}^S \epsilon^{S \rightarrow P}}{n_{J/\psi}^P \epsilon^{S \rightarrow S} - n_{J/\psi}^S \epsilon^{S \rightarrow P}} \quad (4.9)$$

for prompt production, and

$$\frac{N_{\eta_c}^S}{N_{J/\psi}^S} = \frac{n_{\eta_c}^S \epsilon^{P \rightarrow P} - n_{\eta_c}^P \epsilon^{P \rightarrow S}}{n_{J/\psi}^S \epsilon^{P \rightarrow P} - n_{J/\psi}^P \epsilon^{P \rightarrow S}} \quad (4.10)$$

for the inclusive charmonium production in  $b$ -hadron decays.

## 4.5.2 $J/\psi$ polarisation

Non-zero polarisation in the  $J/\psi$  production requires an additional efficiency correction. Efficiency ratios are reweighted in bins of rapidity  $y$  and  $p_T$  (see Fig. 4.3 and Fig. 4.4) using the  $J/\psi$  polarisation measurement [37], using the following weights:

$$w_{i,j} = 1 + \lambda(\theta)_{i,j} \cos^2 \theta, \quad (4.11)$$

where  $\theta$  is the angle between the proton direction in the  $J/\psi$  rest frame and the  $J/\psi$  boost, and the polarisation coefficients  $\lambda(\theta)_{i,j}$  are taken from Ref. [37] for different  $p_T$  and rapidity ranges, marked with indices  $i$  and  $j$  respectively. Normalisation of the weights is performed with the numerical integration of the ROOFIT package. Corrections to the efficiency ratio  $\epsilon_{\eta_c}/\epsilon_{J/\psi}$  are shown in Table 4.4.

		$p_T$		
		(5..7) GeV/ $c$	(7..10) GeV/ $c$	(10..15) GeV/ $c$
$y$	(2.0..2.5)	$0.92 \pm 0.04$	$0.95 \pm 0.02$	$0.98 \pm 0.01$
	(2.5..3.0)	$0.95 \pm 0.02$	$0.97 \pm 0.01$	$0.98 \pm 0.01$
	(3.0..3.5)	$0.96 \pm 0.03$	$0.97 \pm 0.01$	$0.98 \pm 0.01$

Table 4.4: Corrections weights  $w_{i,j}$  due to  $J/\psi$  polarisation, in bins of  $p_T$  and rapidity  $y$ . For the rapidity interval (3.5..4.5) the coefficient is assumed to be 1.0. For each bin correlated and uncorrelated uncertainties are summed

Polarisation in other dimensions is found to be negligible:  $\lambda(\phi)_{i,j} \simeq \lambda(\theta\phi)_{i,j} \simeq 1$ , see Ref. [37].

The event yields enter in ratios and are corrected by the ratio of corresponding efficiencies. The efficiencies are taken from MC, which reasonably describes the difference in the phase space regions. The correction from the polarisation measurement [37] is then introduced. Effects of a possible difference in the  $p_T$  spectrum between  $J/\psi$  and  $\eta_c$  are addressed as a possible source of systematic uncertainty in section 4.8.

### 4.5.3 Fit of the invariant $p\bar{p}$ mass distribution

The corresponding data sample, the set of cuts and details of the selection procedure are addressed above in section 4.4.

The number of reconstructed  $\eta_c$  and  $J/\psi$  candidates is extracted from an unbinned maximum likelihood fit of the  $p\bar{p}$  invariant mass spectrum. The fitting procedure is performed using Minuit minimiser from the ROOFIT package. The chosen algorithm strategy is `migrad`.

The fit range of the  $p\bar{p}$  invariant mass spectrum is chosen to be (2850..3250) MeV/ $c^2$ . For masses below this range the spectrum is distorted due to the trigger effects. Above the upper limit many reflections from higher charmonia states are expected, as explained in section 4.5.5.

Because of the secondary vertex requirement, combinatorial background is lower for charmonium candidates from  $b$ -hadron decays, so that  $\eta_c$  and  $J/\psi$  signals are relatively

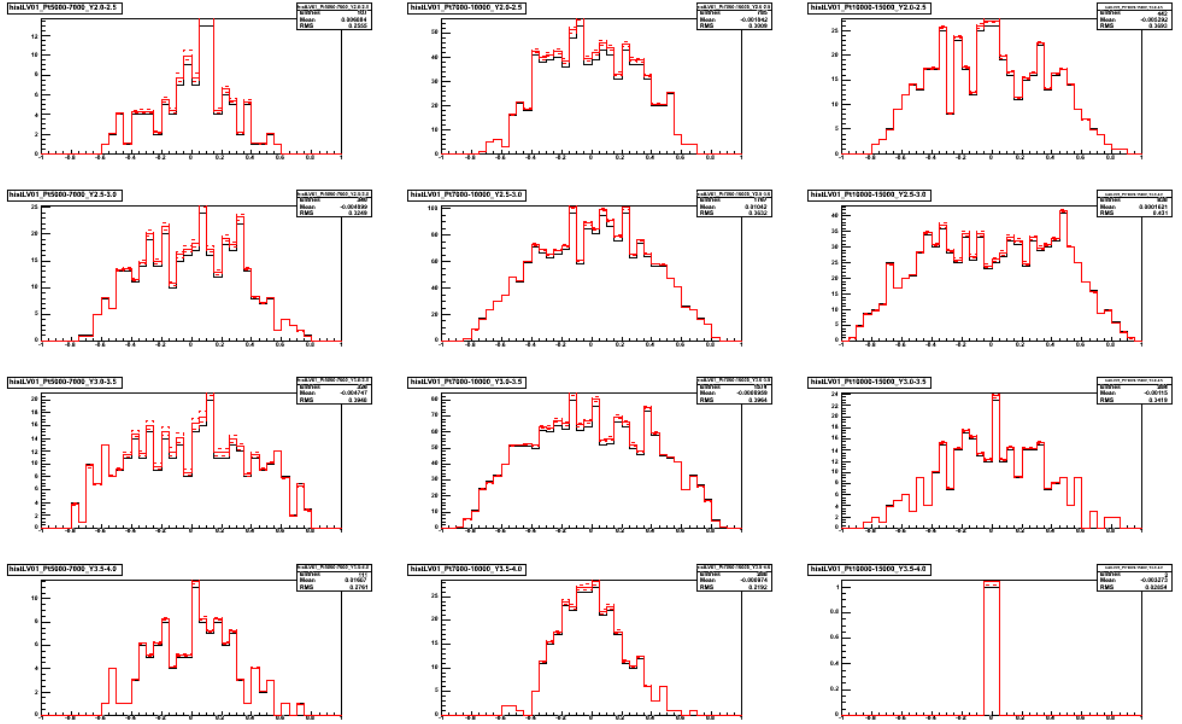


Figure 4.3:  $J/\psi \cos(\theta)$  reweighted in the transverse momentum and rapidity bins, Monte-Carlo simulation. Solid red lines represent reweighted MC sample, dashed red lines represent polarisation parameter error and black crosses are for unweighted MC distributions.

clean. The signal parametrisation was extracted from the  $p\bar{p}$  invariant mass spectrum fit, corresponding to the sample of  $\eta_c$  and  $J/\psi$  candidates from  $b$ -hadron decays, and then applied to describe the prompt charmonium production candidates in section 4.7.

#### 4.5.4 Signal parametrisation

The shape of the signals result from the detector response, and the natural width in the case of the  $\eta_c$  resonance.

For the  $J/\psi$  signal description we use a double-Gaussian function:

$$f_{J/\psi} \sim k \times e^{-\frac{(M_{J/\psi} - M_{p\bar{p}})^2}{(\sigma_{J/\psi}^a)^2}} + (1 - k) \times e^{-\frac{(M_{J/\psi} - M_{p\bar{p}})^2}{(\sigma_{J/\psi}^b)^2}} \quad (4.12)$$

In the case of the  $\eta_c$  signal description, its natural width  $\Gamma_{\eta_c}$  is comparable with the detector resolution  $\sigma^{a,b}$ . The  $\eta_c$  peak is thus described using a convolution of double-

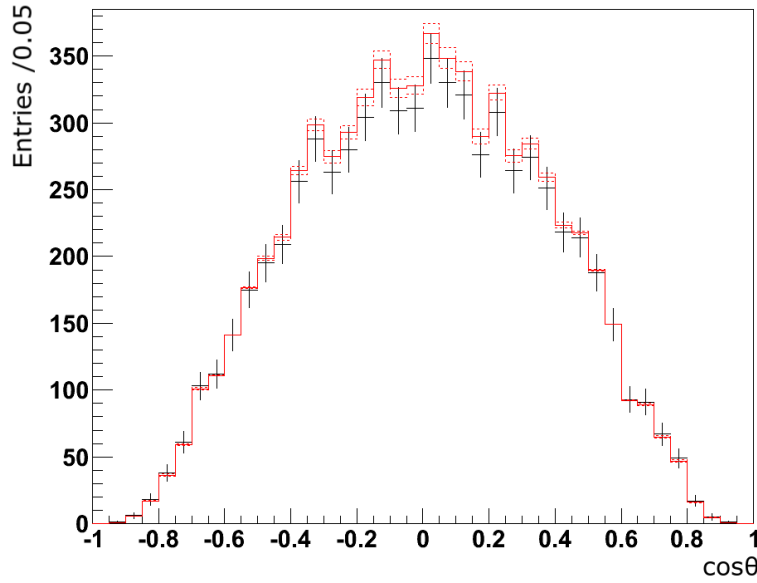


Figure 4.4:  $J/\psi$   $\cos(\theta)$  spectrum integrated over the transverse momentum and rapidity bins, Monte-Carlo simulation. Solid red lines represent reweighted MC sample, dashed red lines represent polarisation parameter error and black crosses are for unweighted MC distributions

Gaussian and Breit-Wigner functions:

$$f_{\eta_c} \sim \left( k \times e^{-\frac{(M_{\eta_c} - M_{p\bar{p}})^2}{(\sigma_{\eta_c}^a)^2}} + (1 - k) \times e^{-\frac{(M_{\eta_c} - M_{p\bar{p}})^2}{(\sigma_{\eta_c}^b)^2}} \right) \otimes \text{BW}(M_{\eta_c}, \Gamma_{\eta_c}) \quad (4.13)$$

A relativistic Breit-Wigner probability density function (PDF) is written as in Ref. [11]:

$$\text{BW}_{relativistic} \sim \frac{1}{(E^2 - M^2)^2 + M^2\Gamma^2(E)} \sim \frac{1}{\frac{(E+M)^2}{4M^2}(E - M)^2 + \frac{1}{4}\Gamma^2(E)}, \quad (4.14)$$

where  $E$  is the centre-mass energy,  $M$  is the mass of decaying resonance and  $\Gamma(E)$  is its natural width:

$$\Gamma(E) = \Gamma \cdot \left( \frac{q(E)}{q(M)} \right)^{2L+1} B_L(q(E), q(M)) \quad (4.15)$$

Only  $S$ -wave should be considered: the  $\eta_c$  spin  $J = 0$ , so due to angular momentum

and helicity conservation the pair of protons can not be created in a state different from  $L = 0$ . In this case, the factor  $B_0(q(E), q(M)) = 1$ . One can see that equation (4.14) differs from zero over the range of a few  $\Gamma$  from central value  $M$  only:  $\int_{-2\Gamma}^{2\Gamma} \text{BW}(E) \simeq 0.70$ . For an  $\eta_c$  resonance the natural width is small compared to its mass:  $\Gamma_{\eta_c}/M_{\eta_c} = (1.00 \pm 0.03)\%$  [11]. Hence  $E \sim M_{\eta_c}$  and with the approximation  $(E + M)^2/4M^2 \simeq 1$  we simplify equation (4.14) to a non-relativistic Breit-Wigner shape:

$$\text{BW} \sim \frac{1}{(E - M_{\eta_c})^2 + \frac{1}{4}\Gamma_{\eta_c}^2} \quad (4.16)$$

This PDF, convoluted with the double-Gaussian, is used for the  $\eta_c$  signal parametrisation in the present analysis.

MC simulation gives the ratio of  $J/\psi$  and  $\eta_c$  resolutions to be  $\sigma_{\eta_c}^a/\sigma_{J/\psi}^a = 0.88 \pm 0.02$ , and the ratio of the two Gaussian widths to be  $\sigma_{J/\psi}^a/\sigma_{J/\psi}^b = 0.50 \pm 0.03$  and the fraction of the ‘‘narrow’’ Gaussian component ( $\sigma^a$ )  $k$  to be about 90% for both prompt charmonium production samples, and charmonium candidates from  $b$ -hadron decays. The above parameter ratios are fixed in the fit to the MC central values and then varied within error bounds to estimate systematic uncertainties. The fit results from the MC sample are shown in Table 4.5.

	$J/\psi$ , prompt sample	$J/\psi$ , $b$ -hadron decays sample	$\eta_c$ , $b$ -hadron decays sample
Mass, $\text{MeV}/c^2$	$3096.84 \pm 0.10$	$3097.32 \pm 0.28$	$2980.12 \pm 0.02$
$\Gamma_{\eta_c}$ , MeV			29.7
$\sigma^a$ , $\text{MeV}/c^2$	$7.1 \pm 0.2$	$7.0 \pm 0.5$	$6.2 \pm 0.1$
$\sigma^b$ , $\text{MeV}/c^2$	$14.1 \pm 1.4$	$15.4 \pm 3.3$	related to $\sigma_{J/\psi}^b$
$k$	$0.90 \pm 0.04$	$0.86 \pm 0.09$	related to $k_{J/\psi}$

Table 4.5: The  $J/\psi$  and  $\eta_c$  fit results from the MC samples. Mass  $M$ , resolution of two Gaussian functions  $\sigma^{a,b}$  and contribution of the ‘‘narrow’’ Gaussian function  $k$  are shown

The  $J/\psi$  peak position  $M_{J/\psi}$  and the mass difference  $M_{J/\psi} - M_{\eta_c}$  are fitted to the data in the analysis of charmonium production in  $b$ -hadron decays. Both  $\eta_c$  to  $J/\psi$  mass difference and the  $\eta_c$  natural width from the fit agree with the PDG (Particle Data Group) values [11] within errors, as seen in Table 4.18. These values for the  $J/\psi$  mass and the difference between the  $J/\psi$  and  $\eta_c$  mass values are then used to apply Gaussian constraints in the fit to the proton-antiproton invariant mass spectrum in the prompt production analysis.

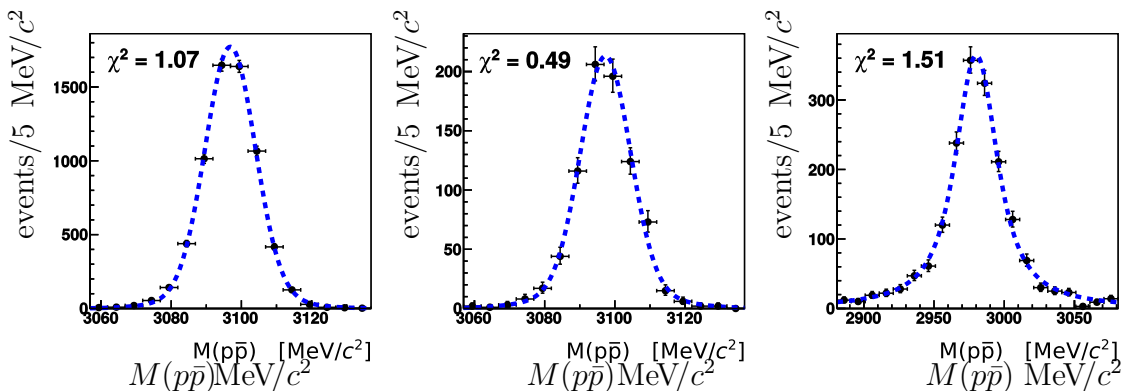


Figure 4.5: The  $p\bar{p}$  invariant mass of the MC samples: prompt  $J/\psi$  production (left), inclusive  $J/\psi$  (centre) and  $\eta_c$  (right) production in  $b$ -hadron decays. The results of the fit are shown in Table 4.5. The effect from the  $\eta_c$  natural width is explicitly excluded

In the analysis of charmonium production from  $b$ -hadron decays, in the fit of the  $p\bar{p}$  invariant mass spectrum the  $J/\psi$  mass resolution is considered as a free parameter, while the ratio of the two Gaussian functions resolutions  $\sigma^a/\sigma^b$  and the ratio of  $\eta_c$  and  $J/\psi$  resolutions  $\sigma_{\eta_c}/\sigma_{J/\psi}$  are fixed to the MC values and the variation of these parameters within error bounds are included in the systematic uncertainty estimate. The natural width of the  $\eta_c$  resonance is also considered as a free parameter in the analysis of charmonium production in  $b$ -hadron decays.

Note, that only the ratios of the resolutions are used from the MC simulation, while the absolute values are determined from the narrow and significant  $J/\psi$  peak from the analysis of the charmonium production in  $b$ -hadron decays. The only other assumption, verified on the MC samples only, is that the resolution is similar for the prompt charmonium production and charmonium production in  $b$ -hadron decays. We argue below, that the knowledge of the resolution does not dominate the systematic uncertainty for the prompt charmonium production measurement nor for the measurement of inclusive charmonium production from  $b$ -hadron decays.

#### 4.5.5 Background parametrisation

The combinatorial background is parametrised using an exponential function.

Besides the combinatorial background, proton-antiproton pairs from (higher) charmonium state decays to three and more particles can produce a reflection in the  $p\bar{p}$  invariant mass spectrum. The  $p\bar{p}$  combinations from the  $\eta_c \rightarrow p\bar{p}X$  processes are not taken into account since they potentially distort the spectrum below the fitting range.

The closest to the range of interest is the  $\eta_c \rightarrow p\bar{p}\eta$  decay. It contributes to the mass range below  $M_{\eta_c} - M_\eta = 2983.7 - 547.9 = 2433.1 \text{ MeV}/c^2$ , well below the lower limit of  $2850.0 \text{ MeV}/c^2$ .

The only notable reflection from the  $J/\psi$  meson is  $J/\psi \rightarrow p\bar{p}\pi^0$  with the contribution up to  $M_{J/\psi} - M_{\pi^0} = 3096.9 - 135.0 = 2961.9 \text{ MeV}/c^2$ , which potentially affects the  $\eta_c$  region. This process is specifically included in the background description.

We describe the contribution from  $J/\psi \rightarrow p\bar{p}\pi^0$  around its threshold region, and parametrise the corresponding  $p\bar{p}$  invariant mass spectrum by a square-root shape:

$$f_{J/\psi \rightarrow p\bar{p}\pi^0}(M) \sim \begin{cases} \sqrt{M_{J/\psi} - M_{\pi^0} - M} & \text{if } M \leq M_{J/\psi} - M_{\pi^0} , \\ 0 & \text{if } M > M_{J/\psi} - M_{\pi^0} , \end{cases} \quad (4.17)$$

convoluted with the double-Gaussian function to account for the detector resolution, where  $M$  is the proton-antiproton invariant mass. This PDF contains no free parameters except a normalisation. With the efficiencies estimated from MC, and the branching fractions of the  $J/\psi \rightarrow p\bar{p}$  and  $J/\psi \rightarrow p\bar{p}\pi^0$  channels known [11], the yields of these channels are linked as:

$$n_{J/\psi \rightarrow p\bar{p}\pi^0} = n_{J/\psi \rightarrow p\bar{p}} \times \frac{\epsilon_{J/\psi \rightarrow p\bar{p}\pi^0}}{\epsilon_{J/\psi \rightarrow p\bar{p}}} \times \frac{\mathcal{B}_{J/\psi \rightarrow p\bar{p}\pi^0}}{\mathcal{B}_{J/\psi \rightarrow p\bar{p}}} . \quad (4.18)$$

Taking  $\mathcal{B}_{J/\psi \rightarrow p\bar{p}\pi^0} / \mathcal{B}_{J/\psi \rightarrow p\bar{p}} = 0.55 \pm 0.04$ , and  $\epsilon_{J/\psi \rightarrow p\bar{p}\pi^0} / \epsilon_{J/\psi \rightarrow p\bar{p}} = 0.06$  for the analysis of charmonium production from  $b$ -hadron decays and  $\epsilon_{J/\psi \rightarrow p\bar{p}\pi^0} / \epsilon_{J/\psi \rightarrow p\bar{p}} = 0.12$  for prompt production analysis (Table 4.3), we conclude, that the  $J/\psi \rightarrow p\bar{p}\pi^0$  channel produces a non-peaking contribution to the  $p\bar{p}$  invariant mass spectrum, which amounts to between 3 and 6% of the  $J/\psi \rightarrow p\bar{p}$  signal. The efficiency is estimated for the restricted invariant mass range.

Applicability of the shape from equation (4.17) is verified using the MC sample, as shown in Fig. 4.6.

The suggested model shows a good agreement with MC,  $\chi^2/\text{ndf} < 1$  for both the prompt charmonium production analysis sample and the sample corresponding to charmonium production from  $b$ -hadron decays, with and without trigger requirements.

#### 4.5.6 Possibility of alternative approach

A more straightforward method to obtain the event yield for prompt production component and the component of charmonium production from  $b$ -hadron decays, would

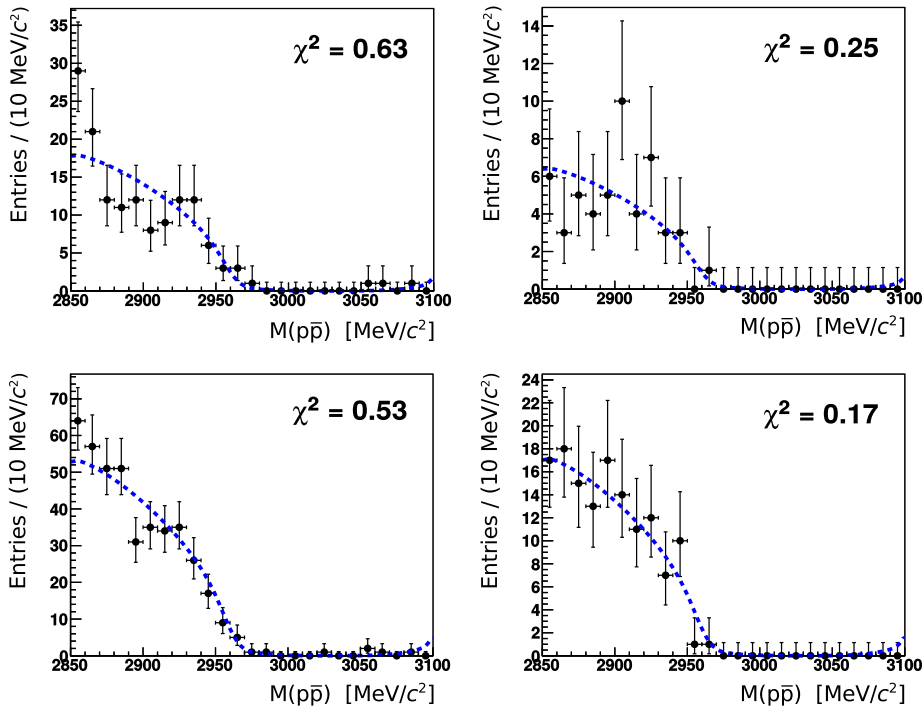


Figure 4.6: Fit of the  $p\bar{p}$  invariant mass from the  $J/\psi \rightarrow p\bar{p}\pi^0$  MC prompt  $J/\psi$  sample (left plots) and a sample of  $J/\psi$  from  $b$ -hadron decays (right plots) with (top plots) and without (bottom plots) trigger requirements

be to perform the 2D fit, as used for the  $J/\psi \rightarrow \mu^+\mu^-$  analysis [49, 37, 50]. However, in the present analysis, the statistics are significantly smaller, and also the signal-to-background ratio is much worse. In addition, the event mixing methods, like the “next” event method used to determine the wrong vertex contribution in the  $J/\psi \rightarrow \mu^+\mu^-$  analysis, do not work here. As a result a few percent of the signal is lost by imposing the prompt charmonium production versus charmonium production in  $b$ -hadron decays separation cuts, and up to 10% of the other component is explicitly subtracted, instead of being fit. The uncertainty introduced is small compared to the overall systematic error of the results.

## 4.6 Inclusive $\eta_c$ and $J/\psi$ production in $b$ -hadron decays

### 4.6.1 Analysis with the 2011 and 2012 data samples

The  $p\bar{p}$  invariant mass spectrum from  $b$ -hadron decays is shown on Fig. 4.7 for the 2011 data sample, and on Fig. 4.8 for the 2012 data sample.

The spectra were fit using the unbinned likelihood method, taking into account the signal and background components. The long-dashed cyan line corresponding to the  $J/\psi$  signal is described using a double-Gaussian function. The long-dashed red line corresponds to the  $\eta_c$  signal and is described using a double-Gaussian function, convoluted with a Breit-Wigner function. The background component, comprising the contribution from the  $J/\psi \rightarrow p\bar{p}\pi^0$  decay with non-reconstructed pion is described by the dashed yellow line, and the combinatorial background is described by the exponential. The  $J/\psi \rightarrow p\bar{p}\pi^0$  contribution is related to the  $J/\psi$  yield, which is defined by the  $J/\psi \rightarrow p\bar{p}$  yield, as explained in section 4.5.5. The relative  $J/\psi \rightarrow p\bar{p}\pi^0$  to  $J/\psi$  contribution is fixed in the fit. The results of the fit are shown in Table 4.6, where only the statistical uncertainties are shown.

	fit 2011 data	fit 2012 data	combined data
$n_{\eta_c}^S$	$645 \pm 133$	$1372 \pm 188$	$2020 \pm 230$
$n_{J/\psi}^S$	$2000 \pm 67$	$4110 \pm 94$	$6110 \pm 116$
$M_{J/\psi}$ , MeV/ $c^2$	$3096.50 \pm 0.34$	$3096.74 \pm 0.23$	$3096.66 \pm 0.18$
$M_{J/\psi} - M_{\eta_c}$ , MeV/ $c^2$	$113.1 \pm 2.4$	$115.8 \pm 1.9$	$114.9 \pm 1.5$
$\sigma_{J/\psi}^a$ , MeV/ $c^2$	$8.6 \pm 0.3$	$8.4 \pm 0.2$	$8.5 \pm 0.2$
$\Gamma_{\eta_c}$ , MeV	$23.0 \pm 9.0$	$27.3 \pm 6.3$	$26.1 \pm 5.2$
exponential slope, $\times 10^{-3}$	$-2.66 \pm 0.09$	$-2.71 \pm 0.06$	$-2.72 \pm 0.04$

Table 4.6: Results of the fit of the proton-antiproton invariant mass spectrum for charmonium candidates from  $b$ -hadron decays, for the 2011 and 2012 data samples. The event yields,  $J/\psi$  mass and the  $J/\psi$  to  $\eta_c$  mass difference,  $\eta_c$  natural width and resolution are shown, as well as the background parameters. The details of the fit are described in the text

Comparing the fit results of the  $J/\psi$  and  $\eta_c$  signal from data (Figs. 4.7 and 4.8, and Table 4.6) and from the MC double-Gaussian signal parametrisation (Fig. 4.5 and Table 4.5), we conclude that the MC underestimates resolution effects by more than 20%.

The resolution and the  $\eta_c$  natural width are then fixed to their central values,

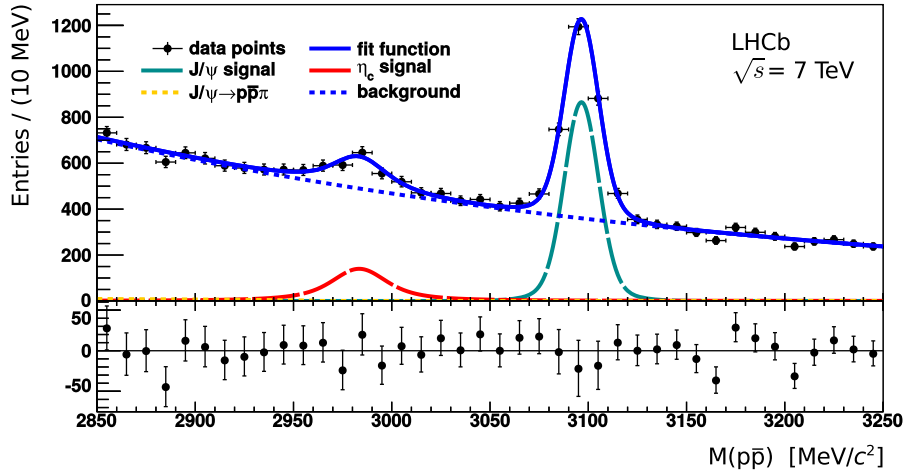


Figure 4.7: Proton-antiproton invariant mass spectrum for candidates coming from a secondary vertex, the 2011 year data sample. Solid blue line represents the fitting curve, long-dashed cyan line corresponds to double-Gaussian function for the  $J/\psi$  signal, long-dashed red line corresponds to the double-Gaussian function, convoluted with a Breit-Wigner function for the  $\eta_c$  signal, dashed yellow line corresponds to  $J/\psi \rightarrow p\bar{p}\pi^0$  spectrum with non-reconstructed pion. More details and fit results are described in the text

obtained from the analysis of charmonium production in  $b$ -hadron decays, in the fit to the  $p\bar{p}$  invariant mass spectrum from the prompt selection,  $\sigma_{J/\psi}^{a,2011} = 8.6 \text{ MeV}/c^2$ ,  $\sigma_{J/\psi}^{a,2012} = 8.4 \text{ MeV}/c^2$ , and  $\Gamma_{\eta_c} = 25.8 \text{ MeV}$ .

The yields of  $\eta_c$  and  $J/\psi$  in the analysis of inclusive production of charmonium from  $b$ -hadron decays, obtained from the fit, are

$$\begin{aligned} (n_{\eta_c}^S)_{2011} &= 645 \pm 133_{stat} \\ (n_{J/\psi}^S)_{2011} &= 2000 \pm 67_{stat} \end{aligned}$$

for the 2011 data, and

$$\begin{aligned} (n_{\eta_c}^S)_{2012} &= 1372 \pm 188_{stat} \\ (n_{J/\psi}^S)_{2012} &= 4110 \pm 94_{stat} \end{aligned}$$

for the 2012 data. To obtain the values of the relative  $\eta_c$  and  $J/\psi$  inclusive yield from  $b$ -hadron decays, the prompt production component also needs to be studied according to equation 4.10.

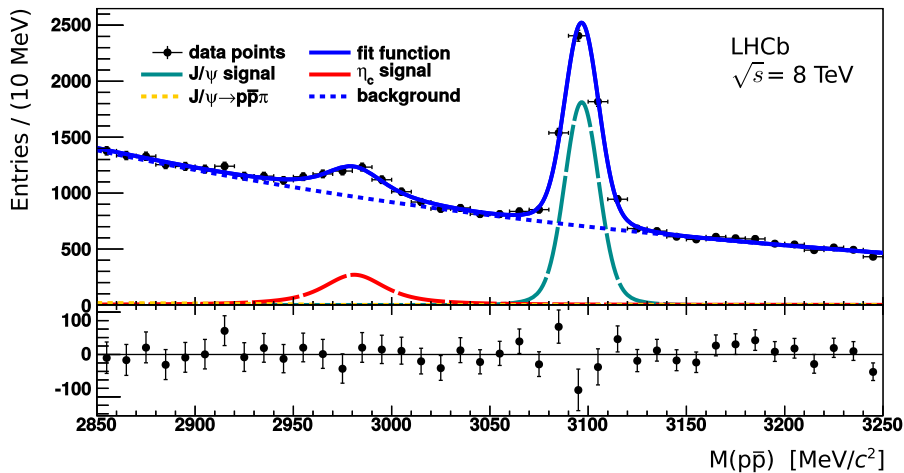


Figure 4.8: Proton-antiproton invariant mass spectrum for candidates coming from a secondary vertex, the 2012 year data sample. Solid blue line represents the fitting curve, long-dashed cyan line corresponds to double-Gaussian function for the  $J/\psi$  signal, long-dashed red line corresponds to the double-Gaussian function, convoluted with a Breit-Wigner function for the  $\eta_c$  signal, dashed yellow line corresponds to  $J/\psi \rightarrow p\bar{p}\pi^0$  spectrum with non-reconstructed pion. More details and fit results are described in the text

#### 4.6.2 Analysis with the combined data sample

In the main part of the analysis the 2011 and 2012 data samples have been analysed separately, and then averaged. Good agreement between the results for the two data samples has been observed. Taking into account a similar signal description parameters as well as those describing background shape, the  $p\bar{p}$  invariant mass spectrum was combined with both 2011 and 2012 data. The combined spectrum is shown on Fig. 4.9.

The results are consistent with the  $p\bar{p}$  invariant mass fit of the two separate, 2011 and 2012, samples, described in the section 4.6, within error bounds. The results of the fit are shown in Table 4.6. Only statistical uncertainties are shown.

### 4.7 Prompt charmonium production

Extraction of the prompt charmonia production is more challenging due to severe combinatorial background. This is despite the more selective cuts employed for the prompt production analysis already at the trigger level. The background level, after applying trigger and selection requirements, remains more than 500 times higher for the prompt production analysis with respect to the inclusive production in  $b$ -hadron decays, while

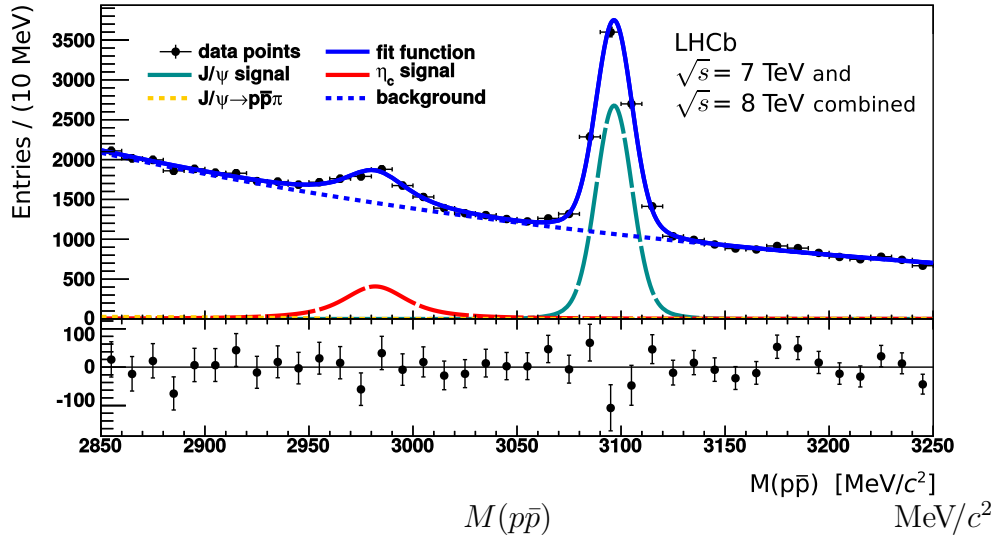


Figure 4.9: The  $p\bar{p}$  invariant mass spectrum for the analysis of charmonium production in  $b$ -hadron decays, with both 2011 and 2012 data combined

the  $J/\psi$  signal yield is only 5 times bigger.

#### 4.7.1 Fit with Gaussian constraints on the $J/\psi$ and $\eta_c$ masses

The result of the unbinned likelihood fit of the  $p\bar{p}$  invariant mass spectrum for the prompt charmonium production analysis is shown on Fig. 4.10 for the 2011 data sample, and on Fig. 4.11 for the 2012 data sample.

The results of the fit, including statistical uncertainties, are shown in Table 4.7.

	fit to 2011 data	fit to 2012 data
$n_{\eta_c}^P$	$13370 \pm 2260$	$22416 \pm 4072$
$n_{J/\psi}^P$	$11052 \pm 1004$	$20217 \pm 1403$
$M_{J/\psi}$ , MeV/ $c^2$	$3096.8 \pm 0.3$	$3096.9 \pm 0.2$
$M_{J/\psi} - M_{\eta_c}$ , MeV/ $c^2$	$109.0 \pm 2.0$	$111.6 \pm 1.5$
polynomial c1, $\times 10^{-3}$	$-38.37 \pm 0.06$	$-38.36 \pm 0.05$
polynomial c2, $\times 10^{-3}$	$5.45 \pm 0.06$	$5.44 \pm 0.05$
polynomial c3, $\times 10^{-3}$	$-0.60 \pm 0.06$	$-0.55 \pm 0.05$

Table 4.7: Results of the fit of the proton-antiproton invariant mass spectrum for prompt candidates from the 2011 and 2012 data. The event yields,  $J/\psi$  mass and  $J/\psi$  to  $\eta_c$  mass difference are shown, as well as the background parameters. Note that for both  $J/\psi$  mass and  $J/\psi$  to  $\eta_c$  mass difference, a Gaussian constraint is applied using the fit results from the analysis of charmonium production in  $b$ -hadron decays. The details of the fit are described in the text

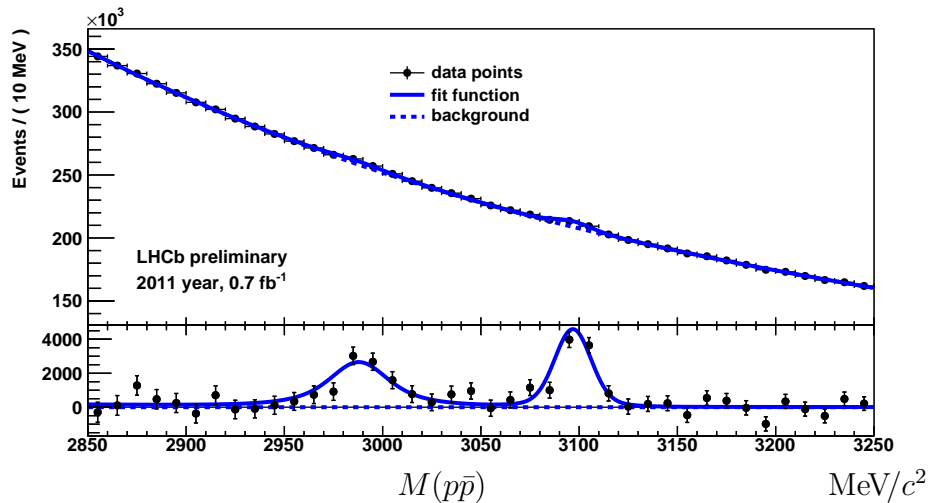


Figure 4.10: Proton-antiproton invariant mass spectrum for candidates coming from a primary vertex (top), and visually subtracted background (bottom), the 2011 data sample. The  $J/\psi$  signal is described by a double-Gaussian function, the  $\eta_c$  signal is described by a double-Gaussian function convoluted with a Breit-Wigner function, a contribution from  $J/\psi \rightarrow p\bar{p}\pi^0$  decay with non-reconstructed pion is taken into account. Gaussian constraints on the  $J/\psi$  mass and the difference  $\Delta M_{J/\psi, \eta_c} = M_{J/\psi} - M_{\eta_c}$ , from the fit of the sample corresponding to charmonium candidates from  $b$ -hadron decays, are applied. See the text for more details and fit results

For the fit of the invariant mass spectrum in the prompt charmonium production analysis signal resolutions are extracted from the fit of the low background  $p\bar{p}$  invariant mass spectrum in the analysis of inclusive charmonium production in  $b$ -hadron decays. Gaussian constraints on the  $J/\psi$  mass and the difference  $\Delta M_{J/\psi, \eta_c} = M_{J/\psi} - M_{\eta_c}$ , from the fit of the sample corresponding to the analysis of the charmonium production in  $b$ -hadron decays, are applied. The  $\eta_c$  natural width in the prompt production analysis fit, is fixed to the average value of 25.8 MeV from the analysis of charmonium production in  $b$ -hadron decays (section 4.6).

The background description is also more difficult, and instead of the exponential function we parametrise the background using a sum of Chebychev polynomials up to the third order. In order to demonstrate that this background description does not produce any peaking shape, and thus does not fake or influence the signal peaks, the linear and non-linear components of the background function are shown separately on Fig. 4.12. The non-linear component does not change convexity sign, so the fit function is not able to generate undesirable effects.

The unbinned maximum likelihood fit yields the following numbers of  $\eta_c$  and  $J/\psi$

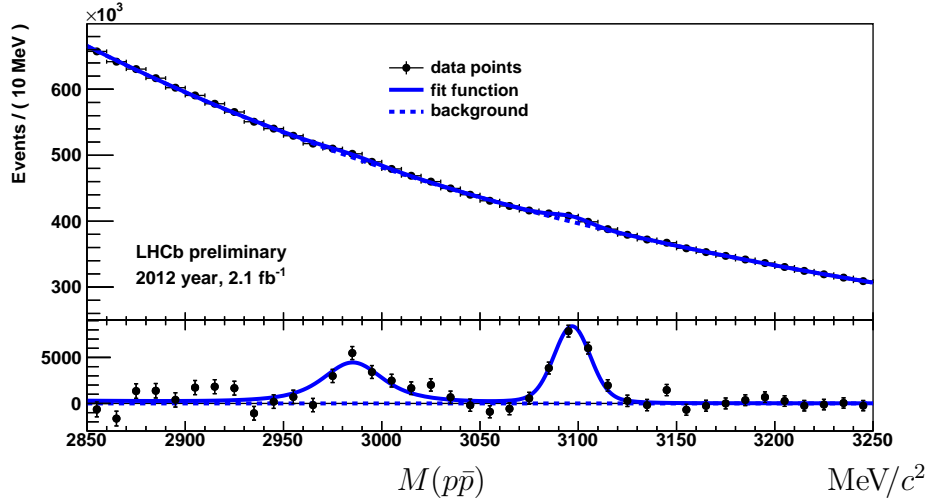


Figure 4.11: Proton-antiproton invariant mass spectrum for candidates coming from a primary vertex (top), and visually subtracted background (bottom), the 2012 data sample. The  $J/\psi$  signal is described by a double-Gaussian function, the  $\eta_c$  signal is described by a double-Gaussian function convoluted with a Breit-Wigner function, a contribution from  $J/\psi \rightarrow p\bar{p}\pi^0$  decay with non-reconstructed pion is taken into account. Gaussian constraints on the  $J/\psi$  mass and the difference  $\Delta M_{J/\psi, \eta_c} = M_{J/\psi} - M_{\eta_c}$ , from the fit of the sample corresponding to charmonium candidates from  $b$ -hadron decays, are applied. See the text for more details and fit results

in the signal peaks:

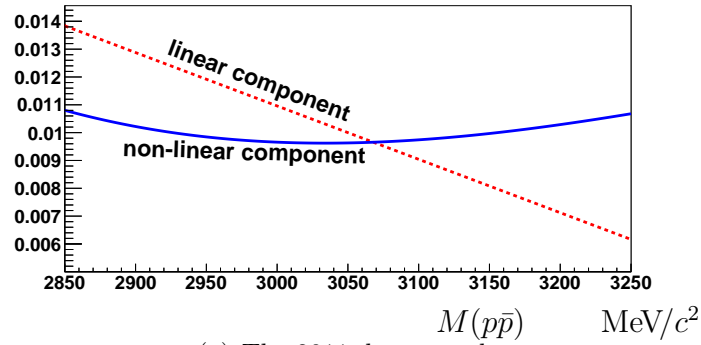
$$\begin{aligned} (n_{\eta_c}^P)_{2011} &= 13370 \pm 2260_{stat} \\ (n_{J/\psi}^P)_{2011} &= 11052 \pm 1004_{stat} \end{aligned}$$

for the 2011 data analysis, and

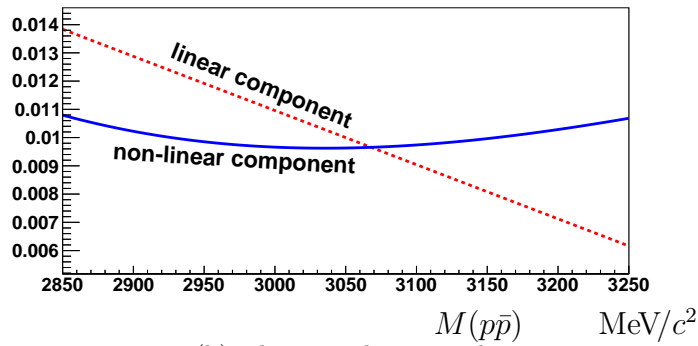
$$\begin{aligned} (n_{\eta_c}^P)_{2012} &= 22416 \pm 4072_{stat} \\ (n_{J/\psi}^P)_{2012} &= 20217 \pm 1403_{stat} \end{aligned}$$

for the 2012 data analysis.

Alternatively, a possibility to describe the combinatorial background using same charge  $pp$  combinations or event mixing technique was studied, see section 4.7.3 for details.



(a) The 2011 data sample



(b) The 2012 data sample

Figure 4.12: Linear (dashed red) and nonlinear (solid blue) components of the function used to describe the combinatorial background of the  $p\bar{p}$  invariant mass spectrum for the prompt production analysis. Both components have the same normalisation for this illustration

#### 4.7.2 Fit with the released $J/\psi$ and $\eta_c$ masses

For the fit of the  $p\bar{p}$  invariant mass spectrum in the prompt production analysis a Gaussian constraint on the  $J/\psi$  mass and the difference  $\Delta M_{J/\psi, \eta_c} = M_{J/\psi} - M_{\eta_c}$ , from the fit corresponding to the sample of charmonium from  $b$ -hadron decays, was applied. The fit with released mass values gives consistent results,  $M_{J/\psi} = 3098.7 \pm 1.0 \text{ MeV}/c^2$ ,  $\Delta M_{J/\psi, \eta_c} = 106.7 \pm 2.9 \text{ MeV}/c^2$  and  $M_{J/\psi} = 3097.6 \pm 0.8 \text{ MeV}/c^2$ ,  $\Delta M_{J/\psi, \eta_c} = 107.1 \pm 2.4 \text{ MeV}/c^2$ , for the 2011 and 2012 data samples, respectively, taking into account large errors from the prompt analysis fit. Only statistical errors are shown for the fit with released mass values.

The result of the  $p\bar{p}$  invariant mass spectrum fit for the prompt charmonium production analysis with released mass values is shown on Fig. 4.13 for the 2011 data sample, and on Fig. 4.14 for the 2012 data sample.

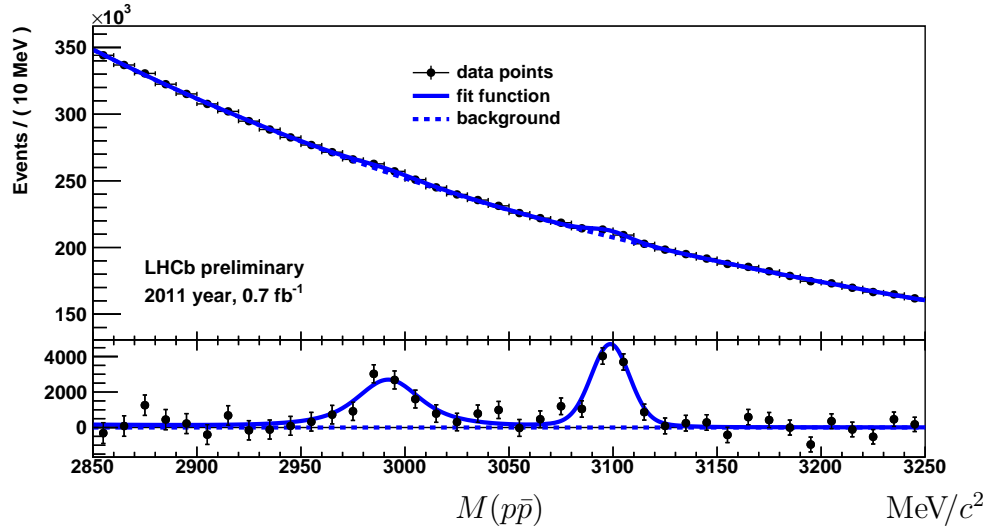


Figure 4.13: Proton-antiproton invariant mass spectrum for candidates coming from primary vertex for 2011 year data (top), with visually subtracted background (bottom). The  $J/\psi$  mass and the difference  $\Delta M_{J/\psi, \eta_c} = M_{J/\psi} - M_{\eta_c}$  are left as free parameters in the fit

For reference purposes, the ratio  $N_{\eta_c}^P/N_{J/\psi}^P$  is shown in Table 4.8 depending on whether  $\Delta_M = M_{J/\psi} - M_{\eta_c}$  is subject to the Gaussian constraint from the analysis of charmonium production in  $b$ -hadron decays, left free parameter in the fit, or fixed to the PDG value, for  $\sqrt{s} = 7$  TeV and 8 TeV data samples.

	$\sqrt{s} = 7$ TeV data sample	$\sqrt{s} = 8$ TeV data sample
Gaussian constraint	$1.24 \pm 0.21$	$1.14 \pm 0.21$
free fit parameter	$1.11 \pm 0.22$	$1.14 \pm 0.21$
fixed to the PDG value	$1.24 \pm 0.21$	$1.23 \pm 0.21$

Table 4.8: The ratio  $N_{\eta_c}^P/N_{J/\psi}^P$  depending on whether  $\Delta_M = M_{J/\psi} - M_{\eta_c}$  is subject to the Gaussian constraint from the analysis of charmonium production in  $b$ -hadron decays, left free parameter in the fit, or fixed to the PDG value, for  $\sqrt{s} = 7$  TeV and 8 TeV data samples

Note, that comparisons and alternative fit procedures, described in this section, have been performed as a cross check, and have not been used to estimate systematic uncertainty.

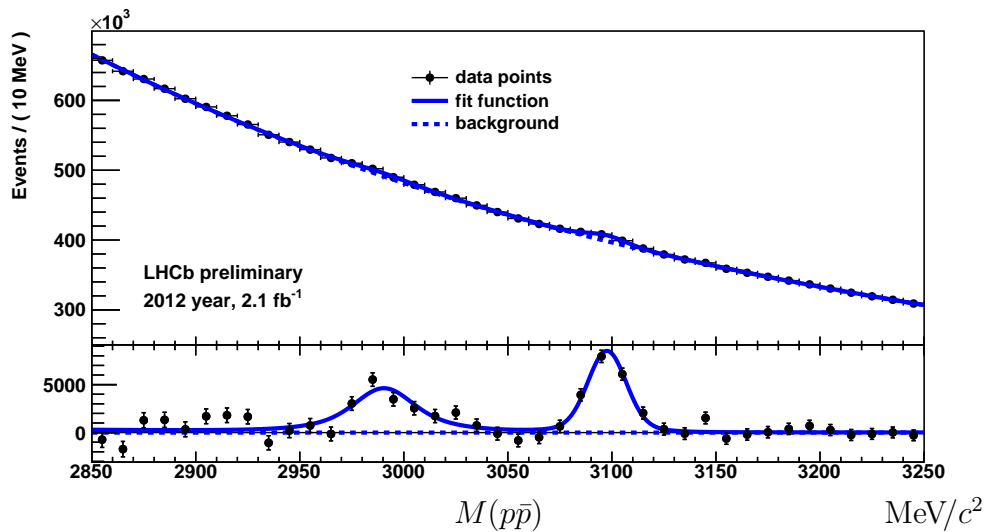


Figure 4.14: Proton-antiproton invariant mass spectrum for candidates coming from primary vertex for 2012 year data (top), with visually subtracted background (bottom). The  $J/\psi$  mass and the difference  $\Delta M_{J/\psi, \eta_c} = M_{J/\psi} - M_{\eta_c}$  are left as free parameters in the fit

### 4.7.3 Possible background description with the event mixing technique

To investigate a data-driven background description the event mixing method is tried. It is expected that the main contribution to the background distribution comes from the random combinations of uncorrelated protons and antiprotons. Thus if we mixed them randomly we would have a distribution which could perfectly describe an uncorrelated part of the background.

This method was applied on the promptly produced  $p\bar{p}$  dataset. All come from the primary vertex therefore one can mix tracks without the risk of forming incorrect vertices. For comparison we apply the same method to the set of muons from the  $c\bar{c} \rightarrow \mu^+\mu^-$  channel. The resulting plots are shown on the Fig. 4.15(a) and 4.15(b) respectively. Whereas the method appears to describe sufficiently well di-muon mass spectrum, it clearly fails to describe the  $p\bar{p}$  mass spectrum.

Suppose we have the number of events  $N_{\text{ev}} = n$ . Then event mixing is done with the following algorithm. The four-momentum  $P_1$  from the first row (event) is chosen. It is then combined with antiparticles  $\bar{P}_3, \bar{P}_4 \dots \bar{P}_n$  from the next  $n - 2$  rows. We require that combinations from the same event are not accepted. Then the procedure is repeated for the antiparticle four-momentum  $\bar{P}_1$ . Finally, this algorithm is repeated for  $P_2 \dots P_n$

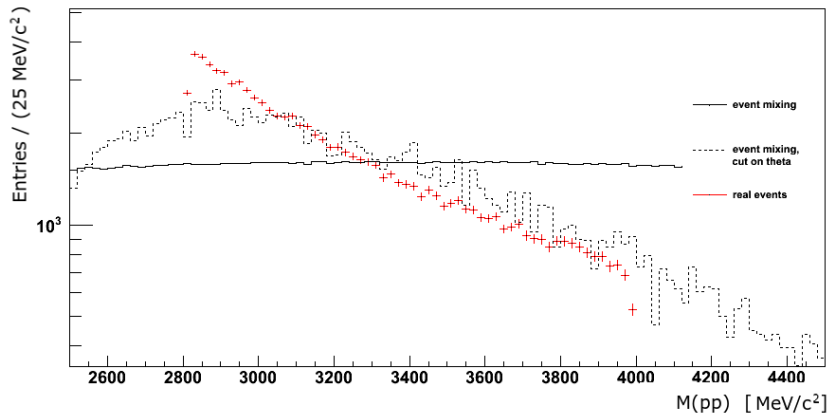
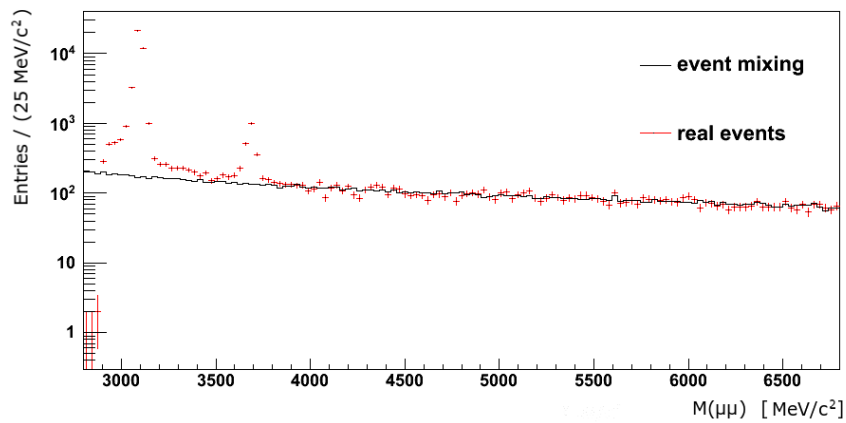
(a)  $p\bar{p}$  invariant mass(b)  $\mu^+\mu^-$  invariant mass

Figure 4.15: Event mixing: the invariant mass of the  $p\bar{p}$  candidates (top) and  $\mu^+\mu^-$  candidates (bottom). Mixed events spectra are represented by the black solid line, red crosses correspond to data points. The dashed black line stays for proton event mixing with an angular constraint

and  $\bar{P}_2 \dots \bar{P}_n$ . As a result, we obtain a collection of invariant mass values.

In this way we significantly increase the number of events:

$$N_{\text{ev}}^{\text{mix}} = n^2 - 3n + 2 \gg N_{\text{ev}} \quad (4.19)$$

for  $n \gg 1$ . Nevertheless one should note that this set of artificially mixed events is somehow degenerate. A momentum  $P(A_i)$  of each (anti)particle occurs  $n - 2$  times in different combinations.

Since the result from proton-antiproton opposite sign event mixing was unsuccessful, we apply constraints on an opening angle between proton and antiproton momenta. Not all events are accepted to the mixed spectrum, but only those which have the opening angle between proton and antiproton momenta similar to that of non-mixed events:

$$|\cos(\theta_{\text{mixed candidate}}) - \cos(\theta_{\text{signal candidate}})| < 1 \times 10^{-4} , \quad (4.20)$$

where  $\cos(\theta_{\text{signal candidate}})$  is the opening angle between proton and anti-proton for signal candidate and  $\cos(\theta_{\text{mixed candidate}})$  is the angle for the candidate from mixing procedure.

Unfortunately, in the case of the  $p\bar{p}$  sample this method did not give satisfactory results even with constraints on the angle between the proton momenta. A possible explanation is that there are some unexpected correlations in the proton-antiproton production.

## 4.8 Systematic uncertainties

This section addresses the estimate of systematic uncertainties. For each analysis, systematic uncertainties corresponding to various sources are estimated by varying parameters used in the fit, and then quadratically added to obtain the total systematic uncertainty. Uncertainties corresponding to the knowledge of the  $J/\psi$  production cross section and the branching fractions of the  $\eta_c \rightarrow p\bar{p}$  and  $J/\psi \rightarrow p\bar{p}$  decay modes are combined in a separate systematic uncertainty.

### 4.8.1 Inclusive $\eta_c$ and $J/\psi$ production in $b$ -hadron decays

For the measurement of the inclusive  $\eta_c$  and  $J/\psi$  production in  $b$ -hadron decays, systematic uncertainties due to detector resolution, background description, feed-down from the  $J/\psi \rightarrow p\bar{p}\pi^0$  and the cross-talk between the prompt charmonium sample and

the charmonium sample from  $b$ -hadron decays, were considered. Tables 4.9 and 4.10 summarise the systematic uncertainty estimates, for the 2011 and 2012 data samples respectively. The total systematic uncertainty is dominated by the background description, probed via background shape variation, fit range variation, and shape variation of the contribution from  $J/\psi \rightarrow p\bar{p}\pi^0$ .

The detector resolution for both  $\eta_c$  and  $J/\psi$  signal peaks is accounted for by the two Gaussian functions as described in subsection 4.5.4. The ratio between the two Gaussian sigmas, as well as their relative contribution, and the ratio between the detector resolution for  $\eta_c$  and  $J/\psi$  signal peaks, are fixed from the MC simulation, thus leaving a single resolution parameter free. The systematic uncertainty related to detector resolution description, was conservatively estimated by assuming similar resolution for  $J/\psi$  and  $\eta_c$ ,  $\sigma_{\eta_c}^a/\sigma_{J/\psi}^a \simeq 1$ , while the ratio  $\sigma_{\eta_c}^a/\sigma_{J/\psi}^a \simeq 0.88$  in the MC simulation.

The corresponding systematic uncertainty was found to be about 2% for both the 2011 and 2012 data samples.

Uncertainty, associated to the cross-talk between the prompt sample and the sample of charmonium from  $b$ -hadron decays, was estimated by varying the fit parameters in the prompt production analysis, as well as by taking into account the systematic uncertainty on the event yields in the prompt production charmonium sample. Contribution of 2.7% and 2.2% were found for the 2011 and 2012 data samples. The effect of limited MC statistics (errors in Table 4.3) leads to additional uncertainty of about 1.3%. Thus the contribution of 3.0% and 2.6% to the total systematic uncertainty was obtained for the 2011 and 2012 data samples respectively. An important effect, related to a potential difference of the  $\eta_c$  and  $J/\psi$  prompt production spectrum, and contributing to the analysis of charmonium production from  $b$ -hadron decays via the cross-talk between the two samples, was estimated separately. It was found to be around 1.2% using the efficiency-weighted  $p\bar{p}$  invariant mass spectrum fit, as described in section 4.8.2.

To estimate systematic uncertainties associated to the background parametrisation we replace an exponential function by an exponential function multiplied by a first order polynomial. Uncertainties due to the background parametrisation were found to be 2.2% and 0.6%, for the 2011 and 2012 data samples.

Independently, the fit range is varied from the baseline interval of (2850..3250) MeV/ $c^2$  to an interval (2870..3230) MeV/ $c^2$ . Further reducing the fit range does not leave enough data points to constrain the background shape. On the other hand, increasing the fit range requires introducing new components in the background description. Uncertainties due to the fit range variation were found to be about 3%.

	$n_{J/\psi}$	$n_{\eta_c}$	$\frac{n_{\eta_c}}{n_{J/\psi}}$	$\frac{N_{\eta_c}}{N_{J/\psi}}$
mean value	2000	645	0.323	0.289
statistical uncertainty	67 (3.4%)	133 (20.6%)	0.068 (21.1%)	0.069 (24.0%)
signal resolution ratio (MC)	< 1 (< 0.1%)	11 (1.7%)	0.006 (1.7%)	0.006 (2.0%)
prompt production spectrum				0.003 (1.2%)
fit range variation	1 (0.1%)	18 (2.9%)	0.009 (2.9%)	0.009 (3.2%)
background shape variation	1 (0.1%)	12 (1.9%)	0.006 (1.9%)	0.006 (2.2%)
$J/\psi \rightarrow p\bar{p}\pi^0$ shape variation	1 (0.1%)	9 (1.4%)	0.005 (1.4%)	0.005 (1.7%)
cross-talk between prompt sample and sample from $b$ -hadron decays				0.009 (3.0%)
systematic uncertainty, quadratic sum	2 (0.2%)	26 (4.1%)	0.013 (4.1%)	0.016 (5.5%)

Table 4.9: Systematic uncertainties in the analysis of charmonium production in  $b$ -hadron decays using the 2011 data sample

	$n_{J/\psi}$	$n_{\eta_c}$	$\frac{n_{\eta_c}}{n_{J/\psi}}$	$\frac{N_{\eta_c}}{N_{J/\psi}}$
mean value	4110	1372	0.334	0.308
statistical uncertainty	94 (2.3%)	188 (13.7%)	0.047 (14.1%)	0.048 (15.5%)
signal resolution ratio (MC)	< 1 (< 0.1%)	24 (1.7%)	0.006 (1.8%)	0.006 (2.0%)
prompt production spectrum				0.004 (1.2%)
fit range variation	3 (0.1%)	39 (2.8%)	0.010 (2.9%)	0.010 (3.2%)
background shape variation	< 1 (< 0.1%)	8 (0.6%)	0.002 (0.6%)	0.002 (0.6%)
$J/\psi \rightarrow p\bar{p}\pi^0$ shape variation	< 1 (< 0.1%)	24 (1.7%)	0.006 (1.8%)	0.006 (2.0%)
cross-talk between prompt sample and sample from $b$ -hadron decays				0.008 (2.6%)
systematic uncertainty, quadratic sum	3 (0.1%)	53 (3.9%)	0.013 (3.9%)	0.015 (5.0%)

Table 4.10: Systematic uncertainties in the analysis of charmonium production in  $b$ -hadron decays using the 2012 data sample

The contribution to the  $p\bar{p}$  invariant mass spectrum from the  $J/\psi \rightarrow p\bar{p}\pi^0$  process is taken into account in the fit. This effect gives a correction of about 1% to the  $\eta_c$  yield. The  $J/\psi \rightarrow p\bar{p}\pi^0$  decay can proceed via  $p\pi^0$  or  $p\bar{p}$  resonances resulting in a modified  $p\bar{p}$  invariant mass spectrum shape. The corresponding uncertainty is thus conservatively estimated by replacing the square-root in equation (4.17) by a linear shape:

$$f_{J/\psi \rightarrow p\bar{p}\pi^0}(M) \sim \begin{cases} M_{J/\psi} - M_{\pi^0} - M & \text{if } M \leq M_{J/\psi} - M_{\pi^0} \\ 0 & \text{if } M > M_{J/\psi} - M_{\pi^0} \end{cases}, \quad (4.21)$$

where  $M$  is the proton-antiproton invariant mass. Uncertainties due to the description of the  $J/\psi \rightarrow p\bar{p}\pi^0$  component of the proton-antiproton mass spectrum were found to be about 2%.

## 4.8.2 Prompt charmonium production

Most of the systematic uncertainties for the prompt production analysis are estimated in the same way as for the analysis of the inclusive production from  $b$ -hadron decays, as described in subsection 4.8.1. Uncertainties related to the signal resolution, the  $\eta_c$  natural width, background description, description of the contribution from  $J/\psi \rightarrow p\bar{p}\pi^0$ , and the  $J/\psi$  polarisation, have been considered. Tables 4.11 and 4.12 summarise the systematic uncertainty estimates, for the 2011 and 2012 data samples respectively. The total systematic uncertainty is dominated by the uncertainty on the  $\eta_c$  natural width.

The uncertainty due to mass resolution ratios, fixed from MC, was estimated in the same way as in subsection 4.8.1, and was found to be 2.5 – 3.0%. The  $J/\psi$  resolution in the prompt production analysis fit is fixed to the value obtained from the fit of the  $p\bar{p}$  invariant mass spectrum in the  $b$ -hadron decay production analysis. We estimate the corresponding systematic uncertainty by varying it within error bounds. Uncertainties due to detector resolution are found to be around 0.5%.

Due to the dependence of the efficiency on the charmonium  $p_T$ , a potential difference of the  $\eta_c$  and  $J/\psi$  production spectrum can lead to the systematic shift of the yield ratio. The related systematic uncertainty was estimated by re-weighting each  $p\bar{p}$  combination using the corresponding efficiency, and subsequent renormalisation of the invariant mass spectrum in order that the average yields remain approximately unchanged. The resulting  $p\bar{p}$  invariant mass spectrum is shown on Fig. 4.16(a) and 4.16(b) for the 2011 and 2012 data respectively.

	$n_{J/\psi}$	$n_{\eta_c}$	$\frac{n_{\eta_c}}{n_{J/\psi}}$	$\frac{N_{\eta_c}}{N_{J/\psi}}$
mean value	11052	13370	1.21	1.24
statistical uncertainty	1004 (9.1%)	2260 (16.9%)	0.22 (18.2%)	0.21 (17.0%)
signal resolution ratio (MC)	10 (0.1%)	417 (3.1%)	0.04 (3.0%)	0.04 (3.0%)
signal resolution variation	138 (1.3%)	98 (0.7%)	0.01 (0.5%)	0.01 (0.5%)
prompt production spectrum			0.06 (5.0%)	0.07 (5.2%)
$\Gamma_{\eta_c}$ variation	60 (0.5%)	1743 (13.0%)	0.15 (12.4%)	0.15 (12.5%)
fit range variation	205 (1.9%)	830 (6.2%)	0.06 (5.2%)	0.06 (5.2%)
background shape variation	166 (1.5%)	695 (5.2%)	0.07 (5.5%)	0.07 (5.5%)
$J/\psi \rightarrow p\bar{p}\pi^0$ shape variation	49 (0.4%)	252 (1.9%)	0.02 (1.4%)	0.02 (1.4%)
cross-talk between prompt sample and sample from $b$ -hadron decays				0.01 (0.5%)
$J/\psi$ polarisation				0.02 (2.0%)
systematic uncertainty, quadratic sum	308 (2.8%)	2111 (15.8%)	0.19 (15.7%)	0.20 (15.9%)

Table 4.11: Systematic uncertainties for the prompt production analysis on the 2011 data

	$n_{J/\psi}$	$n_{\eta_c}$	$\frac{n_{\eta_c}}{n_{J/\psi}}$	$\frac{N_{\eta_c}}{N_{J/\psi}}$
mean value	20217	22416	1.11	1.14
statistical uncertainty	1403 (6.9%)	4072 (18.2%)	0.20 (18.1%)	0.21 (18.2%)
signal resolution ratio (MC)	41 (0.2%)	582 (2.6%)	0.03 (2.4%)	0.03 (2.4%)
signal resolution variation	306 (1.5%)	205 (0.9%)	0.01 (0.6%)	0.01 (0.6%)
prompt production spectrum			0.06 (5.0%)	0.06 (5.2%)
$\Gamma_{\eta_c}$ variation	125 (0.6%)	2821 (12.6%)	0.13 (11.9%)	0.14 (11.9%)
fit range variation	132 (0.7%)	1309 (5.8%)	0.06 (5.4%)	0.06 (5.4%)
background shape variation	303 (1.5%)	1166 (5.2%)	0.06 (5.5%)	0.06 (5.5%)
$J/\psi \rightarrow p\bar{p}\pi^0$ shape variation	144 (0.7%)	645 (2.9%)	0.02 (2.2%)	0.02 (2.2%)
cross-talk between prompt sample and sample from $b$ -hadron decays				0.01 (0.5%)
$J/\psi$ polarisation				0.02 (2.0%)
systematic uncertainty, quadratic sum	491 (2.4%)	3439 (15.3%)	0.17 (15.4%)	0.18 (15.6%)

Table 4.12: Systematic uncertainties for the prompt production analysis on the 2012 data

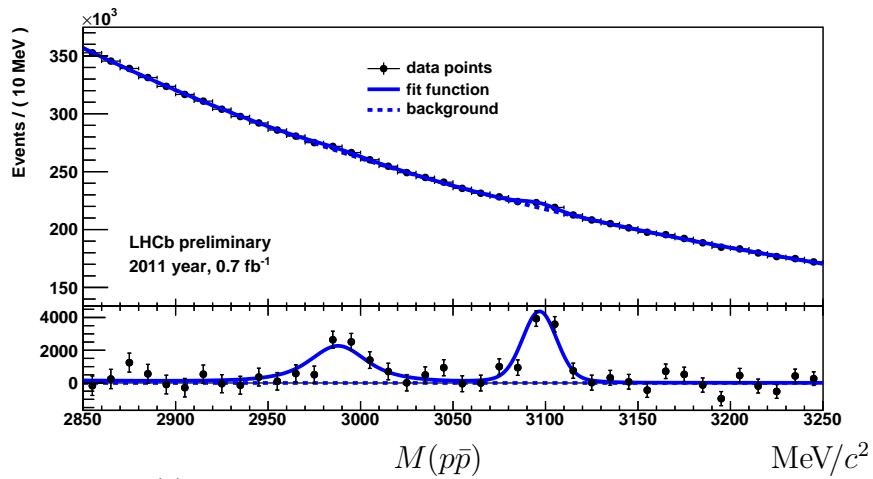
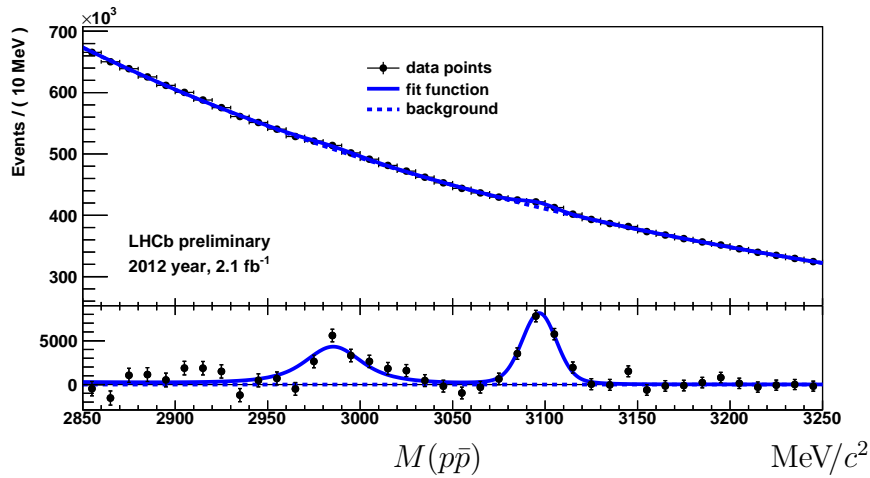
(a) The  $p\bar{p}$  invariant mass spectrum with 2011 data(b) The  $p\bar{p}$  invariant mass spectrum with 2012 data

Figure 4.16: Estimation of the systematic uncertainty from a potential charmonium spectrum difference at production. The  $p\bar{p}$  invariant mass spectrum is reweighted using the efficiency, as described in the text

Since the  $\sqrt{s}$  dependence of the effect is considered to be small, the average of the 2011 and 2012 samples is used to account for possible statistical fluctuations. The resulting uncertainty in  $\frac{N_{\eta_c}}{N_{J/\psi}}$  for the prompt production analysis was found to be 5.2% from the efficiency-weighted spectrum fit. The corresponding uncertainty for the analysis of charmonium production in  $b$ -hadron decays arises from the cross-talk between the prompt production sample and the sample of charmonium produced in  $b$ -hadron decays, and was estimated to be 1.2% (see section 4.8.1).

In order to estimate the systematic uncertainty related to the  $\Gamma_{\eta_c}$  knowledge, we compare the result using the  $\Gamma_{\eta_c}$  value of 25.8 MeV from the  $b$ -hadron decay analysis fit, to that using the  $\Gamma_{\eta_c}$  value of 32.0 MeV from the PDG [11]. The  $\Gamma_{\eta_c}$  values with their uncertainties are shown in Table 4.18. The corresponding uncertainty was estimated to be about 12%. This is the largest systematic uncertainty contribution.

The uncertainty of 5.5%, related to the background description, was obtained using an alternative shape. A third order polynomial multiplied by the exponential function was used. Also the sensitivity of the result to the fit range was studied, and a corresponding systematic uncertainty of 5.2 – 5.4% attributed. This uncertainty originates mainly from the variation of the left boundary of the fit, where trigger kinematic thresholds are close to the fit domain.

The uncertainty related to the shape of the  $p\bar{p}$  invariant mass spectrum from the  $J/\psi \rightarrow p\bar{p}\pi^0$  component is estimated in the same way as described in subsection 4.8.1, and was found to be 1 – 2%.

Uncertainty, associated to the cross-talk between the two samples, was estimated by varying the fit parameters in the analysis of the charmonium production in  $b$ -hadron decays, as well as by taking into account the systematic uncertainty on the event yields in the charmonium sample, produced in  $b$ -hadron decays. This contribution to the total systematic uncertainty was found to be small ( $< 0.1\%$ ) for both the 2011 and 2012 data samples. The uncertainty corresponding to the MC limited statistics, when normalising the cross-talk value, was found to be 0.5 % for both the 2011 and 2012 data samples. This value was taken as an estimate of the contribution to the total systematic uncertainty, associated to the cross-talk between the two samples.

Finally, the  $J/\psi$  polarisation modifies the kinematics of the proton and anti-proton, and thus influences the efficiency and relative  $\eta_c$  to  $J/\psi$  production. The central values of the LHCb  $J/\psi$  polarisation measurement [37] were used to correct the efficiency ratio, as described in section 4.5.2. The same  $J/\psi$  polarisation at  $\sqrt{s} = 7$  TeV and  $\sqrt{s} = 8$  TeV is assumed. The corresponding systematic uncertainty was estimated by

varying polarisation measurement results within error bounds, and has been found to be about 2% for both 2011 and 2012 data samples.

## 4.9 Results on the $\eta_c$ state production

Using the systematic uncertainties discussed in section 4.8.1, the  $\eta_c$  and  $J/\psi$  event yields and their ratio, from the analysis of charmonium production in  $b$ -hadron decays (section 4.6) are found to be:

$$\begin{aligned} (n_{J/\psi}^S)_{2011} &= 2000 \pm 67_{stat} \pm 2_{syst} \\ (n_{\eta_c}^S)_{2011} &= 645 \pm 133_{stat} \pm 26_{syst} \\ (n_{\eta_c}^S/n_{J/\psi}^S)_{2011} &= 0.323 \pm 0.068_{stat} \pm 0.013_{syst} \end{aligned}$$

for the 2011 data sample, and

$$\begin{aligned} (n_{J/\psi}^S)_{2012} &= 4110 \pm 94_{stat} \pm 3_{syst} \\ (n_{\eta_c}^S)_{2012} &= 1372 \pm 188_{stat} \pm 53_{syst} \\ (n_{\eta_c}^S/n_{J/\psi}^S)_{2012} &= 0.334 \pm 0.047_{stat} \pm 0.013_{syst} \end{aligned}$$

for the 2012 data sample.

Using the systematic uncertainties discussed in section 4.8.2, the  $\eta_c$  and  $J/\psi$  event yields and their ratio, from the prompt charmonium production analysis (section 4.7) are found to be:

$$\begin{aligned} (n_{J/\psi}^P)_{2011} &= 11052 \pm 1004_{stat} \pm 316_{syst} \\ (n_{\eta_c}^P)_{2011} &= 13370 \pm 2260_{stat} \pm 2096_{syst} \\ (n_{\eta_c}^P/n_{J/\psi}^P)_{2011} &= 1.21 \pm 0.22_{stat} \pm 0.19_{syst} \end{aligned}$$

for the 2011 data sample, and

$$\begin{aligned} (n_{J/\psi}^P)_{2012} &= 20217 \pm 1403_{stat} \pm 491_{syst} \\ (n_{\eta_c}^P)_{2012} &= 22416 \pm 4072_{stat} \pm 3439_{syst} \\ (n_{\eta_c}^P/n_{J/\psi}^P)_{2012} &= 1.11 \pm 0.20_{stat} \pm 0.17_{syst} \end{aligned}$$

for the 2012 data sample.

Following section 4.5, the ratios of the charmonium states, produced in the inclusive  $b$ -hadron decays, and decaying to  $p\bar{p}$ , are:

$$\left(N_{\eta_c}^S/N_{J/\psi}^S\right)_{2011} = 0.289 \pm 0.069_{stat} \pm 0.016_{syst}$$

for the 2011 data sample, and

$$\left(N_{\eta_c}^S/N_{J/\psi}^S\right)_{2012} = 0.308 \pm 0.048_{stat} \pm 0.015_{syst}$$

for the 2012 data sample.

The bf ratios of the promptly produced charmonium states are:

$$\left(N_{\eta_c}^P/N_{J/\psi}^P\right)_{2011} = 1.24 \pm 0.21_{stat} \pm 0.20_{syst}$$

for the 2011 data sample, and

$$\left(N_{\eta_c}^P/N_{J/\psi}^P\right)_{2012} = 1.14 \pm 0.21_{stat} \pm 0.18_{syst}$$

for the 2012 data sample.

The  $\eta_c$  to  $J/\psi$  yield ratio as measured in the analysis of inclusive charmonium production in  $b$ -hadron decays, using the 2011 and 2012 data samples agree, and can be averaged. Assuming systematic uncertainties to be fully correlated:

$$N_{\eta_c}^S/N_{J/\psi}^S = 0.302 \pm 0.039_{stat} \pm 0.015_{syst} .$$

#### 4.9.1 Ratios of the inclusive yield from $b$ -hadron decays

Correcting for the ratio of the branching fractions, the relative  $\eta_c$  to  $J/\psi$  branching fraction of a mixture of  $b$ -hadrons is:

$$\mathcal{B}_{b \rightarrow \eta_c X} / \mathcal{B}_{b \rightarrow J/\psi X} = \frac{N_{\eta_c}^S}{N_{J/\psi}^S} \times \frac{\mathcal{B}_{J/\psi \rightarrow p\bar{p}}}{\mathcal{B}_{\eta_c \rightarrow p\bar{p}}} . \quad (4.22)$$

Using the branching fractions from Ref. [11],  $\mathcal{B}_{J/\psi \rightarrow p\bar{p}} = (2.17 \pm 0.07) \times 10^{-3}$  and  $\mathcal{B}_{\eta_c \rightarrow p\bar{p}} = (1.42 \pm 0.17) \times 10^{-3}$ , inclusive yield from  $b$ -hadron decays in the phase space volume

$p_T > 6.5 \text{ GeV}/c$ ,  $2.0 < y < 4.5$  is:

$$\mathcal{B}_{b \rightarrow \eta_c X} / \mathcal{B}_{b \rightarrow J/\psi X} = 0.421 \pm 0.055_{stat} \pm 0.022_{syst} \pm 0.045 \mathcal{B}_{J/\psi \rightarrow p\bar{p}, \eta_c \rightarrow p\bar{p}} ,$$

where the third error component corresponds to the uncertainty in the  $J/\psi \rightarrow p\bar{p}$  and  $\eta_c \rightarrow p\bar{p}$  branching fraction measurements. Using in addition the measured  $J/\psi$  inclusive yield from  $b$ -hadron decays [11],  $\mathcal{B}_{b \rightarrow J/\psi X} = (1.16 \pm 0.10)\%$ , one obtains the inclusive yield of  $\eta_c$  from  $b$ -hadron decays for our phase space volume as:

$$\mathcal{B}_{b \rightarrow \eta_c X} = (4.88 \pm 0.64_{stat} \pm 0.25_{syst} \pm 0.67 \mathcal{B}_{J/\psi \rightarrow p\bar{p}, \eta_c \rightarrow p\bar{p}}) \times 10^{-3} ,$$

where the third error component corresponds to the uncertainty in the  $J/\psi \rightarrow p\bar{p}$  and  $\eta_c \rightarrow p\bar{p}$  branching fractions and the  $J/\psi$  inclusive yield from  $b$ -hadron decays measurements.

This is the first measurement of the  $\eta_c$  inclusive yield from  $b$ -hadron decays. The measurement can be further improved by increasing statistics, and by motivating the BES collaboration to provide a relative measurement of the two branching fractions  $\mathcal{B}_{J/\psi \rightarrow p\bar{p}}$  to  $\mathcal{B}_{\eta_c \rightarrow p\bar{p}}$ .

## 4.9.2 Prompt production ratios

Correcting for the ratio of the branching fractions, the relative  $\eta_c$  to  $J/\psi$  prompt production is

$$\sigma_{\eta_c} / \sigma_{J/\psi} = \frac{N_{\eta_c}^P}{N_{J/\psi}^P} \times \frac{\mathcal{B}_{J/\psi \rightarrow p\bar{p}}}{\mathcal{B}_{\eta_c \rightarrow p\bar{p}}} . \quad (4.23)$$

Using the branching fractions from Ref. [11], the relative  $\eta_c$  to  $J/\psi$  prompt production in the LHCb acceptance (rapidity range  $2.0 < y < 4.5$ ) and for  $p_T(J/\psi, \eta_c) > 6.5 \text{ GeV}/c$  is found to be:

$$(\sigma_{\eta_c} / \sigma_{J/\psi})_{2011} = 1.74 \pm 0.29_{stat} \pm 0.28_{syst} \pm 0.19 \mathcal{B}_{J/\psi \rightarrow p\bar{p}, \eta_c \rightarrow p\bar{p}}$$

for the 2011 data sample, corresponding to a centre-of-mass energy  $\sqrt{s} = 7 \text{ TeV}$ , and

$$(\sigma_{\eta_c} / \sigma_{J/\psi})_{2012} = 1.60 \pm 0.29_{stat} \pm 0.25_{syst} \pm 0.17 \mathcal{B}_{J/\psi \rightarrow p\bar{p}, \eta_c \rightarrow p\bar{p}}$$

for the 2012 data sample, corresponding to a centre-of-mass energy  $\sqrt{s} = 8$  TeV. The third error component in the above results corresponds to the uncertainty in the  $J/\psi \rightarrow p\bar{p}$  and  $\eta_c \rightarrow p\bar{p}$  branching fractions.

### 4.9.3 $J/\psi$ production cross-section in the required kinematic region

The  $J/\psi$  cross section is needed as an input to compute the absolute  $\eta_c$  prompt production cross section from the ratio measured in this note. The  $J/\psi$  cross section results from Refs. [37] and [50] are shown in Tables 1 and 3 in Appendix .2 in bins of  $p_T$  and rapidity, also summed up over the LHCb rapidity range, for  $\sqrt{s} = 7$  TeV and  $\sqrt{s} = 8$  TeV respectively.

The results below will assume no polarisation for the  $J/\psi$  production, so that the last column of the Tables 1 and 3 is not used.

Since the data from Ref. [37] in Table 1 (see Appendix .2) have been luminosity and polarisation corrected, they are modified in Table 2, using Refs. [37] and [49], and Analysis note ANA-2013-019, in order to keep only the luminosity correction. The luminosity correction was extracted from  $\sigma/\sigma_{corrected} = 5.2$  pb/5.491 pb  $\approx 0.947$ . The relative systematic uncertainty, excluding the contribution from polarisation, was assumed to be the same. Both central bin values and uncertainties have been corrected.

The  $J/\psi$  cross section is found as the sum of the  $p_T$  bin values, multiplied by the bin width ( $\Delta y = 0.5$ ,  $\Delta p_T = 1$  GeV/ $c$ ). Since the transverse momentum range considered is from 6.5 GeV/ $c$  to 14.0 GeV/ $c$ , the first bin (6.0 GeV/ $c$  to 7.0 GeV/ $c$ ) from the  $J/\psi$  analysis requires special treatment. The  $J/\psi$  cross section for the 6.5 GeV/ $c$  to 7.0 GeV/ $c$  interval is extracted as a part of the 6.0 GeV/ $c$  to 7.0 GeV/ $c$  bin cross section using the  $J/\psi$  cross section interpolation, illustrated on Fig. 4.17(a) and 4.17(b) for the 2011 and 2012 data respectively.

The  $J/\psi$  cross section in the 6.5 GeV/ $c$  to 7.0 GeV/ $c$  interval was found to be

$$\begin{aligned} \sigma_{J/\psi}^{6.5 \text{ GeV}/c < p_T < 7.0 \text{ GeV}/c} &= 77.6 \pm 0.9_{stat} \pm 4.0_{syst} \pm 0.5_{interpolation} \text{ nb} \\ &= 77.6 \pm 0.9_{stat} \pm 4.0_{syst} \text{ nb} \end{aligned}$$

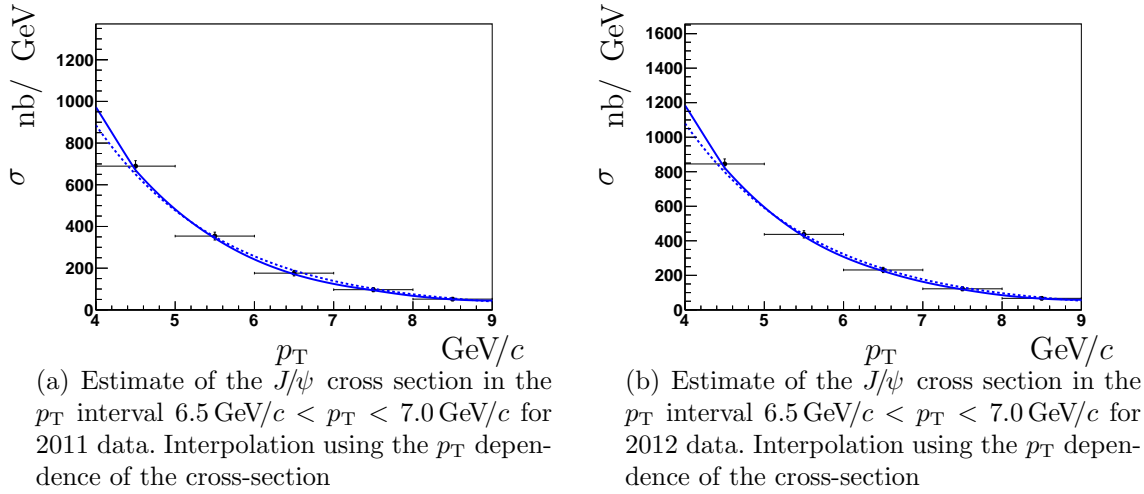


Figure 4.17: Estimate of the  $J/\psi$  cross section in the  $p_T$  interval  $6.5 \text{ GeV}/c < p_T < 7.0 \text{ GeV}/c$  for the 2011 and 2012 data. Interpolation (third order polinomial, solid line) and fit with the exponential function (dashed line) to estimate corresponding systematic uncertainty

for the centre-of-mass energy  $\sqrt{s} = 7 \text{ TeV}$ , and

$$\begin{aligned} \sigma_{J/\psi}^{6.5 \text{ GeV}/c < p_T < 7.0 \text{ GeV}/c} &= 97.5 \pm 0.8_{stat} \pm 1.8_{syst} \pm 0.3_{interpolation} \text{ nb} \\ &= 97.5 \pm 0.8_{stat} \pm 1.8_{syst} \text{ nb} \end{aligned}$$

for the centre-of-mass energy  $\sqrt{s} = 8 \text{ TeV}$ . The interpolation error in the first bin was conservatively estimated by comparing the interpolation to the fit using an exponential function.

The  $J/\psi$  cross section in the  $p_T$  bins is shown in Table 4.13, before summing the values.

Then both statistical and correlated (uncorrelated) uncertainties in the  $J/\psi$  cross section are summed up quadratically. The resulting value is propagated to the  $\sigma_{n_c}$  uncertainty and noted as the fourth error after statistical, systematic uncertainties and the uncertainty from branching fractions.

The  $J/\psi$  cross-sections in the rapidity and  $p_T$  range,  $2.0 < y < 4.5$  and  $p_T$  ( $J/\psi$ ,

$p_T$ , GeV/ $c$	7 TeV			8 TeV		
	cross section	stat. error	syst. error	cross section	stat. error	syst. error
6.5-7	77.6	0.9	4.0	97.5	0.8	4.8
7-8	99.9	1.0	3.3	121.9	0.8	1.4
8-9	54.6	0.9	1.7	66.7	0.6	1.2
9-10	29.2	0.5	0.9	37.2	0.4	0.6
10-11	17.2	0.4	0.6	21.9	0.3	0.3
11-12	9.3	0.3	0.3	13.1	0.2	0.2
12-13	5.8	0.2	0.2	8.1	0.2	0.1
13-14	3.2	0.2	0.1	5.1	0.1	0.1

Table 4.13: The  $J/\psi$  cross section integrated over rapidity range,  $2.0 < y < 4.5$ , in  $p_T$  bins, the  $\sqrt{s} = 7$  TeV and 8 TeV data

$\eta_c$ )  $> 6.5$  GeV/ $c$ , corresponding to the present analysis, are:

$$\begin{aligned}\sigma_{J/\psi} &= 296.9 \pm 1.8_{stat} \pm 16.8_{syst} \text{ nb} \\ &= 296.9 \pm 16.9 \text{ nb}\end{aligned}$$

for the centre-of-mass energy  $\sqrt{s} = 7$  TeV, and

$$\begin{aligned}\sigma_{J/\psi} &= 371.4 \pm 1.4_{stat} \pm 27.1_{syst} \text{ nb} \\ &= 371.4 \pm 27.2 \text{ nb}\end{aligned}$$

for the centre-of-mass energy  $\sqrt{s} = 8$  TeV, where the first error is statistical, and the second one is systematic, and both are quadratically added at the end. This combined error is considered as a systematic error for the absolute  $\eta_c$  production cross section calculation. The  $J/\psi$  production is assumed to be unpolarised.

It is assumed that there is no significant correlation with other systematic effects.

Table 4.14 shows the sources of systematic uncertainty considered in the  $J/\psi$  cross section measurement analyses.

The present analysis comprises no systematic uncertainties associated with muon reconstruction or identification. Other sources of systematic uncertainties, present in Table 4.14, effectively cancel in the production ratio measurements, so that we consider the  $J/\psi$  production measurement systematic uncertainty and other systematic uncertainties of the present analysis to be uncorrelated.

source	systematic uncertainty	
	2011	2012
inter-bin cross-feed	0.5%	0.5%
mass fits	1.0%	2.2%
radiative tail	1.0%	1.0%
muon identification	1.1%	1.3%
tracking efficiency	8.0%	0.9%
track $\chi^2$	1.0%	
vertexing	0.8%	1.0%
trigger	1.7% to 4.5%	4.0%
luminosity	10.0%	5.0%
$\mathcal{B}_{J/\psi \rightarrow \mu^+ \mu^-}$	1.0%	1.0%

Table 4.14: Systematic uncertainty of the  $J/\psi$  cross section measurements for the  $\sqrt{s} = 7$  TeV and  $\sqrt{s} = 8$  TeV analyses

#### 4.9.4 $\eta_c$ production cross-section

In order to obtain the absolute  $\eta_c$  prompt production cross-section, the corresponding  $J/\psi$  prompt production cross section measurement from Refs. [37] and [50] were used for the analyses corresponding to a centre-of-mass energy of  $\sqrt{s} = 7$  TeV and  $\sqrt{s} = 8$  TeV respectively. The  $J/\psi$  cross section measured in section 4.9.3, yields the following  $J/\psi$  cross section values in the rapidity and  $p_T$  range,  $2.0 < y < 4.5$  and  $p_T (J/\psi, \eta_c) > 6.5$  GeV/c, corresponding to the present analysis:

$$(\sigma_{J/\psi})_{7\text{ TeV } 2.0 < y < 4.5 \ p_T > 6.5 \text{ GeV}/c} = 296.9 \pm 1.8 \pm 16.8 \text{ nb}$$

for a centre-of-mass energy  $\sqrt{s} = 7$  TeV, and

$$(\sigma_{J/\psi})_{8\text{ TeV } 2.0 < y < 4.5 \ p_T > 6.5 \text{ GeV}/c} = 371.4 \pm 1.4 \pm 27.2 \text{ nb}$$

for a centre-of-mass energy  $\sqrt{s} = 8$  TeV. Here, we assume the  $J/\psi$  to be produced unpolarised.

Using the above values for the  $J/\psi$  cross section ( $2.0 < y < 4.5$  and  $p_T (J/\psi, \eta_c) > 6.5$  GeV/c), the prompt  $\eta_c$  production cross section is obtained as:

$$\begin{aligned} (\sigma_{\eta_c})_{7\text{ TeV}} &= 0.52 \pm 0.09_{stat} \pm 0.08_{syst} \pm 0.06_{\mathcal{B}_{J/\psi \rightarrow p\bar{p}, \eta_c \rightarrow p\bar{p}}} \pm 0.03_{\sigma_{J/\psi}} \mu\text{b} \\ &= 0.52 \pm 0.09_{stat} \pm 0.08_{syst} \pm 0.06_{\sigma_{J/\psi}, \mathcal{B}_{J/\psi \rightarrow p\bar{p}, \eta_c \rightarrow p\bar{p}}} \mu\text{b} \end{aligned}$$

for a centre-of-mass energy  $\sqrt{s} = 7$  TeV, and

$$\begin{aligned} (\sigma_{\eta_c})_{8\text{TeV}} &= 0.59 \pm 0.11_{stat} \pm 0.09_{syst} \pm 0.06_{\mathcal{B}_{J/\psi \rightarrow p\bar{p}, \eta_c \rightarrow p\bar{p}}} \pm 0.04_{\sigma_{J/\psi}} \mu\text{b} \\ &= 0.59 \pm 0.11_{stat} \pm 0.09_{syst} \pm 0.08_{\sigma_{J/\psi}, \mathcal{B}_{J/\psi \rightarrow p\bar{p}, \eta_c \rightarrow p\bar{p}}} \mu\text{b} \end{aligned}$$

for a centre-of-mass energy  $\sqrt{s} = 8$  TeV. In the above results, uncertainties associated to the  $J/\psi \rightarrow p\bar{p}$  and  $\eta_c \rightarrow p\bar{p}$  branching fractions, and to the  $J/\psi$  cross section measurement, are first shown separately, and then combined (added quadratically) into the last error component. Within the  $\sigma_{J/\psi}$  uncertainty, the statistical uncertainty of the  $J/\psi$  cross section measurement contributes 0.003 for the  $\sqrt{s} = 7$  TeV result, and 0.002 for the  $\sqrt{s} = 8$  TeV result.

#### 4.9.5 Dependence of the $J/\psi$ and $\eta_c$ production cross-section on transverse momentum

The rate of  $\eta_c$  relative to  $J/\psi$ , as a function of  $p_T$ , has been obtained by fitting the  $p\bar{p}$  invariant mass spectrum in three of four bins of  $p_T$ . Fig. 4.18 shows the results for both prompt charmonium production and inclusive charmonium production in  $b$ -hadron decays, for the 2011 and 2012 data samples separately.

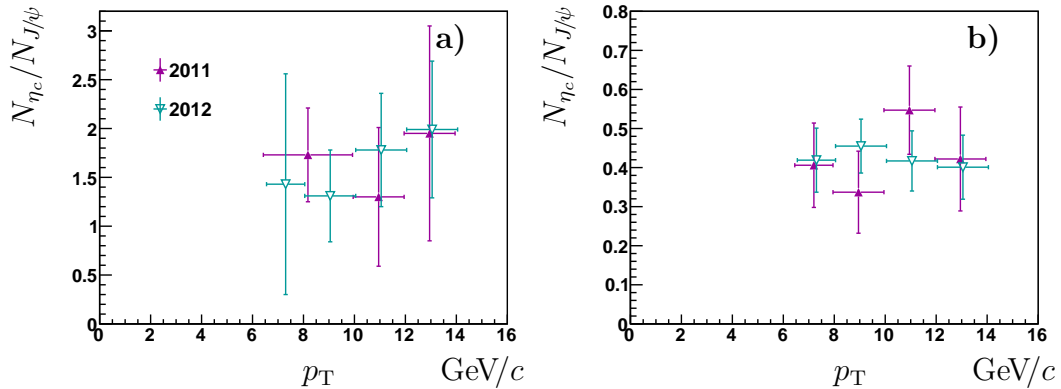


Figure 4.18: The relative  $\eta_c$  to  $J/\psi$   $p_T$  spectrum for the 2011 (filled triangles) and 2012 (empty triangles) data. Prompt production spectra are shown on a) and b) for the prompt charmonium production and inclusive charmonium production in  $b$ -hadron decays, respectively. See the text for more details

Using the  $J/\psi$   $p_T$  spectrum from Refs. [49, 37, 50], the  $\eta_c$   $p_T$  spectrum has been obtained for both prompt charmonium production and inclusive charmonium production in  $b$ -hadron decays. The results are shown on Fig. 4.19.

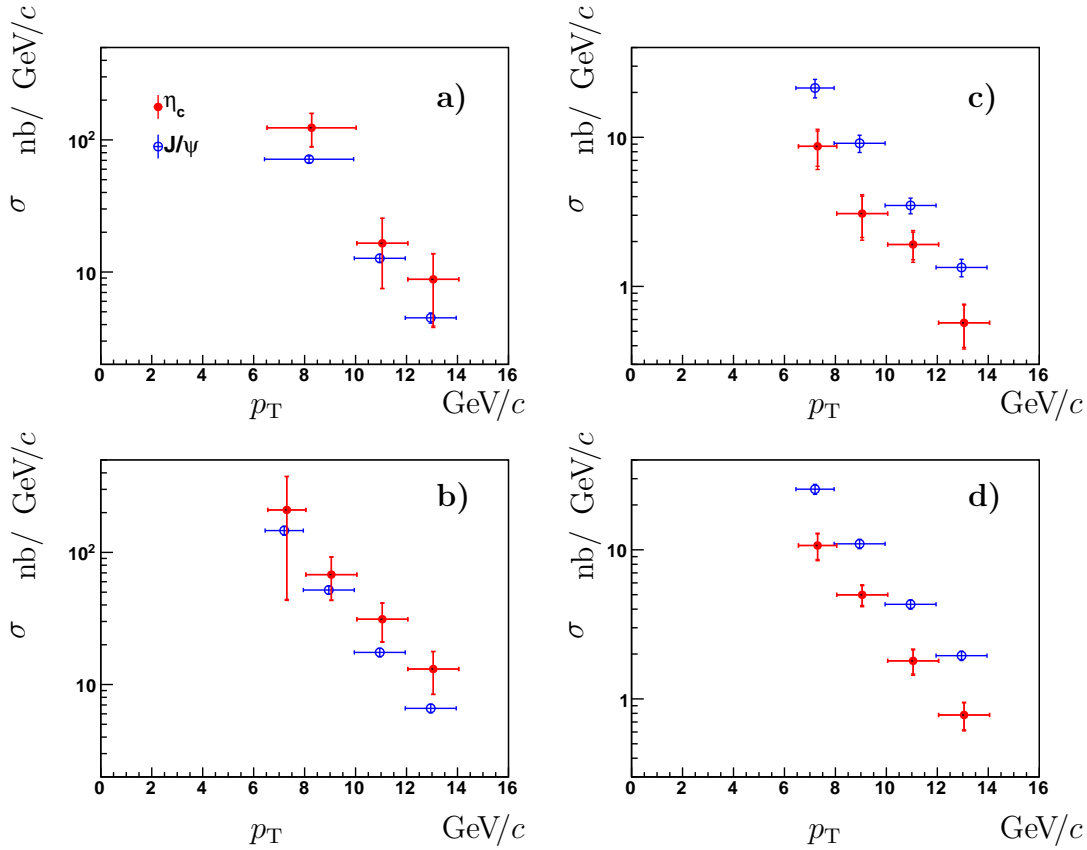


Figure 4.19: The  $p_T$  spectrum for  $\eta_c$  (empty circles) from the present analysis and  $J/\psi$  (filled circles) from Refs. [49, 37, 50]. Prompt production spectra are shown on a) and b) for the 2011 and 2012 data respectively. The spectra, corresponding to inclusive charmonium production in  $b$ -hadron decays, are shown on c) and d) for the 2011 and 2012 data respectively. See the text for more details

Also the results can be compared with those from the MC simulation (Fig. 4.20).

#### 4.9.6 Summary

The prompt  $\eta_c$  production at  $\sqrt{s} = 7$  TeV and at  $\sqrt{s} = 8$  TeV centre-of-mass energy are measured for the first time. Finally the results obtained on the  $\eta_c$  prompt production at  $\sqrt{s} = 7$  TeV and  $\sqrt{s} = 8$  TeV centre-of-mass energy in the LHCb acceptance (rapidity range  $2.0 < y < 4.5$ ) for  $p_T(J/\psi) > 6.5$  GeV/ $c$ , are shown on Fig. 4.21 with the statistical and systematic uncertainties, and the error related to the uncertainty on the  $J/\psi \rightarrow p\bar{p}$  and  $\eta_c \rightarrow p\bar{p}$  branching fractions, shown separately. The error associated to the  $J/\psi$  cross section measurement is included in the systematic error.

The  $J/\psi$  production cross section at  $\sqrt{s} = 7$  TeV was measured using the 2010

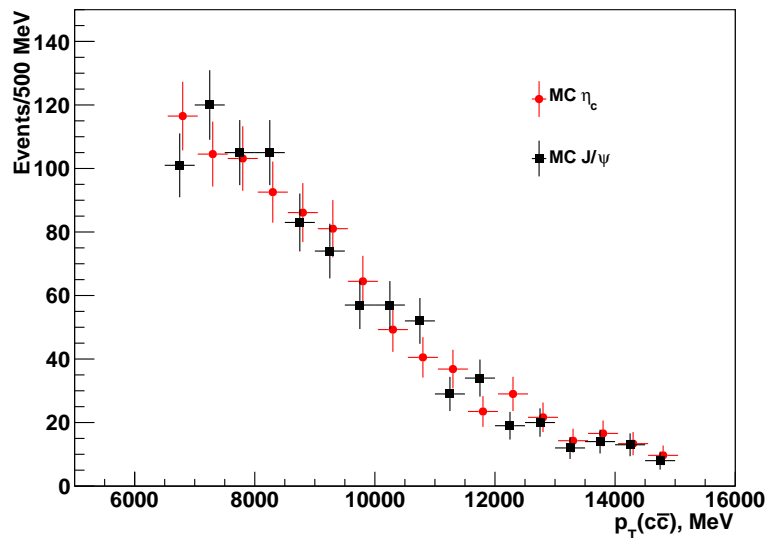
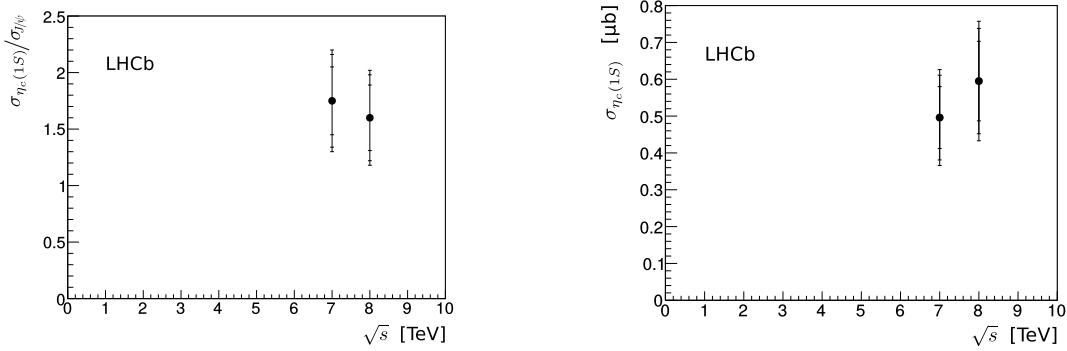


Figure 4.20: MC reconstructed  $p_T$  spectra for promptly produced  $J/\psi$  (squares) and  $\eta_c$  (circles)

data sample [37], while the production cross section ratio was obtained using the independent 2011 data sample. Therefore, the statistical errors of the two measurements are independent, and the statistical uncertainty of the  $J/\psi$  cross section measurement is added in quadrature to the systematic uncertainty related to the  $J/\psi$  cross section measurement.

The  $J/\psi$  production cross section at  $\sqrt{s} = 8$  TeV was measured using  $16 \text{ pb}^{-1}$  at the beginning of data taking in 2012 [50]. This is a part of the  $2.0 \text{ fb}^{-1}$  data sample used for the production cross section ratio measurement at a centre-of-mass energy  $\sqrt{s} = 8$  TeV. However, both analyses used TOS of the different and independent trigger lines, so that both data samples can be considered as independent. Moreover, their overlap is negligible, which is illustrated by the fact that, using the full 2011 year statistics, trigger TOS of the present analysis and at the same time TOS of the di-muon trigger yield only 257 events in the  $p\bar{p}$  invariant mass fit range, compared to  $9.5 \times 10^6$  trigger TOS of the present analysis. Using the full 2012 year statistics, trigger TOS of the present analysis and at the same time TOS of the di-muon trigger yield only 491 events, compared to  $18.2 \times 10^6$  trigger TOS of the present analysis. In both cases, the fraction of overlap events is  $2.7 \times 10^{-5}$ , even if considered both measurements using full statistics. Thus, for the centre-of-mass energy  $\sqrt{s} = 8$  TeV analysis, the production cross section ratio and  $J/\psi$  cross section measurement always rely on different candidates, neglecting muon-



(a) Relative  $\eta_c$  to  $J/\psi$  prompt production cross-section. The errors shown are statistical, systematic, and the error corresponding to the uncertainty in the  $J/\psi \rightarrow p\bar{p}$  and  $\eta_c \rightarrow p\bar{p}$  branching fractions

(b) The  $\eta_c$  prompt production cross-section. The errors shown are statistical, systematic, and the error corresponding to the uncertainty in the  $J/\psi \rightarrow p\bar{p}$  and  $\eta_c \rightarrow p\bar{p}$  branching fractions. The error on the  $J/\psi$  cross section measurement is included in the systematic uncertainty

Figure 4.21: Prompt  $\eta_c$  production cross-section

proton mis-identification, have  $2.7 \times 10^{-5}$  overlap between the events (not candidates) for  $16 \text{ pb}^{-1}$ , and no overlap for the remaining part of the  $2.0 \text{ fb}^{-1}$  data sample. Therefore, similar to the  $\sqrt{s} = 7 \text{ TeV}$  analysis, the statistical uncertainty of the  $J/\psi$  cross section measurement is added in quadrature to the systematic uncertainty related to the  $J/\psi$  cross section measurement.

In the above results, statistical and systematic uncertainty of the  $J/\psi$  cross section measurements are first shown separately, and then combined (added quadratically) into the  $\sigma_{J/\psi}$  uncertainty component.

Systematic uncertainties for the analysis of the production cross section ratio and the  $J/\psi$  cross section measurements are considered to be uncorrelated (different sources of systematic uncertainty in Tables 4.11 and 4.12, and Table 4.14 in section 4.9.3).

## 4.10 The $\eta_c$ and $J/\psi$ angular distributions

Emi Kou suggested that it may be possible to probe the  $J/\psi \rightarrow p\bar{p}$  decay mechanism using observed angular distributions. A comparison between the  $J/\psi \rightarrow p\bar{p}$  and  $\eta_c \rightarrow p\bar{p}$  decays, mediated by three and two gluon decay diagram, respectively (see section 1.6), may yield additional information. A sensitivity to angular distributions is illustrated below by the angle between the proton momentum in the  $J/\psi$  rest frame and the  $J/\psi$

boost, as an example.

The study is performed in the kinematic region  $2 < y < 4.5$  and  $6.5 \text{ GeV}/c < p_T$ . Combined data set of low background charmonium candidates from  $b$ -hadron decays, corresponding to the integrated luminosity of  $\int \mathcal{L} dt = 2.7 \text{ fb}$  and collected in 2011 and 2012 years data samples are used.

The  $\eta_c$  and  $J/\psi$  signals are extracted from the fit of the  $p\bar{p}$  invariant mass spectrum in bins of  $\cos \theta$ . The  $\cos \theta$  range is divided in five bins that allows to maintain statistically significant  $\eta_c$  signal in each bin. The results of the fit are shown on Fig. 4.22.

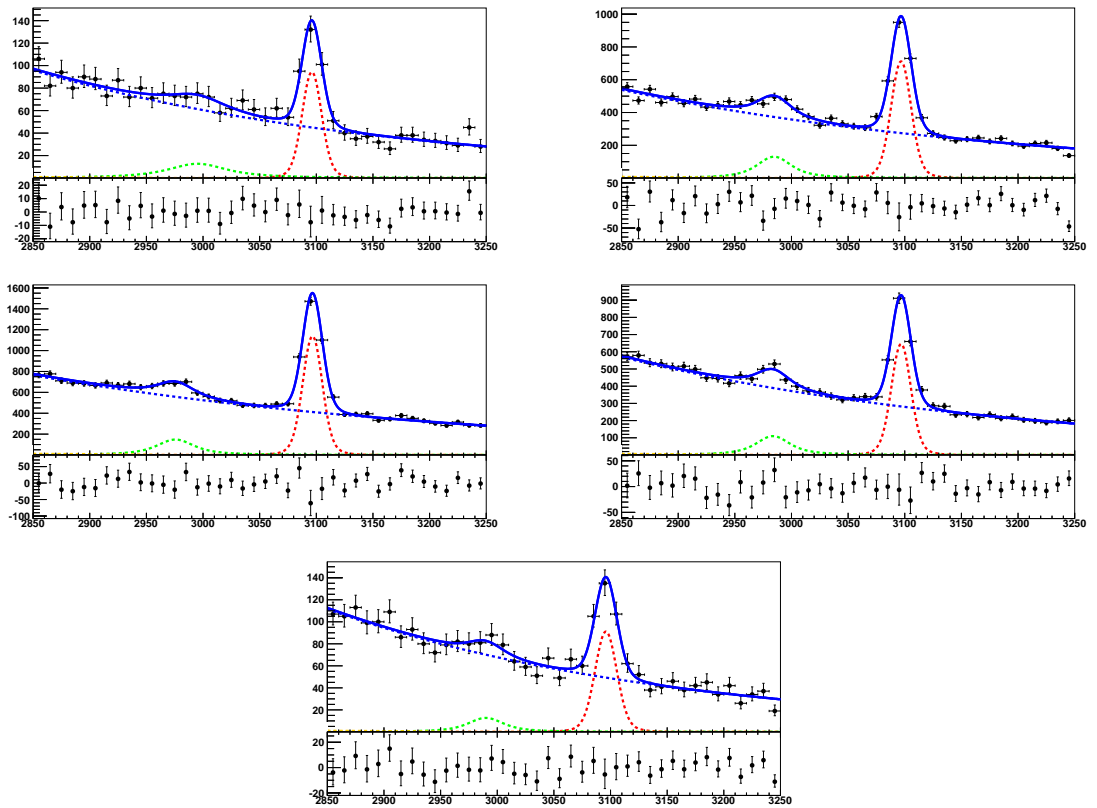


Figure 4.22: Invariant mass spectrum of the  $p\bar{p}$  combinations in bins of  $\cos \theta$ . Selection on  $\cos \theta$  applied, left to right, top to bottom:  $-1.0 < \cos \theta < -0.6$ ,  $-0.6 < \cos \theta < -0.6$ ,  $-0.2 < \cos \theta < 0.2$ ,  $0.2 < \cos \theta < 0.6$ ,  $0.6 < \cos \theta < 1.0$

No angular dependence is expected for the  $\eta_c \rightarrow p\bar{p}$  decay. The  $\cos \theta$  dependence for the  $J/\psi \rightarrow p\bar{p}$  decay is expected to be small due to the significant boost. No acceptance corrections are applied to the  $\cos \theta$  distributions. Consistent angular distributions corresponding to the  $\eta_c$  and  $J/\psi$  decays are expected. Uncertainties in the  $\cos \theta$  bins illustrate expected sensitivity of angular distribution studies.

The obtained distributions in  $\cos \theta$  are fitted with the following probability density

function:

$$f(\theta) \sim 1 + a_{\eta_c, J/\psi} \cos^2 \theta. \quad (4.24)$$

The results of the fit are shown on Figs. 4.23 and 4.24 for the  $\eta_c$  and  $J/\psi$  meson angular distributions, respectively.

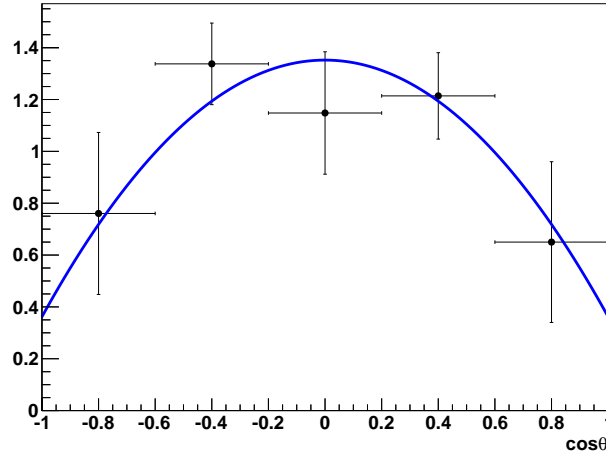


Figure 4.23: Fit of the  $\cos \theta$  distribution of for  $\eta_c \rightarrow p\bar{p}$  candidates

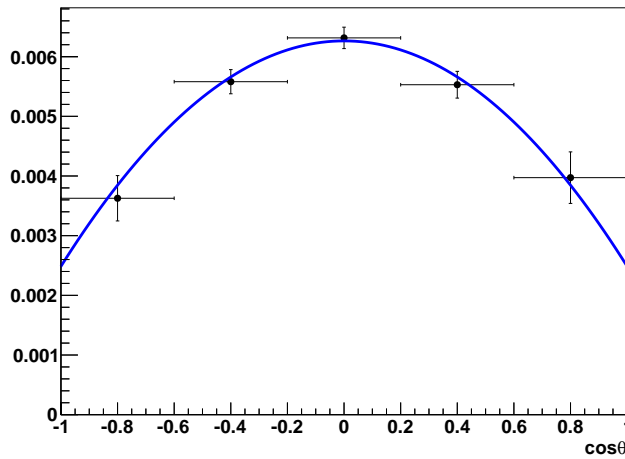


Figure 4.24: Fit of the  $\cos \theta$  distribution of for  $J/\psi \rightarrow p\bar{p}$  candidates

The  $a$  parameters are found to be

$$a_{\eta_c} = -0.73 \pm 0.22$$

$$a_{J/\psi} = -0.60 \pm 0.05,$$

for  $\eta_c$  and  $J/\psi$  spectra, respectively. Note that negative  $a$  values do not mean a signature of the  $\eta_c$  or  $J/\psi$  polarisation.

## 4.11 Measurement of the $\eta_c$ mass and natural width

Using the cleaner sample of charmonium candidates, produced in  $b$ -hadron decays, a measurement of the  $\eta_c$  mass can be addressed relative to the well-reconstructed  $J/\psi$  mass peak. Momentum scale calibration is particularly important for the mass measurement. Systematic uncertainty is further reduced for the measurement of the  $J/\psi$  and  $\eta_c$  mass difference,  $\Delta M_{J/\psi, \eta_c} = M_{J/\psi} - M_{\eta_c}$ . Analysis of the two data samples yields consistent results,

$$\Delta M_{J/\psi, \eta_c}^{2011} = 113.1 \pm 2.4 \pm 0.2 \text{ MeV}/c^2$$

and

$$\Delta M_{J/\psi, \eta_c}^{2012} = 115.8 \pm 1.9 \pm 0.2 \text{ MeV}/c^2$$

for the 2011 and 2012 data respectively. Table 4.15 summarises the corresponding systematic uncertainty estimates, for the 2011 and 2012 data samples.

	2011 data sample	2012 data sample
mean value	113.1	115.8
statistical uncertainty	2.4	1.9
signal resolution ratio (MC)	0.07	0.03
fit range variation	0.07	0.08
background shape variation	0.04	0.03
$J/\psi \rightarrow p\bar{p}\pi^0$ shape variation	0.10	0.18
systematic uncertainty, quadratic sum	0.15	0.20

Table 4.15: Systematic uncertainties (in  $\text{MeV}/c^2$ ) for the measurement of the  $J/\psi$  and  $\eta_c$  mass difference,  $\Delta M_{J/\psi, \eta_c} = M_{J/\psi} - M_{\eta_c}$ , using the 2011 and 2012 data samples

The systematic uncertainty is significantly smaller than statistical errors, so that increasing statistics will improve the measurement precision. The two measurements agree with each other and can be averaged:

$$\Delta M_{J/\psi, \eta_c} = 114.7 \pm 1.5 \pm 0.1 \text{ MeV}/c^2 .$$

This result agrees with the PDG value [11]. The precision improves that of the latest  $B$ -factory measurements, and provides an independent check of the recent BES results [75,

76].

As a further indication of the systematic uncertainty related to the momentum scale calibration, the  $J/\psi$  mass value is determined from the fit of the  $p\bar{p}$  invariant mass spectrum for the 2011 and 2012 data samples,  $M_{J/\psi} = 3096.50 \pm 0.34 \pm 0.03 \text{ MeV}/c^2$  and  $M_{J/\psi} = 3096.74 \pm 0.23 \pm 0.02 \text{ MeV}/c^2$  respectively. The systematic uncertainty is estimated to be small, and details are given in Table 4.16.

	2011 data sample	2012 data sample
mean value	3096.50	3096.74
statistical uncertainty	0.34	0.23
signal resolution ratio (MC)	0.02	0.01
fit range variation	0.01	0.01
background shape variation	0.02	0.01
$J/\psi \rightarrow p\bar{p}\pi^0$ shape variation	< 0.01	0.01
systematic uncertainty, quadratic sum	0.03	0.02

Table 4.16: Systematic uncertainties (in  $\text{MeV}/c^2$ ) for the  $J/\psi$  mass from the analysis of charmonium production in  $b$ -hadron decays, using the 2011 and 2012 data samples

The two measurements are consistent with each other, and can be averaged, yielding the result  $M_{J/\psi} = 3096.66 \pm 0.19 \pm 0.02 \text{ MeV}/c^2$ , which agrees well with the value from Ref. [11].

In addition, comparison of the results for the  $\eta_c$  natural width  $\Gamma_{\eta_c}$  with the PDG value has been performed. The precision does not allow a competitive measurement, but the results serve as another consistency check. A large error in the determination of  $\Gamma_{\eta_c}$  is a consequence of the fact that the detector resolution was determined from the fit to data. The  $J/\psi$  peak does not provide a sufficiently precise constraint. The fit of the  $p\bar{p}$  invariant mass spectrum yielded the following  $\Gamma_{\eta_c}$  values:  $\Gamma_{\eta_c} = 23.0 \pm 9.0 \pm 2.6 \text{ MeV}$  and  $\Gamma_{\eta_c} = 27.3 \pm 6.3 \pm 2.7 \text{ MeV}$  for the 2011 and 2012 data samples respectively. The estimate of the systematic uncertainty is significantly smaller than the statistical error, and is dominated by the detector resolution. The details of systematic uncertainty estimates are given in Table 4.17.

The two values are consistent with each other, and can be averaged, yielding the result  $\Gamma_{\eta_c} = 25.8 \pm 5.2 \pm 1.9 \text{ MeV}$ , which agrees well with the PDG value [11].

The  $J/\psi$  mass  $M_{J/\psi}$ , the mass difference  $M_{J/\psi} - M_{\eta_c}$  and the  $\eta_c$  natural width from the analysis of the 2011 and 2012 data samples, their average and the corresponding PDG values [11] are shown in Table 4.18.

	2011 data sample	2012 data sample
mean value	23.0	27.3
statistical uncertainty	9.0	6.3
signal resolution ratio (MC)	2.1	2.3
fit range variation	1.0	1.1
background shape variation	1.0	0.2
$J/\psi \rightarrow p\bar{p}\pi^0$ shape variation	0.7	0.8
systematic uncertainty, quadratic sum	2.6	2.7

Table 4.17: Systematic uncertainties (in MeV) for the  $\eta_c$  natural width  $\Gamma$  from the analysis of charmonium production in  $b$ -hadron decays, using the 2011 and 2012 data samples

	$M_{J/\psi}$ , MeV/ $c^2$	$M_{J/\psi} - M_{\eta_c}$ , MeV/ $c^2$	$\Gamma_{\eta_c}$ , MeV
2011 data sample	$3096.50 \pm 0.34 \pm 0.03$	$113.1 \pm 2.4 \pm 0.2$	$23.0 \pm 9.0 \pm 2.6$
2012 data sample	$3096.74 \pm 0.23 \pm 0.02$	$115.8 \pm 1.9 \pm 0.2$	$27.3 \pm 6.3 \pm 2.7$
average	$3096.66 \pm 0.19 \pm 0.02$	$114.7 \pm 1.5 \pm 0.1$	$25.8 \pm 5.2 \pm 1.9$
PDG [11]	$3096.916 \pm 0.011$	$113.2 \pm 0.7$	$32.0 \pm 0.9$

Table 4.18: The  $J/\psi$  mass  $M_{J/\psi}$ , the mass difference  $M_{J/\psi} - M_{\eta_c}$  and the  $\eta_c$  natural width from the analysis of the 2011 and 2012 data samples, their average and the corresponding PDG values [11]

Finally, the  $\Gamma_{\eta_c}$ ,  $M_{\eta_c}$  contour plots (Fig. 4.25 and Fig. 4.26) are consistent between the 2011 and 2012 data samples, and with the PDG values [11].

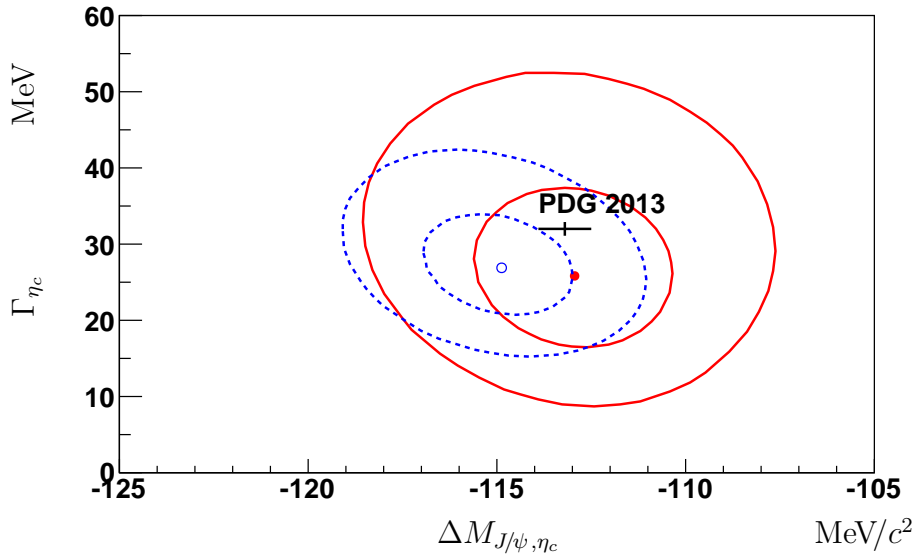


Figure 4.25: The  $\Gamma_{\eta_c}$ ,  $M_{\eta_c}$  contour plots for the 2011 (red solid curves) and 2012 (blue dashed curves) data samples. The two curves indicate one-sigma and two-sigma contours for the one-dimensional distribution. Only statistical uncertainties are shown. The PDG [11] value is indicated as a point with error bars

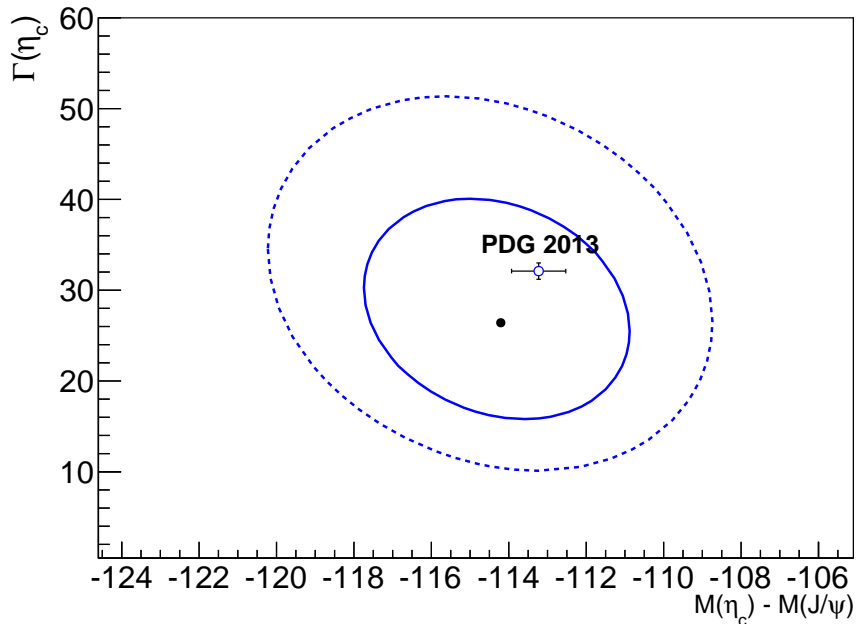


Figure 4.26: Contour plot of  $\Gamma_{\eta_c}$  and  $M_{\eta_c}$  for the combined data sample. The curves indicate 68.3 C.L. (one-sigma) and 95.5 C.L. (two-sigma) for two-dimensional distribution. Only statistical uncertainties are shown. The PDG [11] value is indicated as a point with error bars.

## 4.12 Search for prompt production of the $\chi_{ci}$ and $h_c$ states

Using the prompt production data sample, we perform the  $p\bar{p}$  invariant mass fit in the (3350..3600)  $\text{MeV}/c^2$  range to search for production of the  $\chi_{c0,1,2}$  and  $h_c$  states. Since the  $\chi_{c0}$  resonance has non-negligible width, a Breit-Wigner probability density function is used, convoluted with the single-Gaussian function for the detector response:

$$f \sim e^{-\frac{(M_{\chi_{c0,1,2}, h_c} - M_{p\bar{p}})^2}{(\sigma_{\chi_{c0,1,2}, h_c})^2}} \otimes \text{BW}(M_{\chi_{c0}}, \Gamma_{\chi_{c0}}) \quad (4.25)$$

Using MC samples, detector resolution is estimated to be in average  $\sigma_{\chi_{c0}} \simeq 10.5 \text{ MeV}$ . The invariant mass spectrum in the range (3350..3600)  $\text{MeV}/c^2$  is shown on Fig. 4.27. The spectrum is fit to the signal shape, discussed above and background shape, described in section 4.5.

The result of the fit of the  $\sqrt{s} = 7 \text{ TeV}$  and  $\sqrt{s} = 8 \text{ TeV}$  data sample is shown on Figs. 4.27 and 4.28.

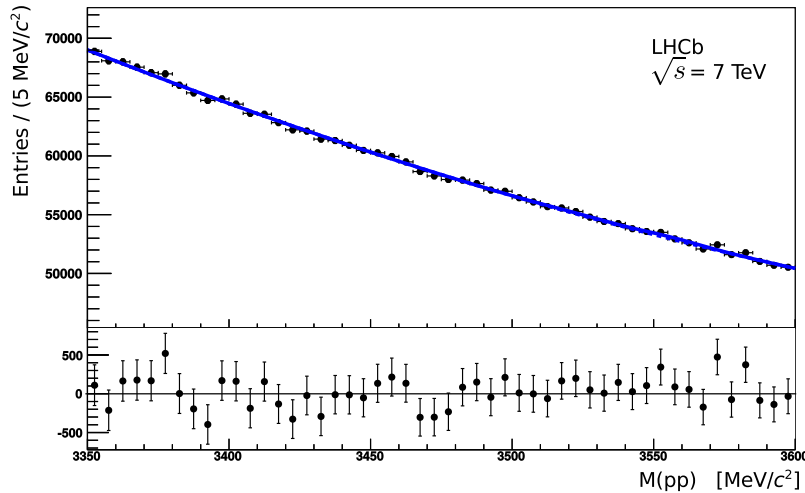


Figure 4.27: The fit of the  $\chi_{c0,1,2}$  and  $h_c$  candidates in  $\sqrt{s} = 7 \text{ TeV}$  data sample.

In the fit, natural widths of the resonances from Ref. [11] are used with the Gaussian constraint applied. The resulting logarithm likelihood profiles are given on Figs. 4.29 and 4.30.

Basing on the logarithm likelihood profiles, upper limits on the resonances relative yield are set at the 90% confidence level. Relative production yields  $N_{\chi_{c0,1,2}, h_c}/N_{J/\psi}$  are

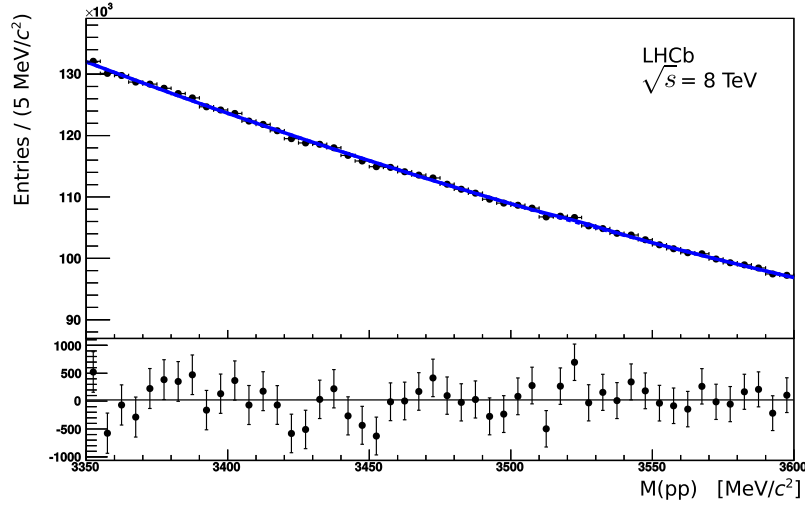


Figure 4.28: The fit of the  $\chi_{c0,1,2}$  and  $h_c$  candidates in  $\sqrt{s} = 8$  TeV data sample.

corrected to the efficiencies ratio from MC. Since the relative yields are related to the production cross-sections

$$N_{\chi_{c0,1,2}, h_c} / N_{J/\psi} = \frac{\sigma_{\chi_{c0,1,2}, h_c} \times \mathcal{B}_{\chi_{c0,1,2}, h_c \rightarrow p\bar{p}}}{\sigma_{J/\psi} \times \mathcal{B}_{J/\psi \rightarrow p\bar{p}}}, \quad (4.26)$$

we can extract the relative prompt production cross-sections with known the branching fractions (see Table 2.1). Results are given in the Tables 4.19 and 4.20 for 7 TeV and 8 TeV centre-of-mass energy, respectively.

state	$N_i / N_{J/\psi}$	$\mathcal{B}_{i \rightarrow p\bar{p}}, \times 10^{-3}$	$\sigma_i / \sigma_{J/\psi}$	$\sigma_i, \mu\text{b}$
$\chi_{c0}$	$< 0.06$	$0.213 \pm 0.012$	$< 0.6$	$< 0.2$
$\chi_{c1}$	$< 0.10$	$0.073 \pm 0.004$	$< 2.9$	$< 0.8$
$h_c$	$< 0.13$	$3.2 \pm 0.5$	$< 0.09$	$< 0.03$
$\chi_{c2}$	$< 0.16$	$0.071 \pm 0.004$	$< 4.8$	$< 1.4$

Table 4.19: The 90% CL limits on the prompt production of  $\chi_{c0}$ ,  $\chi_{c1}$ ,  $h_c$ ,  $\chi_{c2}$  states relative to  $J/\psi$  production at  $\sqrt{s} = 7$  TeV. Upper limits on ratios of the signal yields are also shown. Branching fractions of charmonium states decaying to a proton-antiproton pair from [44] for  $h_c$ , and from Ref. [11] for all the other listed states

The ratio of production cross-sections  $\sigma_i / \sigma_{J/\psi}$  is extracted from the equation 4.26. The uncertainties of the branching ratios  $\mathcal{B}_{J/\psi \rightarrow p\bar{p}}$ ,  $\mathcal{B}_{\chi_{c0} \rightarrow p\bar{p}}$ ,  $\mathcal{B}_{\chi_{c1} \rightarrow p\bar{p}}$ ,  $\mathcal{B}_{h_c \rightarrow p\bar{p}}$  and  $\mathcal{B}_{\chi_{c2} \rightarrow p\bar{p}}$  are taken into account.

To obtain the limit on the absolute value of  $\sigma_i$ , the  $J/\psi$  cross-section, found in section 4.9.3, is used. Error of the  $J/\psi$  production cross-section is taken into account in

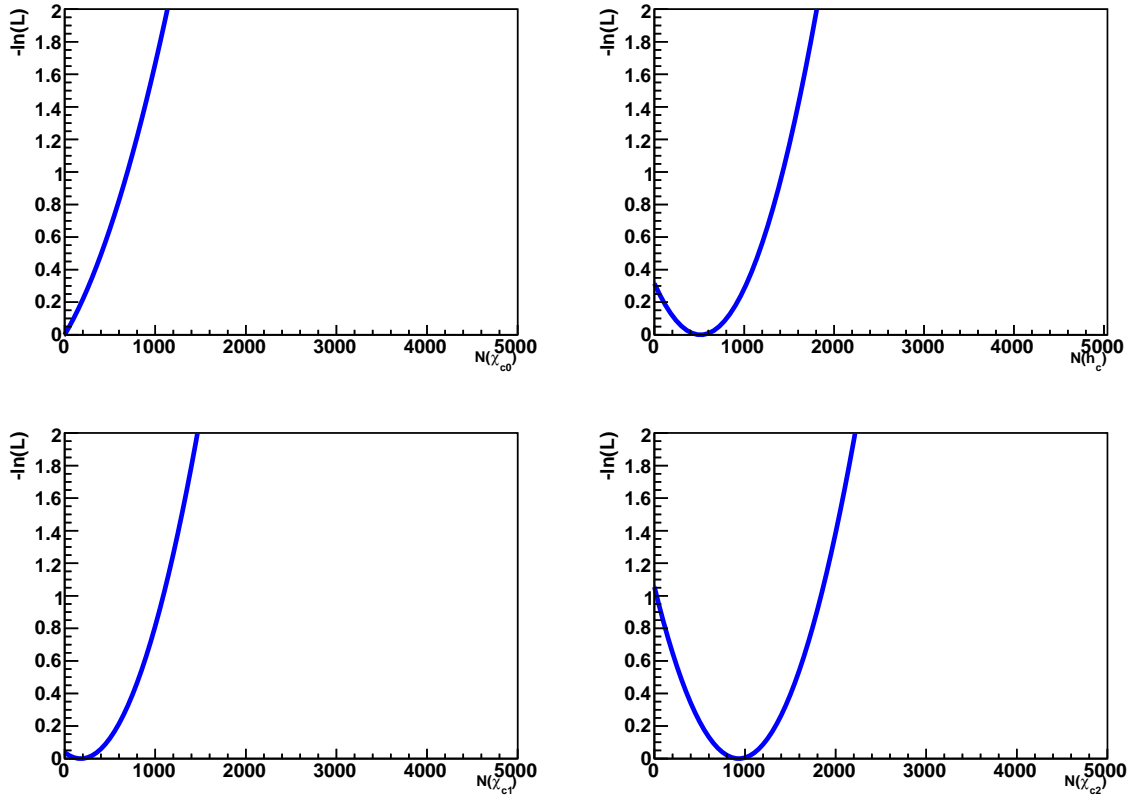


Figure 4.29: Logarithm likelihood profiles of the  $\chi_{c0,1,2}$  and  $h_c$  yields from promptly produced  $p\bar{p}$  candidates of 2011 year data

the same way, as the branching ratio errors.

The LHCb experiment has already performed set of measurements of the  $\chi_{ci}$  production cross-sections [107, 108]. Relative  $\chi_{c1}$  to  $\chi_{c2}$  production cross-sections at  $\sqrt{s} = 7$  TeV were also measured by the CMS experiment [109]. The relative production of the  $\chi_{c0}/\chi_{c1}/\chi_{c2}$  mixture to the  $J/\psi$  production was reported in Ref. [110].

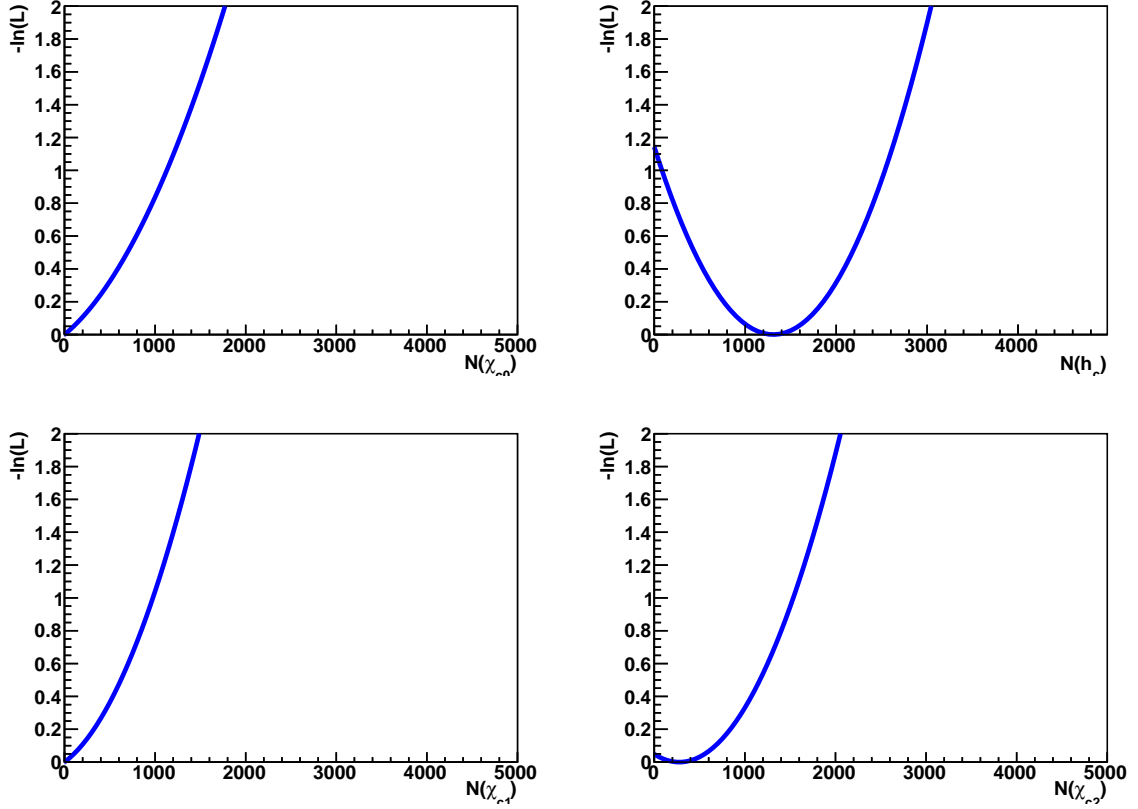


Figure 4.30: Logarithm likelihood profiles of the  $\chi_{c0,1,2}$  and  $h_c$  yields from promptly produced  $p\bar{p}$  candidates of 2012 year data

state	$N_i/N_{J/\psi}$	$\mathcal{B}_{i \rightarrow p\bar{p}} \cdot 10^{-3}$	$\sigma_i/\sigma_{J/\psi}$	$\sigma_i \cdot \mu\text{b}$
$\chi_{c0}$	$< 0.06$	$0.213 \pm 0.012$	$< 0.6$	$< 0.2$
$\chi_{c1}$	$< 0.13$	$0.073 \pm 0.004$	$< 3.7$	$< 1.4$
$h_c$	$< 0.05$	$3.2 \pm 0.5$	$< 0.03$	$< 0.01$
$\chi_{c2}$	$< 0.07$	$0.071 \pm 0.004$	$< 2.2$	$< 0.8$

Table 4.20: The 90% CL limits on the prompt production of  $\chi_{c0}$ ,  $\chi_{c1}$ ,  $h_c$ ,  $\chi_{c2}$  states relative to  $J/\psi$  production at  $\sqrt{s} = 8$  TeV. Upper limits on ratios of the signal yields are also shown. Branching fractions of charmonium states decaying to a proton-antiproton pair from [44] for  $h_c$ , and from Ref. [11] for all the other listed states

# Chapter 5

## Summary

This thesis document addressed studies of the  $\eta_c$  (1S) state properties. Production cross-section of the  $\eta_c$  meson in parton interactions and in inclusive  $b$ -hadron decays, is measured for the first time. The  $\eta_c$  mass and natural width are determined.

Studies of the  $\eta_c$  production provide an important tool for QCD tests distinguishing between many theoretical models, described in sec. 1.5.

The analysis is based on the data collected by the LHCb experiment in 2011-2012 and corresponding to the integrated luminosity of  $\int \mathcal{L} dt \approx 3 \text{ fb}$ . Selected events are chosen with the trigger alley, dedicated to selection of the proton-antiproton final state. Selection criteria were optimised in order to obtain maximal significance of the signal corresponding to the  $J/\psi \rightarrow p\bar{p}$  decays. Contribution from  $p\bar{p}$  combinations from the  $J/\psi \rightarrow p\bar{p}\pi^0$  decays was taken into account, as well as the effect of the cross-talk between the samples.

The most important result of the present analysis is the measurement of the ratios of inclusive prompt production cross-section of  $\eta_c$  and  $J/\psi$  mesons measured in rapidity range of  $2.0 < y < 4.5$ , and transverse momentum range  $p_T > 6.5 \text{ GeV}/c$ . The production cross-section ratio is found to be

$$\left(\sigma_{\eta_c}/\sigma_{J/\psi}\right)_{7 \text{ TeV}} = 1.74 \pm 0.29_{stat} \pm 0.28_{syst} \pm 0.18_{\mathcal{B}_{J/\psi \rightarrow p\bar{p}, \eta_c \rightarrow p\bar{p}}}$$

at the centre-of-mass energy  $\sqrt{s} = 7 \text{ TeV}$  and

$$\left(\sigma_{\eta_c}/\sigma_{J/\psi}\right)_{8 \text{ TeV}} = 1.60 \pm 0.29_{stat} \pm 0.25_{syst} \pm 0.17_{\mathcal{B}_{J/\psi \rightarrow p\bar{p}, \eta_c \rightarrow p\bar{p}}}$$

at the centre-of-mass energy  $\sqrt{s} = 8 \text{ TeV}$ . The given values are thus obtained with a relative precision of about 25% for both 7 TeV and 8 TeV centre-of-mass energies. The

measured production cross-section comprises possible contributions from the heavier charmonium states.

This is the first measurement of prompt  $\eta_c$  production in  $pp$  collisions. The obtained cross-section of the  $\eta_c$  prompt production is in agreement with the colour-singlet leading order calculations, while taking into account colour-octet LO contribution predicted cross-section exceeds the observed one by two orders of magnitude [111]. However the NLO contribution is expected to significantly modify the LO result [112]. Measurements at the nominal LHC energy of 14 TeV will allow studying the energy dependence of the  $\eta_c$  prompt production.

The  $\eta_c$  production as a function of  $p_T$  is obtained by fitting the  $p\bar{p}$  invariant mass spectrum in three or four bins of  $p_T$ . The  $J/\psi$   $p_T$  spectrum from Refs. [37, 50, 49] is used to obtain the  $\eta_c$   $p_T$  spectrum for both prompt production and inclusive  $\eta_c$  production in  $b$ -hadron decays (Figs. 4.18 and 4.19). The  $p_T$  dependence of the  $\eta_c$  production rate exhibits similar behaviour to that of the  $J/\psi$  meson rate in the studied kinematic regime, though with significantly larger uncertainties. Calculations of the NLO contribution to the cross-section are important to compare the observed  $p_T$  dependence to the theoretical predictions [113, 114].

The values of  $\sigma_{J/\psi}(\sqrt{s} = 7 \text{ TeV})$  and  $\sigma_{J/\psi}(\sqrt{s} = 8 \text{ TeV})$  are given in  $p_T$  and rapidity bins in sec. 4.5.2.

With the known  $J/\psi$  cross-section values for 7 TeV and 8 TeV centre-of-mass region, obtained from the  $J/\psi$  cross-section measurement using  $J/\psi \rightarrow \mu^+\mu^-$  LHCb analyses [37, 50, 49], we extracted the absolute  $\eta_c$  production cross-section in the same rapidity and  $p_T$  regions:

$$\begin{aligned} (\sigma_{\eta_c})_{7 \text{ TeV}} &= 0.52 \pm 0.09_{stat} \pm 0.08_{syst} \pm 0.06_{\sigma_{J/\psi}, \mathcal{B}_{J/\psi \rightarrow p\bar{p}}, \eta_c \rightarrow p\bar{p}} \mu\text{b} \\ (\sigma_{\eta_c})_{8 \text{ TeV}} &= 0.59 \pm 0.11_{stat} \pm 0.09_{syst} \pm 0.08_{\sigma_{J/\psi}, \mathcal{B}_{J/\psi \rightarrow p\bar{p}}, \eta_c \rightarrow p\bar{p}} \mu\text{b}, \end{aligned}$$

at a centre-of-mass energy  $\sqrt{s} = 7 \text{ TeV}$  and  $\sqrt{s} = 8 \text{ TeV}$ , respectively. First error corresponds to the statistical uncertainty, second error corresponds to the systematic uncertainty and third error represents the uncertainties coming from branching fractions.

Using an integrated luminosity of  $0.7 \text{ fb}^{-1}$  collected in 2011, and  $2.0 \text{ fb}^{-1}$  collected in 2012, the first measurement of the  $\eta_c$  inclusive yield in  $b$ -hadron decays was performed. By correcting the yield ratio with the ratio of branching fractions  $\mathcal{B}_{J/\psi \rightarrow p\bar{p}}/\mathcal{B}_{\eta_c \rightarrow p\bar{p}} = 1.39 \pm 0.15$  [11], the ratio of the inclusive  $b$ -hadron branching fractions into  $\eta_c$  and  $J/\psi$

final states for charmonium transverse momentum  $p_T > 6.5 \text{ GeV}/c$  is found to be

$$\mathcal{B}_{b \rightarrow \eta_c X} / \mathcal{B}_{b \rightarrow J/\psi X} = 0.421 \pm 0.055_{stat} \pm 0.022_{syst} \pm 0.045_{\mathcal{B}_{J/\psi \rightarrow p\bar{p}, \eta_c \rightarrow p\bar{p}}},$$

where the third uncertainty corresponds to the uncertainty on the  $J/\psi \rightarrow p\bar{p}$  and  $\eta_c \rightarrow p\bar{p}$  branching fractions [11]. Assuming that the transverse momentum  $p_T(\eta_c, J/\psi) > 6.5 \text{ GeV}/c$  requirement does not bias the distribution of charmonium momentum in the  $b$ -hadron rest frame, and using the branching fraction of  $b$ -hadron inclusive decays into  $J/\psi$  mesons from Ref. [11]  $\mathcal{B}_{b \rightarrow J/\psi X} = (1.16 \pm 0.10)\%$ , the inclusive branching fraction of  $\eta_c$  from  $b$ -hadron decays is derived as

$$\mathcal{B}_{b \rightarrow \eta_c X} = (4.88 \pm 0.64_{stat} \pm 0.25_{syst} \pm 0.67_{\mathcal{B}_{b \rightarrow J/\psi X}, \mathcal{B}_{J/\psi, \eta_c \rightarrow p\bar{p}}}) \times 10^{-3},$$

where the third uncertainty component includes also the uncertainty on the  $J/\psi$  inclusive branching fraction from  $b$ -hadron decays. This is the first measurement of the inclusive branching fraction of  $b$ -hadrons decay into a  $\eta_c$  meson. It is consistent with a previous 90% confidence level upper limit restricted to  $B^-$  and  $B^0$  meson decays,  $\mathcal{B}_{B^-, B^0 \rightarrow \eta_c X} < 9 \times 10^{-3}$  at 90% confidence level [11]. A direct determination of the ratio  $\mathcal{B}_{J/\psi \rightarrow p\bar{p}} / \mathcal{B}_{\eta_c \rightarrow p\bar{p}}$ , which may be accessible to the BES collaboration, can significantly reduce the systematic uncertainty of the result.

The  $\eta_c$  state parameters, mass and natural width are also addressed using low-background sample of charmonia from inclusive  $b$ -hadron decays. The results of the fits are represented with the 2D contour plots on the  $m_{\eta_c}$  and  $\Gamma_{\eta_c}$  plane for the 2011 and 2012 samples on Fig. 4.25. Resulting numbers and analysis details are given in sec. 4.11. The values, obtained with the combined data set, are

$$\begin{aligned} m_{\eta_c} &= 2982.0 \pm 1.5 \pm 0.1 \text{ MeV}/c^2 \\ \Gamma_{\eta_c} &= 25.8 \pm 5.2 \pm 1.9 \text{ MeV}, \end{aligned}$$

which are consistent with the PDG average values [11].

Upper limits on the prompt production cross-section of the  $\chi_{c0}$ ,  $\chi_{c1}$ ,  $h_c$  and  $\chi_{c2}$  mesons, relative to the  $J/\psi$  production cross-section, are obtained. Results, given in sec. 4.12, show that sensitivity to the production cross-section of some of these states is compatible to that of the  $J/\psi$  production.

Studying charmonium production in the decays to the proton-antiproton final state

allows important measurement of the absolute  $\eta_c$  production cross-section. Using charmonium decays to other hadronic final states, and in particular to  $\phi\phi$ , will provide a possibility to access the production of other charmonium states, measuring them relatively to the  $\eta_c$  production, where the  $J/\psi$  can not be used for normalisation since  $J^P = 1^-$  states decays to  $\phi\phi$  are forbidden.

Precise determination of masses and natural width of other charmonium states can be performed, extracting pure  $\phi\phi$  component with two-dimensional fit technique or *sPlot* technique [115, 100]. Important measurements of the charmonium mass differences and natural widths can be performed for the  $\chi_c$ ,  $h_c$  and  $\eta_c$  (2S) states.

# Chapter 6

## List of the main results

*All production measurements are performed in  $2.0 < y < 4.5$ ,  $p_T > 6.5$  GeV/c kinematic range*

### Prompt charmonium production

- Production relative to  $J/\psi$ :

▷  $\sqrt{s} = 7$  TeV

$$\left(\sigma_{\eta_c}/\sigma_{J/\psi}\right)_{7\text{ TeV}} = 1.74 \pm 0.29_{stat} \pm 0.28_{syst} \pm 0.18_{\mathcal{B}_{J/\psi \rightarrow p\bar{p}, \eta_c \rightarrow p\bar{p}}}$$

$$\left(\sigma_{\chi_{c0}}/\sigma_{J/\psi}\right)_{7\text{ TeV}} < 0.6 \text{ @ } 90\% \text{ CL}$$

$$\left(\sigma_{\chi_{c1}}/\sigma_{J/\psi}\right)_{7\text{ TeV}} < 2.9 \text{ @ } 90\% \text{ CL}$$

$$\left(\sigma_{h_c}/\sigma_{J/\psi}\right)_{7\text{ TeV}} < 0.09 \text{ @ } 90\% \text{ CL}$$

$$\left(\sigma_{\chi_{c2}}/\sigma_{J/\psi}\right)_{7\text{ TeV}} < 4.8 \text{ @ } 90\% \text{ CL}$$

▷  $\sqrt{s} = 8$  TeV

$$\left(\sigma_{\eta_c}/\sigma_{J/\psi}\right)_{8\text{ TeV}} = 1.60 \pm 0.29_{stat} \pm 0.25_{syst} \pm 0.17_{\mathcal{B}_{J/\psi \rightarrow p\bar{p}, \eta_c \rightarrow p\bar{p}}}$$

$$\left(\sigma_{\chi_{c0}}/\sigma_{J/\psi}\right)_{8\text{ TeV}} < 0.6 \text{ @ } 90\% \text{ CL}$$

$$\left(\sigma_{\chi_{c1}}/\sigma_{J/\psi}\right)_{8\text{ TeV}} < 3.7 \text{ @ } 90\% \text{ CL}$$

$$\left(\sigma_{h_c}/\sigma_{J/\psi}\right)_{8\text{ TeV}} < 0.03 \text{ @ } 90\% \text{ CL}$$

$$\left(\sigma_{\chi_{c2}}/\sigma_{J/\psi}\right)_{8\text{ TeV}} < 2.2 \text{ @ } 90\% \text{ CL}$$

- Absolute production cross-section:

$$\triangleright \sqrt{s} = 7 \text{ TeV}$$

$$(\sigma_{\eta_c})_{7 \text{ TeV}} = 0.52 \pm 0.09_{stat} \pm 0.08_{syst} \pm 0.06_{\sigma_{J/\psi}, \mathcal{B}_{J/\psi \rightarrow p\bar{p}, \eta_c \rightarrow p\bar{p}}} \mu\text{b}$$

$$(\sigma_{\chi_{c0}})_{7 \text{ TeV}} < 0.2 \mu\text{b} @ 90\% \text{ CL}$$

$$(\sigma_{\chi_{c1}})_{7 \text{ TeV}} < 0.8 \mu\text{b} @ 90\% \text{ CL}$$

$$(\sigma_{h_c})_{7 \text{ TeV}} < 0.03 \mu\text{b} @ 90\% \text{ CL}$$

$$(\sigma_{\chi_{c2}})_{7 \text{ TeV}} < 1.4 \mu\text{b} @ 90\% \text{ CL}$$

$$\triangleright \sqrt{s} = 8 \text{ TeV}$$

$$(\sigma_{\eta_c})_{8 \text{ TeV}} = 0.59 \pm 0.11_{stat} \pm 0.09_{syst} \pm 0.08_{\sigma_{J/\psi}, \mathcal{B}_{J/\psi \rightarrow p\bar{p}, \eta_c \rightarrow p\bar{p}}} \mu\text{b}$$

$$(\sigma_{\chi_{c0}})_{8 \text{ TeV}} < 0.2 \mu\text{b} @ 90\% \text{ CL}$$

$$(\sigma_{\chi_{c1}})_{8 \text{ TeV}} < 1.4 \mu\text{b} @ 90\% \text{ CL}$$

$$(\sigma_{h_c})_{8 \text{ TeV}} < 0.01 \mu\text{b} @ 90\% \text{ CL}$$

$$(\sigma_{\chi_{c2}})_{8 \text{ TeV}} < 0.8 \mu\text{b} @ 90\% \text{ CL}$$

### Inclusive $\eta_c$ production in $b$ -hadron decays

- Production relative to  $J/\psi$ :

$$\mathcal{B}_{b \rightarrow \eta_c X} / \mathcal{B}_{b \rightarrow J/\psi X} = 0.421 \pm 0.055_{stat} \pm 0.022_{syst} \pm 0.045_{\mathcal{B}_{J/\psi \rightarrow p\bar{p}, \eta_c \rightarrow p\bar{p}}}$$

- Absolute production cross-section:

$$\mathcal{B}_{b \rightarrow \eta_c X} = (4.88 \pm 0.64_{stat} \pm 0.17_{syst} \pm 0.67_{\mathcal{B}_{b \rightarrow J/\psi X}, \mathcal{B}_{J/\psi, \eta_c \rightarrow p\bar{p}}}) \times 10^{-3}.$$

### The $\eta_c$ mass and natural width

$$m_{\eta_c} = 2982.0 \pm 1.5 \pm 0.1 \text{ MeV}/c^2$$

$$\Gamma_{\eta_c} = 25.8 \pm 5.2 \pm 1.9 \text{ MeV}.$$

# Acknowledgements

First of all I would like to thank the members of jury who kindly agreed to come: Valeri Khoze, Pavel Pakhlov, Achille Stocchi and Hermine Woehri and my referees Giulia Manca and Gines Martinez. I received many clever and useful comments and corrections from their side during preparation of my thesis manuscript.

I was very happy to work in the LHCb group at LAL. During the last three years I had pleasure to work with Yasmine Amhis, Martino Borsato, Patrick Robbe, Marie-Hélène Schune, Benoit Viaud, Sergey Barsuk, Guy Wormster, Bernard Jean-Marie, Jaques Lefrançois, Olga Kochebina, Frédéric Machefert, Michelle Nicol, Alexis Vallier, Jibo He and others.

Particularly I would like to thank Marie-Hélène and Sergey for reading and correcting my thesis manuscript and Michelle for the significant improvement of the language of this text.

I should notice a really great impact of Jibo to the present analysis. Dedicated trigger lines, used in our analysis, is to his credit. Jibo was teaching me at the beginning of my thesis, helping me with the analysis and software.

Emi Kou, a theorist from LAL, is a person who suggested hadronic decay channels for the charmonium studies. I thank her for the theoretical support of my work and useful suggestions concerning the analysis.

I should thank also our analysis reviewers from the LHCb group Maddalena Frosini and David Websdale, Editorial Board reviewer Diego Tonelli, Editorial Board readers George Lafferty and Wouterh Nikhef, the WG group and the group conveners, Giulia Manca, Marco Adinolfi, Vanya Belyaev and Zhenwei Yang, to thank Patrick Koppenburg and Rolf Oldeman, and thank all others who helped with the analysis, writing, reviewing and reading out the paper.

I would also like to thank Sergey for his patience, good attitude and all the help.

# Appendix

## .1 Selection criteria optimisation

Selection criteria in both prompt and secondary analyses were optimised to obtain the maximal value of significance  $S = N_{sig}/\sqrt{N_{bgr} + N_{sig}}$ , see section 4.4 for the detailed description of the optimisation procedure. Optimisation plots are shown for candidates from  $b$ -hadron decays on Fig. 2 and for prompt candidates on Fig. 1.

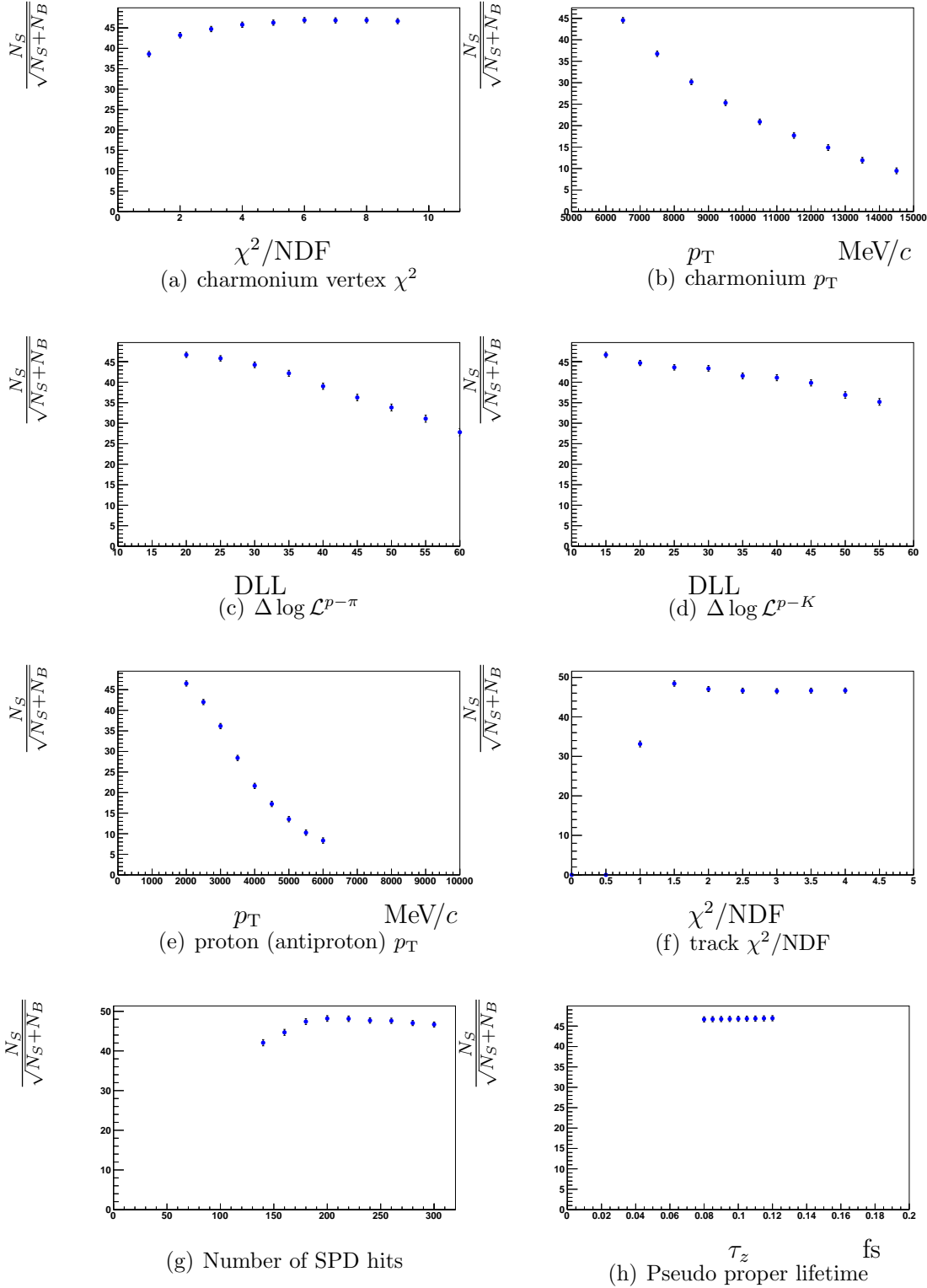


Figure 1: Selection criteria optimisation for the charmonium sample from  $b$ -hadron decays

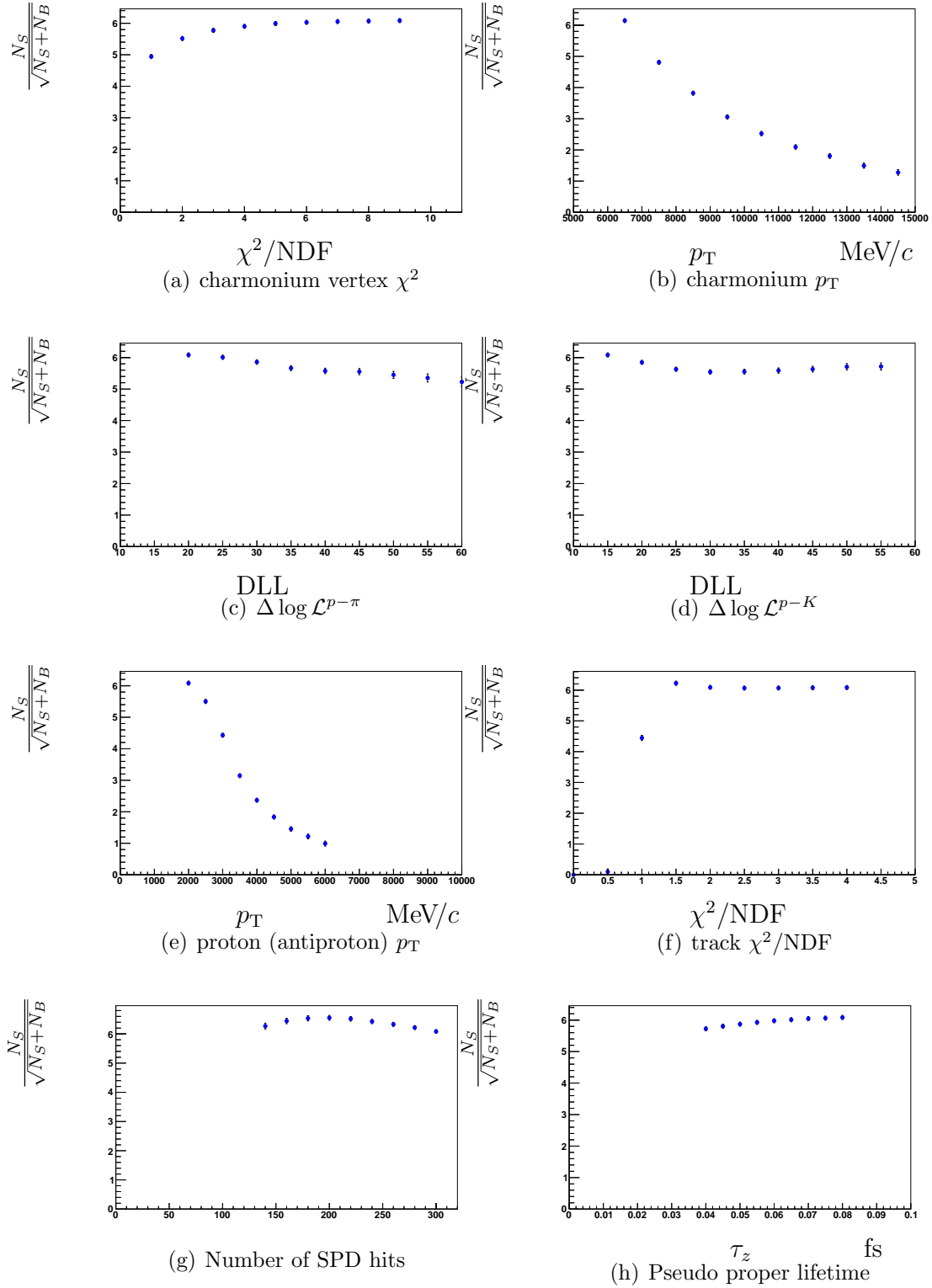


Figure 2: Selection criteria optimisation for prompt the charmonium sample

## **.2 $J/\psi$ cross-section in $p_T$ and rapidity bins**

In order to derive absolute values of the  $\eta_c$  prompt production cross-section and the  $\eta_c$  inclusive yield from  $b$ -meson decays, the  $J/\psi$  production cross-section in the same kinematic region should be known. The  $J/\psi$  inclusive production cross-section in  $p_T$  and rapidity bins, taken from Refs. [37, 50, 49] and the LHCb analysis note ANA-2013-019 is shown in Tables 1, 1 and 3. Given cross-section values correspond to the  $\sqrt{s} = 7$  TeV with and without polarisation corrections introduced in Tables 1 and 1, and to the  $\sqrt{s} = 8$  TeV in Table 3. Detailed procedure of the cross-section calculations and polarisation corrections is described in section 4.9.3.

rapidity	$p_T$ , GeV/c	cross section	stat. error	syst. error uncorr.	syst. error corr.
2.0-2.5	6-7	101.2	1.9	7.3	8.0
	7-8	62.2	1.4	4.1	4.6
	8-9	32.5	0.9	2.1	2.2
	9-10	18.5	0.7	1.2	1.3
	10-11	10.8	0.5	0.7	0.9
	11-12	5.7	0.3	0.4	0.4
	12-13	4.2	0.3	0.3	0.3
	13-14	2.8	0.3	0.2	0.2
2.5-3.0	6-7	94.1	1.3	6.4	2.9
	7-8	50.6	0.9	3.7	1.7
	8-9	28.1	0.7	1.8	0.9
	9-10	15.8	0.5	1.0	0.5
	10-11	8.7	0.4	0.6	0.3
	11-12	5.0	0.3	0.3	0.2
	12-13	3.4	0.2	0.2	0.1
	13-14	2.7	0.2	0.2	0.1
3.0-3.5	6-7	71.7	1.1	4.8	1.9
	7-8	37.8	0.7	2.4	1.2
	8-9	20.3	0.5	1.3	0.6
	9-10	10.8	0.4	0.7	0.3
	10-11	7.7	0.3	0.5	0.3
	11-12	4.0	0.2	0.3	0.1
	12-13	2.6	0.2	0.2	0.1
	13-14	1.4	0.1	0.1	0.1
3.5-4.0	6-7	54.6	1.0	3.5	1.6
	7-8	26.2	0.6	1.7	0.9
	8-9	14.3	0.5	0.9	0.5
	9-10	7.2	0.3	0.5	0.2
	10-11	4.2	0.2	0.3	0.2
	11-12	2.2	0.2	0.1	0.1
	12-13	1.0	0.1	0.1	<0.1
	13-14				
4.0-4.5	6-7	30.6	1.0	1.9	1.4
	7-8	16.7	0.7	1.1	0.9
	8-9	7.8	0.4	0.5	0.4
	9-10	4.0	0.3	0.2	0.2
	10-11	2.5	0.2	0.2	0.2
	11-12				
	12-13				
	13-14				
2.0-4.5	6-7	176.1	1.5	5.8	7.9
	7-8	96.8	1.0	3.2	4.7
	8-9	51.5	0.7	1.6	2.3
	9-10	28.1	0.5	0.9	1.3
	10-11	16.9	0.4	0.5	0.9
	11-12	8.5	0.3	0.3	0.4
	12-13	5.6	0.2	0.2	0.3
	13-14	3.4	0.2	0.1	0.2

Table 1: The  $J/\psi$  cross section in  $p_T$  and rapidity bins,  $\sqrt{s} = 7$  TeV results

rapidity	$p_T$ , GeV/ $c$	cross section	stat. error	syst. error uncorr.	syst. error corr.
2.0-2.5	6-7	109.9	1.9	5.7	6.0
	7-8	60.6	0.9	2.8	3.2
	8-9	35.0	0.9	0.9	2.0
	9-10	18.3	0.7	0.5	1.0
	10-11	11.0	0.5	0.3	0.6
	11-12	6.3	0.4	0.2	0.4
	12-13	4.4	0.3	0.2	0.2
	13-14	2.7	0.3	0.1	0.2
2.5-3.0	6-7	98.5	0.9	3.8	5.6
	7-8	54.0	0.9	2.8	2.8
	8-9	29.4	0.9	0.9	1.6
	9-10	16.5	0.5	0.2	0.9
	10-11	9.3	0.4	0.1	0.5
	11-12	5.6	0.3	0.1	0.3
	12-13	3.3	0.2	0.1	0.2
	13-14	2.5	0.2	0.1	0.1
3.0-3.5	6-7	77.7	0.9	2.8	4.4
	7-8	41.7	0.9	0.9	2.4
	8-9	21.8	0.9	0.9	1.2
	9-10	11.9	0.4	0.1	0.7
	10-11	7.4	0.3	0.1	0.2
	11-12	4.3	0.3	0.1	0.2
	12-13	2.7	0.2	0.1	0.2
	13-14	1.2	0.2	0.1	0.1
3.5-4.0	6-7	55.9	0.9	1.9	3.2
	7-8	27.5	0.9	0.9	1.6
	8-9	15.1	0.5	0.1	0.8
	9-10	7.8	0.4	0.1	0.4
	10-11	4.6	0.3	0.1	0.2
	11-12	2.5	0.2	0.1	0.1
	12-13	1.1	0.1	0.1	0.1
	13-14				
4.0-4.5	6-7	32.2	1.0	1.3	1.8
	7-8	16.1	0.7	0.8	0.9
	8-9	8.0	0.5	0.4	0.4
	9-10	3.9	0.3	0.2	0.2
	10-11	2.1	0.2	0.1	0.1
	11-12				
	12-13				
	13-14				
2.0-4.5	6-7	187.0	0.9	2.5	4.4
	7-8	99.9	1.0	2.2	5.5
	8-9	54.6	0.9	0.8	3.1
	9-10	29.2	0.5	0.3	1.6
	10-11	17.2	0.4	0.2	0.9
	11-12	9.3	0.3	0.1	0.5
	12-13	5.8	0.2	0.1	0.3
	13-14	3.2	0.2	0.1	0.2

Table 2: The  $J/\psi$  cross section in  $p_T$  and rapidity bins,  $\sqrt{s} = 7$  TeV results, with the luminosity correction introduced

rapidity	$p_T$ , GeV/ $c$	cross section	stat. error	syst. error uncorr.	syst. error corr.
2.0-2.5	6-7	126.5	1.65	2.29	9.07
	7-8	68.05	1.07	1.98	4.88
	8-9	39.23	0.74	1.88	2.81
	9-10	22.04	0.52	0.66	1.58
	10-11	13.6	0.39	0.45	0.98
	11-12	8.06	0.28	0.23	0.58
	12-13	5.26	0.22	0.2	0.38
	13-14	3.3	0.17	0.21	0.24
2.5-3.0	6-7	116.27	1.07	4.31	8.34
	7-8	63.25	0.74	1.09	4.53
	8-9	34.85	0.52	0.84	2.5
	9-10	19.54	0.37	0.49	1.4
	10-11	11.59	0.28	0.37	0.83
	11-12	7.29	0.22	0.33	0.52
	12-13	4.31	0.16	0.06	0.31
	13-14	2.94	0.14	0.07	0.21
3.0-3.5	6-7	97.25	0.94	1.76	6.97
	7-8	51.21	0.64	1.23	3.67
	8-9	27.34	0.45	0.98	1.96
	9-10	15.08	0.32	0.7	1.08
	10-11	8.88	0.25	0.15	0.64
	11-12	5.03	0.18	0.11	0.36
	12-13	3.3	0.14	0.1	0.24
	13-14	2.09	0.11	0.09	0.15
3.5-4.0	6-7	73.68	0.84	1.33	5.28
	7-8	37.39	0.56	0.82	2.68
	8-9	20.05	0.4	0.54	1.44
	9-10	11.04	0.29	0.38	0.79
	10-11	6.24	0.2	0.28	0.45
	11-12	3.85	0.18	0.16	0.28
	12-13	2.23	0.13	0.05	0.16
	13-14	1.49	0.1	0.04	0.11
4.0-4.5	6-7	48.4	0.9	0.92	3.47
	7-8	23.95	0.59	0.6	1.72
	8-9	11.83	0.39	0.34	0.85
	9-10	6.64	0.27	0.24	0.48
	10-11	3.4	0.18	0.15	0.24
	11-12	2.05	0.14	0.1	0.15
	12-13	1.04	0.09	0.03	0.07
	13-14	0.45	0.06	0.02	0.03
2.0-4.5	6-7	231.05	1.3	2.7	16.6
	7-8	121.93	0.8	1.4	8.7
	8-9	66.65	0.6	1.2	4.8
	9-10	37.17	0.4	0.6	2.7
	10-11	21.86	0.3	0.3	1.6
	11-12	13.14	0.2	0.2	0.9
	12-13	8.07	0.2	0.1	0.6
	13-14	5.14	0.1	0.1	0.4

Table 3: The  $J/\psi$  cross section in  $p_T$  and rapidity bins,  $\sqrt{s} = 8$  TeV results

# List of Figures

1.1	Elementary particle interactions in the Standard Model. . . . .	8
1.2	The dependency of the $\alpha_{\text{em}}(Q^2)$ running coupling constant on the $Q^2$ . [7]	12
1.3	The quark loop (left) and the gluon loop (right) corrections to the running coupling constant $\alpha_s$ . [7] . . . . .	15
1.4	The $Q^2$ dependence of the $\alpha_s(Q^2)$ coupling constant. [7] . . . . .	16
1.5	Octet and singlet of the lightest baryons with spin 1/2. . . . .	18
1.6	Octet and singlet of the lightest pseudo-scalar mesons. . . . .	18
1.7	Ten baryons with the spin 3/2 form the baryon decuplet. . . . .	19
1.8	Multiplets of the 1/2 spin baryon in SU(4) flavour model. . . . .	20
1.9	Multiplets of the pseudo-scalar mesons in SU(4) flavour model. . . . .	20
1.10	The $\alpha_s$ , at one loop, as a function of quarkonium radius $r$ , with labels indication approximate values of $mv$ for $\Upsilon(1S)$ , $J/\psi$ , and $\Upsilon(2S)$ . [31] .	24
1.11	The $q\bar{q}$ potential as a function of quarkonium radius $r$ . [31] . . . . .	25
1.12	The current experimental status of charmonium spectroscopy, compared to the predictions of a non-relativistic potential model. Experimental levels are solid lines, and theoretical levels are dashed. The open-charm threshold at 3.73 GeV is also shown. Taken from Ref [33] with the Ref [34] updates. . . . .	28
1.13	The diagram of the charmonium production from a B-meson decay. . .	34
1.14	Quark diagram of charmonium decay to the $p\bar{p}$ pair via emission of three gluons. This process is valid for $J^P = 1^-$ states: $J/\psi$ , $h_c$ , $\psi(2S)$ . . . . .	36
1.15	Quark diagram of charmonium decay to the $p\bar{p}$ pair via emission of two gluons. This process is allowed for the most of charmonia, except $J^P = 1^-$ states: $\eta_c$ , $\chi_{c0}$ , $\chi_{c1}$ , $\chi_{c2}$ . . . . .	36

1.16	Scheme of the experimentally observed charmonium states and their notable decay channels with the branching ratios (if known). States above the $D^0\bar{D}^0$ threshold decays preferably to the charmed meson-antimeson pair. [11] . . . . .	38
1.17	Scheme of the experimentally observed bottomonium states and their notable decay channels with the branching ratios (if known). States above the $B^0\bar{B}^0$ threshold decays preferably to the beauty meson-antimeson pair. [11] . . . . .	39
2.1	“Evolution” of the $\eta_c$ mass world average according to the Particle Data Group. [11, 81, 82, 83, 84, 85, 86, 87, 88, 89] . . . . .	48
2.2	“Evolution” of the $\eta_c$ naturel width world average according to the Particle Data Group. [11, 81, 82, 83, 84, 85, 86, 87, 88, 89] . . . . .	49
3.1	The LHC acceleration cascade and positions of four main experiments.	52
3.2	The LHCb integrated luminosity in 2010-2012 years and the luminosity, delivered by the LHC. . . . .	52
3.3	The $b\bar{b}$ production angle plot $\sqrt{s} = 8$ TeV, Monte-Carlo simulation. . .	53
3.4	The side view of the LHCb detector. . . . .	54
3.5	Scheme of the R and the $\phi$ -sensors. [93] . . . . .	55
3.6	VELO detector plates before installation. . . . .	56
3.7	Cross-sections of the VELO silicon layers in the $x/z$ plane (top). Closed (bottom left) and opened (bottom right) VELO stations. . . . .	56
3.8	Resolution on the reconstructed track parameters at the production vertex of the track: momentum resolution as a function of track momentum (left), impact parameter resolution as a function of $1/p_T$ (right). For comparison, the momentum and transverse-momentum spectra of B-decay particles are shown in the lower part of the plots. [92] . . . . .	58
3.9	Distributions of the decay time of $B^+ \rightarrow J/\psi K^+$ (top left), $B^0 \rightarrow J/\psi K^{*0}$ (bottom left), $B_s \rightarrow J/\psi \phi$ (top right), $\Lambda_b^0 \rightarrow J/\psi \Lambda$ (bottom right) and associated residual uncertainties. The data are shown by the black points; the total fit function by the black solid line; the signal contribution by the red dashed line and the background contribution by the blue dotted line. [95] . . . . .	59
3.10	Side scheme of the RICH1 (left) and RICH2 (right) detectors. . . . .	60

3.11	Reconstructed Cherenkov angle as a function of track momentum in the $C_4F_{10}$ radiator (left) [98]. Polar angle $\theta$ versus momentum, for all tracks in simulated $B_d^0 \rightarrow \pi^+\pi^-$ events. The regions of interest for RICH 1 and RICH 2 are indicated by the dashed lines (right) [99]. . . . .	61
3.12	Invariant $\pi^+\pi^-$ mass before (left) and after (right) PID selection applied . The result of an unbinned maximum likelihood fit is overlaid. The main contributions to the fit model are also shown. [101] . . . . .	62
3.13	Invariant mass distributions of the $\Lambda \rightarrow p\pi^-$ both background and signal, is superimposed in blue [98]. . . . .	62
3.14	Proton identification efficiency and pion misidentification rate (left) and kaon misidentification (right) measured on data as a function of track momentum. Two different $\log \mathcal{L}(p - \pi)$ (left) and $\log \mathcal{L}(p - K)$ requirements have been imposed on the samples, resulting in the open and filled marker distributions, respectively. . . . .	63
3.15	The LHCb trigger scheme. . . . .	64
3.16	The efficiency $\varepsilon^{\text{TO S}}$ of L0Hadron is shown for $B^0 \rightarrow D^-\pi^+$ , $B^- \rightarrow D^0\pi^-$ , $D^0 \rightarrow K^-\pi^+$ and $D^+ \rightarrow K^-\pi^+\pi^+$ as a function of $p_T$ of the signal $B$ and $D$ mesons. [104] . . . . .	66
4.1	Distribution of the pseudo-decay time $t_z$ for simulated $J/\psi \rightarrow p\bar{p}$ signal selected by the prompt production analysis. All selection criteria but the $t_z$ requirement are applied. The $t_z$ threshold is shown with the red vertical line. Empty and filled histograms correspond to prompt charmonia and charmonia from b-hadron decays, respectively. . . . .	72
4.2	Distribution of the pseudo-decay time $t_z$ for simulated $J/\psi \rightarrow p\bar{p}$ signal selected by the analysis of charmonia production in b-hadron decays. All selection criteria but the $t_z$ requirement are applied. The $t_z$ threshold is shown with the red vertical line. Empty and filled histograms correspond to charmonia from b-hadron decays and prompt charmonia, respectively. . . . .	73
4.3	$J/\psi \cos(\theta)$ reweighted in the transverse momentum and rapidity bins, Monte-Carlo simulation. Solid red lines represent reweighted MC sample, dashed red lines represent polarisation parameter error and black crosses are for unweighted MC distributions. . . . .	77

- 
- 4.4  $J/\psi \cos(\theta)$  spectrum integrated over the transverse momentum and rapidity bins, Monte-Carlo simulation. Solid red lines represent reweighted MC sample, dashed red lines represent polarisation parameter error and black crosses are for unweighted MC distributions . . . . . 78
- 4.5 The  $p\bar{p}$  invariant mass of the MC samples: prompt  $J/\psi$  production (left), inclusive  $J/\psi$  (centre) and  $\eta_c$  (right) production in  $b$ -hadron decays. The results of the fit are shown in Table 4.5. The effect from the  $\eta_c$  natural width is explicitly excluded . . . . . 80
- 4.6 Fit of the  $p\bar{p}$  invariant mass from the  $J/\psi \rightarrow p\bar{p}\pi^0$  MC prompt  $J/\psi$  sample (left plots) and a sample of  $J/\psi$  from  $b$ -hadron decays (right plots) with (top plots) and without (bottom plots) trigger requirements . . . . . 82
- 4.7 Proton-antiproton invariant mass spectrum for candidates coming from a secondary vertex, the 2011 year data sample. Solid blue line represents the fitting curve, long-dashed cyan line corresponds to double-Gaussian function for the  $J/\psi$  signal, long-dashed red line corresponds to the double-Gaussian function, convoluted with a Breit-Wigner function for the  $\eta_c$  signal, dashed yellow line corresponds to  $J/\psi \rightarrow p\bar{p}\pi^0$  spectrum with non-reconstructed pion. More details and fit results are described in the text . . . . . 84
- 4.8 Proton-antiproton invariant mass spectrum for candidates coming from a secondary vertex, the 2012 year data sample. Solid blue line represents the fitting curve, long-dashed cyan line corresponds to double-Gaussian function for the  $J/\psi$  signal, long-dashed red line corresponds to the double-Gaussian function, convoluted with a Breit-Wigner function for the  $\eta_c$  signal, dashed yellow line corresponds to  $J/\psi \rightarrow p\bar{p}\pi^0$  spectrum with non-reconstructed pion. More details and fit results are described in the text . . . . . 85
- 4.9 The  $p\bar{p}$  invariant mass spectrum for the analysis of charmonium production in  $b$ -hadron decays, with both 2011 and 2012 data combined . . . . . 86

- 4.10 Proton-antiproton invariant mass spectrum for candidates coming from a primary vertex (top), and visually subtracted background (bottom), the 2011 data sample. The  $J/\psi$  signal is described by a double-Gaussian function, the  $\eta_c$  signal is described by a double-Gaussian function convoluted with a Breit-Wigner function, a contribution from  $J/\psi \rightarrow p\bar{p}\pi^0$  decay with non-reconstructed pion is taken into account. Gaussian constraints on the  $J/\psi$  mass and the difference  $\Delta M_{J/\psi, \eta_c} = M_{J/\psi} - M_{\eta_c}$ , from the fit of the sample corresponding to charmonium candidates from  $b$ -hadron decays, are applied. See the text for more details and fit results 87
- 4.11 Proton-antiproton invariant mass spectrum for candidates coming from a primary vertex (top), and visually subtracted background (bottom), the 2012 data sample. The  $J/\psi$  signal is described by a double-Gaussian function, the  $\eta_c$  signal is described by a double-Gaussian function convoluted with a Breit-Wigner function, a contribution from  $J/\psi \rightarrow p\bar{p}\pi^0$  decay with non-reconstructed pion is taken into account. Gaussian constraints on the  $J/\psi$  mass and the difference  $\Delta M_{J/\psi, \eta_c} = M_{J/\psi} - M_{\eta_c}$ , from the fit of the sample corresponding to charmonium candidates from  $b$ -hadron decays, are applied. See the text for more details and fit results 88
- 4.12 Linear (dashed red) and nonlinear (solid blue) components of the function used to describe the combinatorial background of the  $p\bar{p}$  invariant mass spectrum for the prompt production analysis. Both components have the same normalisation for this illustration . . . . . 89
- 4.13 Proton-antiproton invariant mass spectrum for candidates coming from primary vertex for 2011 year data (top), with visually subtracted background (bottom). The  $J/\psi$  mass and the difference  $\Delta M_{J/\psi, \eta_c} = M_{J/\psi} - M_{\eta_c}$  are left as free parameters in the fit . . . . . 90
- 4.14 Proton-antiproton invariant mass spectrum for candidates coming from primary vertex for 2012 year data (top), with visually subtracted background (bottom). The  $J/\psi$  mass and the difference  $\Delta M_{J/\psi, \eta_c} = M_{J/\psi} - M_{\eta_c}$  are left as free parameters in the fit . . . . . 91
- 4.15 Event mixing: the invariant mass of the  $p\bar{p}$  candidates (top) and  $\mu^+\mu^-$  candidates (bottom). Mixed events spectra are represented by the black solid line, red crosses correspond to data points. The dashed black line stays for proton event mixing with an angular constraint . . . . . 92

4.16	Estimation of the systematic uncertainty from a potential charmonium spectrum difference at production. The $p\bar{p}$ invariant mass spectrum is reweighted using the efficiency, as described in the text . . . . .	100
4.17	Estimate of the $J/\psi$ cross section in the $p_T$ interval $6.5 \text{ GeV}/c < p_T < 7.0 \text{ GeV}/c$ for the 2011 and 2012 data. Interpolation (third order polynomial, solid line) and fit with the exponential function (dashed line) to estimate corresponding systematic uncertainty . . . . .	106
4.18	The relative $\eta_c$ to $J/\psi$ $p_T$ spectrum for the 2011 (filled triangles) and 2012 (empty triangles) data. Prompt production spectra are shown on a) and b) for the prompt charmonium production and inclusive charmonium production in $b$ -hadron decays, respectively. See the text for more details	109
4.19	The $p_T$ spectrum for $\eta_c$ (empty circles) from the present analysis and $J/\psi$ (filled circles) from Refs. [49, 37, 50]. Prompt production spectra are shown on a) and b) for the 2011 and 2012 data respectively. The spectra, corresponding to inclusive charmonium production in $b$ -hadron decays, are shown on c) and d) for the 2011 and 2012 data respectively. See the text for more details . . . . .	110
4.20	MC reconstructed $p_T$ spectra for promptly produced $J/\psi$ (squares) and $\eta_c$ (circles) . . . . .	111
4.21	Prompt $\eta_c$ production cross-section . . . . .	112
4.22	Invariant mass spectrum of the $p\bar{p}$ combinations in bins of $\cos\theta$ . Selection on $\cos\theta$ applied, left to right, top to bottom: $-1.0 < \cos\theta < -0.6$ , $-0.6 < \cos\theta < -0.6$ , $-0.2 < \cos\theta < 0.2$ , $0.2 < \cos\theta < 0.6$ , $0.6 < \cos\theta < 1.0$ . . . . .	113
4.23	Fit of the $\cos\theta$ distribution of for $\eta_c \rightarrow p\bar{p}$ candidates . . . . .	114
4.24	Fit of the $\cos\theta$ distribution of for $J/\psi \rightarrow p\bar{p}$ candidates . . . . .	114
4.25	The $\Gamma_{\eta_c}$ , $M_{\eta_c}$ contour plots for the 2011 (red solid curves) and 2012 (blue dashed curves) data samples. The two curves indicate one-sigma and two-sigma contours for the one-dimensional distribution. Only statistical uncertainties are shown. The PDG [11] value is indicated as a point with error bars . . . . .	119
4.26	Contour plot of $\Gamma_{\eta_c}$ and $M_{\eta_c}$ for the combined data sample. The curves indicate 68.3 C.L. (one-sigma) and 95.5 C.L. (two-sigma) for two-dimensional distribution. Only statistical uncertainties are shown. The PDG [11] value is indicated as a point with error bars. . . . .	119

---

4.27	The fit of the $\chi_{c0,1,2}$ and $h_c$ candidates in $\sqrt{s} = 7$ TeV data sample. . . .	120
4.28	The fit of the $\chi_{c0,1,2}$ and $h_c$ candidates in $\sqrt{s} = 8$ TeV data sample. . . .	121
4.29	Logarithm likelihood profiles of the $\chi_{c0,1,2}$ and $h_c$ yields from promptly produced $p\bar{p}$ candidates of 2011 year data . . . . .	122
4.30	Logarithm likelihood profiles of the $\chi_{c0,1,2}$ and $h_c$ yields from promptly produced $p\bar{p}$ candidates of 2012 year data . . . . .	123
1	Selection criteria optimisation for the charmonium sample from $b$ -hadron decays . . . . .	132
2	Selection criteria optimisation for prompt the charmonium sample . . .	133

# List of Tables

1.1	A list of the SM fermions. The corresponding quantum numbers are given for the leptons and quarks: mass, electrical charge $Q$ , weak isospin $T_3^W$ and hypercharge $Y_W$ for the left handed and right handed states. The $e$ and $\mu$ masses are known with $\mathcal{O}(10^{-8})$ precision. Neutrino mass limits are given at 95% Confidence Limit for $\nu_e$ and $\nu_\tau$ and at 90% for $\nu_\mu$ . For quarks only isospin projection $T_3$ , strangeness $S$ and charm $C$ are defined [?, 11]. Different quantum numbers, associated with the rest of the quark flavours, are not considered in this overview, but may be found in Ref. [?].	10
1.2	Inclusive branching fractions $\times 10^{-3}$ for mixtures of $b$ -hadrons to decay into charmonium states. [29]	34
1.3	Quantum numbers of quarkonium states and a minimal number of virtual gluons and photons produced in annihilation. The subscript $d$ refers to a gluonic colour-singlet state that is totally symmetric under permutations of gluons. [29] [43]	35
2.1	Known charmonium states below the $D\bar{D}$ pair mass threshold. Branching fractions of charmonium states decaying to a proton-antiproton pair are from [44] for $h_c$ , and from Ref. [11] for all the other listed states	41
2.2	The LHCb results on the $J/\psi$ production into $2.0 < y < 4.5$	42
2.3	The inclusive yield of charmonium from $b$ -hadron decays [11].	45
2.4	Measurement of the $\eta_c$ properties. Refs. [75] and [76] perform simultaneous fit of the 6 and 16 $\eta_c$ decay channels respectively. Ref. [79] uses recoil mass of the $\eta_c$ .	50
4.1	Selection criteria for prompt charmonium candidates and charmonium candidates from $b$ -hadron decays	70

4.2	Selection criteria for prompt charmonium candidates and charmonium candidates from $b$ -hadron decays . . . . .	74
4.3	Efficiencies and cross-talk for prompt charmonium production and for charmonium production from $b$ -hadron decays, as obtained from MC. The errors reflect the available MC statistics . . . . .	75
4.4	Corrections weights $w_{i,j}$ due to $J/\psi$ polarisation, in bins of $p_T$ and rapidity $y$ . For the rapidity interval (3.5.4.5) the coefficient is assumed to be 1.0. For each bin correlated and uncorrelated uncertainties are summed	76
4.5	The $J/\psi$ and $\eta_c$ fit results from the MC samples. Mass $M$ , resolution of two Gaussian functions $\sigma^{a,b}$ and contribution of the “narrow” Gaussian function $k$ are shown . . . . .	79
4.6	Results of the fit of the proton-antiproton invariant mass spectrum for charmonium candidates from $b$ -hadron decays, for the 2011 and 2012 data samples. The event yields, $J/\psi$ mass and the $J/\psi$ to $\eta_c$ mass difference, $\eta_c$ natural width and resolution are shown, as well as the background parameters. The details of the fit are described in the text . . . . .	83
4.7	Results of the fit of the proton-antiproton invariant mass spectrum for prompt candidates from the 2011 and 2012 data. The event yields, $J/\psi$ mass and $J/\psi$ to $\eta_c$ mass difference are shown, as well as the background parameters. Note that for both $J/\psi$ mass and $J/\psi$ to $\eta_c$ mass difference, a Gaussian constraint is applied using the fit results from the analysis of charmonium production in $b$ -hadron decays. The details of the fit are described in the text . . . . .	86
4.8	The ratio $N_{\eta_c}^P/N_{J/\psi}^P$ depending on whether $\Delta_M = M_{J/\psi} - M_{\eta_c}$ is subject to the Gaussian constraint from the analysis of charmonium production in $b$ -hadron decays, left free parameter in the fit, or fixed to the PDG value, for $\sqrt{s} = 7$ TeV and 8 TeV data samples . . . . .	90
4.9	Systematic uncertainties in the analysis of charmonium production in $b$ -hadron decays using the 2011 data sample . . . . .	95
4.10	Systematic uncertainties in the analysis of charmonium production in $b$ -hadron decays using the 2012 data sample . . . . .	96
4.11	Systematic uncertainties for the prompt production analysis on the 2011 data . . . . .	98
4.12	Systematic uncertainties for the prompt production analysis on the 2012 data . . . . .	99

4.13	The $J/\psi$ cross section integrated over rapidity range, $2.0 < y < 4.5$ , in $p_T$ bins, the $\sqrt{s} = 7$ TeV and 8 TeV data . . . . .	107
4.14	Systematic uncertainty of the $J/\psi$ cross section measurements for the $\sqrt{s} = 7$ TeV and $\sqrt{s} = 8$ TeV analyses . . . . .	108
4.15	Systematic uncertainties (in $\text{MeV}/c^2$ ) for the measurement of the $J/\psi$ and $\eta_c$ mass difference, $\Delta M_{J/\psi, \eta_c} = M_{J/\psi} - M_{\eta_c}$ , using the 2011 and 2012 data samples . . . . .	116
4.16	Systematic uncertainties (in $\text{MeV}/c^2$ ) for the $J/\psi$ mass from the analysis of charmonium production in $b$ -hadron decays, using the 2011 and 2012 data samples . . . . .	117
4.17	Systematic uncertainties (in MeV) for the $\eta_c$ natural width $\Gamma$ from the analysis of charmonium production in $b$ -hadron decays, using the 2011 and 2012 data samples . . . . .	118
4.18	The $J/\psi$ mass $M_{J/\psi}$ , the mass difference $M_{J/\psi} - M_{\eta_c}$ and the $\eta_c$ natural width from the analysis of the 2011 and 2012 data samples, their average and the corresponding PDG values [11] . . . . .	118
4.19	Limits on $\chi_{c0,1,2}$ , $h_c$ mesons production at $\sqrt{s} = 7$ TeV . . . . .	121
4.20	Limits on $\chi_{c0,1,2}$ , $h_c$ mesons production at $\sqrt{s} = 8$ TeV . . . . .	123
1	The $J/\psi$ cross section in $p_T$ and rapidity bins, $\sqrt{s} = 7$ TeV results . . .	135
2	The $J/\psi$ cross section in $p_T$ and rapidity bins, $\sqrt{s} = 7$ TeV results, with the luminosity correction introduced . . . . .	136
3	The $J/\psi$ cross section in $p_T$ and rapidity bins, $\sqrt{s} = 8$ TeV results . . .	137

# Bibliography

- [1] E. D. Bloom, D. H. Coward, H. DeStaebler, J. Drees, G. Miller, L. W. Mo, R. E. Taylor, M. Breidenbach, J. I. Friedman, G. C. Hartmann, and H. W. Kendall. High-energy inelastic  $ep$  scattering at  $6^\circ$  and  $10^\circ$ . *Phys. Rev. Lett.*, 23:930–934, Oct 1969.
- [2] M. Breidenbach, J. I. Friedman, H. W. Kendall, E. D. Bloom, D. H. Coward, H. DeStaebler, J. Drees, L. W. Mo, and R. E. Taylor. Observed behavior of highly inelastic electron-proton scattering. *Phys. Rev. Lett.*, 23:935–939, Oct 1969.
- [3] S. Abachi et al. Search for high mass top quark production in  $p\bar{p}$  collisions at  $\sqrt{s} = 1.8$  TeV. *Phys.Rev.Lett.*, 74:2422–2426, 1995.
- [4] K. Kodama et al. Observation of tau neutrino interactions. *Phys.Lett.*, B504:218–224, 2001.
- [5] Serguei Chatrchyan et al. Observation of a new boson at a mass of 125 GeV with the CMS experiment at the LHC. *Phys.Lett.*, B716:30–61, 2012.
- [6] G. Aad et al. Observation of a new particle in the search for the Standard Model Higgs boson with the ATLAS detector at the LHC. *Phys.Lett.*, B716:1–29, 2012.
- [7] T. Morii, C.S. Lim, and S.N. Mukherjee. *The Physics of the Standard Model and Beyond*. World Scientific, 2004.
- [8] D. Griffiths. *Introduction to Elementary Particles*. Physics textbook. Wiley, 2008.
- [9] L.H. Ryder. *Quantum Field Theory*. Cambridge University Press, 1996.
- [10] R.P. Feynman, F.B. Morinigo, W.G. Wagner, and B. Hatfield. *Feynman Lectures on Gravitation*. Advanced Book Program. Westview Press, 2002.

- 
- [11] J. Beringer et al. Review of particle physics. *Phys. Rev.*, D86:010001, 2013. and 2013 partial update for the 2014 edition.
- [12] Ahmed Ali and Gustav Kramer. Jets and qcd: A historical review of the discovery of the quark and gluon jets and its impact on qcd. *Eur.Phys.J.*, H36:245–326, 2011.
- [13] W.E. Caswell and G.P. Lepage. Effective Lagrangians for Bound State Problems in QED, QCD, and Other Field Theories. *Phys.Lett.*, B167:437, 1986.
- [14] Hideki Yukawa. On the interaction of elementary particles. *Proc.Phys.Math.Soc.Jap.*, 17:48–57, 1935.
- [15] John G. Conway and Ralph D. McLaughlin. Possible Existence of a New Hyperon. *Phys.Rev.*, 96:541, 1954.
- [16] Alex R. Dzierba, Curtis A. Meyer, and Adam P. Szczepaniak. Reviewing the evidence for pentaquarks. *J.Phys.Conf.Ser.*, 9:192–204, 2005.
- [17] B. McKinnon et al. Search for the  $\theta^+$  pentaquark in the reaction  $\gamma \rightarrow pK^-K^+n$ . *Phys. Rev. Lett.*, 96:212001, Jun 2006.
- [18] R. De Vita et al. Search for the  $\theta^+$  pentaquark in the reactions  $\gamma p \rightarrow \bar{k}^0 K^+ n$  and  $\gamma p \rightarrow \bar{k}^0 K^0 p$ . *Phys. Rev. D*, 74:032001, Aug 2006.
- [19] B. Aubert et al. Evidence for the  $B^0 \rightarrow p\bar{p}K^{*0}$  and  $B^+ \rightarrow \eta_c K^{*+}$  decays and study of the decay dynamics of  $b$  meson decays into  $p\bar{p}h$  final states. *Phys. Rev. D*, 76:092004, Nov 2007.
- [20] S.K. Choi et al. Observation of a narrow charmonium-like state in exclusive  $B^\pm \rightarrow K^\pm \pi^+ \pi^- J/\psi$  decays. *Phys.Rev.Lett.*, 91:262001, 2003.
- [21] Bernard Aubert et al. Search for the  $Z(4430)^-$  at BABAR. *Phys.Rev.*, D79:112001, 2009.
- [22] S.K. Choi et al. Observation of a resonance-like structure in the  $\pi^\pm \psi'$  mass distribution in exclusive  $B \rightarrow K \pi^\pm \psi'$  decays. *Phys.Rev.Lett.*, 100:142001, 2008.
- [23] Roel Aaij et al. Observation of the resonant character of the  $Z(4430)^-$  state. *Phys.Rev.Lett.*, 112:222002, 2014.

- [24] Wolfgang Ochs. The Status of Glueballs. *J.Phys.*, G40:043001, 2013.
- [25] A.E. Blinov, Valery A. Khoze, and N.G. Uraltsev. Physics of Top and CP Violation in  $B$  Decays in the Light of the Argus Measurements. *Int.J.Mod.Phys.*, A4:1933, 1989.
- [26] J.J. Aubert et al. Experimental Observation of a Heavy Particle J. *Phys.Rev.Lett.*, 33:1404–1406, 1974.
- [27] J.E. Augustin et al. Discovery of a Narrow Resonance in  $e^+e^-$  Annihilation. *Phys.Rev.Lett.*, 33:1406–1408, 1974.
- [28] V. Luth, A. Boyarski, H.L. Lynch, Martin Breidenbach, F. Bulos, et al. The Quantum Numbers and Decay Widths of the  $\psi'(3684)$ . *Phys.Rev.Lett.*, 35:1124–1126, 1975.
- [29] N. Brambilla et al. Heavy quarkonium physics. 2004.
- [30] Geoffrey T. Bodwin, Eric Braaten, and G. Peter Lepage. Rigorous QCD analysis of inclusive annihilation and production of heavy quarkonium. *Phys.Rev.*, D51:1125–1171, 1995.
- [31] N. Brambilla, S. Eidelman, B.K. Heltsley, R. Vogt, G.T. Bodwin, et al. Heavy quarkonium: progress, puzzles, and opportunities. *Eur.Phys.J.*, C71:1534, 2011.
- [32] Aneesh V. Manohar. Heavy quark effective theory and nonrelativistic qcd lagrangian to order  $\alpha_s/m^3$ . *Phys. Rev. D*, 56:230–237, Jul 1997.
- [33] T. Barnes, S. Godfrey, and E.S. Swanson. Higher charmonia. *Phys.Rev.*, D72:054026, 2005.
- [34] T. Barnes. The XYZs of charmonium at BES. *Int.J.Mod.Phys.*, A21:5583–5591, 2006.
- [35] M. Jacob and G.C. Wick. On the general theory of collisions for particles with spin. *Annals of Physics*, 281(1–2):774 – 799, 2000.
- [36] John C. Collins and Davison E. Soper. Angular distribution of dileptons in high-energy hadron collisions. *Phys. Rev. D*, 16:2219–2225, Oct 1977.
- [37] R. Aaij et al. Measurement of  $J/\psi$  polarization in  $pp$  collisions at  $\sqrt{s} = 7$  TeV. *Eur. Phys. J.*, C73:2631, 2013.

- [38] Pietro Faccioli, Carlos Lourenco, and Joao Seixas. Rotation-invariant relations in vector meson decays into fermion pairs. *Phys.Rev.Lett.*, 105:061601, 2010.
- [39] Pietro Faccioli, Carlos Lourenco, Joao Seixas, and Hermine K. Wohri. Rotation-invariant observables in parity-violating decays of vector particles to fermion pairs. *Phys.Rev.*, D82:096002, 2010.
- [40] Gerhard A. Schuler. Quarkonium production and decays. *Phys.Rept.*, 1994.
- [41] Gouranga C. Nayak, Jian-Wei Qiu, and George F. Sterman. Fragmentation, factorization and infrared poles in heavy quarkonium production. *Phys.Lett.*, B613:45–51, 2005.
- [42] Gouranga C. Nayak, Jian-Wei Qiu, and George F. Sterman. Fragmentation, NRQCD and NNLO factorization analysis in heavy quarkonium production. *Phys.Rev.*, D72:114012, 2005.
- [43] Valeri Khoze. Private communication.
- [44] Sergey Barsuk, Jibo He, Emi Kou, and Benoit Viaud. Investigating charmonium production at LHC with the  $p\bar{p}$  final state. *Phys.Rev.*, D86:034011, 2012.
- [45] P. Abreu et al.  $J/\psi$  production in the hadronic decays of the Z. *Phys.Lett.*, B341:109–122, 1994.
- [46] O. Adriani et al.  $\chi_c$  production in hadronic Z decays. *Phys.Lett.*, B317:467–473, 1993.
- [47] D. Buskulic et al. Measurements of mean lifetime and branching fractions of  $b$ -hadrons decaying to  $J/\psi$ . *Phys.Lett.*, B295:396–408, 1992.
- [48] R. Aaij et al. Measurement of  $J/\psi$  production in  $pp$  collisions at  $\sqrt{s} = 2.76$  TeV. *JHEP*, 02:041, 2013.
- [49] R. Aaij et al. Measurement of  $J/\psi$  production in  $pp$  collisions at  $\sqrt{s} = 7$  TeV. *Eur. Phys. J.*, C71:1645, 2011.
- [50] R. Aaij et al. Production of  $J/\psi$  and  $\Upsilon$  mesons in  $pp$  collisions at  $\sqrt{s} = 8$  TeV. *JHEP*, 06:064, 2013.
- [51] R Aaij et al. Measurement of B meson production cross-sections in proton-proton collisions at  $\sqrt{s} = 7$  TeV. *JHEP*, 1308:117, 2013.

- [52] Vardan Khachatryan et al. Prompt and non-prompt  $J/\psi$  production in  $pp$  collisions at  $\sqrt{s} = 7$  TeV . *Eur.Phys.J.*, C71:1575, 2011.
- [53] G. Aad et al. Measurement of the differential cross-sections of inclusive, prompt and non-prompt  $J/\psi$  production in proton-proton collisions at  $\sqrt{s} = 7$  TeV . *Nucl.Phys.*, B850:387–444, 2011.
- [54] T. Abe et al. Belle II Technical Design Report. *arXiv e-prints*, 2010.
- [55] D. Boutigny et al. BaBar technical design report. 1995.
- [56] S. Anderson et al. Measurements of inclusive  $B \rightarrow \psi$  production. *Phys.Rev.Lett.*, 89:282001, 2002.
- [57] Bernard Aubert et al. Study of inclusive production of charmonium mesons in  $B$  decay. *Phys.Rev.*, D67:032002, 2003.
- [58] T. Himel, G. Trilling, G.S. Abrams, M.S. Alam, C.A. Blocker, et al. Observation of the  $\eta_c(2980)$  Produced in the Radiative Decay of the  $\psi'(3684)$ . *Phys.Rev.Lett.*, 45:1146, 1980.
- [59] R. Balest et al. Inclusive decays of  $B$  mesons to charmonium. *Phys.Rev.*, D52:2661–2672, 1995.
- [60] K. Abe et al. Observation of  $\chi_{c2}$  production in B meson decay. *Phys.Rev.Lett.*, 89:011803, 2002.
- [61] R Aaij et al. Measurement of  $\psi(2S)$  meson production in  $pp$  collisions at  $\sqrt{s} = 7$  TeV. *Eur.Phys.J.*, C72:2100, 2012.
- [62] Serguei Chatrchyan et al.  $J/\psi$  and  $\psi(2S)$  production in  $pp$  collisions at  $\sqrt{s} = 7$  TeV. *JHEP*, 1202:011, 2012.
- [63] B. Abelev et al. Inclusive  $J/\psi$  production in  $pp$  collisions at  $\sqrt{s} = 2.76$  TeV. *Phys.Lett.*, B718:295–306, 2012.
- [64] K.H. Ackermann et al. STAR detector overview. *Nucl.Instrum.Meth.*, A499:624–632, 2003.
- [65] Christopher Beresford Powell. Quarkonia production at the STAR detector. *J.Phys.Conf.Ser.*, 455:012038, 2013.

- [66] P. del Amo Sanchez et al. Observation of  $\eta_c(1S)$  and  $\eta_c(2S)$  decays to  $K^+K^-\pi^+\pi^-\pi^0$  in two-photon interactions. *Phys.Rev.*, D84:012004, 2011.
- [67] J.P. Lees et al. Measurement of the  $\gamma\gamma^* \rightarrow \eta_c$  transition form factor. *Phys.Rev.*, D81:052010, 2010.
- [68] S. Uehara et al. Study of charmonia in four-meson final states produced in two-photon collisions. *Eur.Phys.J.*, C53:1–14, 2008.
- [69] D.M. Asner et al. Observation of eta-prime(c) production in gamma gamma fusion at CLEO. *Phys.Rev.Lett.*, 92:142001, 2004.
- [70] A. Heister et al. Search for  $\gamma\gamma \rightarrow \eta_b$  in  $e^+e^-$  collisions at LEP-2. *Phys.Lett.*, B530:56–66, 2002.
- [71] R. Mizuk et al. Evidence for the  $\eta_b(2S)$  and observation of  $h_b(1P) \rightarrow \eta_b(1S)\gamma$  and  $h_b(2P) \rightarrow \eta_b(1S)\gamma$ . *Phys.Rev.Lett.*, 109:232002, 2012.
- [72] G. Bonvicini et al. Measurement of the  $\eta_b(1S)$  mass and the branching fraction for  $\Upsilon(3S) \rightarrow \gamma\eta_b(1S)$ . *Phys.Rev.*, D81:031104, 2010.
- [73] Bernard Aubert et al. Evidence for the eta(b)(1S) Meson in Radiative Upsilon(2S) Decay. *Phys.Rev.Lett.*, 103:161801, 2009.
- [74] Andreas Gessler. Latest results on  $b$ -hadron spectroscopy from CDF. *J.Phys.Conf.Ser.*, 110:022011, 2008.
- [75] M. Ablikim et al. Measurements of the mass and width of the  $\eta_c$  using  $\psi' \rightarrow \gamma\eta_c$ . *Phys.Rev.Lett.*, 108:222002, 2012.
- [76] M. Ablikim et al. Study of  $\psi(3686) \rightarrow \pi^0 h_c, h_c \rightarrow \gamma\eta_c$  via  $\eta_c$  exclusive decays. *Phys.Rev.*, D86:092009, 2012.
- [77] A. Vinokurova et al. Study of  $B^{+-} \rightarrow K^\pm(K_S K \pi)^0$  Decay and Determination of  $\eta_c$  and  $\eta_c(2S)$  Parameters. *Phys.Lett.*, B706:139–149, 2011.
- [78] Bernard Aubert et al. Study of B-meson decays to  $\eta_c K^*$ ,  $\eta_c(2S)K^*$  and  $\eta_c \gamma K^*$ . *Phys.Rev.*, D78:012006, 2008.
- [79] K. Abe et al. Observation of a new charmonium state in double charmonium production in  $e^+e^-$  annihilation at  $\sqrt{s}10.6$  GeV. *Phys.Rev.Lett.*, 98:082001, 2007.

- 
- [80] R.E. Mitchell et al.  $J/\psi$  and  $\psi(2S)$  Radiative Decays to  $\eta_c$ . *Phys.Rev.Lett.*, 102:011801, 2009.
- [81] J. Beringer et al. Review of Particle Physics, 2012-2013. Review of Particle Properties. *Phys. Rev. D*, 86(1):010001, 2012.
- [82] K. Nakamura et al. Review of Particle Physics, 2010-2011. Review of Particle Properties. *J. Phys. G*, 37(7A):075021, 2010.
- [83] C. Amsler et al. Review of Particle Physics, 2008-2009. Review of Particle Properties. *Phys. Lett. B*, 667(1-5):1–6, 2008.
- [84] W. M. Yao et al. Review of Particle Physics, 2006-2007. Review of Particle Properties. *J. Phys. G*, 33:1–1232, 2006.
- [85] S. Eidelman et al. Review of Particle Physics, 2004-2005. Review of Particle Properties. *Phys. Lett. B*, 592:1–5, 2004.
- [86] K. Hagiwara et al. Review of Particle Physics, 2002-2003. Review of Particle Properties. *Phys. Rev. D*, 66(1):010001, 2002.
- [87] D. E. Groom et al. Review of Particle Physics, 2000-2001. Review of Particle Properties. *Eur. Phys. J. C*, 15:1–878, 2000.
- [88] C. Caso et al. Review of Particle Physics, 1998-1999. Review of Particle Properties. *Eur. Phys. J. C*, 3(1-4):1–794, 1998.
- [89] R. M. Barnett et al. Review of Particle Physics, 1996-1997. Review of Particle Properties. *Phys. Rev. D*, 54(1):1–708, 1996.
- [90] Oliver Sim Brüning, Paul Collier, P Lebrun, Stephen Myers, Ranko Ostojic, John Poole, and Paul Proudlock. *LHC Design Report*. CERN, Geneva, 2004.
- [91] Jr. Alves, A. Augusto et al. The LHCb Detector at the LHC. *JINST*, 3:S08005, 2008.
- [92] LHCb technical design report: Reoptimized detector design and performance. 2003.
- [93] Barbosa-Marinho et al. *LHCb VELO (Vertex Locator): Technical Design Report*. Technical Design Report LHCb. CERN, Geneva, 2001.

- [94] J. Tilburg. Tracking performance in lhcb. *The European Physical Journal C - Particles and Fields*, 34(1):s397–s401, 2004.
- [95] Roel Aaij et al. Measurements of the  $B^+$ ,  $B^0$ ,  $B_s^0$  meson and  $\Lambda_b^0$  baryon lifetimes. *JHEP*, 1404:114, 2014.
- [96] N. Brook et al. LHCb RICH1 Engineering Design Review Report. Technical Report LHCb-2004-121. CERN-LHCb-2004-121, CERN, Geneva, Oct 2005.
- [97] M. Adinolfi et al. LHCb RICH 2 engineering design review report. Technical Report LHCb-2002-009, CERN, Geneva, Mar 2002. revised version number 1 submitted on 2002-05-21 14:24:22.
- [98] M. Adinolfi et al. Performance of the LHCb RICH detector at the LHC. *Eur. Phys. J. C*, 73(arXiv:1211.6759. CERN-LHCb-DP-2012-003. LHCb-DP-2012-003):2431. 25 p, Nov 2012.
- [99] S. Amato et al. *LHCb RICH: Technical Design Report*. Technical Design Report LHCb. CERN, Geneva, 2000.
- [100] M. Pivk and F.R. Le Diberder. *Plot: a quick introduction*. Imperial College Press, Covent Garden, London, UK, page 173, 2006.
- [101] R Aaij et al. Measurement of  $b$ -hadron branching fractions for two-body decays into charmless charged hadrons. *JHEP*, 1210:037, 2012.
- [102] Irina Machikhiliyan and the LHCb calorimeter group. Current status and performance of the LHCb electromagnetic and hadron calorimeters. *Journal of Physics: Conference Series*, 293(1):012052, 2011.
- [103] Antunes-Nobrega et al. *LHCb trigger system: Technical Design Report*. Technical Design Report LHCb. CERN, Geneva, 2003.
- [104] R Aaij, J Albrecht, F Alessio, S Amato, E Aslanides, et al. The LHCb Trigger and its Performance in 2011. *JINST*, 8:P04022, 2013.
- [105] Alessio Federico. Status and Results of the LHCb Experiment. *Acta Phys. Pol. B*, 43(LHCb-PROC-2012-016. CERN-LHCb-PROC-2012-016):1399–1412. mult. p, Mar 2012.

- [106] Pascal Perret. Status and Prospects for Heavy Flavour Physics at LHC. Future and prospects in flavour physics from LHCb, ATLAS and CMS. *PoS, HQL2010:081*. 6 p, Dec 2010. LHCb-TALK-2010-146.
- [107] R Aaij et al. Measurement of the relative rate of prompt  $\chi_{c0}$ ,  $\chi_{c1}$  and  $\chi_{c2}$  production at  $\sqrt{s} = 7\text{TeV}$ . *J. High Energy Phys.*, 10(arXiv:1307.4285. CERN-PH-EP-2013-114. LHCb-PAPER-2013-028):115. 22 p, Jul 2013.
- [108] R Aaij et al. Measurement of the cross-section ratio  $\sigma(\chi_{c2})/\sigma(\chi_{c1})$  for prompt  $\chi_c$  production at  $\sqrt{s} = 7\text{ TeV}$ . *Phys. Lett. B*, 714(arXiv:1202.1080. LHCb-PAPER-2011-019. CERN-PH-EP-2011-227):215–223. 13 p, Feb 2012.
- [109] Serguei Chatrchyan et al. Measurement of the relative prompt production rate of  $\chi(c2)$  and  $\chi(c1)$  in  $pp$  collisions at  $\sqrt{s} = 7\text{ TeV}$ . *Eur.Phys.J.*, C72:2251, 2012.
- [110] R Aaij et al. Measurement of the ratio of prompt  $\chi_c$  to  $J/\psi$  production in  $pp$  collisions at  $\sqrt{s} = 7\text{ TeV}$ . *Phys. Lett. B*, 718(arXiv:1204.1462. CERN-PH-EP-2012-068. LHCb-PAPER-2011-030):431–440. 21 p, Apr 2012.
- [111] Sudhansu S. Biswal and K. Sridhar.  $\eta_c$  production at the Large Hadron Collider. *J.Phys.*, G39:015008, 2012.
- [112] F. Maltoni and A.D. Polosa. Observation potential for  $\eta_b$  at the Tevatron. *Phys.Rev.*, D70:054014, 2004.
- [113] Andrea Petrelli, Matteo Cacciari, Mario Greco, Fabio Maltoni, and Michelangelo L. Mangano. NLO production and decay of quarkonium. *Nucl.Phys.*, B514:245–309, 1998.
- [114] Johann H. Kuhn and E. Mirkes. QCD corrections to toponium production at hadron colliders. *Phys.Rev.*, D48:179–189, 1993.
- [115] M. Pivk and F.R. Le Diberder. A statistical tool to unfold data distributions. *Nuclear Instruments and Methods in Physics Research Section A: Accelerators, Spectrometers, Detectors and Associated Equipment*, 555(1-2):356 – 369, 2005.